The University of Nottingham
UNITED KINGDOM · CHINA · MALAYSIA

VIBRATION OF VISCOELASTIC SESSILE DROPLETS

BY JOSEPH K. BENNETT, BSc.
Student ID:4291356

Thesis submitted to the University of Nottingham for the degree of Master of Science (by Research)

Supervisor: Doctor James Sharp
project duration: October 2016-October 2017

Abstract

The surface of viscoelastic polymer solution droplets supported on substrates (sessile droplets) were excited through the application of an impulse supplied by mechanical oscillation of the surface upon which the sessile droplet was resting. The oscillations of these sessile droplets were filmed using a high-speed camera, and the footage was analysed to determine the waveform of the surface waves on the sessile droplets. This waveform was then Fourier transformed to give the vibrational spectra of the surface waves. These spectra were then used to compute the frequency dependent storage modulus (G') and loss modulus (G'') of the polymer solution. This was done by treating the droplet as a liquid bath with a width defined by the wave vector of the surface waves, and a depth defined by the average height of the droplet.

A theoretical model for viscoelastic waves in a liquid bath of finite depth was then used to calculate a theoretical power spectrum which corresponded to the experimental data, which in turn would produce values for the storage and loss moduli.

Finally, the contact angle dependence of the vibrational response of the sessile droplets was analysed in order to determine how the geometry of the sessile droplets effects the results of the experiment.

Contents

1 Introduction
1.1 Motivations……1
1.2 Background……2

2 Theory
2.1 Viscoelasticity
2.1.1 Viscosity……5
2.1.2 Elasticity……6
2.1.3 Viscoelasticity……6
2.2 surface tension……10
2.3 sessile droplets
2.3.1 Contact angle……12
2.3.2 Profile length……13
2.3.3 Capillary waves on sessile droplets……13
2.3.4 Damping of capillary waves ……16
2.4 Capillary waves on levitated droplets……18
2.5 The Jäckle model for surface waves on viscoelastic liquids……19

3 Experimental techniques
3.1 Polymer solution preparation……24
3.2 Substrate fabrication……25
3.2.1 Aluminium……25
3.2.2 Candle soot……26
3.2.3 Polystyrene……26
3.2.4 Polydimethylsiloxane (PDMS)……27
3.2.5 Silicon……27
3.2.6 Wax……27
3.3 Contact angle measurement……28
3.4 Video analysis……30
3.5 Frequency measurements……37

3.6 Dynamic light scattering analysis……..……...41
3.6.1 The general Stokes Einstein equation……..42
3.6.2 The autocorrelation function……43
3.6.3 Solution preparation……..…...46
3.6.4 Measuring procedure……..…48
3.6.5 Results……..….50

4 Surface tension of Polymer solutions
4.1 Introduction……..……55
4.2 the Young-Laplace equation……..……56
4.3 Experimental procedure……..……58
4.4 Results……63

5 Vibration of Sessile droplets
5.1 Introduction……..65
5.2 Experimental overview……..66
5.3 Pre-vibration……..……..72
5.4 Impulse amplitude……..……...73
5.5 Sessile droplet growth……..73
5.6 High contact angle substrates……..74
5.7 Experimental procedure……..74
5.8 Initial results……..……..76
5.9 Power spectrum analysis……..……96
5.10 Results……...102

6 Conclusion and future work
6.1 Conclusion……..119
6.2 Future work……..……120
6.2.1 Modification to the Jäckle equation……..120
6.2.2 Further investigation of the Jäckle model ……..121
6.2.3 Direct comparison between surface wave characteristics and viscoelastic properties……121
6.2.4 Electrostatic levitation……121
6.2.5 Complex biological fluid analysis……..122

Appendix
A.1 Average height of spherical cap……..125
weighted by volume

References ……..127

Chapter 1

Introduction

1.1 Motivation

The vibration of microlitre droplets has been studied for some time now as a means by which physical properties of liquids can be extracted from extremely small quantities of fluid. Such studies have yielded results which have found applications in areas such as fuel injection systems [1] and ink jet printing [2], along with many other potential applications in medical diagnosis. Such applications include so called "lab on a chip" devices [3] which can measure the chemical and physical properties of extremely small quantities of biological material (such as blood) and potentially be able to diagnose a range of illnesses such as bacterial or parasitical infections [4]. This kind of technology could prove invaluable when it comes to providing cost effective healthcare solutions in the developing world. Such devices may also find applications in the developed world, in areas such as home diagnostics, or reducing the costs of current medical diagnosis. A number of devices have also been constructed which can detect the presence of certain chemicals, producing a small electrical current (or some other measurable change) when specific chemicals interact with the surface [5]. This allows for these devices to be directly interfaced into computers, allowing for faster and more accurate diagnostic analysis.

An alternative approach to the analysis of microlitre volumes of liquids is to analyse their physical properties, such as how they response to mechanical stimulation. An example of such a technique involves studying the surface waves on sessile and pendant droplets of fluids to determine physical properties such as viscosity [6] and elasticity [7] of the liquid being studied. Previously studies of microlitre droplets have involved equipment which can be prohibitively expensive, as well as difficult to both construct and operate. Techniques such as magnetic levitation [8,9] have been successfully used in the past to derive the physical properties of complex liquids, including both the viscous and elastic components of their shear modulus [10]. Another method for analysing complex liquids is known as sessile droplet vibration. Sessile droplets are droplets of liquid than are placed upon a flat surface (known as a substrate) and allowed to adopt a shape which is energetically favourable. By mechanically stimulating these droplets, measurements of the standing waves which form across their surface can be take and used to determine the physical properties of the liquid in question. Sessile drop vibration techniques using superamphiphobic substrates (substrates that are both superhydrophobic and superoleophobic, repelling both polar and non-polar liquids) have also been used to successfully determine the physical properties of complex fluids [11,12].

Unfortunately, both techniques utilise equipment and materials which make their wider applications limited. This equipment is simply either too large, too expensive, or too difficult to produce to make its wider application viable, especially when one of the main driving motivations behind this research is to make this kind of analysis easier to conduct and more affordable.

This technology could find many applications in the commercial sector [13], where current techniques for chemical analysis are expensive, time consuming, or might decrease production efficiency. The chemical industry in particular is a prime candidate for the application of such technology, as inexpensive and reliable methods of analysing chemicals in a non-invasive manner could be very useful in the process of chemical synthesis, as well as potentially decreasing costs associated with research and development. Such techniques could also be easily applied in the medical fields, such as for the study of complex biological fluids for diagnostic purposes. For example, by studying the physical properties of blood as it coagulates (clots), Conditions such as thrombophilia could be diagnosed. This disorder is characterised by a patient's blood coagulating at an increased rate, which can potentially lead to blood clots within the body, which can very easily prove fatal. If such a condition could be diagnosed from the simple physical stimulating of a single drop of blood, such a disorder could be easily screened for and potentially save lives.

Because of this, there is a great deal of interest in deriving a method by which the mechanical properties of complex fluids can be easily and inexpensively determined. Such a technique could find applications in both the commercial and medical sectors, potentially proving invaluable in situation where low cost and ease of use are paramount. Such a technique would also be useful in situations where only a very small amount of a substance is available, or the substance is question is particularly expensive to produce.

The aim of this thesis is to develop such a technique and prove its value in determining the physical properties of a selection of viscoelastic polymer solutions. In addition, this analytical technique must be able to be used on opaque liquids, allowed for it to be used to analyse liquids such as blood.

1.2 Background

The investigation of drop vibration can be traced back to Lord Rayleigh [14] and Lord Kelvin [15], who derived mathematical models for the vibrational modes along the surface of a levitated droplet of inviscid liquid (liquids which have zero viscosity). This concept was expanded upon by Chandrasekhar [16], who expanded upon the concept by creating a mathematical model for the oscillation of a viscous liquid sphere. These models remained as theoretical models for a number of years, until the development of techniques such acoustic [17-23], aerodynamic [24,25], electrostatic [26], and magnetic levitation [27] allowed for these theoretical models to be experimentally verified.

Acoustic levitation [17-22] involves the creation of a high pressure standing wave, within which exist nodes of high pressure which are capable of supporting small droplets of liquid. Shen et al investigated the oscillation of acoustically levitated water droplets [17] and found that their physical behaviour agreed with the theoretical predictions made by Lord Rayleigh's model [15].

Aerodynamic levitation involves supporting the liquid droplet on a jet of gas expelled from a nozzle under pressure. Just like acoustic levitation, this technique can be used to determine the physical properties of liquids, such as their surface tension [23], density, and viscosity [24,25].

Acoustic and aerodynamic levitation techniques both share the issue of often having to deal with additional noise which is generated by the mechanism through which the droplets are levitated, which is not an issue which is shared by magnetic or electrostatic levitation.

When a material is placed within a magnetic field, it will produce a magnetic field of its own which will oppose the magnetic field in which it has been placed. Materials in which such an induced diamagnetic effect is the only magnetic contribution which the material makes are simply known as diamagnetic materials. Typically, the magnetic force produced by a diamagnetic material (such as water) is very small, however the force produced by the diamagnetic material is proportional to the gradient of the magnetic field in which it has been placed. If a large enough magnetic field is applied to a diamagnet, the diamagnetic response can become large enough to overcome gravity, allowing the object to levitate.

Diamagnetic levitation has recently been used by Hill and Eaves [8,28] to investigate the oscillations of viscous spheres of liquid, as well as Sharp et al to investigate the oscillations of viscoelastic droplets of polymer solutions [29].

Electrostatic levitation involves placing a charged droplet of liquid inside an electrical field, typically between two charged plates. The force exerted by the field of the charge droplet is enough to counteract the force of gravity, allowing the droplet to levitate. This technique requires notably less power than magnetic levitation and is slightly easier to carry out, however it does have a major drawback in that since the droplet is electrically charged, its physical properties are altered, which means that any measurements being taken on the physical behaviour of the droplet are compromised due to the fact that the droplet is charged.

Recently there has been increasing interest in the vibration of sessile droplets, as they offer the potential of being able to conduct experiments with the analytical capabilities of levitation experiments without the associated issues (such as cost). Harrold et al [11] investigated the behaviour of viscoelastic sessile droplets on superamphiphobic substrates (substrates that repel both polar and non-polar liquids), using the same mathematical analysis that Sharp [29] used to analyse the behaviour of levitated viscoelastic droplets. A liquid droplet on a superamphiphobic surface with a radius below the capillary length should maintain a spherical shape, with a contact angle close to 180°. Because of this, the physics of the two systems should be very similar. This line of logic proved fruitful, resulting in a model for sessile drops which could be used to derive the viscoelastic properties of complex fluids.

The technique utilized by Harrold et al [11] requires the use of superamphiphobic substrates [30]. Superamphiphobia is an artificial state (no naturally occurring superamphiphobic surfaces are known to exist) where a surface will repel both polar and non-polar liquids. Such surfaces are extremely difficult to fabricate and are often very fragile, which in turn limits the technique's capacity for real world application. Substrates that produce smaller contact angles are much easier to produce, leading to a number of authors attempting to produce theories that would accurately describe the behaviour of the sessile droplet vibration, regardless of contact angle [31-34]. By using the concept of standing waves forming on the surface of a sessile droplet (illustrated in figure 1.1) Noblin et al successfully derived a model that described the vibrational characteristics of sessile droplets of simple liquids [35]. Sharp et al used Noblin's work to demonstrate the potential of using sessile drop vibration to determine the physical properties of liquids. Sharp et al also demonstrated that the resonance frequency of sessile drops was heavily influenced by contact angle, which was shown to be a result of the geometry of the sessile droplet [36].

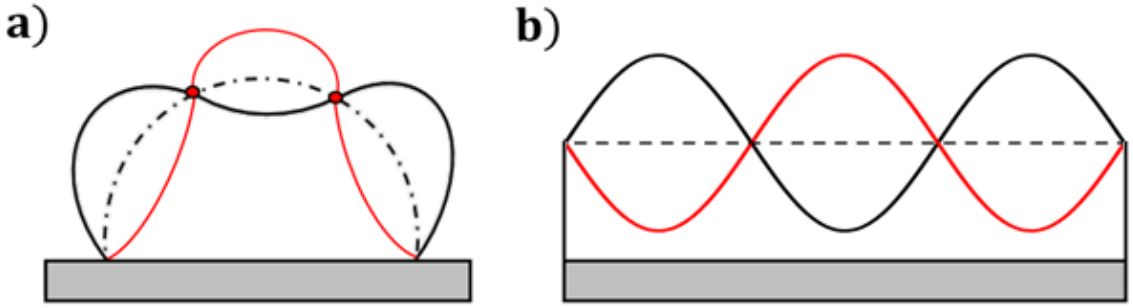


Figure 1.1: a) A diagram of the surface oscillations of a sessile droplet. The dashed line shows the position of the surface at rest, with the solid black and red lines showing the extremes of surface deformation as the droplet's surface oscillates. The point at which the solid and dashed lines intersect one another are the node points of the standing wave (red circles). Figure b) shows how the waves on the surface of the sessile droplet in figure a) can be represented as a standing wave.

In this thesis, the oscillation of viscoelastic sessile droplets on substrates with a range of contact angles will be measured, with the aim of determining how the contact angle influences the frequency and damping of the surface waves on sessile droplets. Following this, attempts will be made to produce a model with which the storage and loss moduli of viscoelastic sessile droplets with varying contact angles can be determined. This will involve modelling sessile droplets as thin films of finite depth and applying a viscoelastic wave model derived by Jäckle [37] in order to calculate what are known as the Storage and Loss modulus for a range of viscoelastic solutions. The Storage modulus measures how much energy is stored within a viscoelastic material after a shear displacement, representing the elastic response of the material. The loss modulus measures how much energy is lost from the system (dissipated as heat), representing the viscous response of the material.

The hope is that this model will be able to determine the viscoelastic properties of any sessile droplet, regardless of contact angle. Such a model would prove invaluable for determining the physical properties of small quantities of viscoelastic liquids, and would prove invaluable in many areas of commercial and scientific research where traditional rheological measuring techniques cannot be applied.

Chapter 2
Theory

This section will contain a brief introduction to the physics of viscoelasticity, as well as covering the necessary information required to understand the physics of sessile droplet vibration.

2.1 Viscoelasticity

2.1.1 Viscosity

Viscosity is a measure of a liquid's resistance to deformation under shear stress. All liquids have a viscosity, with a handful of exceptions which have been dubbed 'superfluids' [38], which can only exist under certain well-controlled conditions. An example of a superfluid is liquid helium-4 (an isotope of helium) which has been cooled to 2.17 k (under one atmosphere of pressure). Viscosity can be thought of as a quantity that represents the internal friction of a system. As particles and molecules flow past each other, they will experience friction which will oppose their movement. A fluid which possesses only viscous characteristics are know as Newtonian fluids.

No know fluid possesses purely viscous characteristics, however many fluids such as water can be treated as Newtonian fluids under standard conditions. Viscosity is commonly defined via the use of the two-plate model (figure 2.1), in which a viscous liquid is placed between two plates, one of which will remain stationary, and the other is moved parallel to the surface of the liquid resulting in a lateral shear stress being applied to the liquid.

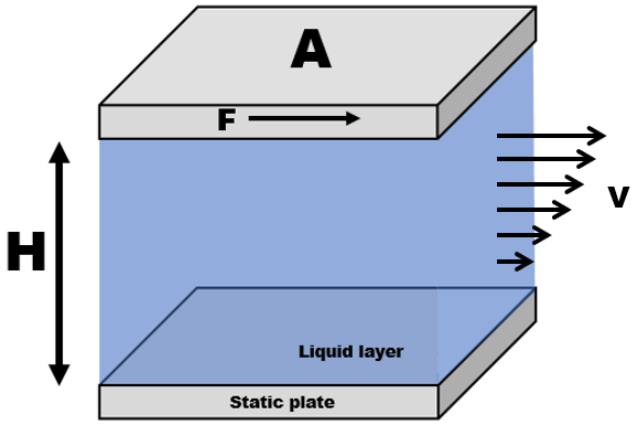


Figure 2.1: A diagram demonstrating the parameters by which viscosity is defined. A viscous liquid in positioned between plates separated by distance H, with surface area A.

The shear stress, τ is defined as the lateral force which is applied to the moving plate divided by the area of the plate. The rate at which the shear stress is applied to the liquid (the shear rate), $\dot{\gamma}$ is defined as the velocity of the moving plate divided by the distance between the two plates.

$$\tau = \frac{F}{A} \tag{2.1}$$

$$\dot{\gamma} = \frac{V}{H} \tag{2.2}$$

The viscosity (measured in Pascal seconds, Pas) of the liquid is defined as the shear stress divided by the shear rate. This is the mathematical definition of Newton's law of viscosity.

$$\eta = \frac{\tau}{\dot{\gamma}} \tag{2.3}$$

A fluid is Newtonian if at a given temperature it obeys this mathematical law, regardless of the shear rate. Non-Newtonian fluids will not have a constant viscosity, instead their viscosity is dependent upon the shear rate ($\dot{\gamma}$).

2.1.2 Elasticity

Elastic materials obey Hooke's law, which states that the extent of deformation of an elastic material is proportional to the force applied to the material, provided that the elastic limit of the material has not been exceeded.

Ideal elastic materials possess a perfect memory, meaning that they will return to their original state once the force which caused their deformation is removed, providing that the deformation is small and do not causes plastic deformation. The energy which is exerted in the initial deformation of a perfectly elastic material is stored within the material, and released once the deforming force is removed.

2.1.3 Viscoelasticity

Viscoelastic materials possess both viscous and elastic characteristics when under deformation. These characteristics also depend on the time period over which these deformations are taking place. Maxwell was the first to describe viscoelastic materials by creating a model (shown in figure 2.2) which treated viscoelastic oscillations as the oscillations of spring attached to a dashpot (a device commonly used to damp oscillations). This model became the basis on which viscoelastic models were based, and is the reason why viscoelastic materials are sometimes referred to as Maxwell materials.

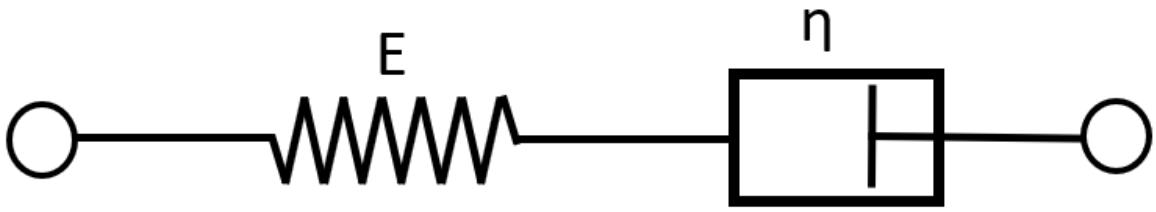
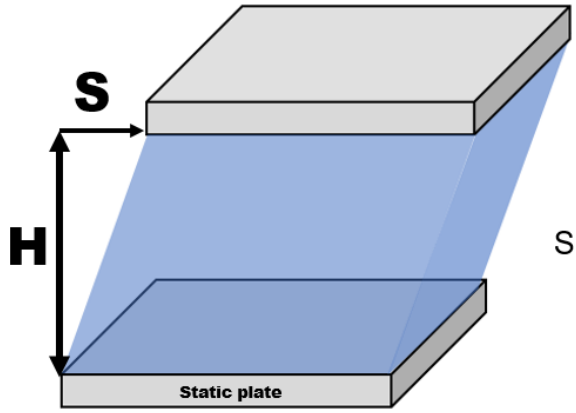


Figure 2.2: A diagram depicting the Maxwell model for viscoelastic materials, consisting of a spring with elasticity E and dashpot which damps the oscillations of the spring, simulating a viscosity η. This model provides a visual representation of the contributing factors that result in viscoelasticity.

The two-plate model (figures 2.1 and 2.3) can be used to define what is known as the shear modulus, which is the shear stress divided by the shear strain (γ).



$$\text{Shear strain } (\gamma) = \frac{\text{lateral deformation}}{\text{depth of material}} = \frac{S}{H}$$

$$\text{Shear stress } (\tau) = \frac{\text{Lateral force}}{\text{Area of plate}} = \frac{F}{A}$$

$$\text{Shear modulus } (G) = \frac{\tau}{\gamma}$$

Figure 2.3: The two-plate model for quantifying viscosity, as shown in figure 2.1. S represents the lateral deformation of the liquid contained between the two plates, given by the distance by which the top plate has moved parallel to the bottom plate.

A linear viscoelastic fluid is a fluid which has a linear relationship between the strain that is currently being experienced by the liquid and the history of strain of the fluid:

$$\tau(t) = \int_{-\infty}^{t} G(t - t')\dot{\gamma}(t')dt' \tag{2.4}$$

Where G(t) is the relaxation modulus of the fluid. In order to determine exactly what this is rheologists typically preform an oscillatory shear test. This test is normally carried out using a Couette device, which is essentially a pair of concentric cylinders, one of which is fixed in place and the other is able to rotate around its central axis. The material that is to be tested is placed between the two cylinders, and the free cylinder is then rotated back and forth in a harmonic motion. This device effectively replicates the two-plate model (as shown in figures 2.1 and 2.3), and allows for physical measurements of the material to be taken. To take a measure of the relaxation modulus, the moving plate (or moving cylinder, in the case of a Couette device) is set to move back and forth with a simple harmonic motion, with shear displacement:

$$\gamma(t) = \alpha\sin(\omega t) \tag{2.5}$$

Where γ is the shear strain, α is the amplitude of the oscillation, and ω is the angular frequency of the oscillation. Differentiating this equation yields:

$$\dot{\gamma}(t) = \alpha\omega\cos(\omega t) \tag{2.6}$$

Inserting this equation into equation 2.4 results in the equation:

$$\tau(t) = \int_{-\infty}^{t} G(t - t')\alpha\omega\cos(\omega t')\, dt' \tag{2.7}$$

Making the substitution Q=t-t' allows for this integral to be transformed, resulting in the equation:

$$\tau(t) = \alpha\omega \int_{0}^{\infty} G(Q)\cos(\omega(t - Q))\, dQ \tag{2.8}$$

The next step is to rewrite the cosine function in the form on an exponential. Substituting the equation:

$$\cos(\omega(t-Q)) = \mathrm{Re}[\exp[i\omega(t-Q)]] \tag{2.9}$$

Into equation 2.8 yields the equation:

$$\tau(t) = \alpha\omega \mathrm{Re}\left[\exp[i\omega t]\int_0^\infty G(Q)\exp[-i\omega Q]\,dQ\right] \tag{2.10}$$

This equation is now in the form of a one-sided Fourier transform. Since the equation has no dependence on t, it is simply just a complex number. By convention the complex shear modulus (G*) is defined as:

$$G^* = i\omega\int_0^\infty G(Q)\exp[-i\omega Q]\,dQ \tag{2.11}$$

With the real and imaginary parts:

$$G^* = G' + iG'' \tag{2.12}$$

The two-plate model can be used to help visualise exactly what the complex shear modulus actually represents. If the free plate in the two-plate model (or the free cylinder in a Couette device) is made to oscillate back and forth in a lateral direction, then the liquid between the two plates will oscillate at the same frequency (figure 2.4a). If the liquid is purely elastic (inviscid), then the oscillation of the liquid will be in phase with the oscillation of plate. However, liquids with a viscous component will oscillate out of phase with the plate (figure 2.4b).

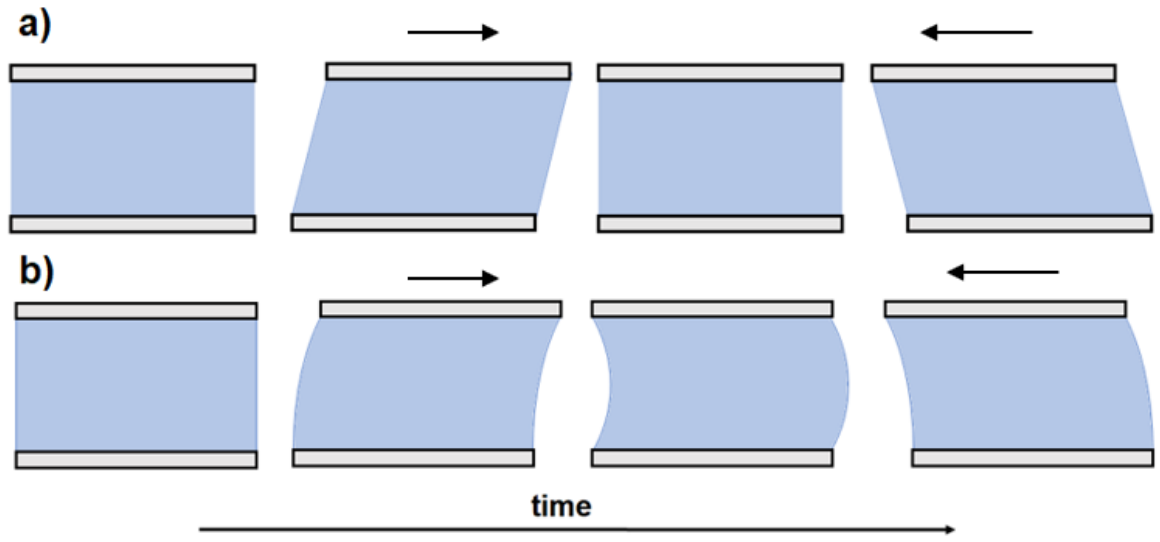


Figure 2.4: A diagram to demonstrate the physical shape of liquids positioned between two plates, in which the top plate is oscillating back and forth with a fixed frequency. Diagram a) shows the response of a purely elastic liquid, whereas diagram b) shows the response of a liquid with viscous characteristics. Note how the motion of liquid is synchronised with the movement of the top plate in diagram a, but slightly delayed in diagram b. The arrows indicate the direction of motion of the top plate.

The viscous and elastic components of the complex shear modulus can be deduced by examining the phase difference (δ) between the oscillation of the plate and the oscillation of the liquid.

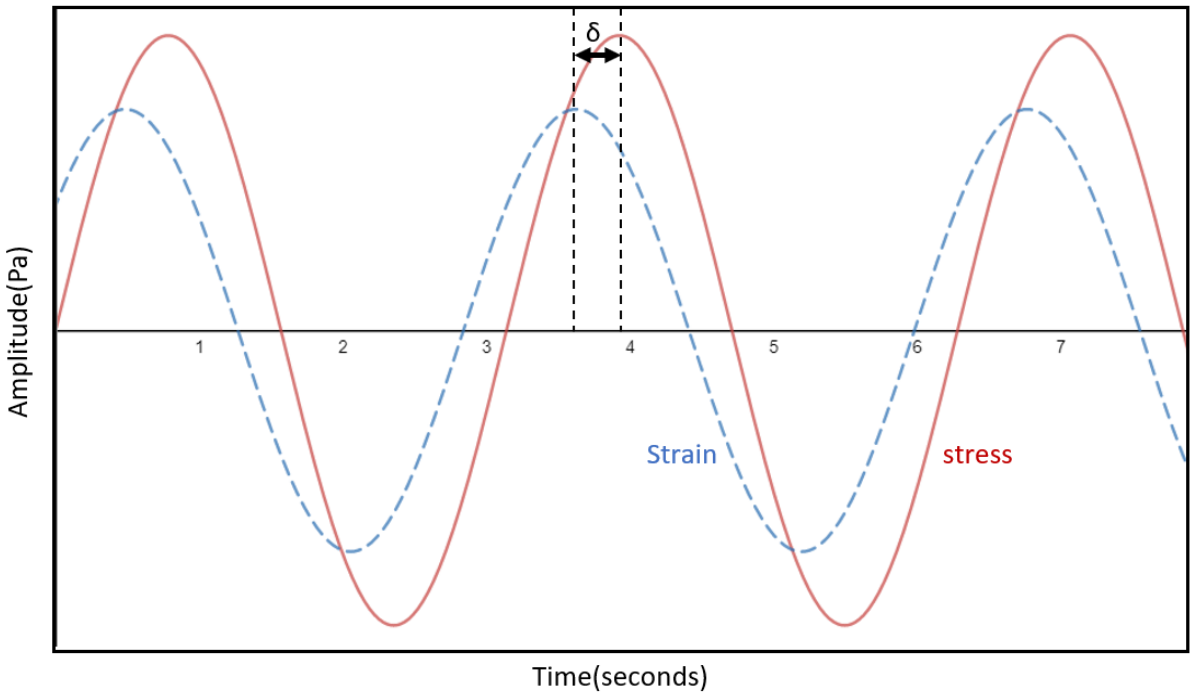


Figure 2.5: A graphical representation of the shear stress, τ (solid line), and shear strain, γ (dashed line) within a viscoelastic material over time. The phase difference is given as δ.

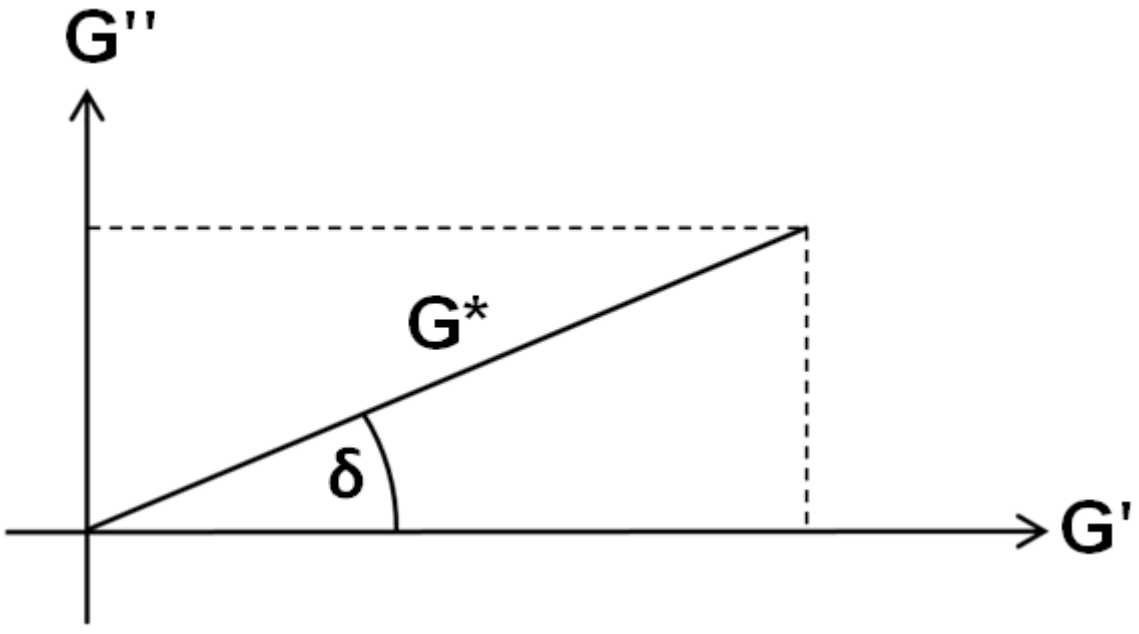


Figure 2.6: A trigonometric representation of the complex shear modulus (G*) of viscoelastic materials. G′ represents the elastic (storage) modulus, and G″ represents the viscous (loss) modulus. δ represents the phase difference between the shear stress and shear strain as shown in figure 2.4.

A purely elastic material will have no phase difference, meaning that G*=G′, whereas a purely viscous material will have a 90° phase difference, meaning that G*=G″. Viscoelastic materials possess both viscous and elastic characteristics, and therefore will have a phase difference between zero and 90°.

The Storage modulus (G′) is a measure of the elastic characteristics of the material and represents how well energy storage occurs when the material undergoes deformation. The loss modulus (G″) is a measure of the viscous characteristics of the material and represents how energy is lost when the material is deformed (dissipated through heat loss).

The complex shear modulus of a material can be used to calculate its complex viscosity by using the equation:

$$|\eta^*| = \frac{\sqrt{G'+G''}}{2\pi f} \tag{2.13}$$

where η* is the complex viscosity, G′ and G″ are the storage and loss moduli and f is the frequency of oscillation. This equation has been shown to hold true for low frequencies of oscillation [39]. The real and imaginary components of the complex viscosity are as follows:

$$\eta' = \frac{G'}{2\pi f} \tag{2.14}$$

$$\eta'' = \frac{G''}{2\pi f} \tag{2.15}$$

Where η′ is the real component of the complex viscosity, and η″ is the imaginary component of the complex viscosity.

2.2 Surface tension

Sessile and pendant drop vibrations are dominated by the surface tension of the droplet, provided that the radius of these droplets is below what is known as the capillary length. Surface tension, Ω is defined as the energy required to create an interface between a medium and a vacuum (or more commonly air). When molecules are fully surrounded by neighbouring molecules, forces such as Van der Waal and hydrogen bond interactions act between the molecules. Once a molecule moves to the surface of the media it will have fewer neighbouring molecules to interact with, resulting in what are known as dangling bonds. This is the cause of the phenomenon known as surface tension. The value of surface tension for water at 20°C is 72 mJ/m^2, whereas polymer solutions such as a 3.0% solution of Poly(acrylamide-co-acrylic) acid (which will be used in this investigation) will have a surface tension of 63 mJ/m^2 at 20°C (according to Harold et al [11]). Typically, γ is used to denote surface tension, however since γ was used previously in this paper to denote shear stress, Ω will be used instead in order to avoid confusion. The interfacial tension between two media can be defined as the amount of work that needs to be done to create a new interface between the two media in question. This is why surface tension is measured in joules per unit area. This can be displayed mathematically as:

$$\Omega = \frac{\delta W}{\delta A} \tag{2.16}$$

where δW is the amount of work done to create the interface, and δA is the change in surface area of the interface. Surface area is therefore measured in Jm-2, or Nm-1.

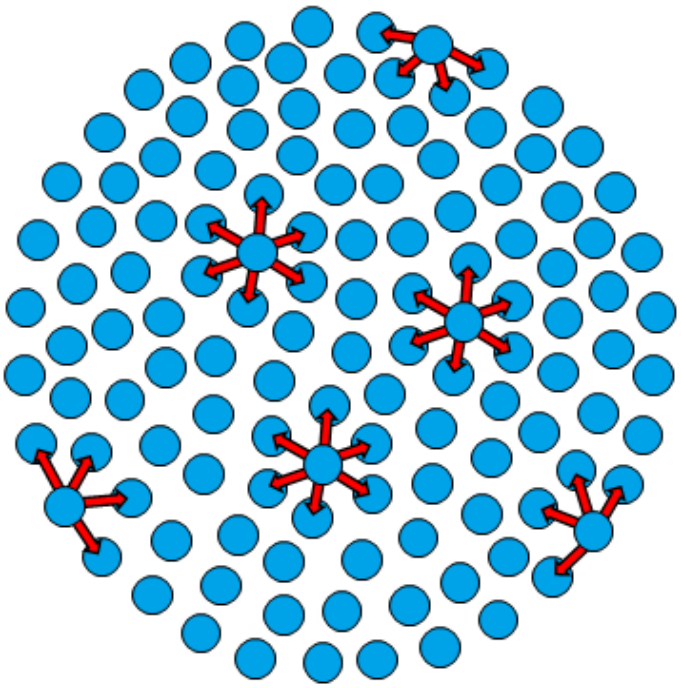


Figure 2.7: A diagram to represent the intermolecular forces present in a small droplet of liquid. The molecules of the liquid in question are represented by blue circles. The red arrows represent the exertion of intermolecular attractions (such as dipole interactions or Van der Waals forces). These arrows are only shown on certain molecules for the sake of clarity. The molecules on the inside of the droplet are attracted to numerous other molecules at the same time. Molecules on the surface of the droplet are surrounded by fewer molecules due to their physical position, and therefore exert a stronger attractive force on each individual neighbouring molecule.

Since molecules at the surface of a medium have higher free energy than those in the bulk of the media, it is energetically favourable for the material to adopt a shape in which its surface area is minimised. If for example, a droplet of liquid is suspended in free space, it will form a spherical shape to minimise its surface area and therefore decrease the amount of free energy present within the system [40].

If the volume of this droplet (are depicted in figure 2.7) is increased, its radius will eventually exceed what is known as the capillary length. Above the capillary length, the surface tension will not be enough to maintain the spherical shape of the droplet and if placed under the influence of gravity the droplet will be deformed. Below the capillary length, surface tension effects are dominant, and the droplet will remain spherical. The mass of the droplet does not increase linearly with surface area, resulting in the effects of gravity eventually overcoming those of surface tension.

Typically, the value for the capillary length is very small, for example the capillary length for water under standard conditions is about 2.7mm. The capillary length for a particular liquid can be calculated using the equation:

$$Lc = \sqrt{\frac{\Omega}{\rho g}} \tag{2.17}$$

Where Ω is the surface tension of the liquid, ρ is the density of the liquid, and g is the acceleration due to gravity.

2.3 Sessile droplets

A sessile drop is a droplet of liquid balanced on a substrate. The shape of this droplet is determined by the surface energies associated with the phase boundaries of the drop (as shown in figure 2.8). When the droplet is first applied to the substrate, the droplet will change shape until the forces acting upon the three-phase contact line are in equilibrium.

2.3.1 Contact angle

The three-phase contact line is the part of the surface of the droplet which is simultaneously in contact with the gas phase (air), the liquid phase, and the solid phase (substrate). The balance of these forces can be described in terms of the surface energies associated with the phase boundaries of the droplet.

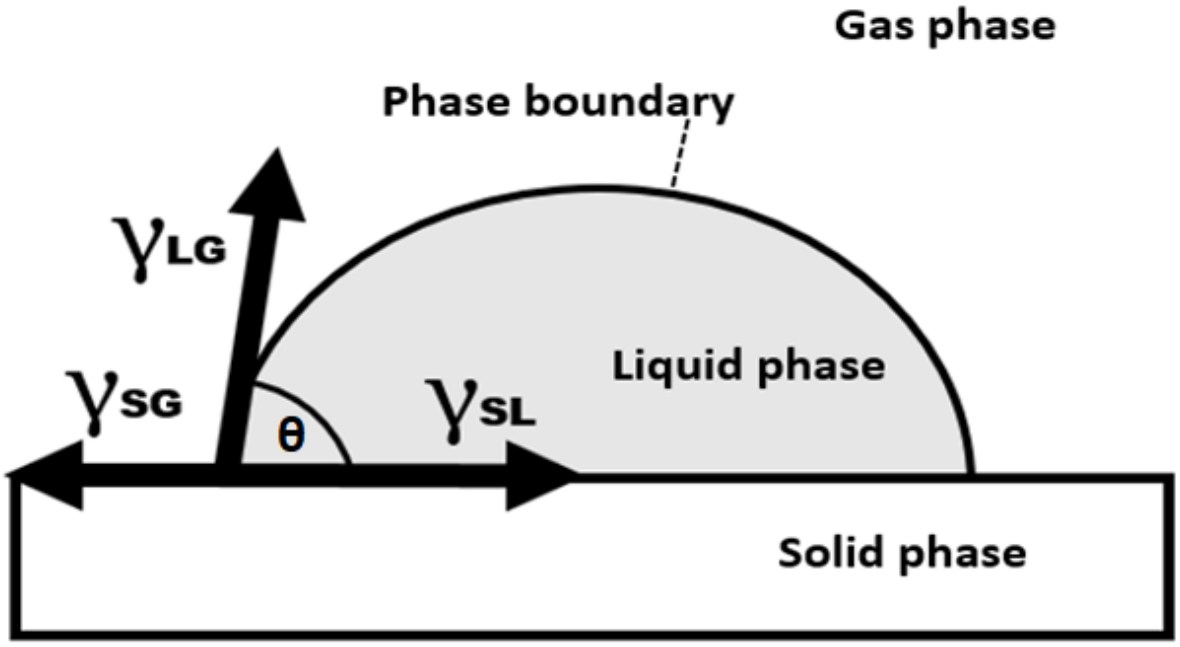


Figure 2.8: A diagram showing the balance of surface energies (Ω_{LG}, Ω_{SG}, and Ω_{SL}) around the three-phase contact line of a sessile droplet in a state of equilibrium. Ω_{LG}, Ω_{SG}, and Ω_{SL} are the surface energies of the liquid-gas phase boundary, the solid-gas phase boundary, and the solid-liquid phase boundary respectively. Θ is known as the contact angle of the sessile drop.

The equilibrium state between the surface tension of the liquid-gas, substrate-gas, and substrate-liquid interfaces is described by the Young's equation:

$$\Omega = \Omega_{SL} + \Omega_{LG}\cos(\theta) \tag{2.18}$$

where all variables have already been defined in figure 2.8. The equilibrium state is determined by resolving the forced acting on the droplet along the horizontal axis. The contact angle, θ is determined by how well the liquid wets the substrate. Many different factors contribute to how well a liquid will wet a substrate.

Differences in the chemical nature of the liquid and substrate may result in the substrate and the liquid being unable to form favourable interactions. This typically occurs when either the liquid or substrate is polar, and the substrate/liquid is non-polar. Surface roughness is also a major contributing factor, for if the area of the phase boundary that would be formed between the liquid and substrate is too great, it might be more energetically favourable for the droplet to form a smaller phase boundary. This would result in an extremely high contact angle, as the droplet effectively forms a sphere on the substrate.

2.3.2 Profile length

For levitated droplets the profile length was previously defined as the circumference of the droplet, however a more general definition is needed when referring to sessile droplets. The profile length is more commonly defined as the length of the liquid to gas (air) interface, or phase boundary (as shown in figure 2.8 and 2.9). This measurement is taken in the xy plane, which bisects the droplet across its centre.

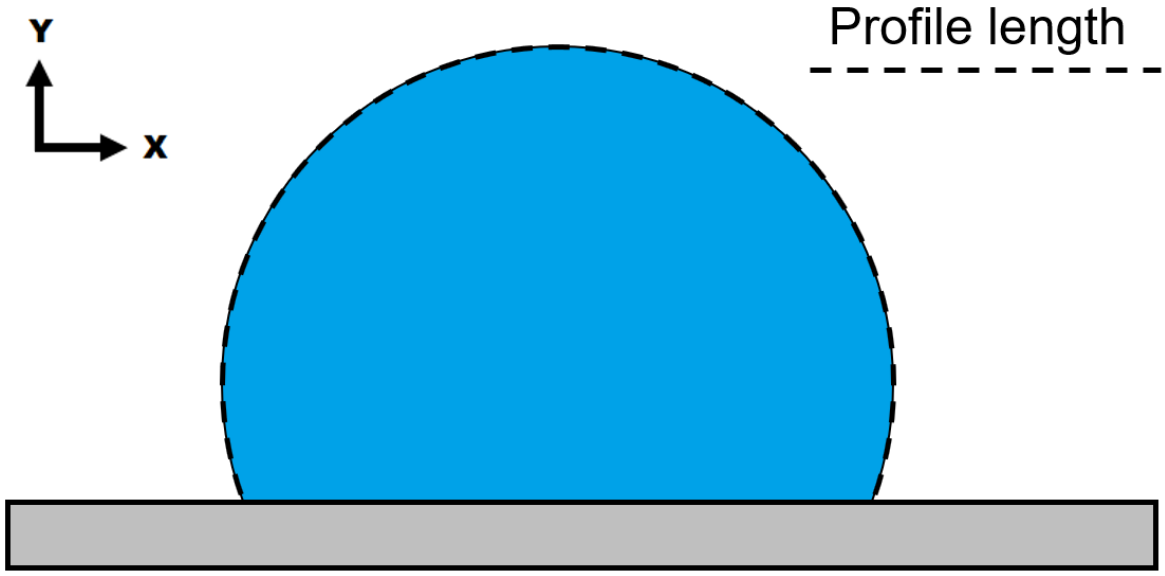


Figure 2.9: The definition of the profile length of a sessile droplet.

2.3.3 Capillary waves on sessile liquid droplets

A capillary wave is a wave which is travelling along the phase interface of a media which has a wavelength and amplitude that are both below the capillary length. When referring to sessile droplets, these capillary waves are often simply referred to as surface waves. Not all surface waves are capillary waves, as some are dominated by gravity, as opposed to surface tension. Waves on the surface of the open ocean (i.e. deep water) are good examples of surface waves which are dominated by gravity.

By using the model derived by Noblin et al [35], surface waves on sessile droplets can be modelled as standing waves propagating across the liquid-gas interface of the droplet (as previously illustrated in Figure 1.1). The mode number (n) of these standing waves is defined as the number of half wavelengths that can fit around the profile length of the sessile droplet.

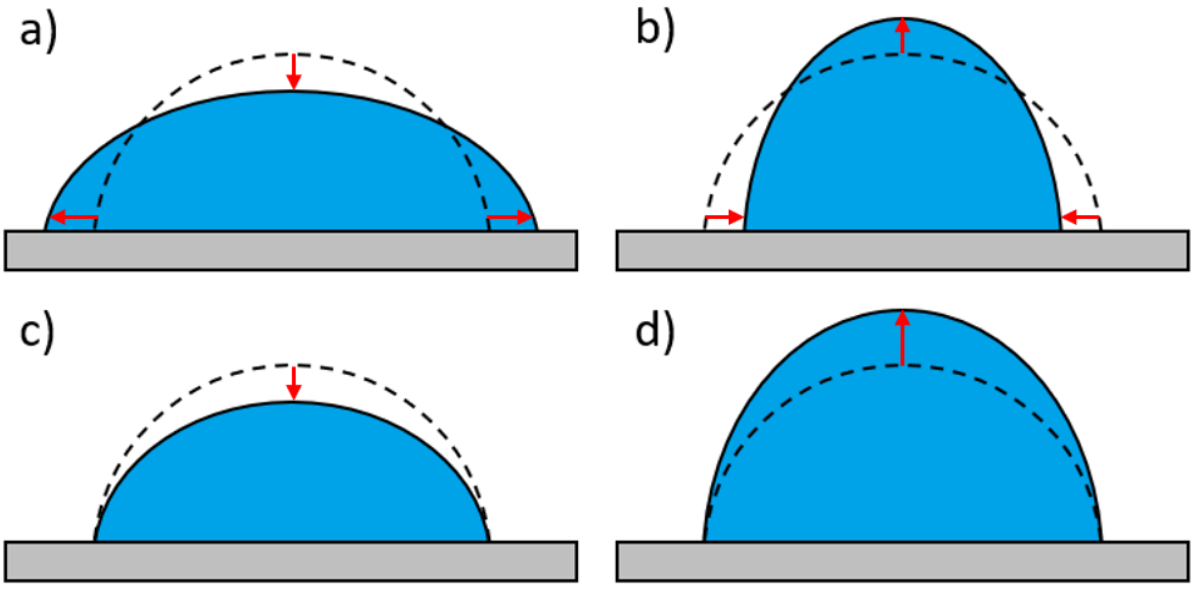


Figure 2.10: A diagram of the two possibilities for the first mode of oscillation, where one half of a wavelength can fit across the surface of the sessile droplet, and the three phase interface points correspond to nodes of the standing wave. The red arrows indicate the direction of oscillation. Figures a and b show the minimum and maximum amplitude of the surface wave corresponding to n=1 when the contact line is allowed to move across the surface of the substrate. Figures c and d show the minimum and maximum amplitude of the surface wave corresponding to n=1 when sessile droplet is pinned to the substrate.

Figures 2.10a and 2.10b show how the contact line of the sessile droplet moves back and forth as the droplet oscillates at the first mode of oscillation (n=1). In the following experiment this mode of oscillation will not be investigated as the movement of the contact line (as shown in figure 2.10a and 2.10b) introduces damping effects to the oscillation of the surface waves.

In order to accurately measure the viscosity of the liquid, the damping of the surface waves should only be influenced by the viscosity of the liquid, therefore in this investigation only modes of oscillation which allow the contact line to remain pinned in position will be investigated. Figure 2.10c and 2.10d shows an alternative form the first mode of oscillation, however this mode of oscillation would involve the volume of droplet changing over time. Since the mathematical models being used assumes that the liquids being used are incompressible, this mode of oscillation is not possible.

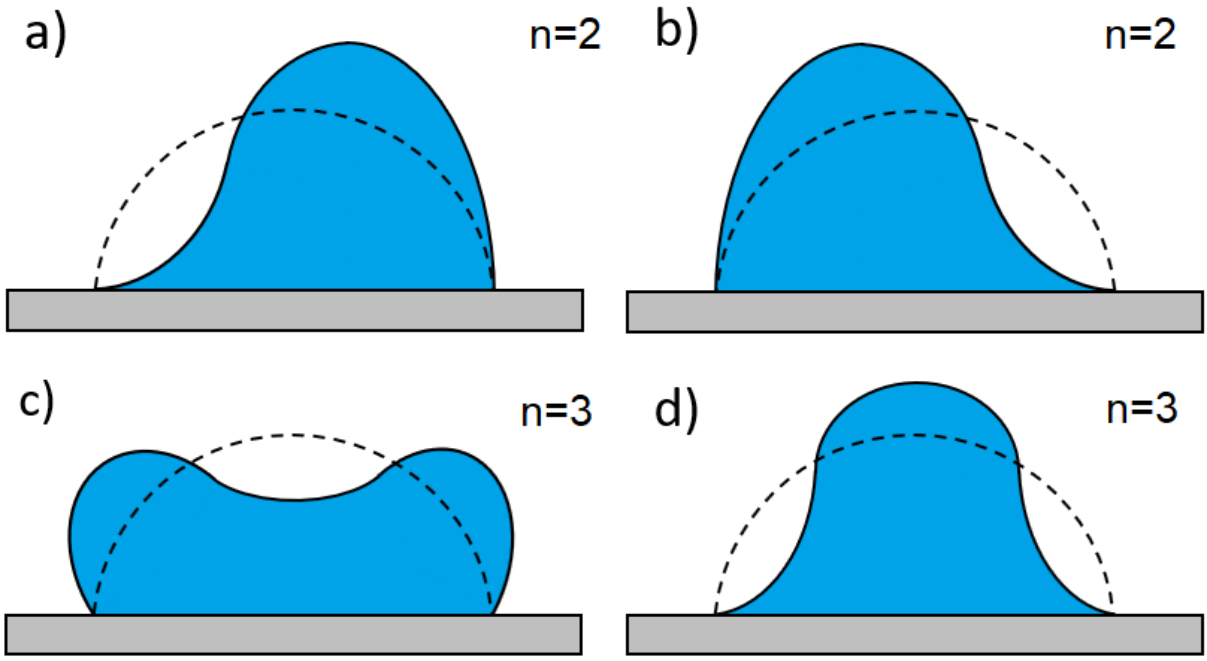


Figure 2.11: A diagram of the second and third mode of oscillation for a sessile droplet. Figures a and b show the two extremes of amplitude for surface wave corresponding to n=2. Figures c and d show the two extremes of amplitude for surface wave corresponding to n=3.

Figure 2.11 shows the second and third mode of oscillation of sessile droplets, which are the only modes of oscillation which will be examined in this thesis.

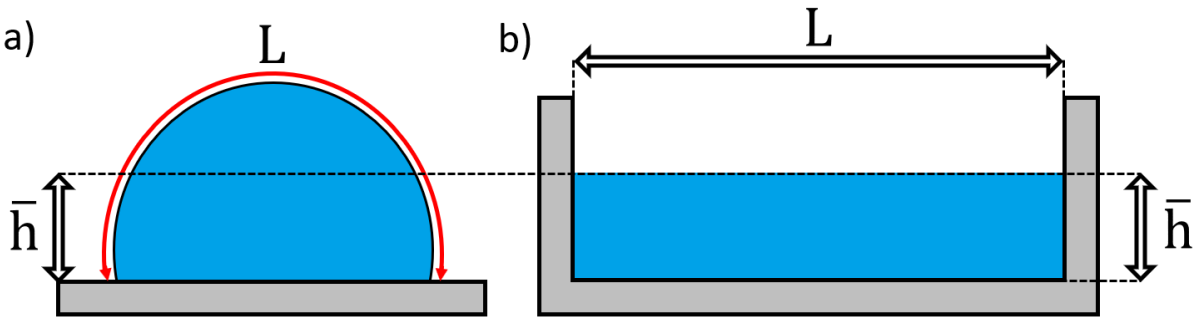


Figure 2.12: The Noblin model of sessile droplets. The sessile drop (a) is modelled as a liquid bath (b) with a length equal to the sessile drops profile length L and depth $\bar{h}$ (as defined previously).

Noblin's model only allows for a half integer number of wavelengths to exist along the surface of the sessile droplet. For the first mode of oscillation (figure 2.10), a half wavelength exists along the surface of the sessile droplet. For the second mode of oscillation (figure 2.11a and 2.11b) a full wavelength exists across the surface of the sessile droplet. For the third mode of oscillation (figure 2.11c and 2.11d) one and a half wavelengths exists across the surface of the sessile droplet, etc. This can be expressed in the equation:

$$L = \frac{n\lambda}{2} \tag{2.19}$$

where L is the profile length of the sessile droplet, n is the mode of oscillation, and λ is the wavelength of the capillary wave.

Noblin's model (figure 2.12) for surface waves on sessile droplets [35] treats the sessile drop as a liquid bath depth $\bar{h}$, with its length L equal to the profile length L. The depth of the bath is assumed to be equal to the average height of the sessile drop. Noblin approximated the height of the sessile drop to be the ratio of the drop's volume to the cross-sectional area of an XY plane intersect taken half way up the drop. The dispersion relation for the capillary waves on the surface of this liquid bath is given by:

$$\omega^2 = \left(g\rho + \frac{\Omega}{\rho}q^3\right)\tanh\left(q\bar{h}\right) \tag{2.20}$$

where ω is the angular frequency ($2\pi f$), g is the acceleration due to gravity, ρ is the density of the liquid, and Ω is the surface tension of the liquid. The wavenumber q is defined as $2\pi/\lambda$, where λ is the wavelength of the surface wave and can be defined as $2L/n$, as these are the only allowed wavelengths that can exist around the surface of the sessile droplet at resonance. Combining the definition for the wavenumber and the definition for the wavelength yields the equation:

$$q = \frac{\pi n}{L} \tag{2.21}$$

Provided that the radius of the sessile drop is below the capillary length, the effects of gravity will be nominal, allowing the gq term in equation 2.20 to be omitted, resulting in the equation:

$$\omega^2 = \frac{\Omega}{\rho}q^3\tanh\left(q\bar{h}\right) \tag{2.22}$$

Substituting equation 2.21 into equation 2.22, and substituting ω for $2\pi f$, yields the equation:

$$4\pi^2 f^2 = \frac{\Omega\pi^3 n^3}{\rho L^3}\tanh\left(q\bar{h}\right) \tag{2.23}$$

which can then be rearranged to form the equation:

$$f^2 = \frac{\Omega\pi n^3}{4\rho L^3}\tanh\left(q\bar{h}\right) \tag{2.24}$$

To compensate for the fact that the sessile drop is not actually a bath of finite depth, Sharp et al [36] determined a scaling factor between the theoretical prediction of the Noblin model and experimental data. The scaling factor was determined to be $\tanh(q\bar{h}) \approx 0.6561$.

2.3.4 Damping of capillary waves

The oscillation of sessile drops can be modelled as a damped harmonic oscillation:

$$A(t) = A_0 \mathrm{Sin}(2\pi f t + c)\exp(-\Gamma t) \tag{2.25}$$

where A_0 is the initial amplitude of the oscillation, f is the frequency, c is the phase shift, t is time, and Γ is the damping coefficient.

There are several sources of damping within sessile drops, the first of which is known as bulk viscous damping which occurs due to friction between molecules within the liquid generated when the sessile drop is oscillating. The damping of capillary waves on sessile droplet was recently consider by Sharp [41]. Since the oscillation of the capillary waves are being modelled as a damped harmonic oscillation, it is assumed the oscillation of the capillary waves decay exponentially with time, such that $e^{-\Gamma t}$. Bulk viscous damping [42] can be described with the equation:

$$\Gamma_{bulk} = \frac{2\eta}{\rho} q^2 \tag{2.26}$$

where all variables have been previously defined. Using the definition of the wavenumber (equation 2.21), along with the restriction of the Noblin model which only allows a half integer number of wavelengths to exist around the surface of a sessile droplet, equation 2.15 becomes:

$$\Gamma_{bulk} = \frac{2\eta}{\rho}\left(\frac{n\pi}{L}\right)^2 \tag{2.27}$$

Another source of damping is known as boundary layer damping, which occurs due to the fact that the sessile drop is pinned to the substrate, meaning that the velocity of the surface waves must reach zero when they reach the three-phase contact line. As demonstrated by Sharp [41] and Milner [43], for a surface wave travelling on a liquid bath, the velocity of the wave must decrease from its original value (its velocity as it travels through the bulk of the media) to zero over a distance given by the equation:

$$\delta = \left(\frac{\eta}{\pi\rho f}\right)^{\frac{1}{2}} \tag{2.28}$$

This equation can then be used to define the damping coefficient associated with boundary layer damping:

$$\Gamma_{boundary} = \frac{\omega\delta}{L} \tag{2.29}$$

Just like the Noblin model, it is assumed that the profile length is equal to the length of this theoretical liquid bath. By modifying and combining a number of these equation, and equation that defines the boundary layer damping coefficient using the variables in the Noblin model can be derived. The first step is to square equation 2.29, yielding the equation:

$$\Gamma_{boundary}^{\ 2} = \frac{\omega^2\delta^2}{L^2} \tag{2.30}$$

Next, the equation for angular frequency ($\omega=2\pi f$) is squared, and substituted into equation 2.30, yielding the equation:

$$\Gamma_{boundary}^{\ 2} = \frac{4\pi^2 f^2\delta^2}{L^2} \tag{2.31}$$

Equation 2.24 is then substituted into equation 2.31 to yield the equation:

$$\Gamma_{boundary}^{\ 2} = \frac{n^3\pi^3\delta^2\Omega}{\rho L^5}\tanh\left(q\overline{h}\right) \tag{2.32}$$

Finally, equation 2.28 is squared and substituted into equation 2.32, which (after taking the square root of the equation), yields:

$$\Gamma_{boundary} = \left(\frac{n^3\pi^2\eta\Omega\tanh(q\bar{h})}{f\rho^2L^5}\right)^{\frac{1}{2}} \quad (2.33)$$

Sharp [41] successfully showed that the L^{-2} dependence of the damping coefficient Γ_{bulk} (as defined in equation 2.17) closely matches the measurements taken for droplets with contact angles larger than 70°. For contact angles below 70° boundary layer damping effects become more significant.

2.4 Capillary waves on levitated droplets

By treating the gas phase as a perfect vacuum Pincus et al [44] derive a model for the dispersion relation (the relation between a wave's frequency and wavelength) for the surface waves of a semi-infinite media. This dispersion relation was found to be:

$$4\pi^2\rho(f + i\Delta f)^2 = \frac{4i(f+i\Delta f)(G_{ii}(f)-iG_i(f))k^2}{f} + \Omega k^3 \quad (2.34)$$

where q is the wavenumber and Δf is the width of the Fourier transform peak associated with the oscillation and is related to the damping coefficient of the oscillation by $\Delta f=\Gamma/\pi$. G' and G'' are respectively the elastic and viscous components of the complex shear modulus (known as the storage and loss moduli). A full explanation of the storage and loss moduli can be found in section 2.1.3.

By combining this model with Noblin's model [35] for capillary waves across the surface of a sessile drop which only permit certain wave modes to exist. This condition makes the definition of the wavevector $k=n\pi/L$.

By equating the real and imaginary parts of equation 2.34 and using $k=n\pi/L$ as the definition of the wavevector, an expression for the storage and loss moduli can be derived.

$$G' = \frac{\rho f^2L^2}{n^2}\left(1 - \frac{\pi\Omega n^3}{4\rho L^3(\Delta f^2+f^2)}\right) \quad (2.35)$$

$$G'' = \frac{\rho f\Delta fL^2}{n^2}\left(1 + \frac{\pi\Omega n^3}{4\rho L^3(\Delta f^2+f^2)}\right) \quad (2.36)$$

where G' and G'' are the storage (elastic) and loss (viscous) moduli respectively. These equations were used by Harrold et al [11] to examine the viscoelastic properties of spherical sessile droplets composed of a polymer solution. The values calculated using this method was found to closely correlate with data acquired from dynamic light scattering analysis. They were also used by Temperton et al [10] to examine the properties of magnetically levitated viscoelastic droplets, which were shown to agree with experimental data obtained from rheometric measurements (using a Malvern Kinexus rheometer).

Unfortunately, these equations fail to produce accurate results for the storage and loss moduli when they are applied to sessile droplets. Since the addition of a solid-liquid phase interface makes these equations invalid, another approach must be taken when analysing the viscoelastic properties of sessile droplets.

2.5 The Jäckle model for surface waves on viscoelastic liquids

By applying boundary conditions to monochromatic waves travelling through a viscoelastic liquid of finite depth Jäckle [37] derived an equation for the dynamic susceptibility of standing surface waves on an infinite liquid bath of finite depth. The dynamic susceptibility of a surface wave is the ratio of the surface displacement to the external force per unit area being applied to the surface. The dynamic susceptibility of a wave is proportional to its power spectrum, which can be derived directly from the wave's waveform.

The dynamic susceptibility of a surface wave travelling across a viscoelastic fluid is dependent upon both the viscous and elastic components of the liquid. This means that by measuring the waveform of a surface wave travelling across a viscoelastic fluid, the dynamic susceptibility, and in turn the viscoelastic properties of the fluid can in principle be derived. Jäckle began by considering a standing wave on a viscoelastic liquid bath of infinite depth, and infinite width.

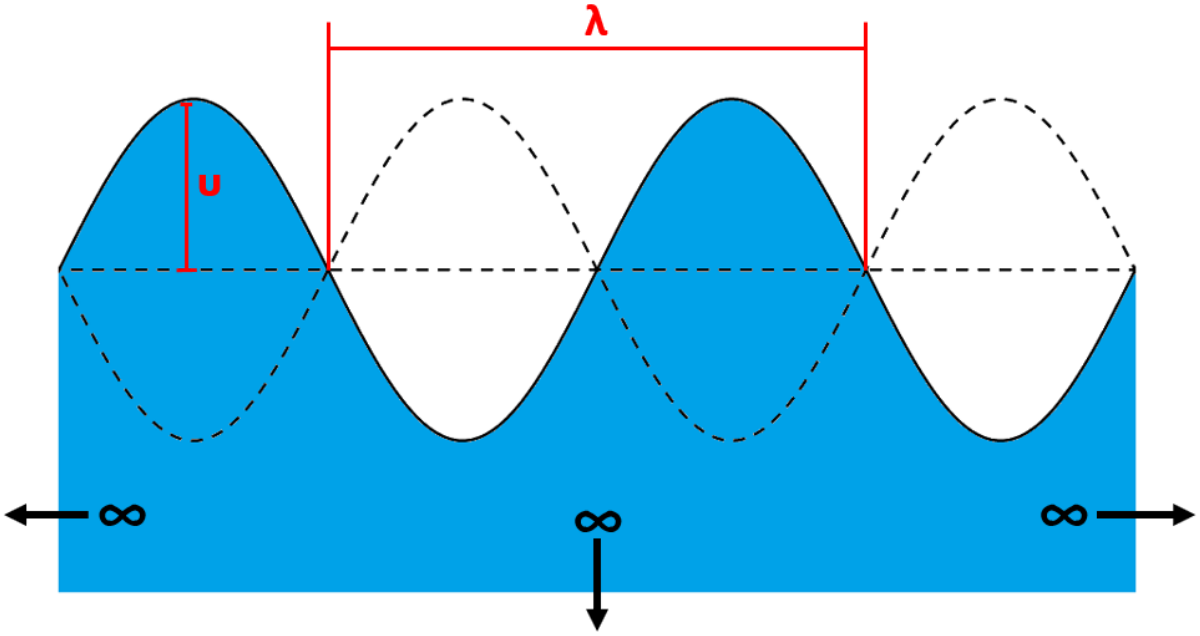


Figure 2.13: A diagram of a standing wave on the surface of an infinite viscoelastic liquid bath. The wavelength of the stand wave is given by λ and the amplitude of the wave is given by u.

When a standing wave is present in a media, the velocity of the media at the nodes of the wave is always zero. This is true regardless of how deep into the media the standing wave penetrates.

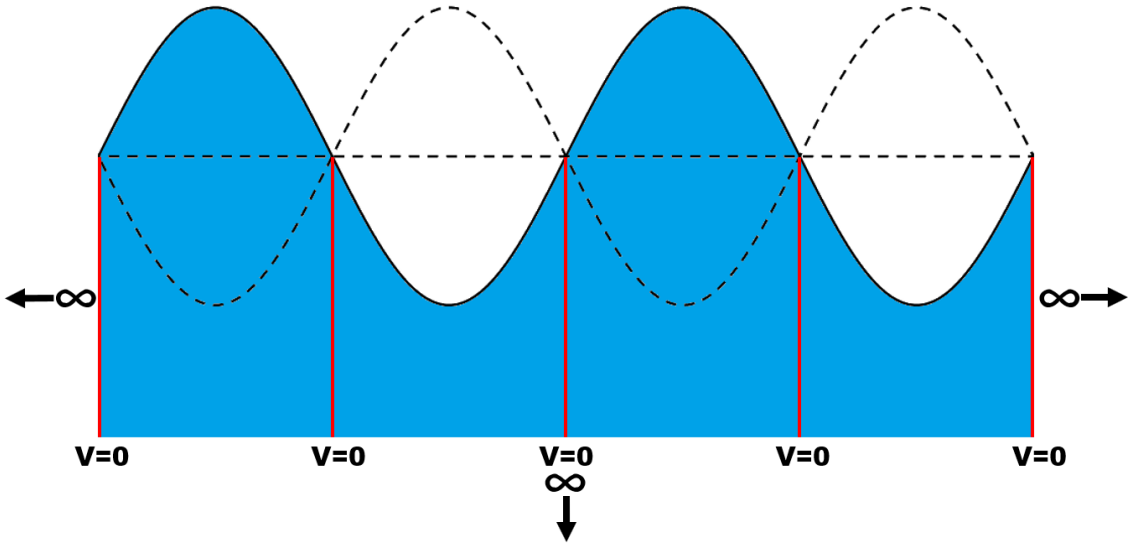


Figure 2.14: A diagram to show the nodal points (highlighted in red) along the standing wave in figure 2.13 where the vertical velocity of the media is always zero.

Since these standing waves are completely stationary at the nodal points (as shown in figure 2.14), these points can be considered to be solid boundaries, as a standing wave that was confined by a solid boundary (for example, the edge of a liquid bath) would also have zero velocity at the point where the wave met the boundary point. Because of this, the wavelength of the standing wave (as shown in figure 2.13) can be used to define the length of a theoretical liquid bath of infinite depth. This allows for the infinite liquid bath model to have its width reduced from infinity to a finite value, while allowing the mathematical model to remain valid.

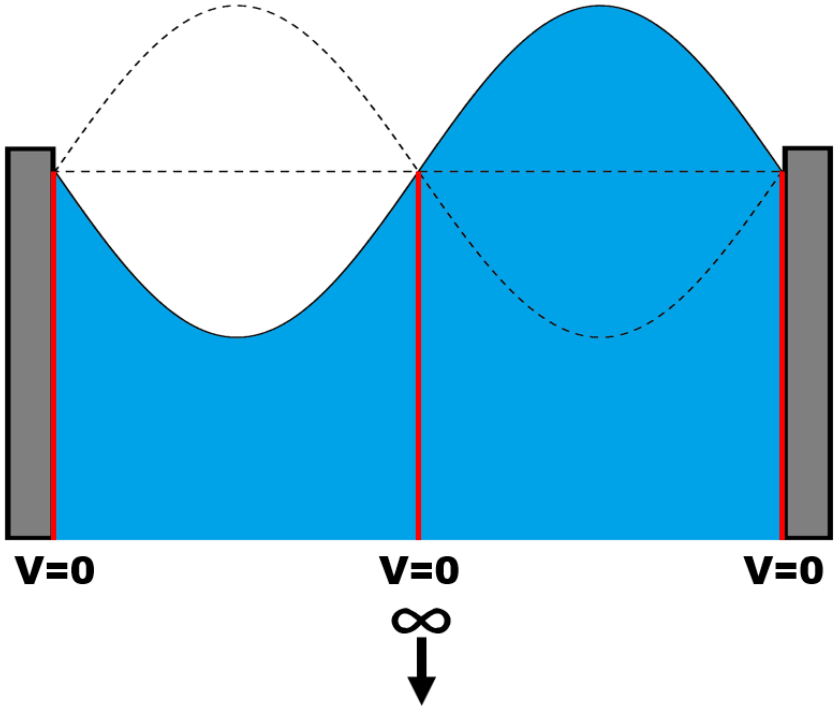


Figure 2.15: A diagram of a standing wave on a liquid bath of infinite depth and finite width. The velocity of the standing wave is zero at the points where the liquid meets the edge of the bath, just like the velocity of a standing wave is zero at its nodal points.

The second condition which can be applied to this system is one relating to the depth of the liquid. As the surface wave penetrates deeper into the liquid, its velocity gradient decreases, until eventually it will have an amplitude and velocity of zero when it reaches the bottom of the bath (assuming a non-slip boundary condition). The nature of the wave will also change as it moves into the bulk of the liquid, changing from a transverse s-wave on the surface into a longitudinal p-wave in the bulk.

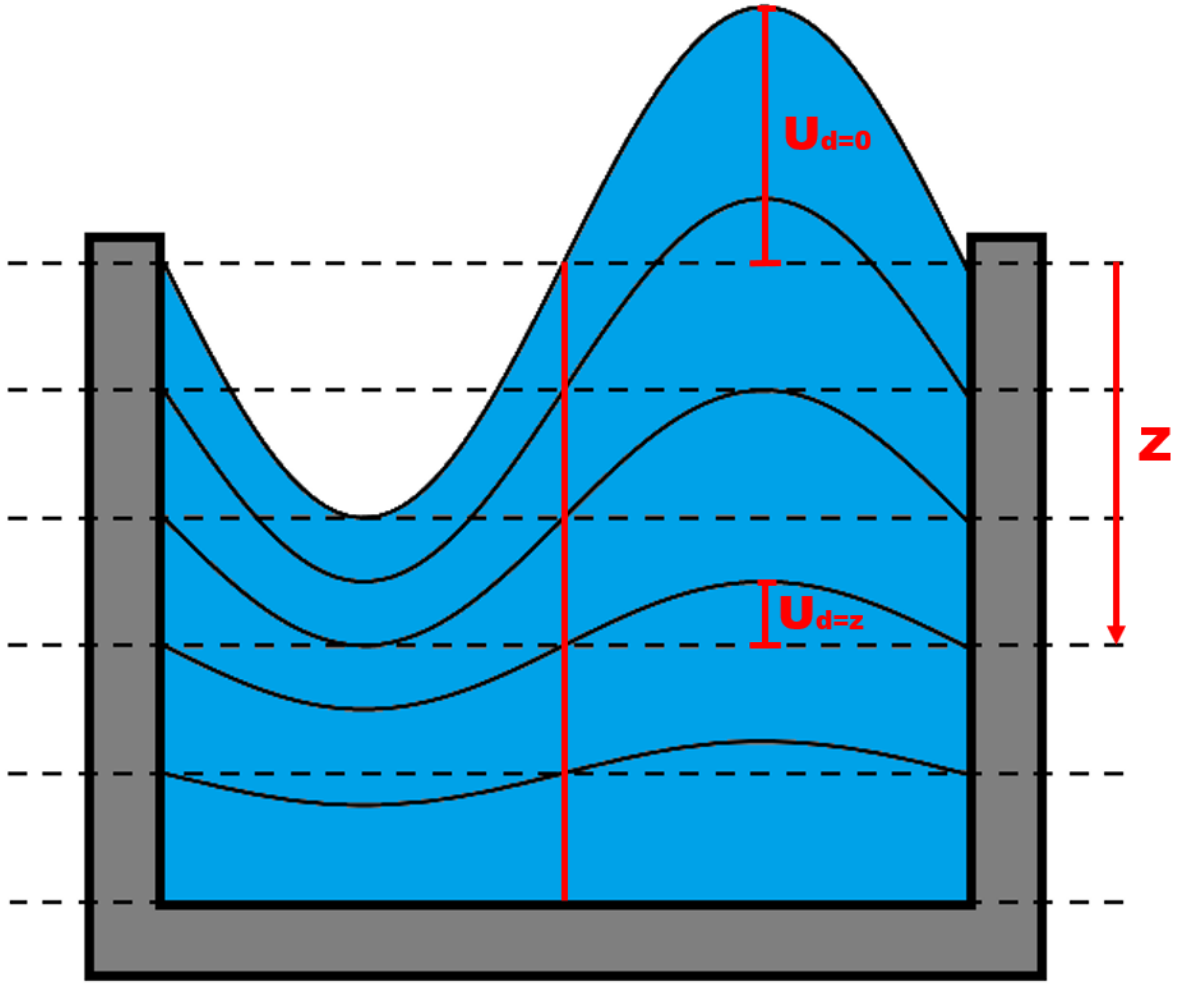


Figure 2.16: A diagram to show the amplitude (and by extension the velocity) of a standing wave on a liquid bath of finite depth decreases as the depth of the liquid increases.

The terms "s-wave" and "p-wave" are typically used in the field of geophysics when describing seismic waves. Seismic waves themselves are viscoelastic waves, as the material which seismic waves travel through (rocks, ores etc) display viscous and elastic characteristics [45].

An s-wave, or a surface wave is a transverse wave which moves across the surface of the media through which it travels through. A p-wave, or primary wave, is a longitudinal (or compression) wave which travels through the bulk of the media. P-waves are known as primary waves because they travel faster than s-waves, and therefore proceed them.

The elastic component of this viscoelastic material will dictate the frequency, and by extension the wavelength of the surface wave, whereas the viscosity of the material will dictate how rapidly the surface wave is damped. The depth of the liquid bath also dictates how rapidly the surface wave is damped. Using this information Jäckle was able to derive an equation for the dynamic susceptibility of the surface waves on a liquid bath of finite depth by treating the surface waves as being confined in both the horizontal and vertical axis (note this equation is two dimensional). Jäckle's equation for the dynamic susceptibility of monochromatic viscoelastic waves is:

$$\chi_{zz}(q,\omega) = \frac{1}{\rho\omega}\frac{A\left(K\sinh\left(q\bar{h}\right)-q\sinh\left(K\bar{h}\right)\right)-Bq\left(\cosh\left(q\bar{h}\right)-\cosh\left(K\bar{h}\right)\right)}{AD-BC} \tag{2.37}$$

$$A = 2q^2\cosh(q\bar{h}) - [q^2 + K^2]\cosh\left(K\bar{h}\right) \tag{2.38}$$

$$B = 2qK\sinh\left(q\bar{h}\right) - [q^2 + K^2]\sinh\left(K\bar{h}\right) \tag{2.39}$$

$$C = -i\nu[q^2 + K^2]\sinh\left(q\bar{h}\right) + 2i\nu qK\sinh\left(K\bar{h}\right) + \left(\frac{q}{\omega}\right)\left[\left(\frac{\Omega}{\rho}\right)q^2 + g\right]\left(\cosh\left(q\bar{h}\right) - \cosh\left(K\bar{h}\right)\right) \tag{2.40}$$

$$D = -i\nu[q^2 + K^2]\frac{K}{q}\cosh\left(q\bar{h}\right) + 2i\nu qK\cosh\left(K\bar{h}\right) + \left(\frac{1}{\omega}\right)\left[\left(\frac{\Omega}{\rho}\right)q^2 + g\right]\left(K\sinh\left(q\bar{h}\right) - K\sinh\left(K\bar{h}\right)\right) \tag{2.41}$$

$$K = \sqrt{q^2 - \left(\frac{i\omega}{\nu}\right)} \tag{2.42}$$

$$\omega = 2\pi f \tag{2.43}$$

In which ν is the complex viscosity of liquid, $\bar{h}$ is the depth of the liquid, q is the wavenumber (defined previously), ρ is the density of the liquid, Ω is the surface tension of the liquid, and g is the force of gravity. Since this experiment is dealing with the surface waves of sessile drops which are below the capillary length, the influence of gravity can be consider nominal, and therefore the gravitational term can be omitted.

From the theory of linear response [46], the power spectrum of thermally driven height fluctuations on the surface of a free liquid is given by:

$$u_z = \frac{2k_B T\chi''_{zz}(k,\omega)}{\omega} \tag{2.44}$$

where u_z is the height of the thermally driven fluctuation, T is the temperature of the liquid, ω is the angular frequency of the standing wave created by thermally driven fluctuations, and χ''_{zz} is the imaginary component of the dynamic susceptibility.

Linear response theory is used to explain how a system in equilibrium responds to external influence. In this situation the energy which is being applied to the system is thermal energy. As stated previously χ is the dynamic susceptibility of the system, which is the ratio of the displacement of a surface wave to the external force per unit area. The amplitude of the wave is therefore the energy of the system multiplied by the factor of χ''_{zz}/ω. Since the actual energy of the wave does not change the frequency or rate of damping, the physical shape of the power spectrum is independent of the energy of the wave (as shown in figure 2.17).

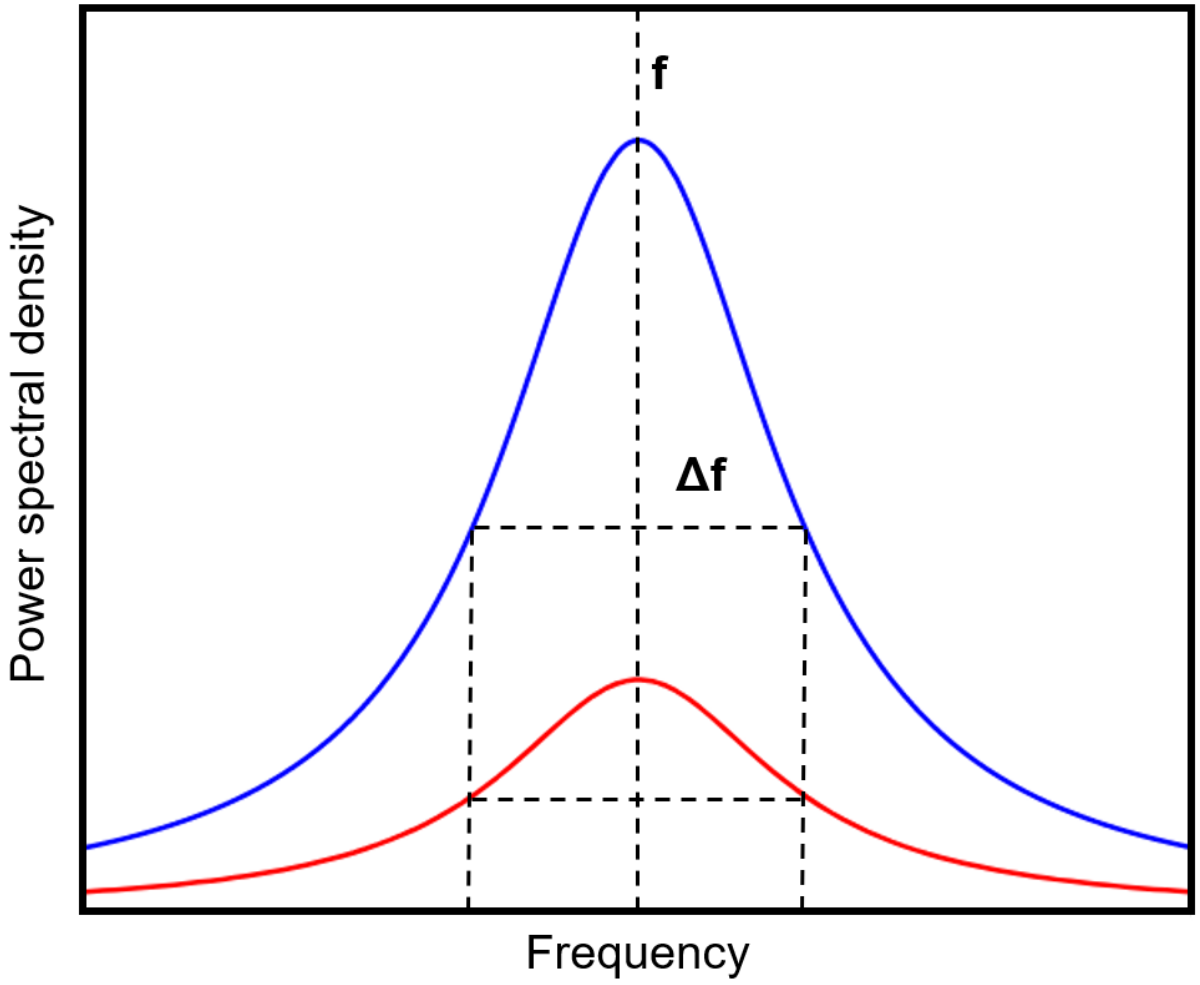


Figure 2.17: A simple diagram to demonstrate the fact that scaling a power spectrum by a constant does not change the width of the frequency peak or its position. The blue line is the scaled power spectrum (analogues to equation 2.27), and the red line is the common factor (analogous to χ''_{zz}/ω).

The common factor of χ''_{zz}/ω therefore provides a mechanism through which the physical properties of a medium (its dynamic susceptibility) can be related to the power spectrum of surfaces waves on said medium. Since the dynamic susceptibility of the medium is shown to be dependent on the storage (G') and loss (G'') moduli of the medium, this allows for the properties of a viscoelastic liquid to be derived directly from the power spectrum of surface wave oscillations.

Chapter 3

Experimental techniques

3.1 Polymer solution preparation

All experiments within this thesis are preformed using Poly(acrylamide-co-acrylic) acid solutions. The Poly(acrylamide-co-acrylic) acid (hence forth referred to simply as PAA) has a molecular weight of 15M Da and was supplied by Sigma-Aldrich UK. This is the same PAA which was previously used by the research group by authors such as Harrold et al [11], so a direct comparison between results can be made.

Six different concentrations of PAA solution were made using deionised water. These concentrations were 0.5wt%, 1.0wt%, 1.5wt%, 2.0wt%, 2.5wt%, and 3.0wt%. The density of these polymer solutions was measured why weighing known volumes of the solution.

Polymer concentration (% by weight)	Density (Kg/m^3)
0.5	997.0
1.0	1004.9
1.5	1012.0
2.0	1017.0
2.5	1022.0
3.0	1025.0

Table 3.1: The concentration dependent density of Poly(acrylamide-co-acrylic) acid solutions.

The molecular structure of PAA is made up of repeating units of acrylamide and acrylic acid (as shown in figure 3.1). PAA is both nontoxic and water soluble, allowing for ease of handling and use. Changes in pH also have very little effect on the viscosity of PAA solutions [47], making it a good choice for modelling viscoelasticity, as the additional variable of pH does not need to be considered. PAA solutions also show a rapid increase in viscosity with only a small increase in concentration. At 0.5wt% PAA appears to have the viscosity of water, whereas a 3.0wt% PAA solution of the molecular weight chosen has a consistency of thick treacle.

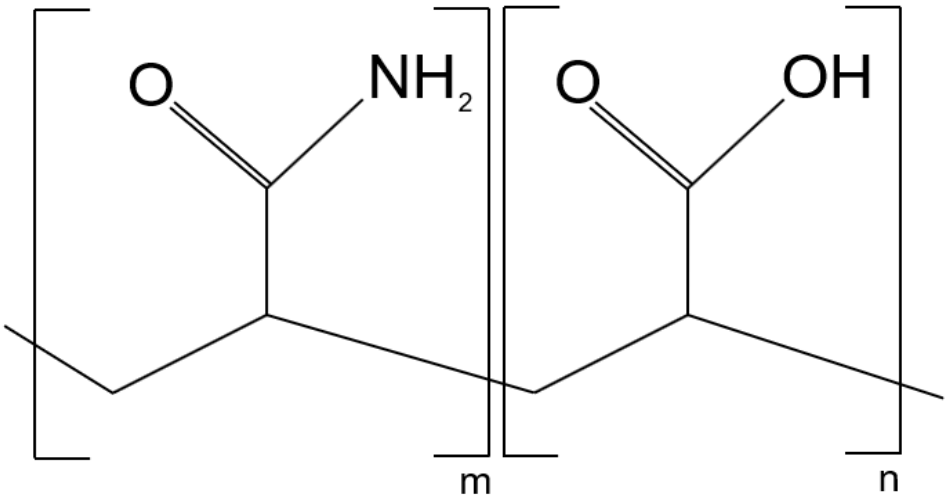


Figure 3.1: The molecular structure of Poly(acrylamide-co-acrylic) acid. The polymer chain is comprised of two repeating subunits, an acrylamide subunit (m) and an acrylic acid subunit (n).

The PAA solutions were made by first weighting the required mass of amorphous PAA and deionised water. The PAA was then gradually added to the deionised water. Once the PAA had been added, the vial containing the solution was sealed using parafilm and dated. The time taken for the PAA to dissolve increased notably with the amount of PAA being added to the water. For the 0.5wt% solution, the PAA dissolved within minutes, whereas the 3.0wt% took days to properly dissolve. The reason why the deionised water was not simply added to PAA is because that if the solute and solvent were mixed in this way the crystals tended to clump together at the bottom of the vial. This can prevent the PAA from properly dissolving, and would result in the solutions needing to be stirred in order to properly mix the solution, which could result in the polymer concentration being changed, as the instrument being used to stir the polymer might remove polymer from the solution. Since the molecular weight of this polymer solution is so high, there is also the possibility that stirring the solution would result is chain scission, which is when the polymer chain is physically broken. Shortening the polymer chains would have a notably effect of the physical properties of the polymer solutions, and therefore situations which could cause such an occurrence are to be avoided.

3.2 Substrate fabrication

This section describes the substrates which were used in the sessile droplet experiment (chapter 5), as well as the techniques used to create them.

3.2.1 Aluminium

In this experiment small disks of Aluminium (with a diameter of 4cm) were used. To ensure the disks were not contaminated, they were first cleaned with methanol to ensure the surfaces were as clean as possible.

3.2.2 Candle soot

This superamphiphobic substrate (repels both polar and non-polar chemicals) was produced by first holding a clean glass slide over a parrafin candle, allowing for a thin layer of carbon particles (roughly 30nm in diameter) to build up on the surface of the glass slide. This surface alone is extremely hydrophobic, with a water contact angle of 160°, however in this state it is extremely delicate and can be easily damaged. To improve the resilience of the substrate, the layer of carbon particles was covered in a silica shell. This was achieved by subjecting the substrate to tetraethoxysilane (TEOS, 98%, Sigma-Aldrich) and ammonia vapour (28%, VWR) at room temperature for three days. The substrate was then heated to remove the carbon nanoparticles, leaving only the silica shell. Finally, the silica shell was coated in a semi-fluorinated silane. This was done via chemical vapour deposition of (tridecafluoro-1,1,2,2- tetrahydrooctyl)-1-trichlorosilane (97%, Sigma UK) for three hours.

The physical structure of this substrate (extremely rough) combined with its chemical composition results in a surface which is extremely repellent to both polar and non-polar liquids.

These substrates were gifted to the university from Dorris Vollmer's research ground (Max Planck Institute for Polymer Science, Mainz University).

3.2.3 Polystyrene

Polystyrene (abbreviated to PS) is an extremely common aromatic polymer made the monomer of styrene, the chemical structure of which is illustrated in figure 3.2 The polystyrene used in this experiment was acquired from Sigma-Aldrich UK and had a molecular weight of 35,000 g/mol. This polystyrene was dissolved in toluene (2wt%) and spin coated onto clean glass slides (4x4cm). The spin coater had a setting of 3,000 rpm and was spun for a period of five seconds. These glass slides were then placed in an oven at 85°C for three hours to remove the toluene, leaving a thin layer of PS of the glass slide.

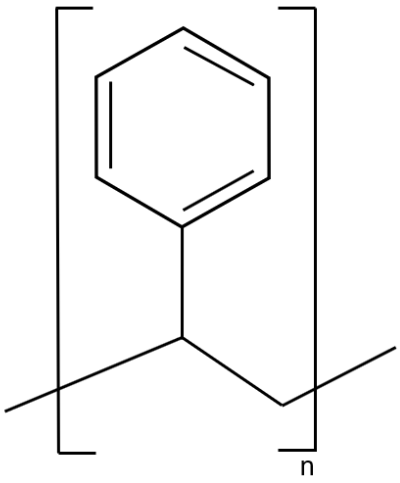


Figure 3.2: the chemical structure of polystyrene

3.2.4 Polydimethylsiloxane (PDMS)

Polydimethylsiloxane (PDMS) is a simple silicone polymer, the structure of which is shown in figure 3.3. PDMS is produced using the Müller-Rochow process [48]. In this process, elemental silicon is reacted with methyl chloride (CH_3Cl) using a copper catalyst. Methyl chloride is created by reacting methanol (CH_3OH) with hydrogen chloride (HCl). This process creates a mixture of methylchlorosilanes, which are then separated via distillation, and purified. The PDMS used in this experiment was acquired from Dow Corning (with the trade name of Sylgard 184) and had a molecular weight of 24,000g/mol. Slides of PDMS were prepared by first mixing ten parts polymer resin to one part cross-linking agent, and spin coating the mixture onto clean glass slides (in the same manner as described in section 3.2.3). These slides were then left for twenty-four hours in order to allow for the polymerisation reaction to conclude.

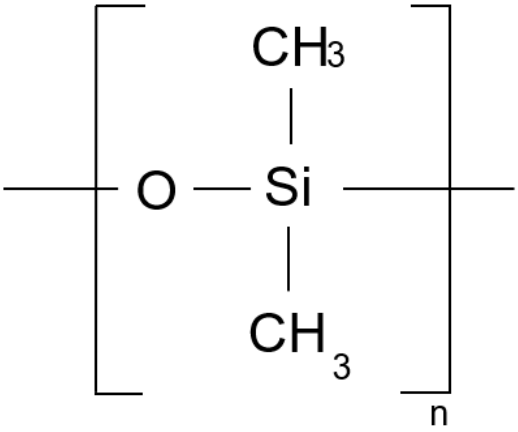


Figure 3.3: the chemical structure of Polydimethylsiloxane

3.2.5 silicon

In this experiment, p-type silicon wafers (doped with boron) were used in order to produce a low contact angle substrate. Each wafer was coated with a very thin layer of silicon dioxide (with a thickness of around 1.8nm). These silicon wafers were acquired from Compart Technology ltd and were made from electronics-grade silicon, which had been previously cleaned. Small 4x4cm squares of silicon wafer were cut using a scribing tool. Due to the extreme level of purity, these silicon wafers were kept in a sealed container, and were discarded after use.

3.2.6 Wax

Paraffin wax is a collection of long chain alkane molecule (hydrocarbons), all of which have the chemical formula C_nH_{2n+2}. Molten wax was deposited onto a glass slide (4x4cm), on top of which another glass slide was placed. This produced a thin layer of molten wax between the two slides. Once the wax had solidified, the top slide was carefully removed, leaving a smooth wax surface on the bottom slide.

3.3 Contact angle measurements

The contact angle of a sessile droplet is defined as the angle between the tangent of the surface of the sessile droplet and the surface of the substrate on which the sessile droplet is sitting, as shown in Figure 2.8.

The contact angle of a sessile droplet depends both on the composition of the droplet, and the surface upon which the sessile droplet is sitting. In this experiment a range of polymer concentrations were used, along with a number of different substrates. The substrates chosen provided a large variation of contact angles.

The contact angle was measured by first depositing a sessile droplet onto the substrate in question. The next step was to backlight the droplet so that surface of the droplet can be easily distinguished. Next, high resolution photographs of the droplet were taken using a Genie HM640 camera.

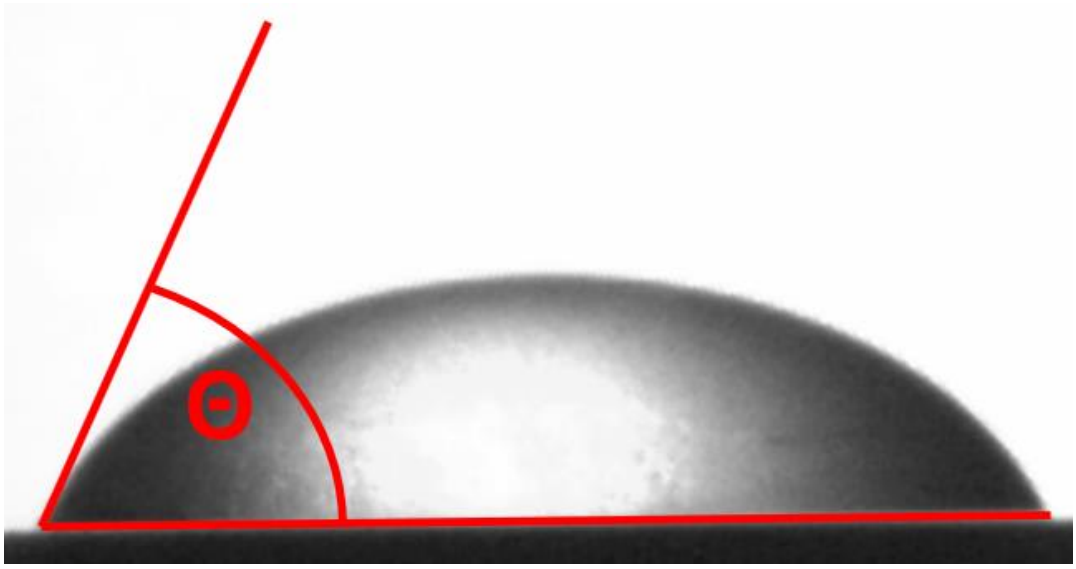


Figure 3.4: The contact angle of a sessile droplet, defined as the angle made by the intersection of the liquid/gas interface and the liquid/solid interface.

The contact angle was then measured using an ImageJ plugin which takes the physical outline of the sessile droplet and calculates the contact angle from this information [49]. This technique (shown in figure 3.5) proved to be far more reliable than manually measuring the contact angle, and was therefore the method used to determine the contact angle of the sessile droplets

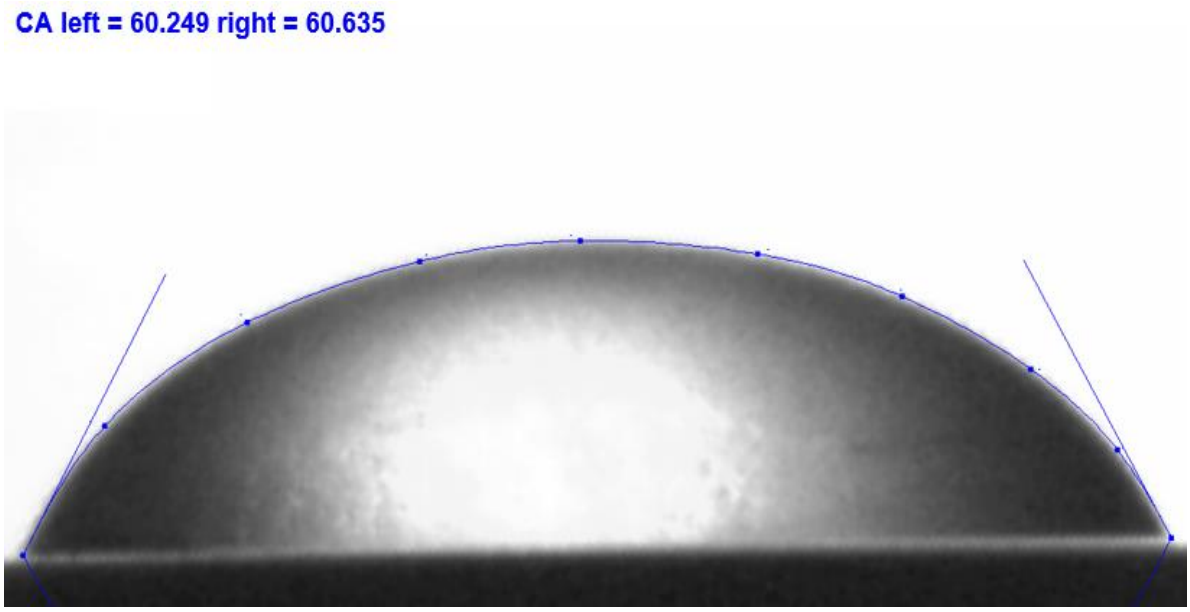


Figure 3.5: The contact angle of a sessile droplet, measured by utilising a specially designed ImageJ plugin [49]. Reference points along the surface of the sessile droplet are used to calculate the position of the droplet's surface and by extension the contact angle of the droplet.

The contact angles of the sessile droplets were measured for each substrate that was mentioned in section 3.2, for each polymer solution (as described in section 2.1). Several different measurements were taken for each substrate and concentration, the results of which were averaged together. The results of these measurements are shown below.

Substrate	0.5wt%	1.0wt%	1.5wt%	2.0wt%	2.5wt%	3.0wt%
Silicon	30±1°	30±1°	33±1°	35±1°	37±1°	38±1°
Aluminium	55±1°	60±1°	70±1°	75±1°	80±1°	82±1°
Polystyrene	60±1°	70±1°	75±1°	75±1°	85±1°	92±1°
Wax	90±1°	90±1°	91±1°	93±1°	93±1°	95±1°
PDMS	90±1°	93±1°	95±1°	96±1°	97±1°	97±1°
Candle soot	145±1°	145±1°	145±1°	145±1°	145±1°	145±1°

Table 3.2: The substrate dependent contact angles of sessile droplets with varying polymer concentrations.

As can be seen in Table 3.2 the contact angle of sessile droplets increased with an increase in polymer concentration, with the exception of candle soot. Candle soot produced a contact angle of 145° for all polymer concentrations. Photographic evidence for the increase of sessile droplet contact angle with an increase in polymer concentration is shown in figure 3.6.

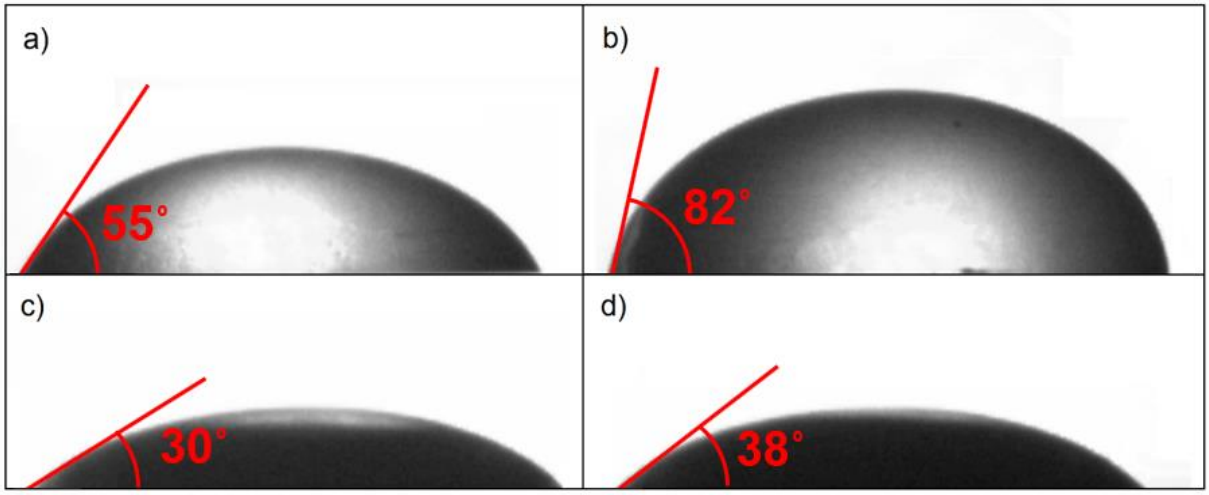


Figure 3.6: a) A 0.5wt% PAA solution sessile droplet on an aluminium substrate. b) A 3.0wt% PAA solution sessile droplet on an aluminium substrate. c) A 0.5wt% PAA solution sessile droplet on a silicon substrate. d) A 3.0wt% PAA solution sessile droplet on a silicon substrate.

The contact angle of the sessile droplets was not found to vary with profile length, provided that the capillary length was not exceeded.

3.4 Video analysis

In the sessile drop vibration experiment (chapter 5), microlitre sessile droplets are stimulated via a mechanical impulse. The surface waves generated from this impulse are then filmed using a high-speed camera (with a frame rate of five hundred frames per second). Figure 3.7 shows how the shape of these sessile droplets change over time. Figure 3.7a shows how the sessile droplet begins at a state of rest, figure3.7b shows the sessile droplet immediately after the impulse is applied to the substrate, and figures 3.7c to 3.7L demonstrate the oscillation of the sessile droplet over time.

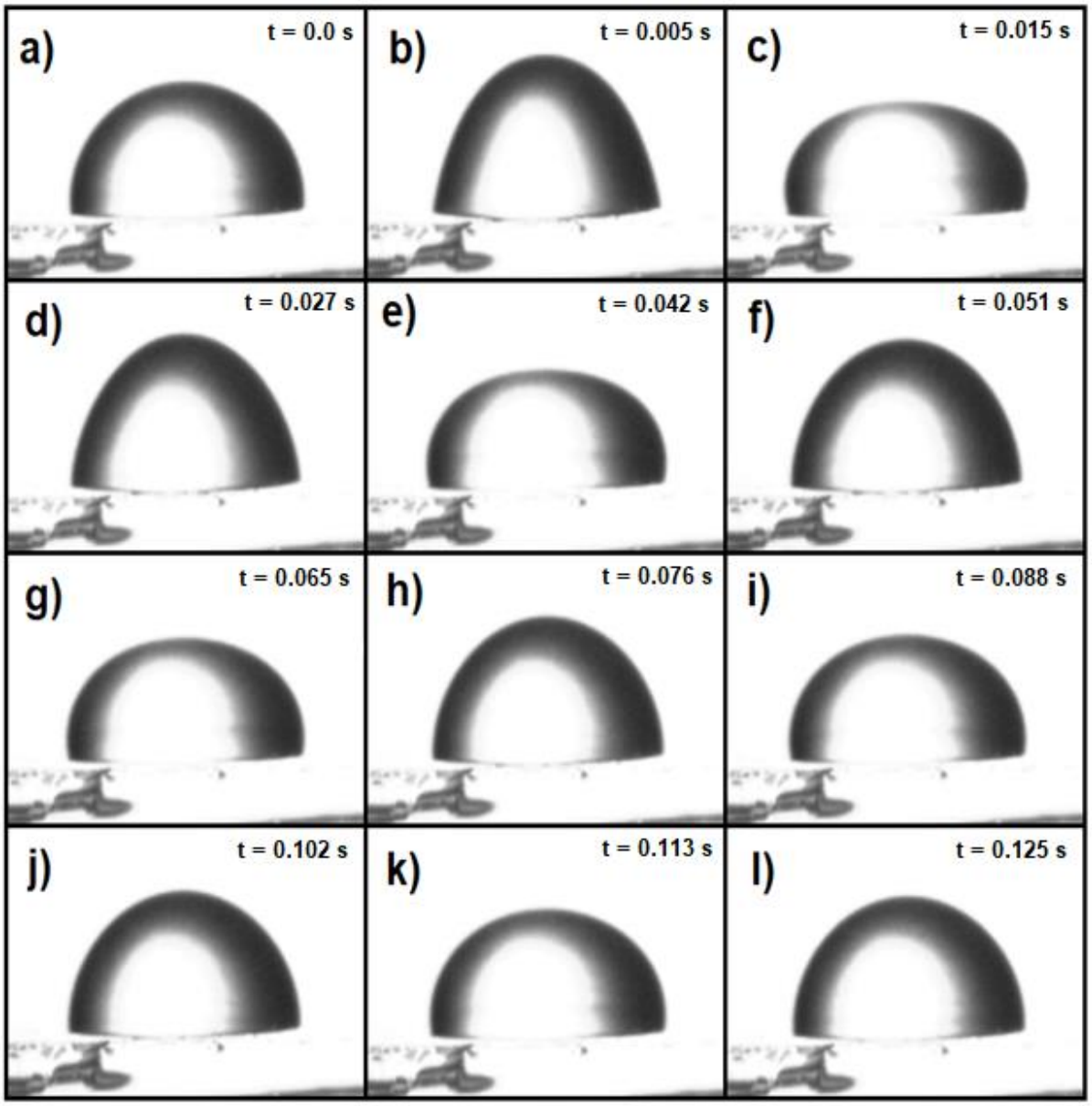


Figure 3.7: A collection of frames extracted from a video recording of the surface waves on a viscoelastic sessile droplet before (frame a) and immediately after being stimulated via a mechanical impulse (frames b to l).

The AVI video files acquired from this experiment were analysed using a specially created Matlab program (written by Sharp and modified by the Author). Firstly, each video was cut so that only the time period of interest would be analysed. The analysis would begin when the surface wave was at its peak amplitude, as shown in figure 3.8b. Since only the lowest possible wave modes were being analysed, the high order modes, which were often stimulated initially, were allowed to die down before analysis began. This normally resulted in analysis beginning at the start of the second cycle of oscillation (figure 3.7d/f), rather than the first (figure 3.7b). The video file was also cut at the point at which the oscillations of the sessile droplet's surface had completely died down, so that the surface of the sessile droplet was once again at rest.

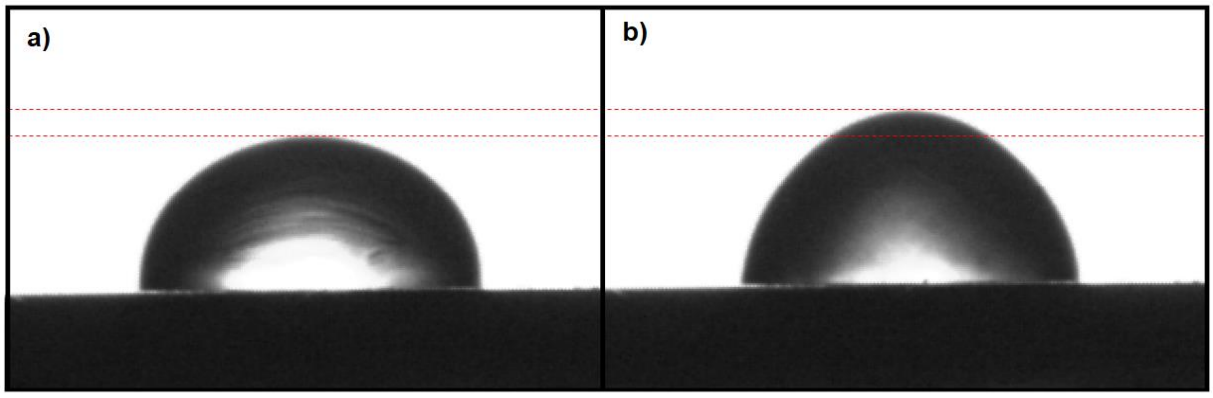


Figure 3.8: images of a sessile droplet at rest (a) and at the point at which the stimulated surface wave is at its maximum amplitude (b).

The AVI files were then broken down into their component images, which were subsequently converted into matrix form. Since these video files were already greyscale, the numerical representation within this matrix of each individual pixel would be between zero and one (one being totally black and zero being totally white). A threshold value was then applied to this matrix in order to convert each initial image into a binary (black and white) image. Matrix values above this threshold level were given the value of zero and those below the threshold value were given the value of one.

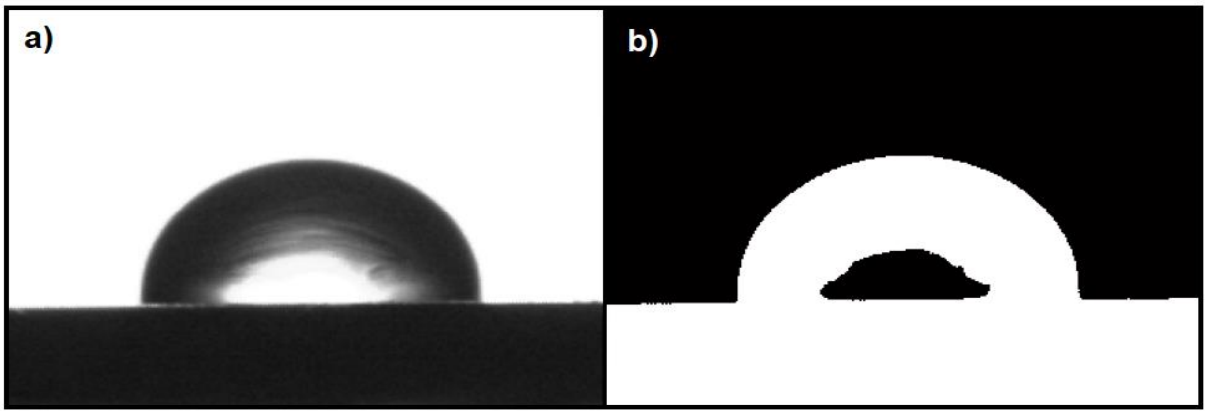


Figure 3.9: Images of a sessile droplet before (a) and after (b) it is converted into a binary image.

Applying this threshold value resulted in a binary image (Figure 3.9b) that could be further processed. The exact threshold value that was used was 0.8, which was determined by comparing the shapes of the droplets before and after thresholding was applied, and finding the value which resulted in the most accurate representation of the droplet. As long as the camera was correctly focused then the required value for the threshold was not difficult to determine, as the contrast between the backlighting and the actual droplet was significant (as shown in Figure 3.8). Once the images had been converted into binary images, they were then cropped to remove the substrate, making sure to keep the sessile droplet centred in the image.

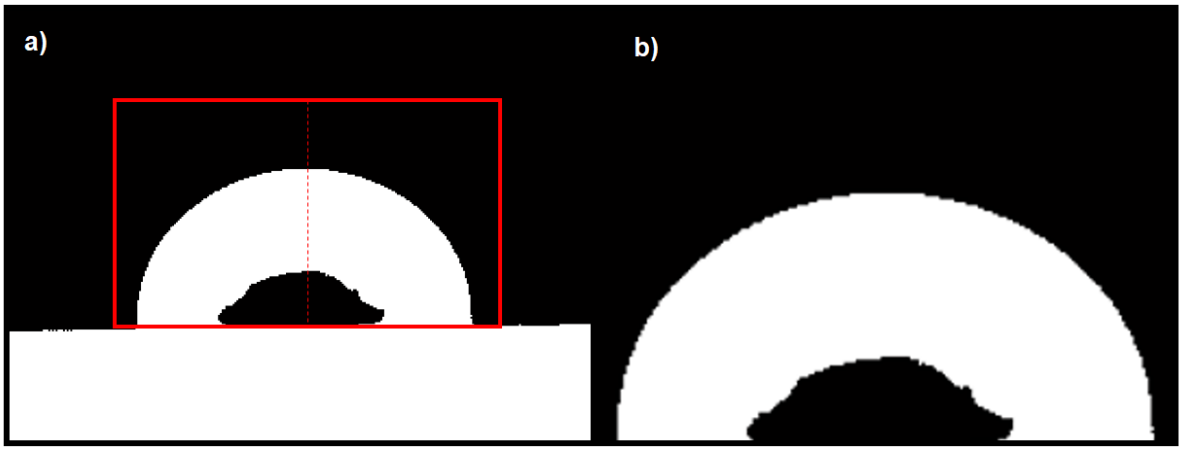
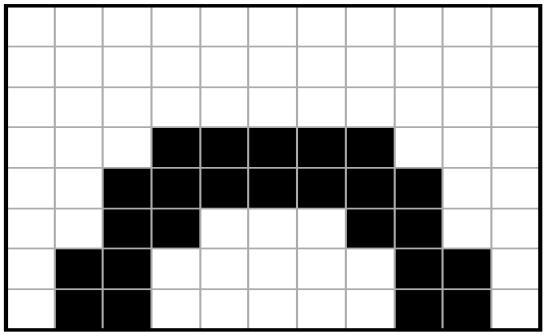


Figure 3.10: A binary image of a sessile droplet before (a) and after being cropped (b). The red box in figure (a) indicates the position at which the image was cropped.

The first stage of analysis is to measure the rate at which the sessile droplet oscillates. To do this, the central vertical column of the matrix corresponding to every image in the video sequence is analysed. This column is represented in figure 3.10a by a dotted red line, and is highlighted in red in figure 3.11b.

a)



b)

0	0	0	0	0	0	0	0	0	0	0
0	0	0	0	0	0	0	0	0	0	0
0	0	0	0	0	0	0	0	0	0	0
0	0	0	1	1	1	1	1	0	0	0
0	0	1	1	1	1	1	1	1	0	0
0	0	1	1	0	0	0	1	1	0	0
0	1	1	0	0	0	0	0	1	1	0
0	1	1	0	0	0	0	0	1	1	0

Figure 3.11: A mock image of a sessile droplet in pixel (a) and matrix form (b). The matrix column highlighted in red is the column which will be used to calculate the height of the droplet. Note: this a mock image and is not to scale.

This central column is analysed from the top down, and is assessed to find the position of the first 'one' in the column. This position in the matrix is then recorded, as it marks the upper most point of the droplet at that point in that particular video frame. The height of the droplet at any given time can therefore be acquired by finding the distance between the first 'one' in the column and the end of the column, then multiplying this distance by the number of millimetres per pixel (acquired through calibration measurements). The height of the sessile droplet can then we plotted against time (derived from the frame rate) to give a visualisation of the oscillation of the sessile droplet over time (Figure 3.12).

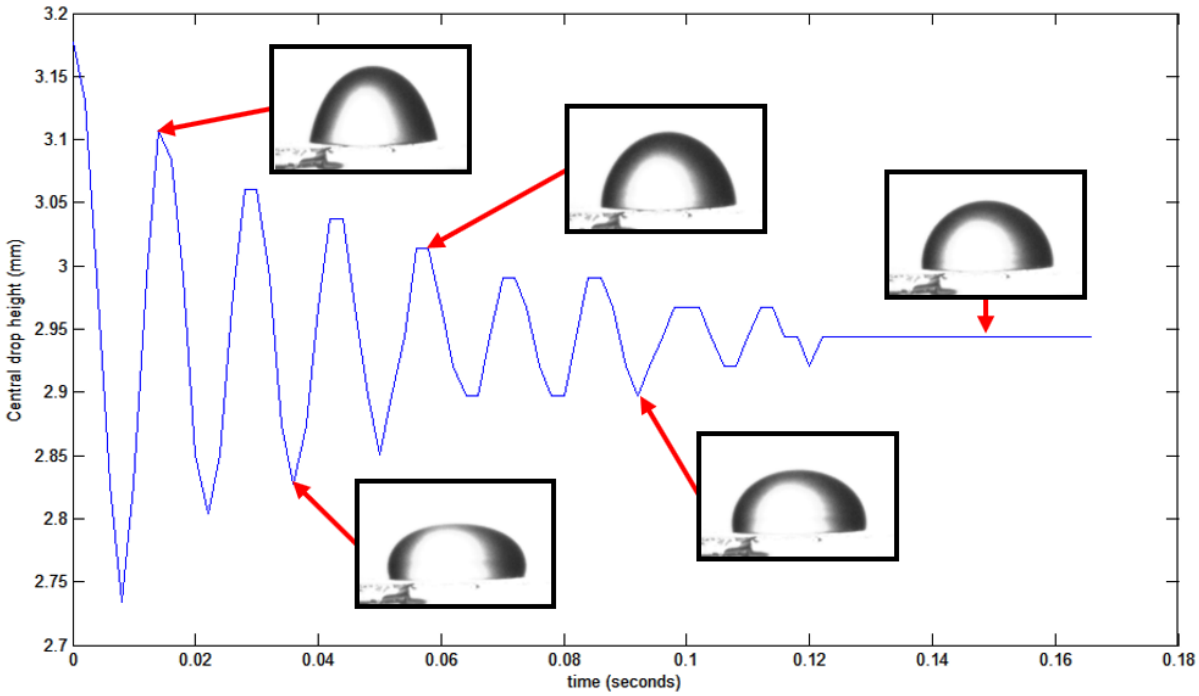


Figure 3.12: A graphical representation of the height of an oscillating sessile droplet over time, with corresponding video images.

The Noblin model treats the entire oscillation of the sessile droplet as a standing wave across the surface of the sessile droplet. Any longitudinal waves that travel across the interior of the sessile droplet are considered to be part of this surface wave, and not caused by other modes of oscillation. Because of this, a single measurement (in the vertical axis) of the amplitude of the surface wave is sufficient to model the oscillation of the sessile droplet. Once the frequency of the oscillation has been measured, the next step is to analyse the profile length of the droplet. This is done by analysing the matrix representation of the very last frame of the cropped video (where the droplet is stationary). Each row of the matrix is analysed in the same manner as the central column was analysed previously, first from the left, and then from the right. This results in two sets of coordinates for each row, corresponding to the edges of the droplet. These two data sets are then combined in order to produce an ordered list of coordinates which describe the edge of the droplet.

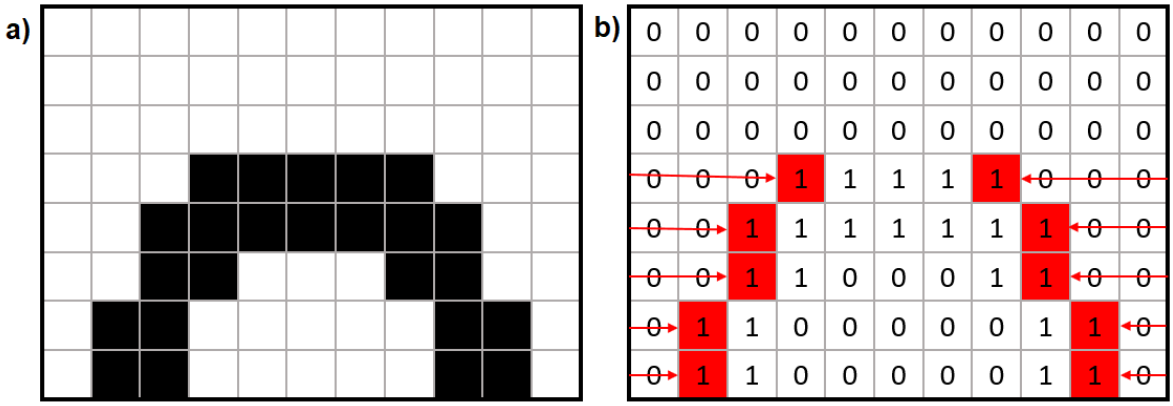


Figure 3.13: A mock image of a sessile droplet in pixel (a) and matrix form (b). The red arrows in figure b indicate the direction by which the matrix row is analysed in order to find the surface of the droplet (highlighted in red). Note: this image is not to scale.

The final stage in determining the profile length is to calculate the distance between each coordinate in sequence using basic Pythagorean theorem. The total distance between two coordinate points being the square root of the vertical difference between the two points squared, plus the horizonal distance between the two points squared.

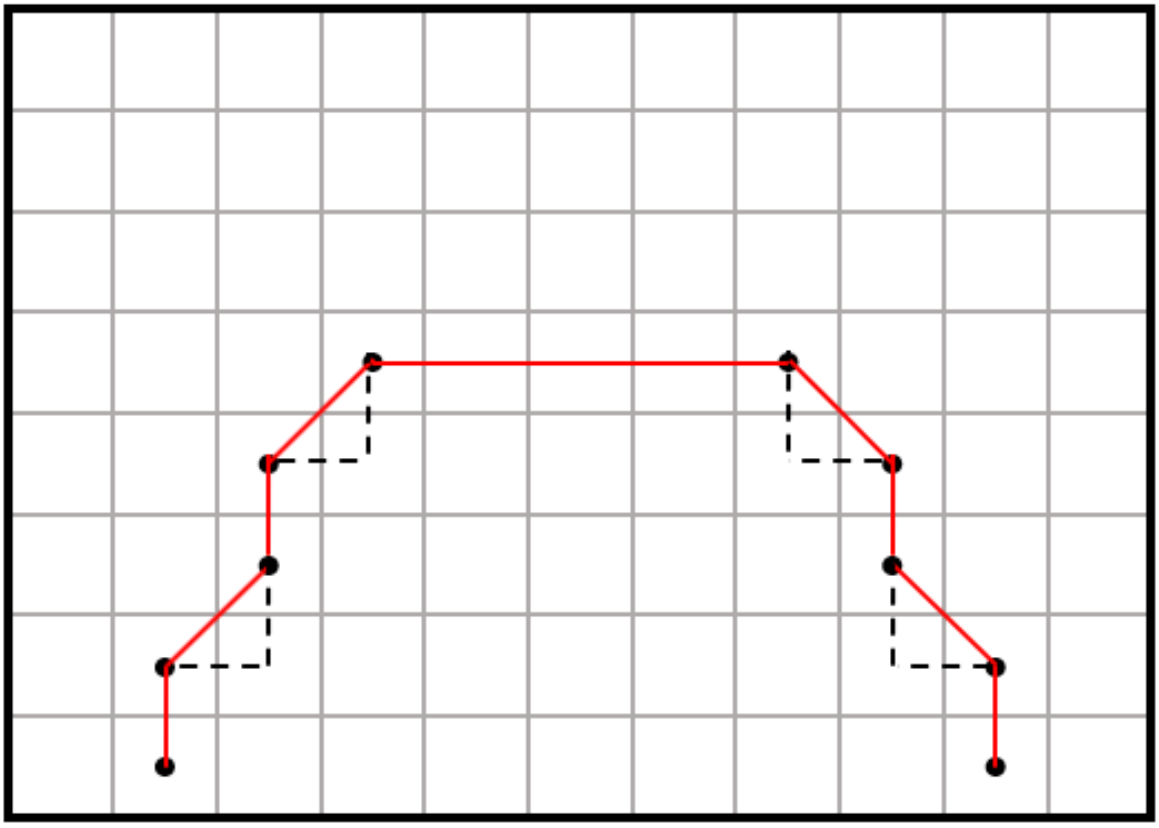


Figure 3.14: A diagram showing show the distance between the pixels identified in figure 3.13b is calculated. This in turn shows how the total profile length of the droplet is calculated.

Summing the distances between each individual point together results in the total profile length of the droplet (in pixels). Finally, this value must be multiplied by the measured number of millimetres per pixel in order to find the actual profile length of the droplet (as shown in figure 3.14). This technique for measuring the profile length of the sessile droplet was tested by comparing results produced by this method with results obtained from manually measuring the profile length from photographs, using photo editing software (GIMP). The results obtained from manual measurements agreed with the results from the computational method demonstrated in figure 3.14.

Two tests were carried out to ensure that the measurements that were taken were accurate. The first test was designed to ensure that the contact line remained pinned to the substrate. If the contact line was to move across the substrate, the sessile droplet would oscillate in a manner depicted in Figures 2.10a and 2.10b. This type of oscillation would result in addiction energy being lost to the substrate (this concept was covered in section 2.3.3).

The second test was to ensure that the profile length of the sessile droplet did not change as droplet oscillated. If the profile length did change, it would indicate that the sessile droplet was not effectively pinned to the substrate. A change in the profile length might also suggest that the viscoelastic liquid's volume was changing over time (which is not accounted for the mathematical model being tested, in which the liquid is treated as being incompressible) A change in volume could potentially occur if small bubbles of air were formed within the liquid as the droplet oscillated. If either the profile length or volume of the sessile droplet were found to change during the experiment, the mathematical model being proposed would be rendered useless.

In order to determine if the profile length and volume of the droplet remained constant throughout the experiment, a separate program was written by the author in order to record the shape of the sessile droplet over time. This new program was heavily modified version of the original program used by Harold et al [11] which had been further improved upon by the Author. Instead of only taking measurements from the final frame in the video which was being analysed, the new program would analyse every frame of the video, breaking each individual frame down into a binary matrix (as shown in figure 3.11b). Once each frame had been converted into binary matrices, the profile length of the sessile droplet is measured (as shown in figure 3.14) and recorded.

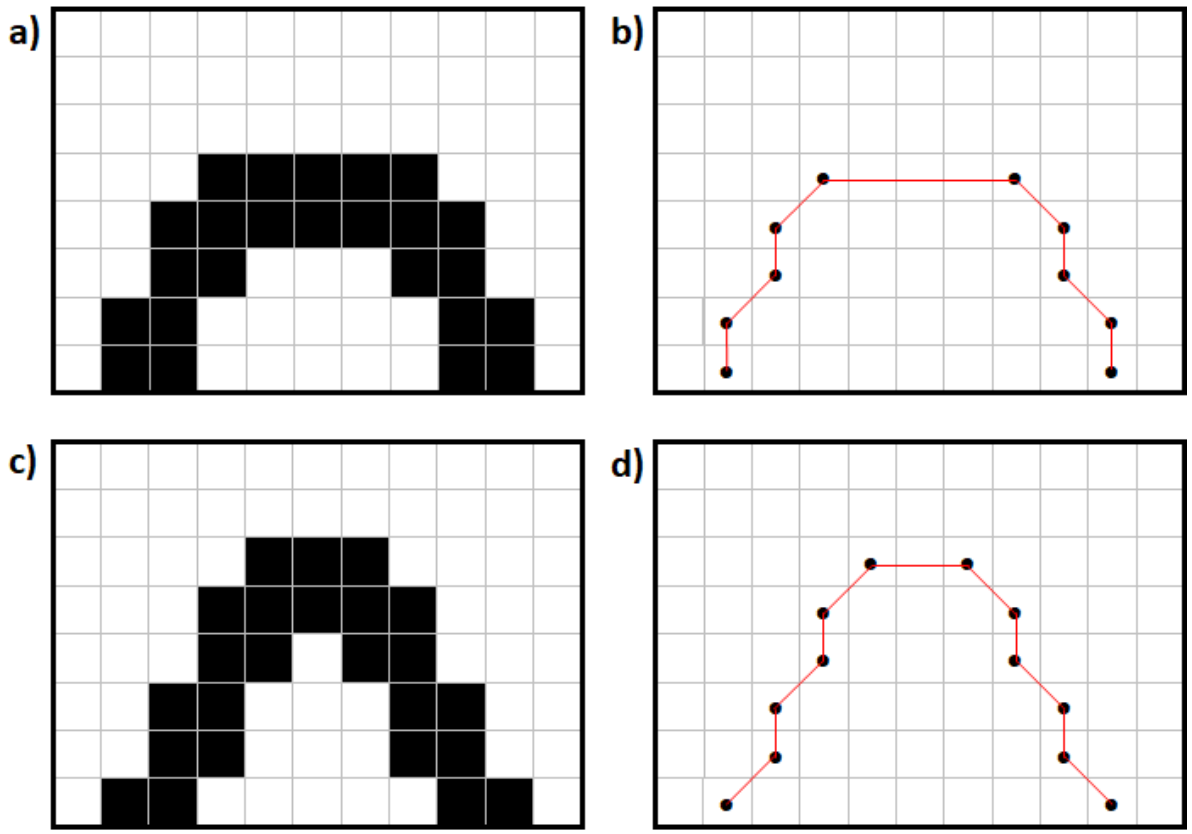


Figure 3.15: A diagram to show how the profile length of sessile droplets are measured at different staged of droplet oscillation. Figures a and c show mock images of a sessile droplet at different moment in time (during oscillation). Figures b and d illustrate the measured profile lengths acquired from images a and c respectively.

By measuring the profile length of sample droplets over time (as depicted in figure 3.15), the program determined that the profile length of the sessile droplet did not change over time, with the exception of cases where the contact line of the droplet moved.

The contact line of the sessile droplet was also checked by this program. This was done simply by analysing the data which was acquired from the binary matrix generated from each individual frame (as shown in figure 3.13).

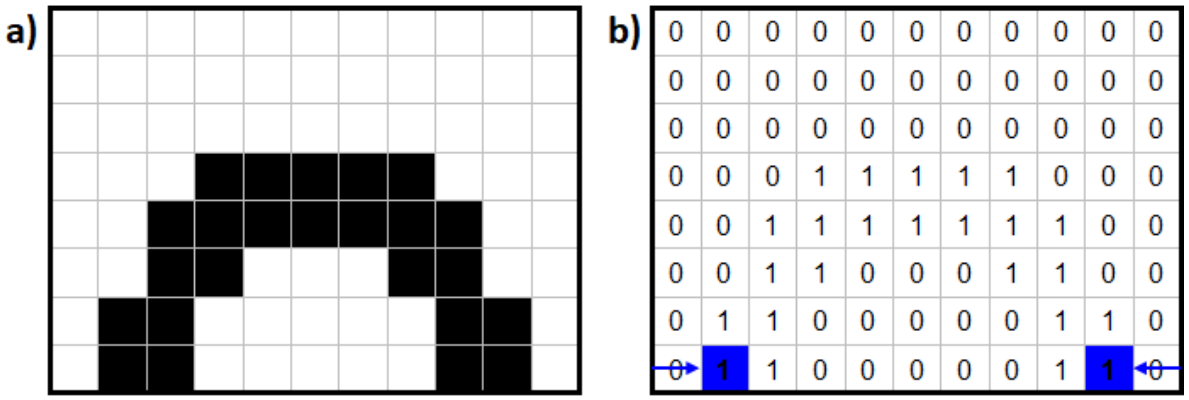


Figure 3.16: A diagram to show how the contact line of the sessile droplet is measured. Just like in figure 3.13, a binary image (a) is converted into a binary matrix (b). The bottom row of this matrix is then analysed by reading the row from each end to find the first none zero entry.

Once the position of the bottom of the sessile droplet has been found, the number of pixels between these points and the edge of the matrix is calculated and recorded. Once all of the frames have been processed, the position of the contact line over time can be analysed. If for example the number of pixels between the left hand sides of the matrices and the left side of the droplet was found to not be consistent over time, then it can be concluded that the contact line had moved during oscillation.

Movement of the contact line of the sessile droplets being investigate was initially a problem during this investigate. However, by reducing the magnitude of the impulse used to stimulate the sessile droplet, and by vibrating the droplet before the experiment was conduction, the movement of the contact line was eliminated. The details on how exactly the contact line movement was eliminated are covered more extensively in section 5.3.

3.5 Frequency measurements

Initially the technique used to determine the frequency (f) and spectral width (Δf) of the sessile droplet surface waves was to fit an exponentially decaying frequency curve to the curve of surface amplitude over time, as shown in figure 3.17. This produced values for the frequency of oscillating and a value for Δf.

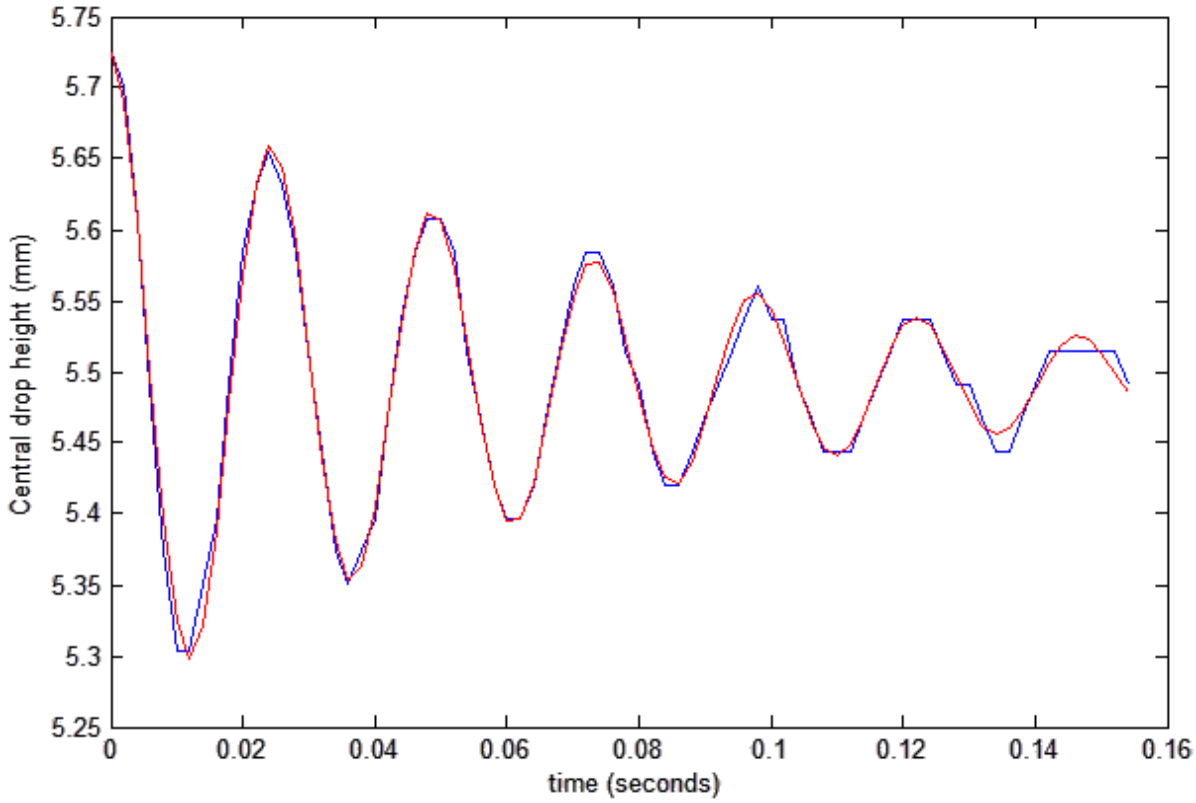


Figure 3.17: A graphical representation of the height of an oscillating sessile droplet over time (blue), with a fitted decaying frequency curve (red).

A slightly different technique for deriving the frequency(f) and spectral width (Δf) was used in this experiment. Previously the Fourier transform of surface oscillations was analysed to find the position and width of the spectral peak. In this initial experiment (the results of which were shown in figure 3.17), an exponentially decaying frequency curve was fitted to the curve of surface amplitude over time. This produced values for the frequency of oscillation and a value for Δf.

Initially the plan was to use the values of the frequency and damping parameter to create Lorentzian curves which resembled the power spectrum of the surface wave. However, due to the presence of lighting artefacts and the possibility of the surface waves not being monochromatic it was decided that a different approach should be used.

By taking the Fourier transform of the waveform of the surface wave (figure 3.17) the waveform can be broken down into its component waves to form the power spectrum for the surface waves.

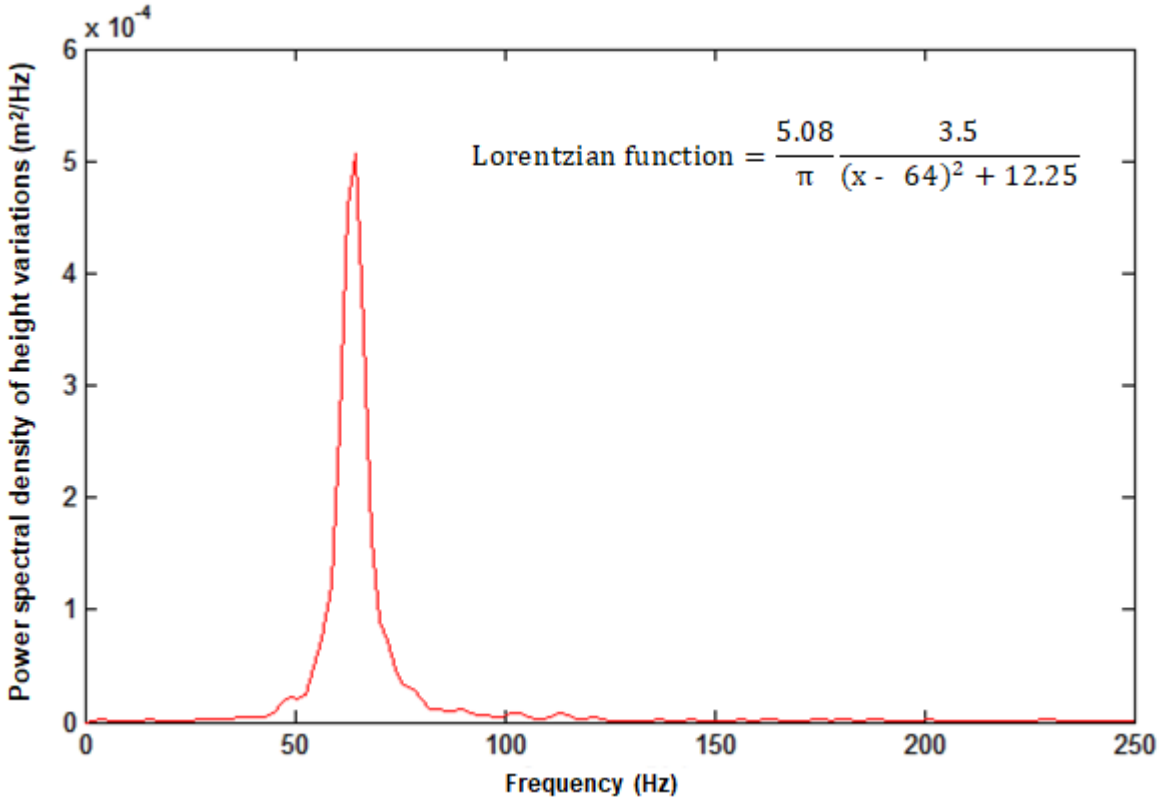


Figure 3.18: An example of a power spectrum obtained via the Fourier transform of the waveform of a sessile droplet surface wave. The equation for the equivalent Lorentzian function is displayed on the graph.

As can been seen in figure 3.18, the surface wave is well defined, resulting in only one peak in the power spectrum. The peak position corresponds to the frequency of the surface wave, and the width (full width at half height) of this peak corresponds to the amount of damping experience by the surface wave (Δf).

The light source used in this experiment was powered by alternating current, as a result the amount of light produced by the light source varies over time. This variation is light level is extremely small but can present issues when it comes to measuring the position of the sessile droplet's surface.

Mains current alternates at 50 Hz, which results in the light intensity oscillating at 100 Hz. This oscillation in illumination results in the intensity of light coming from the light source to fluctuate slightly, changing the brightness of the image. This causes problems when pixels have a value close to the threshold value of 0.8 since a slight change in light intensity can move the value of the pixel over the threshold limit and therefore change how it is defined in the binary image. This results in pixels that are close to the threshold oscillating back and forth between black and white in the binary images, making the surface appear to be oscillating. These artefacts can be clearly seen on the waveform of the surface waves once the initial surface wave oscillation has died down (figure 3.19).

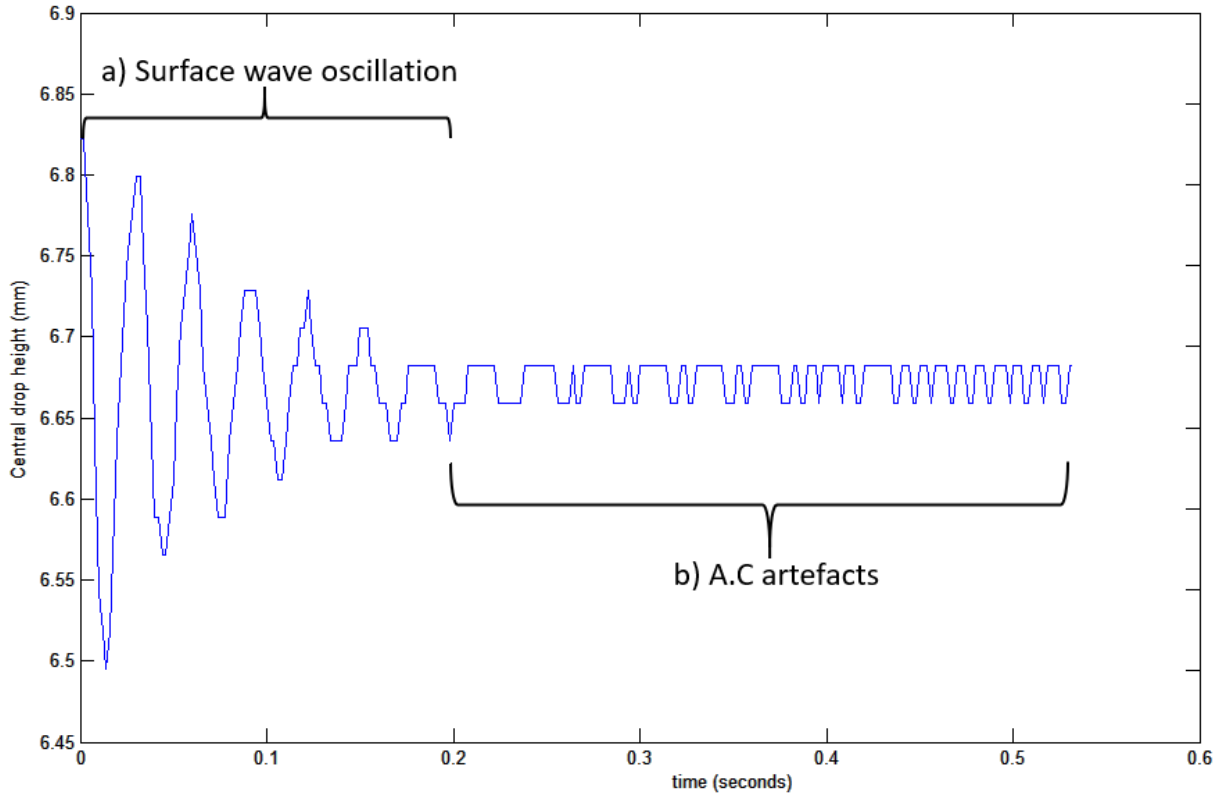


Figure 3.19: A graphical representation of the height of an oscillating sessile droplet over time. The first part of the graph (a) shows the surface wave of the sessile droplet. The second part of the graph (b) covers a period in which the sessile droplet is no longer in motion. The oscillations in the height is instead caused by variation in light levels caused by the AC current supplying the light source.

By analysing the waveform via Fourier transform, the surface waves and the artefacts created due to an AC power supply can be separated (as shown in figure 3.20). These lighting artefacts may still cause a problem when the frequency of oscillation being investigated is near 100 Hz (or any multiple of one hundred). The effects of this can be notably reduced by cutting the video as soon as the surface wave oscillation has died down, although this effect can still have a significant impact in situations where the amplitude of the surface wave itself in very small, such as for high polymer concentrations on low contact angle substrates.

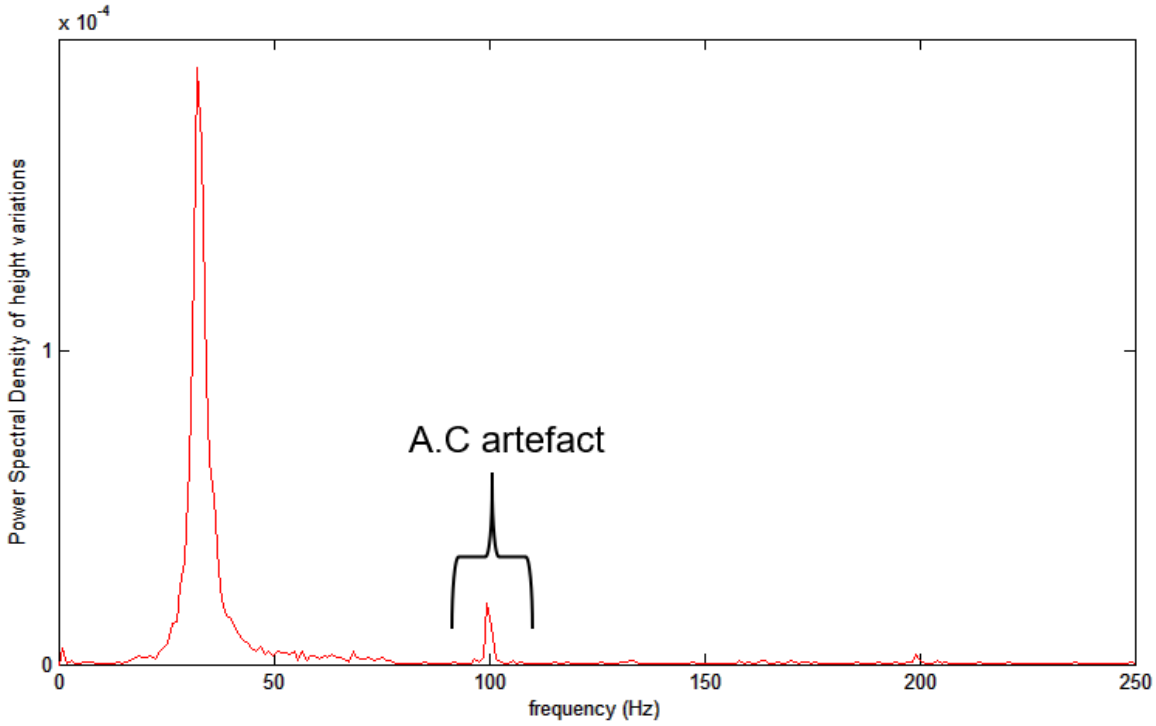


Figure 3.20: The Fourier transform of the waveform in figure 5.14. the AC artefact at 100Hz can be clearly seen as a distinct peak, alongside the peak associated with the actual surface wave.

3.6 Dynamic light scattering analysis

In order to obtain a comparison between the values of G′ and G″ for the polymer solutions which were being studied, the solutions were analysed using a technique known as dynamic light scattering [50] (Abbreviated to DLS). DLS is a technique commonly used to determine the physical size of particles and therefore finds common application in pharmaceutical research. The size of particles can have a significant effect on how a particle will interact with its environment. This is especially true in biochemistry, where a particle's size may determine if it can fit through a biological membrane, such as cell membranes. The size of a particle may also affect how well it dissolves in a solution, as well as potentially affecting the rate at which it reacts with other chemicals. Particles with larger surface area to volume ratios will react quicker than those with a smaller surface area to volume ratio due to how well exposed the chemicals which make up the particle in question are exposed to the chemical which they are reacting with. DLS can also be used to study the size, interactions, and aggregation of proteins [51,52]. Although the technique is typically used for determining particle size, it can be modified in such a way as to allow for the measurement of both the storage and loss moduli of viscoelastic liquids.

DLS works by directing a laser beam at a sample of liquid (with known physical properties) containing the particles which are to be examined and analysing the laser light which is scattered off the particles suspended in the liquid. By analysing the change in the laser light that is scattered off the particles over time, the physical size of the particle can be determined. DLS can also be used to determine the physical properties of liquids, provided that the physical size of the particles that are suspended within the liquid is already known.

In this experiment, PAA solutions of varying concentrations will be analysed via DLS. The data acquired from this experiment will then be used to calculate the frequency dependent storage (G′) and loss (G″) moduli for each concentration of polymer solution. This information will then be compared to the results of the sessile drop vibration experiment (chapters 5).

3.6.1 The general Stokes Einstein equation

The principle behind dynamic light scattering is that particles that are dissolved in a liquid will undergo Brownian motion which is governed not only by the temperature of the liquid, but also by the physical size of the particle and the viscosity of the liquid in which they are dissolved [53].

The mean squared displacement of a particle which is moving freely in an ideal viscous (Newtonian) fluid will increase linearly over time. The gradient of this displacement is known as the diffusion coefficient of the particle and can be defined as:

$$\langle \Delta r^2(t) \rangle = 2\bar{d}Dt \tag{3.1}$$

where t is the time which the particle has been in motion, and $\bar{d}$ is the number of dimensions in which the particle is free to move in (typically 3).

In a simple liquid which possesses no elastic component, a simplified version of the Stokes-Einstein relation can be used to relate the diffusion coefficient to the viscosity of the liquid:

$$D = \frac{k_B T}{3\pi d\eta'} \tag{3.2}$$

where T is the temperature of the media, η' is the viscosity of the media (the real component of the viscosity), and d is the diameter of the particle. This simplified version of the Stokes-Einstein relation however does not work for viscoelastic liquids as it does not take into account the energy loss and storage which takes place within viscoelastic materials.

In order to accurately describe the motion of a particle undergoing thermal fluctuations within a viscoelastic liquid, a generalized Langevin equation is used, this equation is a modified version of Newton's second law. This takes the form of:

$$mu(t) = f(t) - \int_0^t \zeta(t-\tau)v(\tau)d\tau \tag{3.3}$$

where m is the mass of the particle, u is the particle's acceleration, f is the total force acting on the particle, and ζ is a time-dependant memory function that compensates for the elastic component of the system.

Einstein [54] solved this equation for the case where only thermal fluctuations contribute to the force acting on the particle to produce the general Stokes-Einstein relation:

$$G^*(\omega) = \frac{k_B T}{\pi s i \omega \langle \Delta r^2(i\omega) \rangle} \tag{3.4}$$

where G* is the frequency dependent complex shear modulus of the medium and ω is the angular frequency.

3.6.2 The autocorrelation function

A DLS device works by measuring laser light which is scattered off particles which are suspended in a medium. As these particles move, the amount of light being scattered will also change. The rate at which the scattered signal changes over time is therefore related to the rate what which these particles are moving through the medium. An autocorrelation function is produced by comparing the changes in the scattered signal over time and measures how much the signal correlates with its previous state (hence the name auto-correlation).

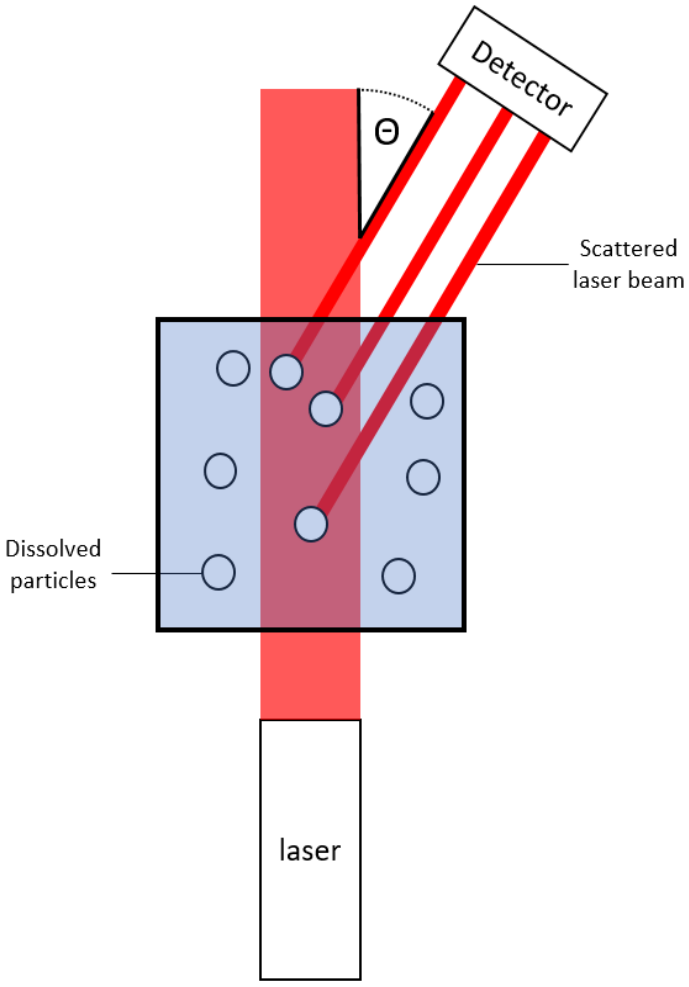


Figure 3.21: The experimental setup used to examine viscoelastic polymer solution via dynamic light scattering (not to scale). The diagram shows a monochromatic laser beam passing through a polymer solution containing nanoparticles. These nanoparticles scatter the initial laser beam through an angle of Θ. This scattered laser light is then detected via the use of a photodetector.

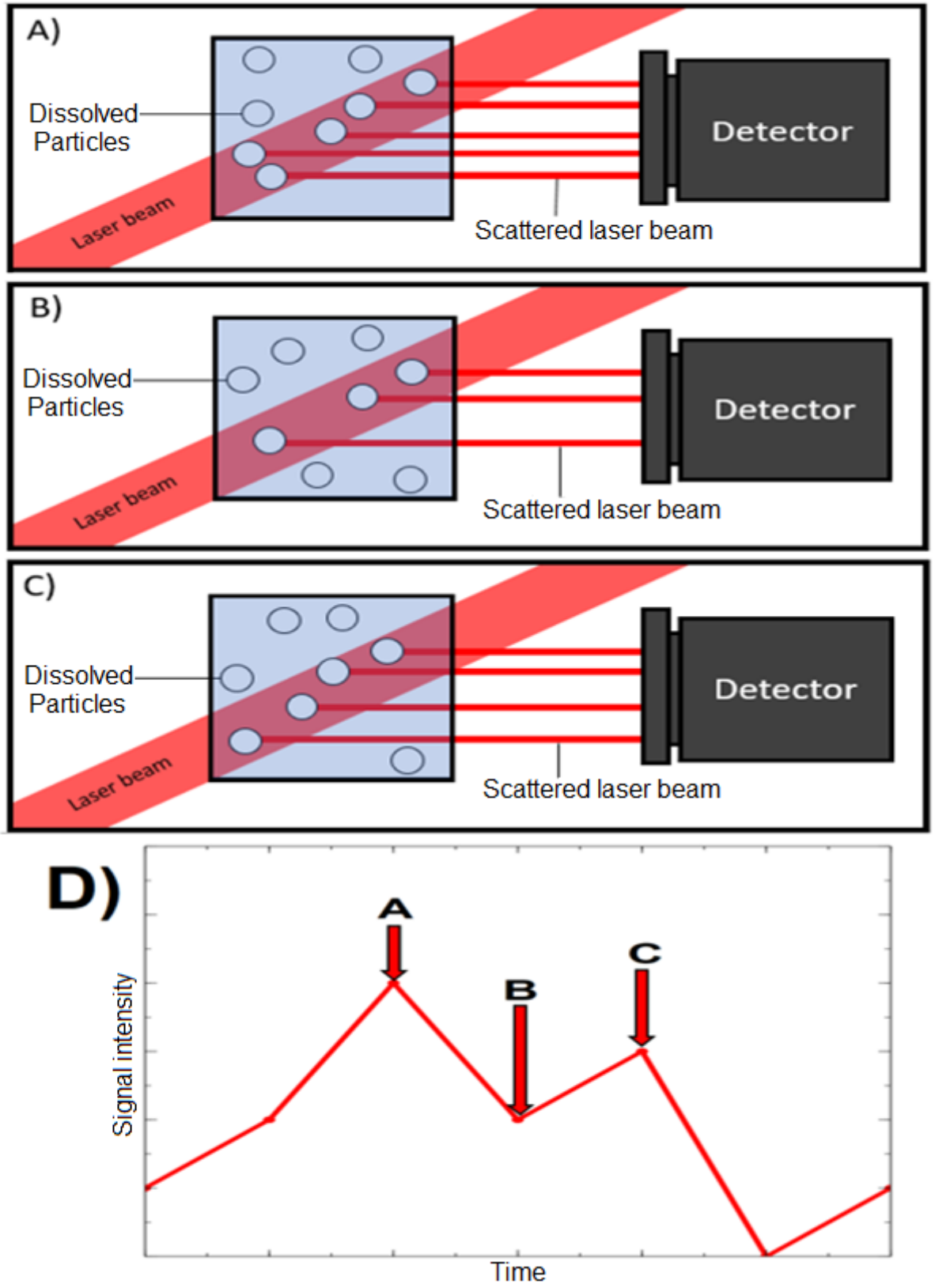


Figure 3.22: A collection of diagrams to demonstrate how the intensity of scattered laser light is measured over time. Figures A, B, and C show how the intensity of scattered light changes as the particles moves around in the solution over time. Figure D shows how the intensity of scattered light is plotted against time.

Once the intensity of the scattered laser light has been measured over time, the autocorrelation function can be calculated. This is done by comparing the values for the scattered intensity with a copy of the intensity data which has been shifted out of phase with the original data. This is shown in figure 3.23. The difference between the original data and the shifted data is known as the lag time (τ).

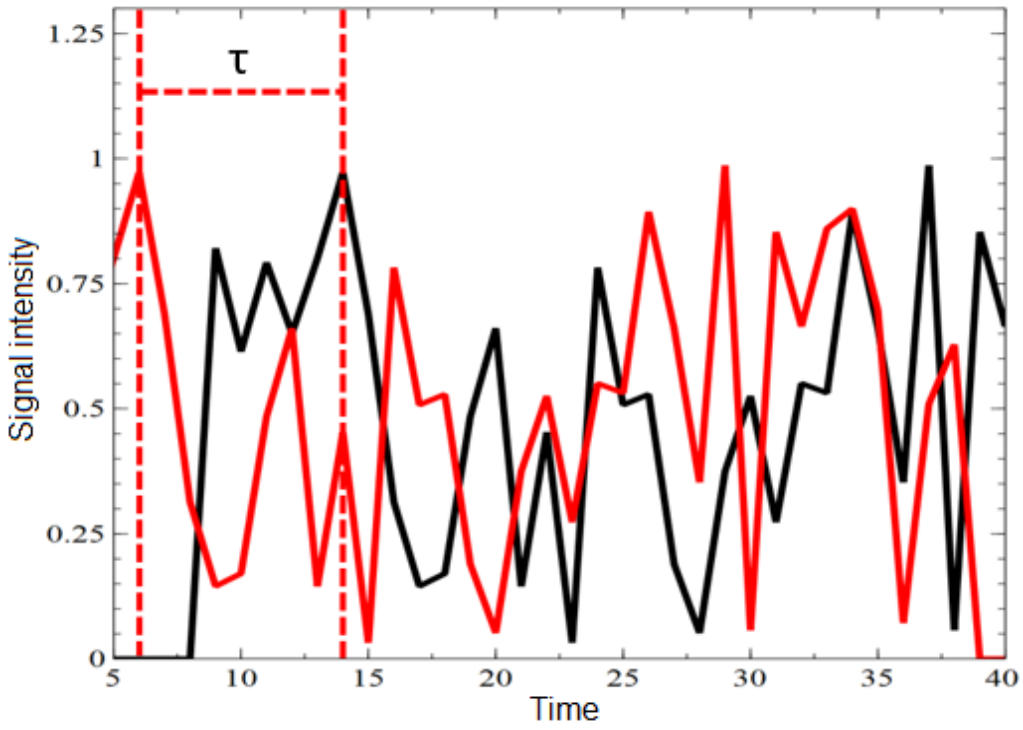


Figure 3.23: A diagram demonstrating how the autocorrelation function is calculated. The original data (red) for the intensity of scattered laser light over time is compared to a copy (black) which has been shifted out of phase with the original data. The phase difference in these two data sets is known as the lag time, τ.

The autocorrelation function is calculated using the equation:

$$g(\tau) = \frac{1}{T}\int_0^T I(t)I(t+\tau)d\tau \tag{3.5}$$

where T is the time period over which the measurements were taken, I(t) is the intensity as time t, and I(t+τ) is the intensity at time t+τ, where τ is the lag time between the original data set and the copy of the data (as shown in figure 3.23). The mean squared displacement of the particle can be written in terms of the autocorrelation function:

$$\langle \Delta r^2(\tau) \rangle = \frac{6}{\Psi^2}\left[\log\left(g_1(0)\right) - \log\left(g_1(\tau)\right)\right] \tag{3.6}$$

where $g_1(\tau)$ is the value of the autocorrelation function at a time τ, and Ψ is the scattering vector, $g_1(0)$ is the value of the autocorrelation function at zero time (or intercept), The correlation time τ is the inverse of the angular frequency, and Ψ is the scattering vector, which is given by:

$$\Psi = \frac{4\pi n}{\lambda}\sin\left(\frac{\theta}{2}\right) \tag{3.7}$$

where n is the refractive index of the media, θ is the angle through which the laser light is scattered, and λ is the wavelength of the laser.

Weitz [55] showed that the mean squared displacement can be expanded around t to give:

$$\langle \Delta r^2(t) \rangle \approx \langle \left(\Delta r^2 \left(\frac{1}{\omega} \right) \right) \rangle (\omega t)^{\alpha(\omega)} \tag{3.8}$$

where α is the power law exponent describing the logarithmic slope of the MSD over time. For a particle moving in a purely viscous media, the gradient of the logarithmic slope of the MSD will be one, whereas a particle moving in a purely elastic media will have a MSD logarithmic slope of zero. This is because the particle will be unable to make any net progress away from its point of origin due to elastic forces opposing its motion. Since a viscoelastic material possesses both viscous and elastic characteristics, the logarithmic slope of the MSD of a particle moving within a viscoelastic media will be between zero and one.

Finally, by evaluating the Fourier transform of the power law behaviour of the mean squared displacement and substituting the result into equation 3.4 results in the equation:

$$G^*(\omega) = \frac{k_B T}{\pi d \langle \Delta r^2 \left(\frac{1}{\omega} \right) \rangle \Gamma[1+\alpha(\omega)]} \tag{3.9}$$

where G* is the frequency dependent complex shear modulus of the medium in terms of the particle's size and the mean squared displacement of the particle over time.

Utilizing Euler's formula results in equations which describe both the elastic and viscous modulus (G′ and G″ respectively):

$$G'(\omega) = G^*(\omega) \cos \left[\frac{\pi \alpha(\omega)}{2} \right] \tag{3.10}$$

$$G''(\omega) = G^*(\omega) \sin \left[\frac{\pi \alpha(\omega)}{2} \right] \tag{3.11}$$

3.6.3 Solution preparation

In order for the polymer solutions to be analysed via dynamic light scattering, nanoparticles of a known size must first be added to the solution. For this experiment polystyrene nanoparticles with a diameter of 100nm (Sigma-Aldrich UK) where chosen, the size of which were verified via DLS analysis. equation 3.8 can be rearranged in order to calculate the physical size of the dissolved particles. This is by far the most common way in which dynamic light scattering is utilized, frequently being used in fields such as pharmacology to determine the physical size of pharmaceutical compounds [56]. By dissolving the nanoparticles in deionised water and analysing the autocorrelation function acquired from DLS analysis, in conjunction with the known viscosity of pure water, the size of the nanoparticles was verified to be 100nm. This was done using the equation:

$$d = \frac{k_B T}{\pi G^*(\omega) \langle \Delta r^2 \left(\frac{1}{\omega} \right) \rangle \Gamma[1+\alpha(\omega)]} \tag{3.12}$$

which is simply equation 3.9 rearranged make the particle diameter d the subject of equation. The concentration of the nanoparticles within the solution is very important, as it can have a significant impact on the results of the analysis.

If the concentration of nanoparticles within the solution is too low then not enough laser light will be scattered, resulting in the scattered signal being dominated by background noise. However, if the concentration of nanoparticles is too high, them a phenomenon known as bridging can occur. Bridging (illustrated in figure 3.24) is where polymer chains adhere to more than one nanoparticle at the same time, effectively tethering the two particles together. This results in the motion of the two nanoparticles being linked via the bridging polymer, meaning that their motion will be coupled with that of the particle which they are attached to via the polymer bridge, and therefore cannot move freely under the influence of Brownian motion.

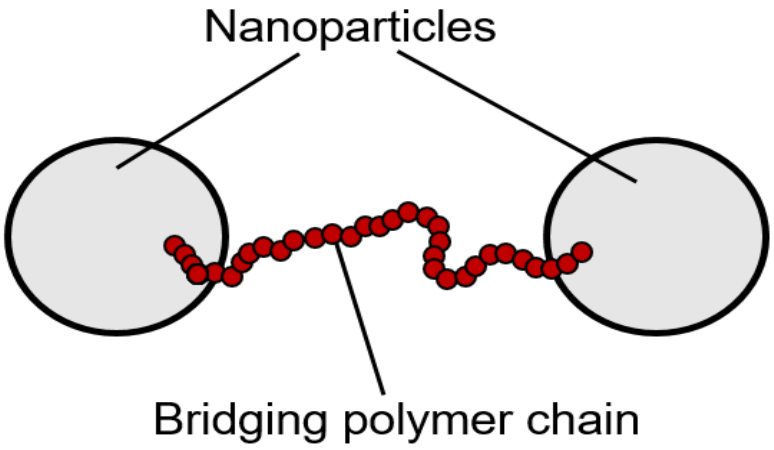


Figure 3.24: An illustration of the bridging effect, where a single polymer chain becomes attached to two different nanoparticles, effectively tethering one to the other.

The higher the concentration of nanoparticles within the solution, the higher the probability that one nanoparticles will be within close proximity to another, and therefore the higher the probability that a polymer bridge between the two particles will occur. A concentration of 0.05% by volume was used to ensure that a strong signal was produced from the scattered laser light, while simultaneously keeping bridging effects to a minimum.

A second consideration is that high levels of nanoparticles within the polymer solution might lead to aggregation of the nanoparticles. Such an occurrence would corrupt the results of the experiment. Because of this, the concentrated nanoparticle solution was sonicated (subjected to ultrasonic sound waves) in order to break up any potential aggregates that had formed before the nanoparticles were added to the polymer solutions.

3.6.4 Measuring procedure

Doped polymer solutions (as described in section 3.6.3) with a PAA concentration of 0.5-3.0wt% were created (as described in section 3.1, only with the addition of nanoparticles), with care being taken to make sure that the ratio of water to PAA was correct, regardless of the addition of the polystyrene nanoparticles. These solutions where then analysed using a Malvern nano ZS90 Zetasizer. Each solution was analysed ten times at 293 K with a run time of three minutes. The autocorrelation function obtained from analysing the variation in intensity of scattered light over time (as shown in figure3.25 and 3.26) were then exported from the Malvern Zetasizer program and averaged together.

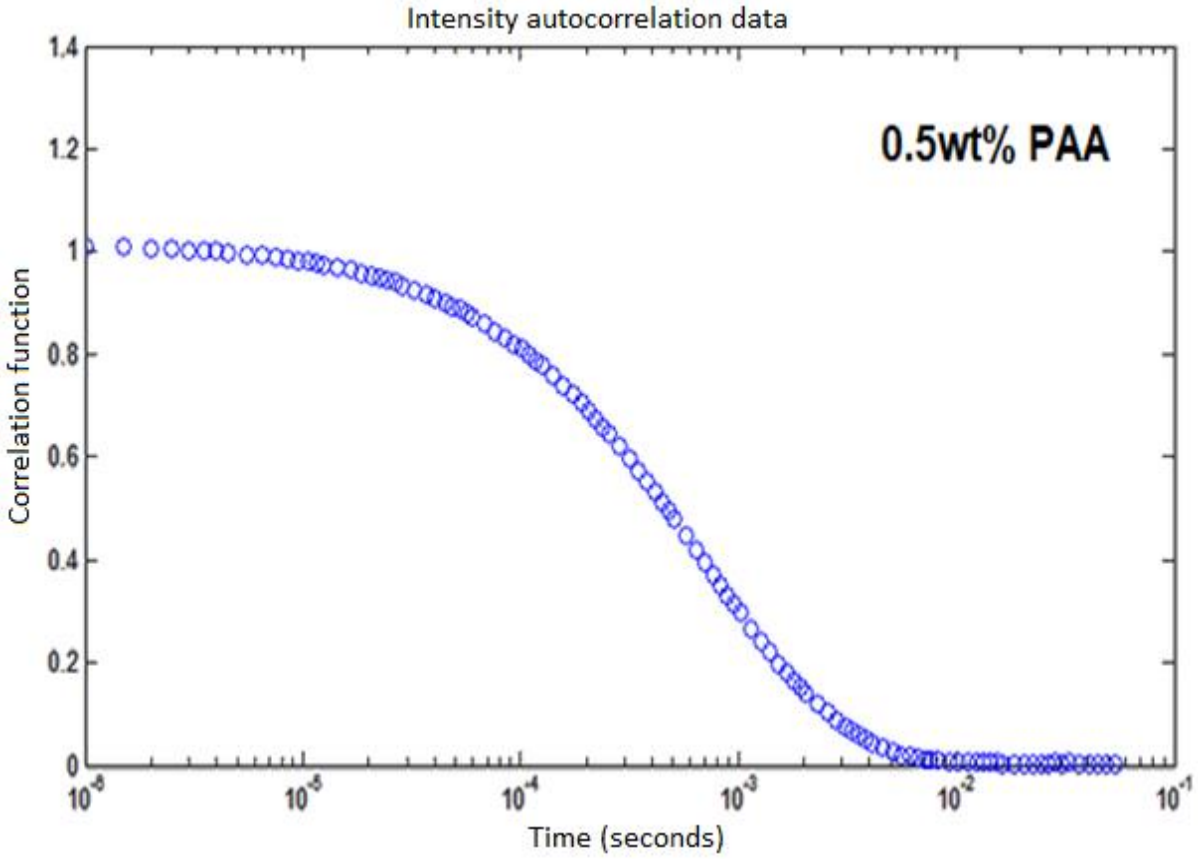


Figure 3.25: The auto-correlation function obtained from the dynamic light scattering analysis of a sample of 0.5wt% PAA solution.

From this autocorrelation function, the mean squared displacement of the particles over time could be calculated by utilising equation 3.6.

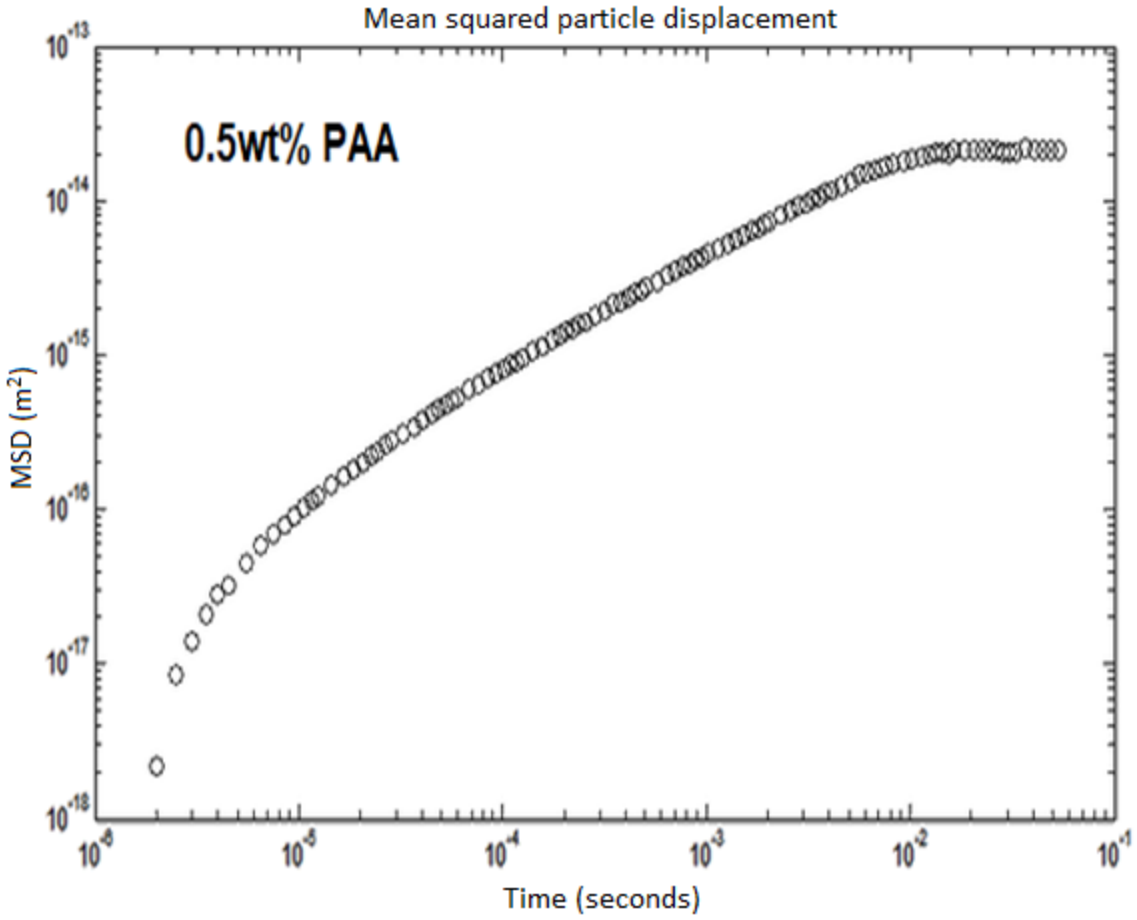


Figure 3.26: The mean squared displacement of polystyrene nanoparticles dissolved in a 0.5wt% PAA solution.

The average autocorrelation function was then analysed (as described in section 3.6.2) and used to calculate (using a specially designed Matlab program) the mean squared displacement of the nanoparticles (as shown in figure 3.13) and the logarithmic slope of the mean squared displacement. This information is then used to calculate the frequency dependant storage(G′) and loss(G″) moduli of the viscoelastic polymer solutions (using equations 3.9, 3.10, and 3.11).

3.6.5 DLS results

The results of this analysis are shown in figures 3.27 and 3.29. The errors were calculated from the slight variation in nanoparticle size and the deviation of the autocorrelation functions that were acquired.

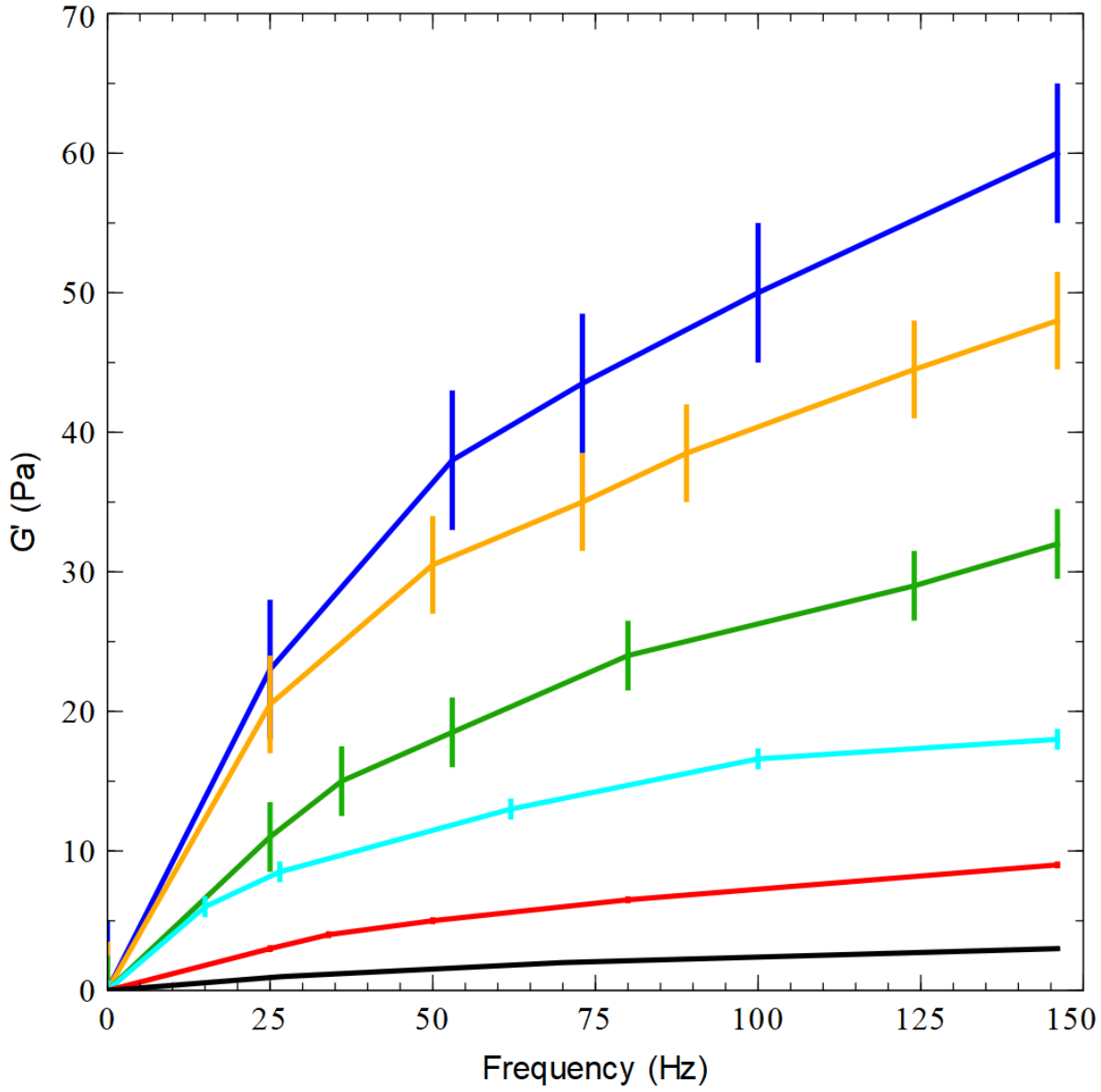


Figure 3.27: the frequency dependent storage modulus of PAA polymer solutions of varying concentration acquired via DLS analysis. (0.5wt%- black, 1.0wt%-red, 1.5wt%-cyan, 2.0wt%-green, 2.5wt%-yellow, 3.0wt%- blue).

Figure 3.27 displays the results for the frequency dependent storage modulus of the PAA solutions. The increase in the frequency dependent storage modulus with an increase in polymer concentration is to be expected, as the additional polymer chains would increase the elasticity of the solution. Since this experiment was carried out on the same material and the same equipment as used by Harrold et al [11], a direct comparison can be made between the two sets of results.

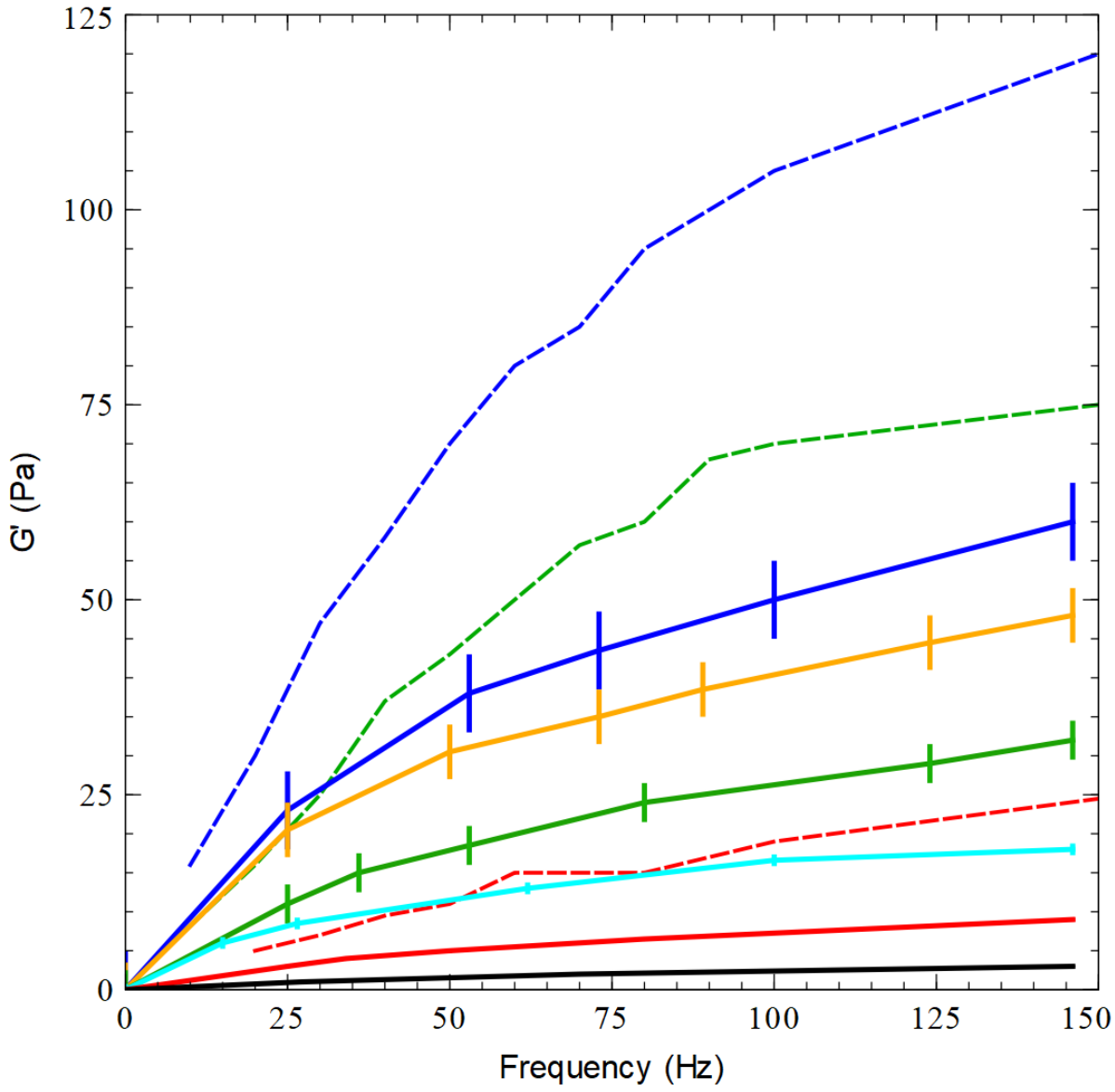


Figure 3.28: the frequency dependent storage modulus of PAA polymer solutions of varying concentration acquired via DLS analysis. (0.5wt%- black, 1.0wt%-red, 1.5wt%-cyan, 2.0wt%-green, 2.5wt%-yellow, 3.0wt%- blue). The red, green, and blue dashed lines represent the results acquired by Harold et al [11] for PAA concentration of 1.1wt%,2.0wt%, and 3.0wt% respectively.

As can be seen in figure 3.28, the results for the storage modulus are notably lower than the results obtained by Harold et al. This deviation could come from a number of different sources, such as aggregation of the nanoparticles used the DLS analysis, or the polymer solutions not being properly dissolved in the solution before the analysis began. This deviation will be discussed further at the end of the chapter.

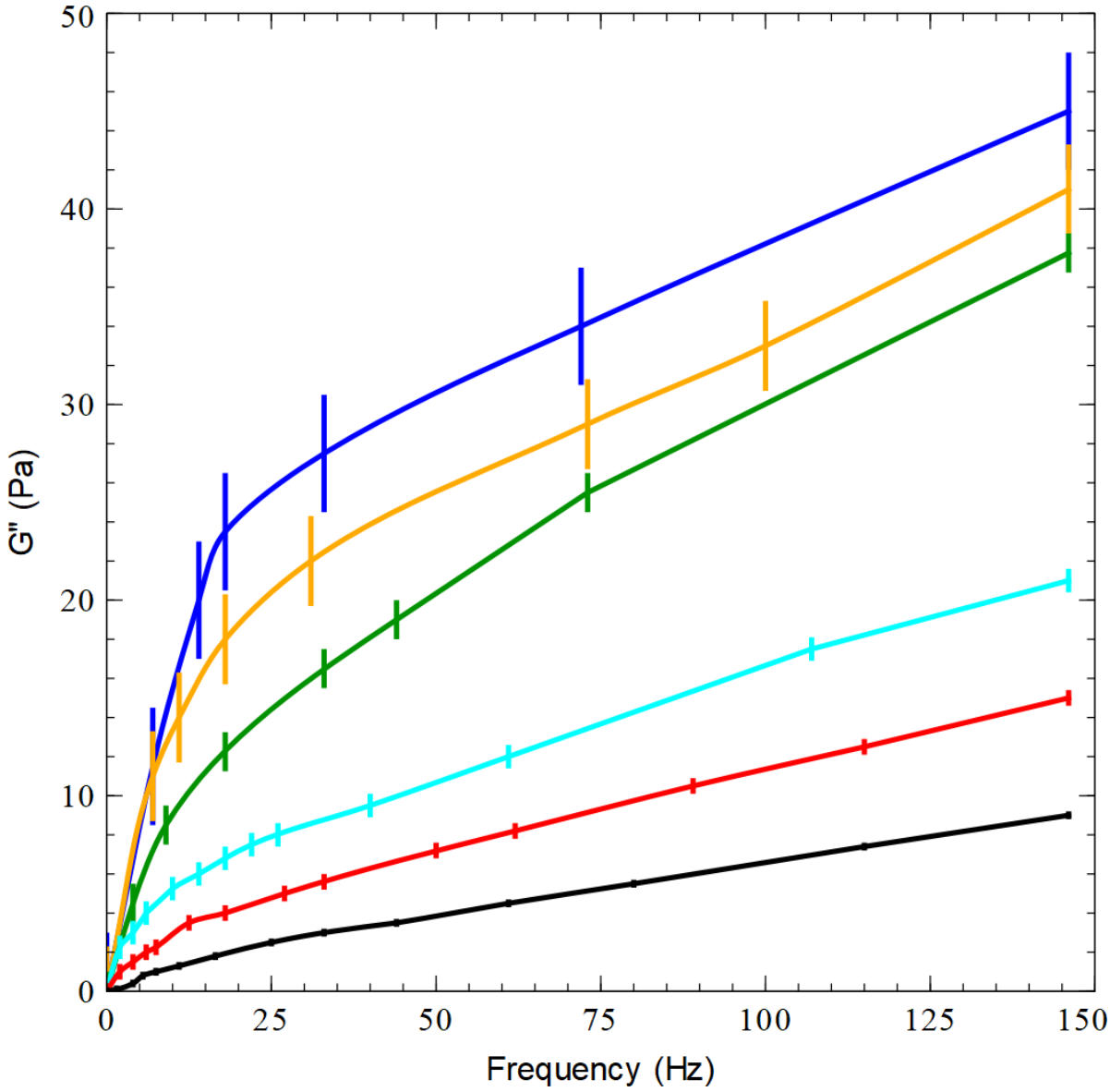


Figure 3.29: the frequency dependent loss modulus of PAA polymer solutions of varying concentration acquired via DLS analysis. (0.5wt%- black, 1.0wt%-red, 1.5wt%-cyan, 2.0wt%-green, 2.5wt%-yellow, 3.0wt%- blue).

Figure 3.29 displays the results for the frequency dependent loss modulus of the PAA solutions. The gradual increase in the frequency dependent modulus with an increase in polymer concentration is again what would be expected from these result, as increasing the polymer concentration would naturally make the solutions more viscous. Again, a direct comparison between these results and the results obtained by Harold et al [11] can be made.

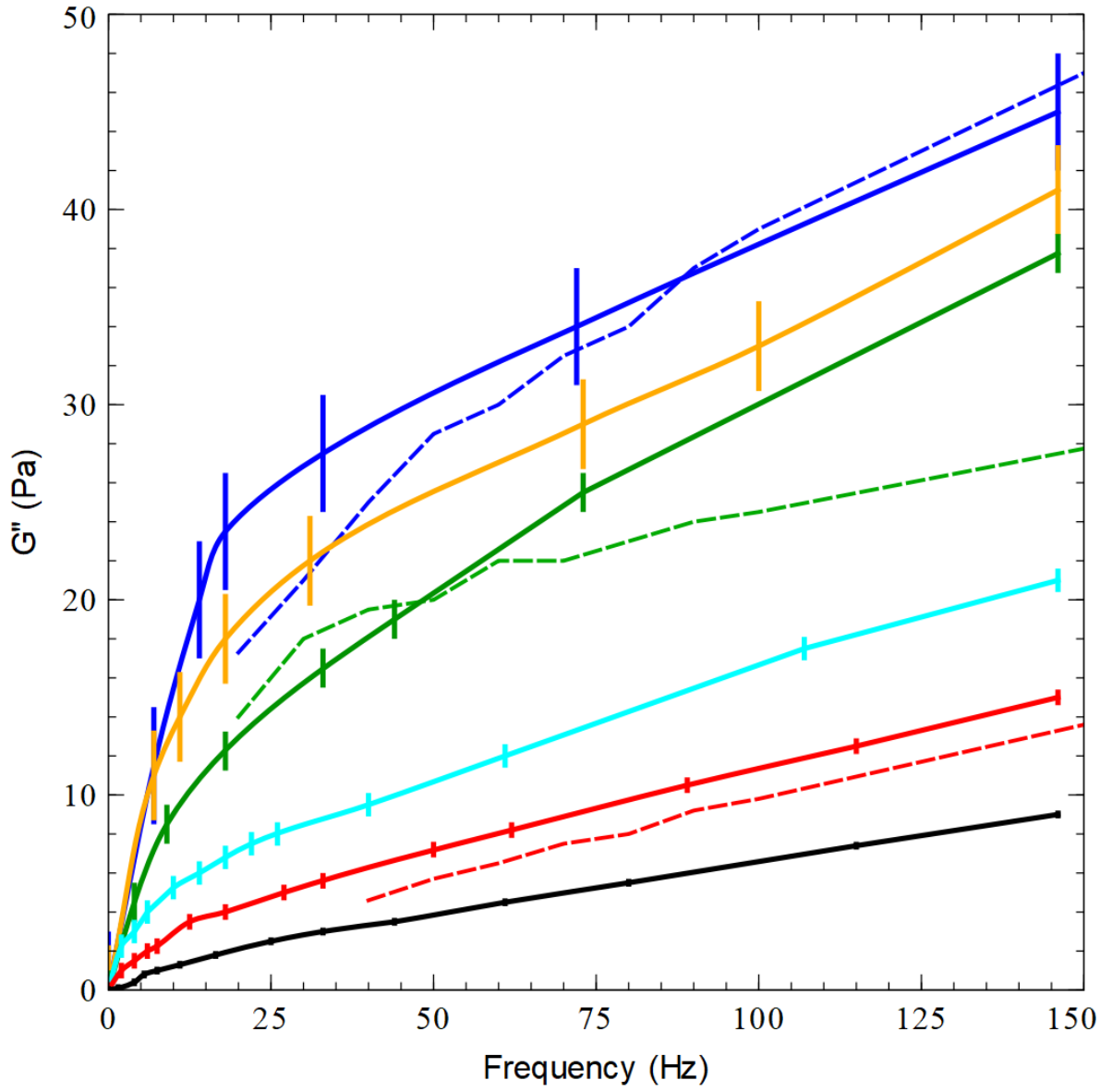


Figure 3.30: the frequency dependent loss modulus of PAA polymer solutions of varying concentration acquired via DLS analysis. (0.5wt%- black, 1.0wt%-red, 1.5wt%-cyan, 2.0wt%-green, 2.5wt%-yellow, 3.0wt%- blue). The red, green, and blue dashed lines represent the results aquired by Harold et al [11] for PAA concentration of 1.1wt%,2.0wt%, and 3.0wt% respectively.

The results for the loss modulus (G″) seem to at least partially agree with the results obtained by Harrold et al (as shown in figure 3.30), while the results for the storage (G′) modulus (figure 3.29) seem to be notably lower. This discrepancy could come from the two sets of solutions having slightly different polymer concentrations, or may have been prepared in a slightly different manner. Lower concentrations had much lower scatter in their autocorrelation functions compared to higher concentrations. This is most likely a result of light scattering off the polymer chains themselves. Alternatively, it could indicate the presence of small aggregations of polymer which have clumped together, resulting in certain parts of the solution having a higher density than others.

This would seem highly unlikely as the solutions were given ample time to dissolve properly and were aggerated before they were analysed. Visual analysis of the solutions would also suggest that this is not the case. In order to test if the nanoparticles had indeed aggregated, they were analyses by placing a sample of the nanoparticles into distilled water and analysed using dynamic light scatter. Instead of using a particle of a known size to calculate the viscoelastic properties of the liquid which the particles were suspended in, the liquid's viscosity was known, and used to calculate the size of the suspended particle (using equation 3.12). This test indicated that the suspended nanoparticles had not aggregated since they were used by Harold et al, and still had a diameter of 100nm.

The DLS analysis of the PAA solutions were carried out multiple times in an attempt to deduce why there was such a noticeable difference between the results for the storage modulus obtained by Harold et al and the results obtained in this investigation. Unfortunately, no satisfactory answer was found, as repeated analysis of the PAA solutions did not yields notably different results. Completely new polymer samples were also created and tested, with no noticeable variation in results. The variation in the loss modulus is notably less significant than the difference in the storage modulus. This might imply that something has happened to the polymer while in storage which compromised the elasticity of the polymer. This is of course only speculation, and since the polymer was stored correctly in a sealed container in a chemical cupboard, corruption on the polymer (especially over little more than a year) would appear to be very unlikely.

A slight anomaly in these results might be the sudden increase in G″ between the 1.5wt% and 2.0wt% PAA solutions, as shown in figure 3.29. A similar increase in viscosity can be seen in the in results obtained by Harrold et al. This might be as a result of polymer entanglement [57], where polymer chains become entangled with one another and thus increase the overall viscosity of the solution. Despite the fact that all of the solution studied here are above what is known as overlap concentration (0.1%), meaning that all the solutions contain overlapping (or entangled) polymer chains, the frequency of the occurrence of overlapping polymer chains increases with the concentration of polymer chains.

These results will now be used to compare the results of a proven analytical technique (DLS) with the resulting from the experimental analytical technique described in chapter 5.

Chapter 4

Surface tension of Polymer solutions

4.1 Introduction

The surface tension of a liquid (section 2.2) has a noticeable effect on surface waves. Since surface waves deform the surface of a liquid, increasing and decreasing the liquid's surface area over time, the surface tension results in the mechanical energy being first converted into potential energy stored in the dangling bonds on the newly formed interface, and then lost as thermal energy when the interface is destroyed. As such, surface tension plays an important role in how surface waves are damped.

Since the surface tension (Ω) is a variable which appears in the Jäckle equation (section 2.5), this variable must first be measured in order to apply the Jäckle model to the vibration of sessile droplets.

The technique that was chosen for determining the surface tension of the polymer solutions which are being investigated (section 3.1) is known as the pendant drop tensiometry [58-59]. This technique was chosen because it allows for the surface tension of a liquid to be acquired from a microlitre volume of liquid. This is in keeping with the general goal of developing analytical techniques for viscoelastic fluids using small sample sizes.

The pendant drop method involves analysing the extent to which a pendant droplet (with a radius that exceeds the capillary length) is deformed under the influence of gravity.

4.2 The Young-Laplace equation

A pendant droplet that is under the influence of gravity and has a radius that exceeds the capillary length will undergo deformation. The initially spherical shape of the droplet is elongated to form the characteristic 'pendant' shape, which is where the name 'pendant droplet' is derived from.

The extent to which the pendant drop is deformed under gravity is determined by the surface tension of the droplet. The higher the surface tension, the more the pendant droplet will maintain its spherical shape. By measuring the extent to which the pendant droplet has been deformed, the surface tension of the liquid can be determined.

A pendant drop at equilibrium will obey the Young-Laplace equation [60], which relates the pressure exerted across an interface with the curvature and surface tension of said interface:

$$\Omega\left(\frac{1}{R_1}+\frac{1}{R_2}\right) = \Delta P - \Delta\rho g z \tag{4.1}$$

where $R_1$and $R_2$are the two primary radii of curvature of the pendant drop, ΔP is the pressure difference across the surface of the droplet, ρ is the density of the droplet, $\Delta\rho$ is the difference between the density of the droplet and the density of the surrounding media (which in this case was air under standard conditions), g is the force of gravity, and z is the height of the droplet. As previously defined, Ω is the surface tension of the pendant droplet.

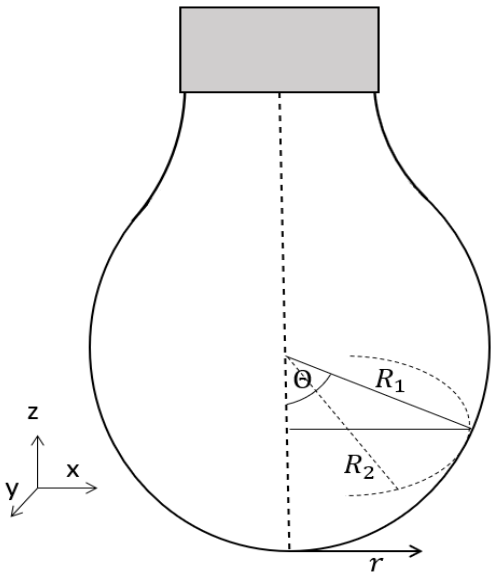


Figure 4.1: A pendant droplet suspended from a pipette tip, with the two primary radii of curvature (R_1 and R_2) shown. The angle between the radius of curvature and the central axis of the droplet is given by Θ. R_1 is the radius of curvature in the zx plane, and R_2 is the radius of curvature in the xy plane.

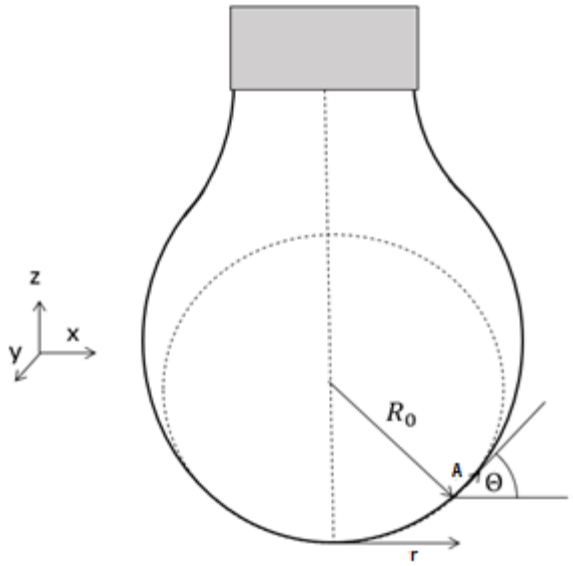


Figure 4.2: A pendant droplet suspended from a pipette tip, with the principle radius of curvature R_0 show. The arc length is denoted by A, and Θ denoted the angle between the arc tangent and the x axis (r). Θ is the same angle as Θ in figure 4.1.

By taking advantage of the pendant droplet's axisymmetry, equation 4.1 can be expressed in terms of the cylindrical coordinates r, z, and the tangent angle Θ. The Young-Laplace equation can be expressed as a set of dimensionless differential equations in terms of the arc length A (defined in figure 4.2):

$$\frac{d\Theta}{d\bar{A}} = 2 - B_0\bar{z} - \frac{\sin(\Theta)}{\bar{r}} \tag{4.2}$$

$$\frac{d\bar{r}}{d\bar{A}} = \cos(\Theta) \tag{4.3}$$

$$\frac{d\bar{z}}{d\bar{A}} = \sin(\Theta) \tag{4.4}$$

where the bar indicates dimensionless quantities which have been scaled by R_0 [60]. B_o is known as the Bond number (or Eötvös number), which is effectively a numerical representation of the shape of the pendant drop. The lower this number, the more the pendant drops shape is being deformed under the effects of gravity. The Bond number can be directly related to the shape of the droplet with the equation:

$$B_0 = \frac{\Delta\rho g R_0^2}{\Omega} \tag{4.5}$$

where R_0 is the primary radius of curvature, as shown in figure 4.2. The associated boundary conditions for these equation:

$$\bar{r} = 0, \bar{z} = 0, \text{and } \Theta = 0 \text{ at } \bar{A} = 0$$

The Bond number itself can be acquired simply by rearranging equation 4.2 to make the Bond number the subject of the equation.

$$B_0\bar{z} = 2 - \frac{d\theta}{d\bar{A}} - \frac{\sin(\theta)}{\bar{r}} \tag{4.6}$$

Finally, by rearranging equation 4.5, an equation for the surface tension of the droplet can be derived.

$$\Omega = \frac{\Delta\rho g R_0^2}{B_0} \tag{4.7}$$

These equations allow for the surface tension of a deformed pendant droplet to be acquired by measuring the geometry of its surface.

4.3 Experimental procedure

In this experiment a pipette tip with diameter of 1.44mm was positioned in front of a lighting screen (as shown in figure 4.3). PAA solutions where then passed through the pipette tip to form extended pendant droplets. After the pendant droplets had reached the point of equilibrium (the shape of the droplet had stabilized) they were photographed using a Genie HM640 camera.

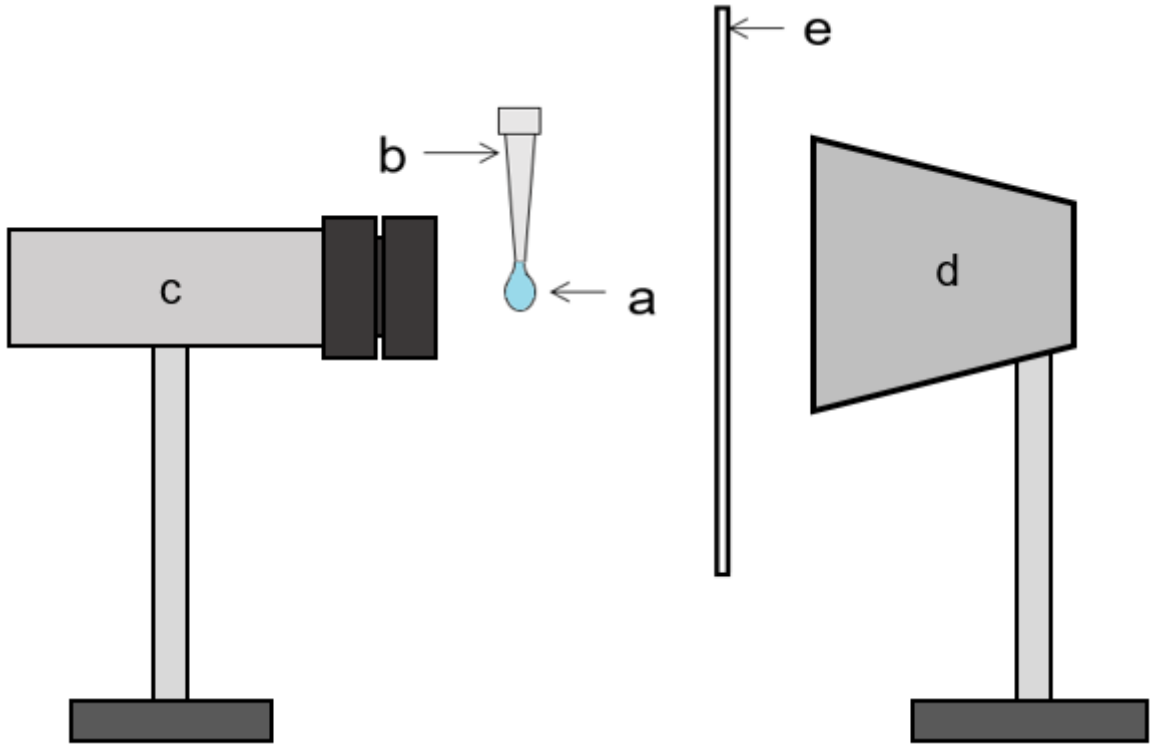


Figure 4.3: The experimental apparatus used to photograph pendant droplets. The pendant droplet (a) was suspended from the end of a pipette tip (b) in front of a Genie HM 640 camera (c). This pendant droplet was backlit by a desk lamp (d), the light from which was dispersed by a lighting screen (e). This camera was calibrated to have a pixel width with the equivalent of 0.028 millimetres per pixel.

Once these photos were taken, the calibration of the measurements was carried out by measuring the width of the pipette tip (in pixels) and using the known value for the diameter of the pipette tip to work out the millimetre to pixel ratio required for the calibration. This measurement was carried out using the photo editing software Gimp.

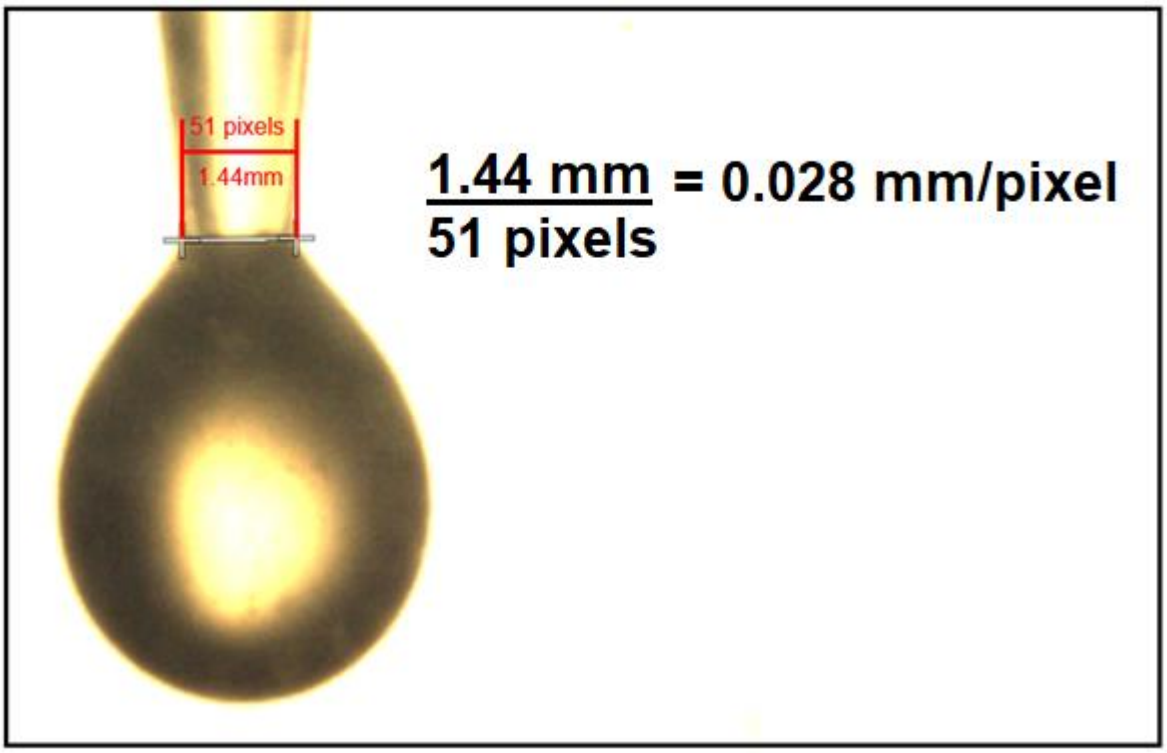


Figure 4.4: A photograph of a pendant droplet which was used to calibrate the measurements being taken. The width (physical diameter 1.44mm) of the pipette tip in the image was measured (in pixels) and used to calculate the calibration constant (the number of millimetres per pixel in the image).

The next step was to load these imaged into a specially developed Matlab program (written by Dr Mike Smith of Nottingham university). The images were cropped so that the pipette tip was removed from the image. The image was then converted into a binary image (as shown in section 3.4) A threshold value of 0.8 was used since it was determined that this gave the most accurate binary image representation of the pendant droplet.

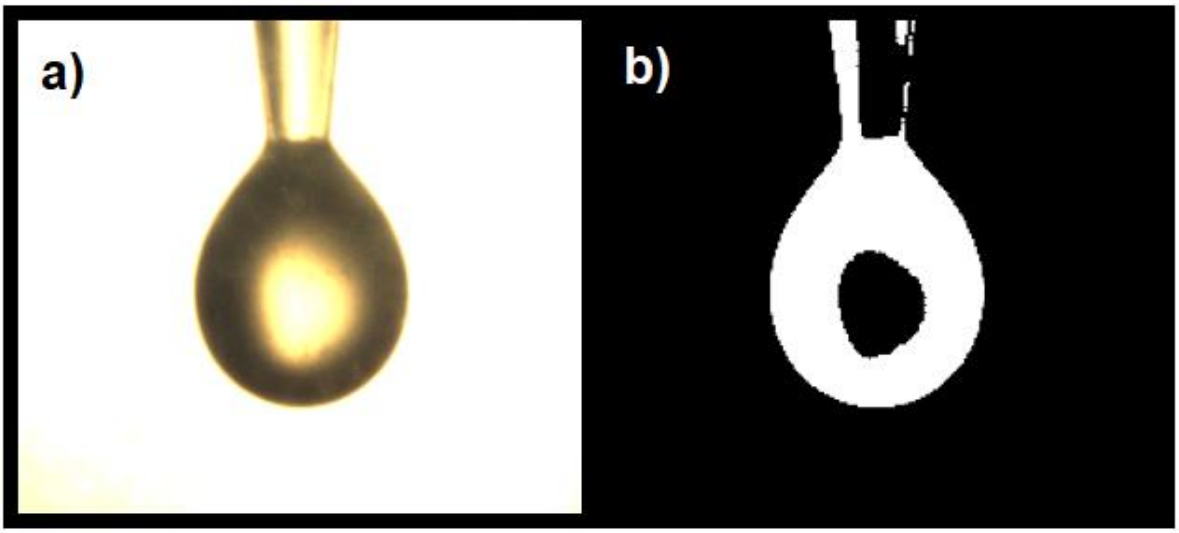


Figure 4.5: An image of a pendant droplet before (a) and after (b) being converted into a binary image.

Once the image had been converted into a binary image, the surface of the pedant droplet was determined by finding the first none zero entry in each row of the matrix representation of the binary image (first measuring from the left, and then from the right). This resulted in two lists of coordinates which describe the left and right side of the pendant droplet. This technique was described in detail in section 3.4. A representation of these pixel coordinates is shown in figure 4.6

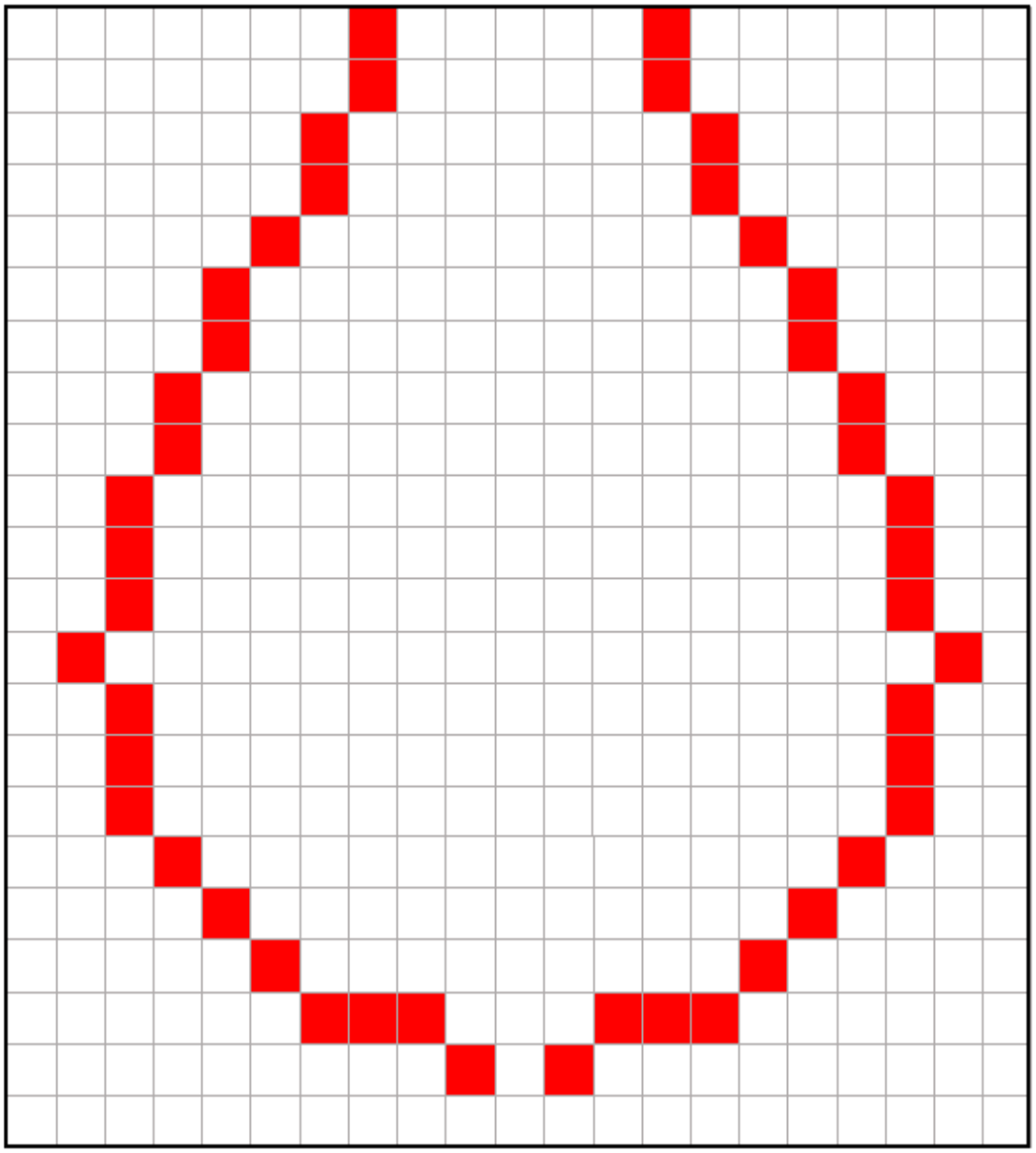


Figure 4.6: A diagram to show the results of the edge detection process for a pendant droplet. (note this is a mock image and is not to scale).

The small gap at the bottom of the pendant outline in figure 4.6 is then filled in to form a complete outline of the pendant droplet. Once this has been achieved the central point of the droplet was calculated. The vertical position of the central point was taken to be in line with the maximum width of the droplet. The horizontal position was taken to be in line with the apex of the droplet (as illustrated in figure 4.7).

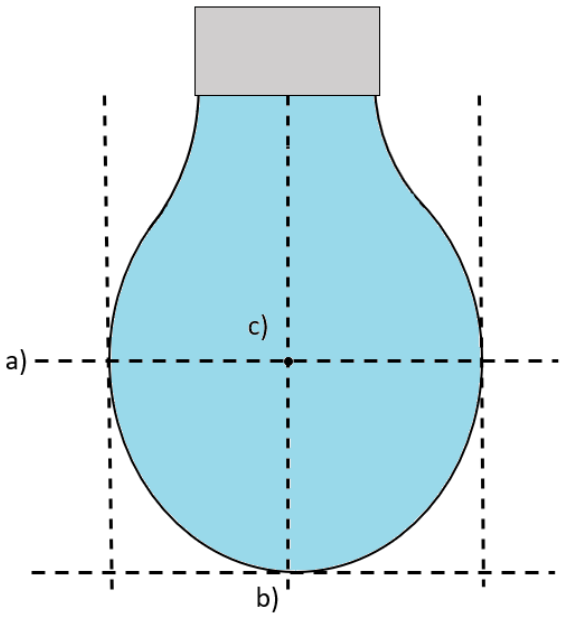


Figure 4.7: An illustration of the central point of a pendant droplet. The vertical position (a) is defined by the maximum width of the droplet, and the horizontal position (b) is defined by the apex of the droplet.

Once this central point has been determined, small increments in the pendant droplet's surface can be used to calculate the Bond number for the pendant droplet (the theory behind which is covered in section 4.2).

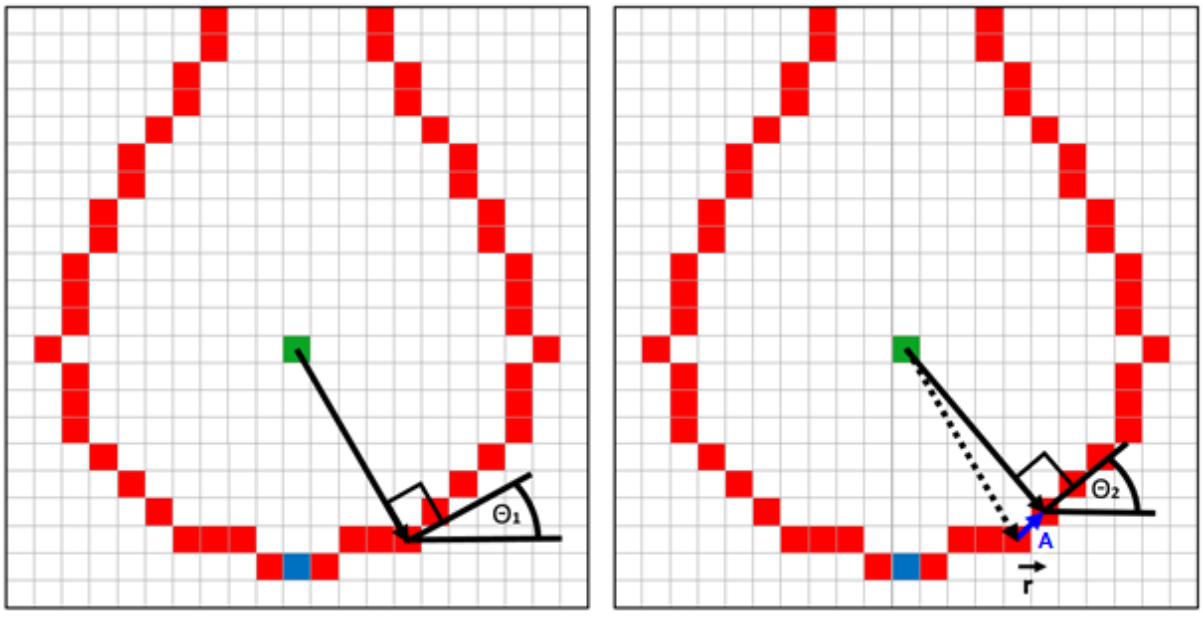


Figure 4.8: A diagram to show how the Bond number is calculated. The tangent to the surface at a particular point along the surface is considered to be at right angles to the line between the being examined and the central point of the droplet (shown in green). The arc length A and the tangent angles Θ_1 (figure a) and Θ_2 (figure b) are shown on the diagram. The value for $d\Theta$ is the difference between Θ_1 and Θ_2.

Finally, a circle was fitted to the surface so that its lowest point overlapped the lowest point of the pendant drop. The radius of this circle was then extended so that the fitted circle overlaps the edge of the pendant drop as much as possible (as illustrated in figure 4.9). Once the optimum fitting of the circle has been established, the radius of this circle ($R_{0)}$ was recorded.

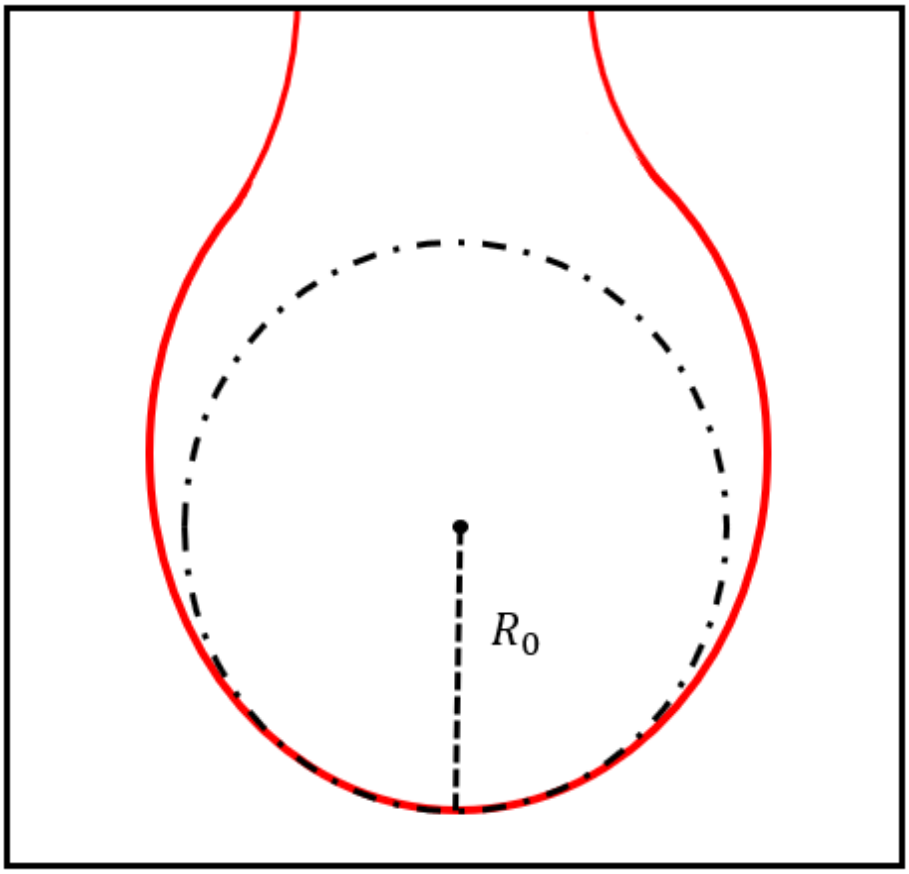


Figure 4.9: A diagram showing how the radius of curvature of a pendant droplet is determined. A circle is fitted to the outline of the pendant droplet, with its lowest point corresponding to the lowest point of the pedant droplet. The radius (R_0) is extended until the closest fit to the pendant drop outline is found.

Once all of these measurements were taken, the surface tension could be calculated. First, the Bond number was calculated (equation 4.6) using the variables dΘ, A and r (shown in figure 4.8). This Bond number was then used in conjunction with the radius R_0 (as shown in figure 4.9) to calculate the surface tension of the droplet (using equation 4.7).

4.4 Results

For the pendant drop surface tension experiment, each polymer solution was measured several times, the results of which are shown below.

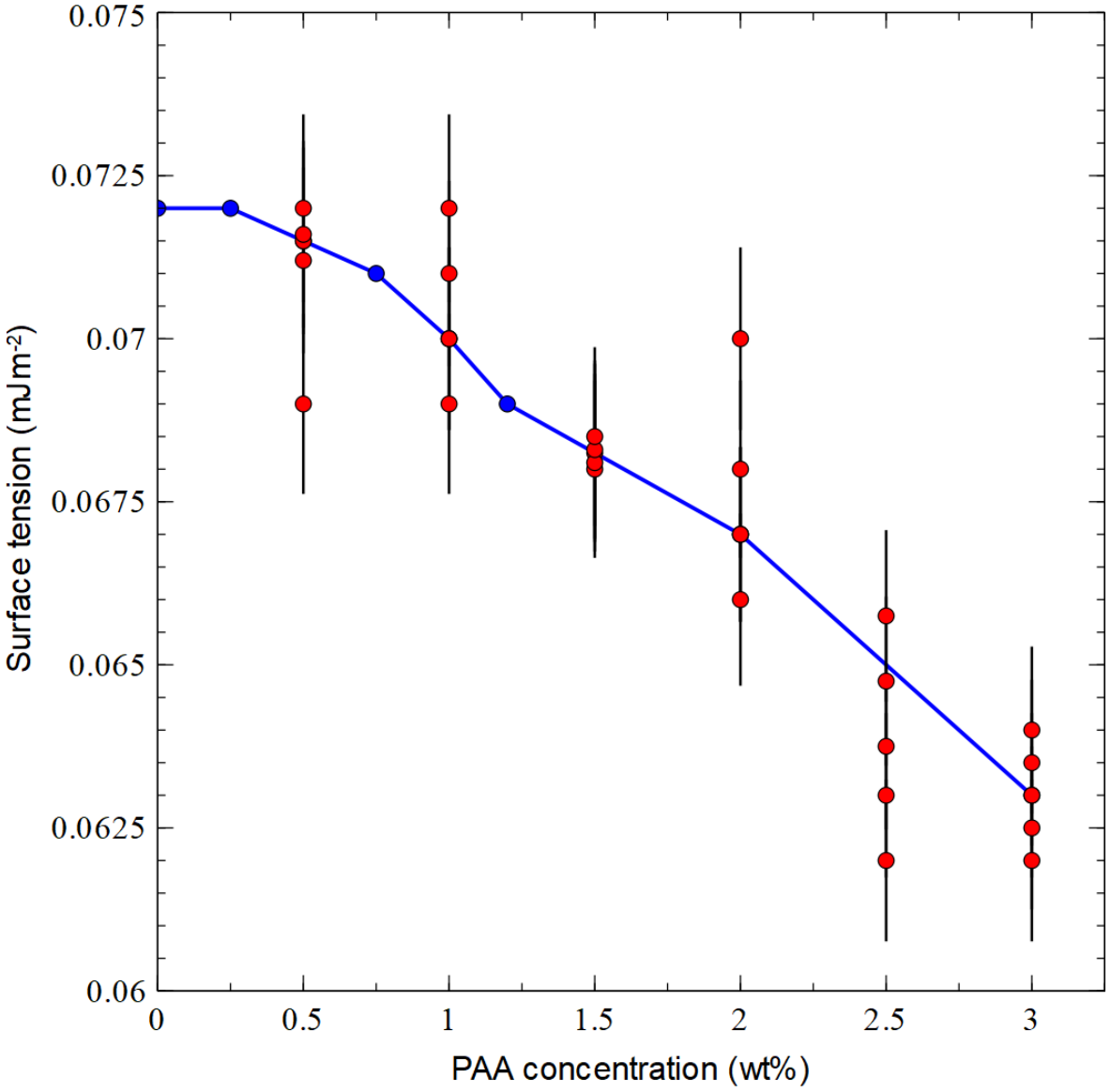


Figure 4.10: The measured values for surface tension (measured in mJ^{-2}) plotted against polymer concentration (shown in red). The blue points on the graph show the results acquired by Harold et al [11].

The results shown in figure 4.10 show a decrease in surface tension as polymer concentration is increased. The most probable cause of the decrease in surface tension of the droplet is the movement of nonpolar polymer chains to the surface of the droplet (as a result on these polymer chains becoming more concentrated). This would result in a decrease in the number of hydrogen bonds across the surface of the droplet, which in turn would reduce the surface tension of the interface (as depicted in figure 4.11).

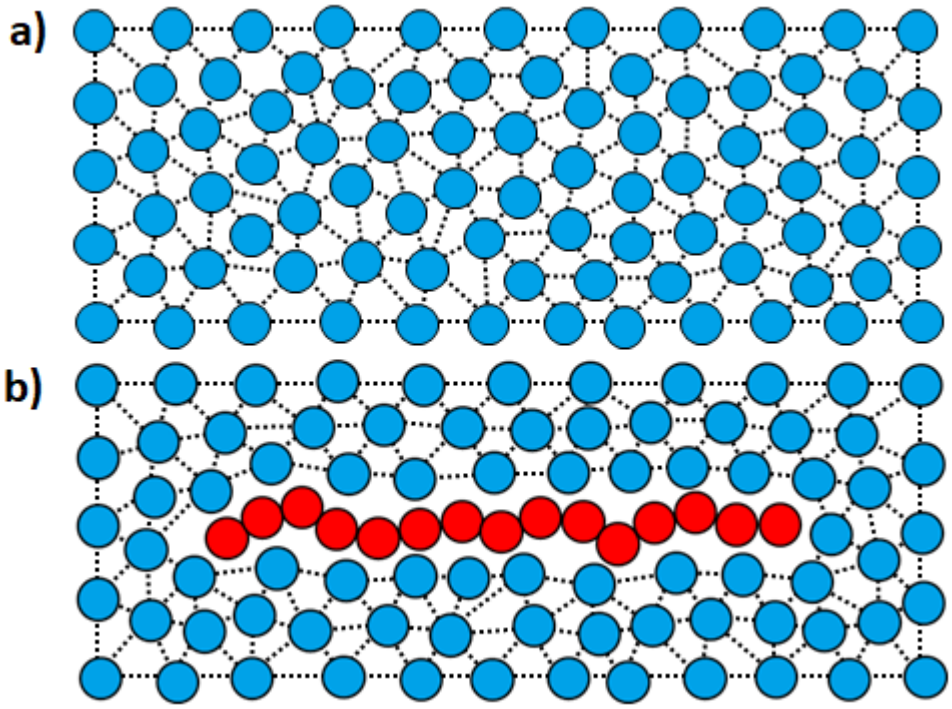


Figure 4.11: A diagram demonstrating how the intermolecular bonds between molecules in a liquid (depicted in blue) can be interrupted by the addition of a non-polar polymer chain. Figure a shows liquid molecules with uninterrupted intermolecular bonds (represented by dashed black lines). Figure b shows how a nonpolar polymer chain (depicted in red) can come between liquid molecules and interrupt the bonds between them.

These results are in agreement with the surface tension measurements that were carried out by Harrold et al [11], with only a very minor deviation between the two sets of results (as shown in figure 4.10). These results were used as the values for the surface tension of the polymer solutions used in the experimental sessile droplet analytical technique described in chapter 5.

PAA concentration (wt%)	Surface tension (J/m^2)
0.5	0.0711
1.0	0.0704
1.5	0.0682
2.0	0.0676
2.5	0.0639
3.0	0.0630

Table 4.1: The results of the surface tension analysis of the PAA polymer solutions.

Chapter 5

Vibration of viscoelastic sessile droplets

5.1 Introduction

In this experiment attempts will be made to determine the viscoelastic properties of PAA polymer solutions by studying the oscillations of viscoelastic sessile drops. As explained in section 1.1, the ability to determine the physical properties of fluids from a very small sample has numerous potential applications in a wide range of fields, from chemical research to medical diagnosis. As mentioned previously, techniques for achieving this have already been developed. These include techniques involving magnetically levitated droplets [8,27-29], or sessile droplets supported on superamphiphobic (non-wetting) substrates (as was invested by Harrold et al) [11]. The problem with both of these techniques is that they are difficult and costly to carry out. Investigating sessile droplets on non-superamphiphobic substrates could potentially result in a way of analysing viscoelastic materials without the expense of other techniques. If the effects of contact angle can be compensated for, then theoretically it should be possible to analyse sessile droplets on any surface.

Attempts have been made to model capillary waves on a sessile droplet mathematically, however as of yet no mathematical model is known to exist that can accurately describe such waves. The reason for this is that the addition of the substrate boundary condition significantly complicates how waves are confined. Previous experiments conducted by Sharp et al [10] showed that the frequency of oscillation for sessile liquid droplets is dependent on their contact angle. This factor complicates the process of producing a technique which can universally applied to viscoelastic sessile droplets.

In an attempt to overcome these issues, the sessile droplets (PAA solution) examined in this experiment will be modelled as viscoelastic liquid baths, the depth of which will be defined as the average height of the droplet, and the width of which will be defined using the wave vector of the surface waves that will be stimulated on said sessile droplets.

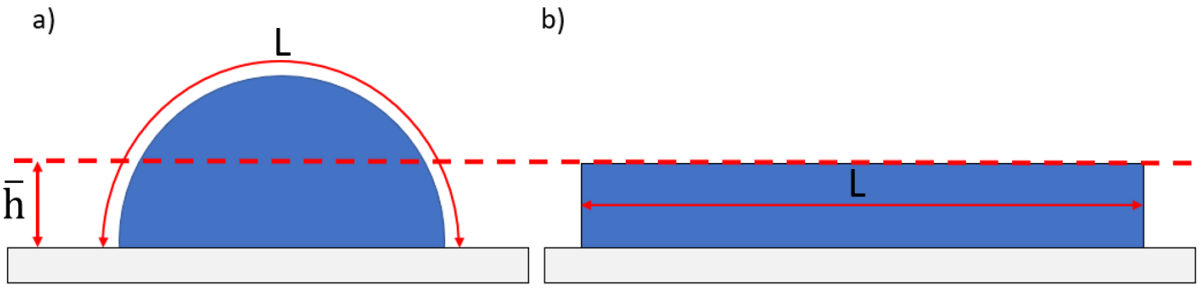


Figure 5.1: A diagram to show how a sessile droplet (a) is modelled as a liquid bath (b), as described in the Noblin model. The depth of the liquid bath $\bar{h}$ is equal to the average height of the sessile droplet, whereas the width of the liquid bath is defined by the profile length of the droplet.

This theoretical liquid bath model (as described in the Noblin model) was then used in conjunction with the Jäckle model for surface waves on a viscoelastic fluid bath in an attempt to calculate the storage and loss moduli for the polymer solution which comprised the sessile droplet. This was done by first measuring the waveform of the surface waves on the sessile droplets using a high-speed camera, and acquiring the power spectrum for this waveform via Fourier transformation. This power spectrum was then used to calculate G' and G'' through the utilisation of the Jäckle model, as well as information such as the value of the surface tension for the polymer solutions that was acquired in chapter 4 (figure 4.10).

5.2 Experimental overview

A range of polymer solutions and substrates were first created, as described in sections 3.1 and 3.2 respectively. The substrates that were used in this experiment were chosen because they would provide a wide range of contact angles, allowing for the contact angle dependence of sessile droplet oscillations to be examined. Two substrates which provided similar contact angles (wax and PDMS) were chosen in order to see if the chemical composition of the substrate itself had any effect on the behaviour of the sessile droplets.

A Genie HM640 high speed camera was utilised in this experiment to film the sessile droplets as they oscillated. Previous experiments on sessile droplets such as those carried out by Sharp [41] and Harrold et al [11] utilised the deflection of a laser to measure the vibration of sessile droplets, as shown in. This was done by using the sessile droplet itself as a lens through which the laser passed. As the sessile droplet vibrated, its shape would deform and result in the laser light being refracted at a different angle as a function of time. This would mean that the laser light that was exiting the sessile droplet would change its angle of refraction at the same rate as the sessile droplet vibrated. This change in refraction angle would cause the laser beam to move back and forth over a photodiode as the sessile droplet oscillated. The intensity from this photodiode over time was then used to calculate the rate at which the sessile droplet was oscillating.

Despite previous successes in using a laser beam to measure the oscillation of sessile droplets, a high-speed camera was instead chosen due to a number of limitations associated with the laser technique. The first of these limitations is that this technique is not particularly easy to carry out successfully. Another limitation of this technique is that it can only be carried out on transparent liquids. This would mean that liquids such as paint or blood could not be analysed using this technique. An alternative approach is to reflect the laser light off the sessile droplets, instead of allowing the laser light to pass through the droplet, however this technique is even more difficult to successfully carry out. This technique would also need to use a laser wavelength which did not get absorbed by the liquid in question, since the laser needs to be reflected off the liquid in order to reach the photoreceptor. If the laser wavelength being used was strongly absorbed by the liquid, the amount of light being reflected off the liquid would be reduced resulting in less light reaching the photodiode. This would in turn make taking accurate measurements of the droplet's oscillation difficult. This problem could be solved by potentially using a more sensitive photoreceptor to detect the laser light reflected off the sessile droplet. However, given that this technique is already difficult to carry out successfully, the addition of the potential issue of laser light absorption makes this particular method unattractive. Video analysis allows for any type of liquid to analysed, as well as allowing for the mode number of the surface waves to be determined (which cannot be done through laser analysis).

The experimental apparatus used in this experiment was assembled as shown below.

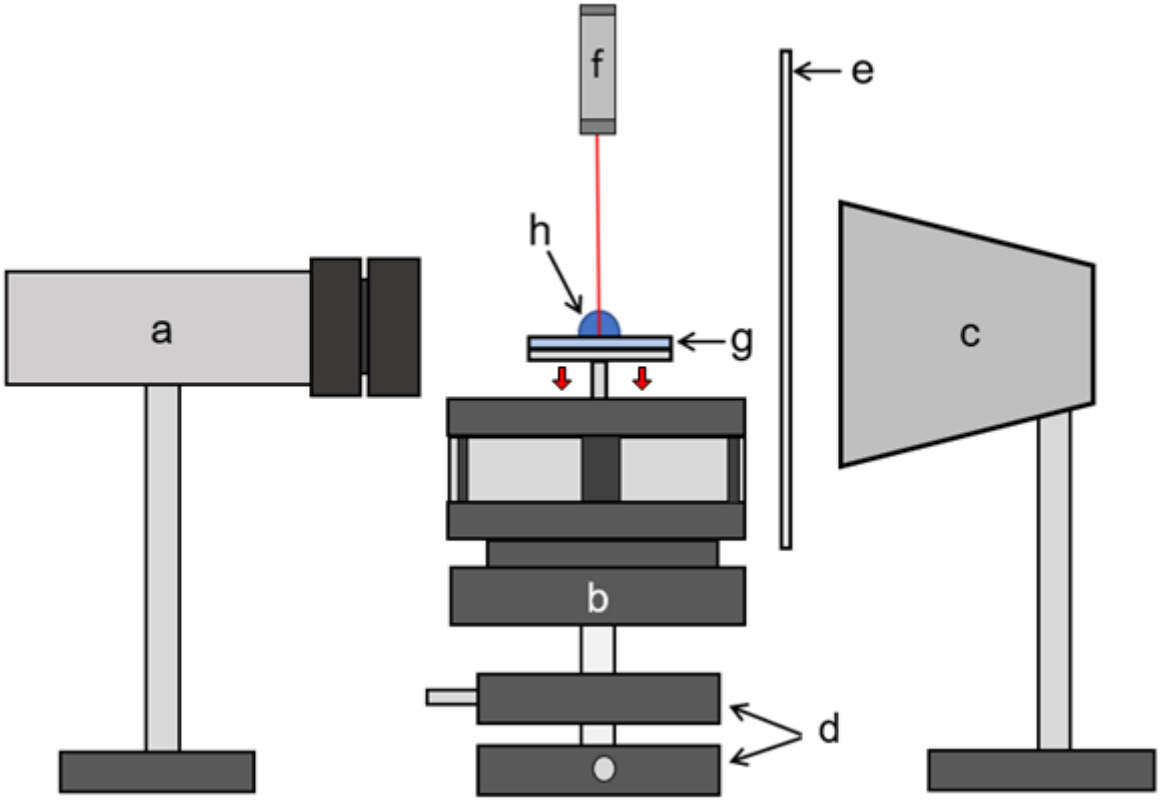


Figure 5.2: The experimental apparatus used for the sessile droplet vibration experiment. This setup included a Genie HM640 high speed camera(a), a Pasco scientific SF-9324 wave-driver(b), a desk lamp acting as a light source (c), two translation stages (d), a lighting screen used to evenly disperse the light from the desk lamp (e), and modified laser pointer with a cylindrical lens used to create a line of reference of the substrate below(f). The substrate which is to be experimented upon (g) is secured to the wave-driver platform with double sided adhesive tape. The sessile droplet(h) is then positioned on the substrate and aligned using the translation stages. The wave-driver applies a small downward impulse to the platform which the substrate is attached to (the red arrows indicate the direction of motion of the wave-driver platform). The wave-driver platform returns to its original position once the impulse is applied. The camera had a framerate of 500 frames per second, and was calibrated to 0.033 millimetres per pixel.

The glass slides upon which the substrates had been deposited were secured onto a horizontal platform attached to a wave-driver. This wave-driver was attached to an amplifier, which was in turn connected to a data acquisition card (which was then connected to a computer). LabView (National Instruments) allowed for direct control of the DAQ card and the high-speed camera (which was connected to the same computer as the DAQ card via an ethernet connection), allowing for the entire experiment to be controlled via a graphical user interface. A standard desk lamp (5.2c) was used to provide the backlighting for this experiment, with a lighting screen (5.2e) used to provide a uniform lighting effect behind the sessile drop.

The wave-driver itself (5.2b) was attached to two translation stages(5.2d), allowing for adjustments to be made freely along the xy plane. A cylindrical lens was placed in front of a very low power laser (a modified laser pointer) in order to create a laser line on the surface of the substrate. This laser line was used to align the sessile droplet to the right position so that the image calibration was correct.

The calibration for the measurements was done by securing a measuring ruler in line with the laser line (at right angles to the camera and the light source, as shown in figure 5.3) and measuring the number of pixels between two points along the measuring ruler (the distance of which can be seen by reading the markings on said ruler).

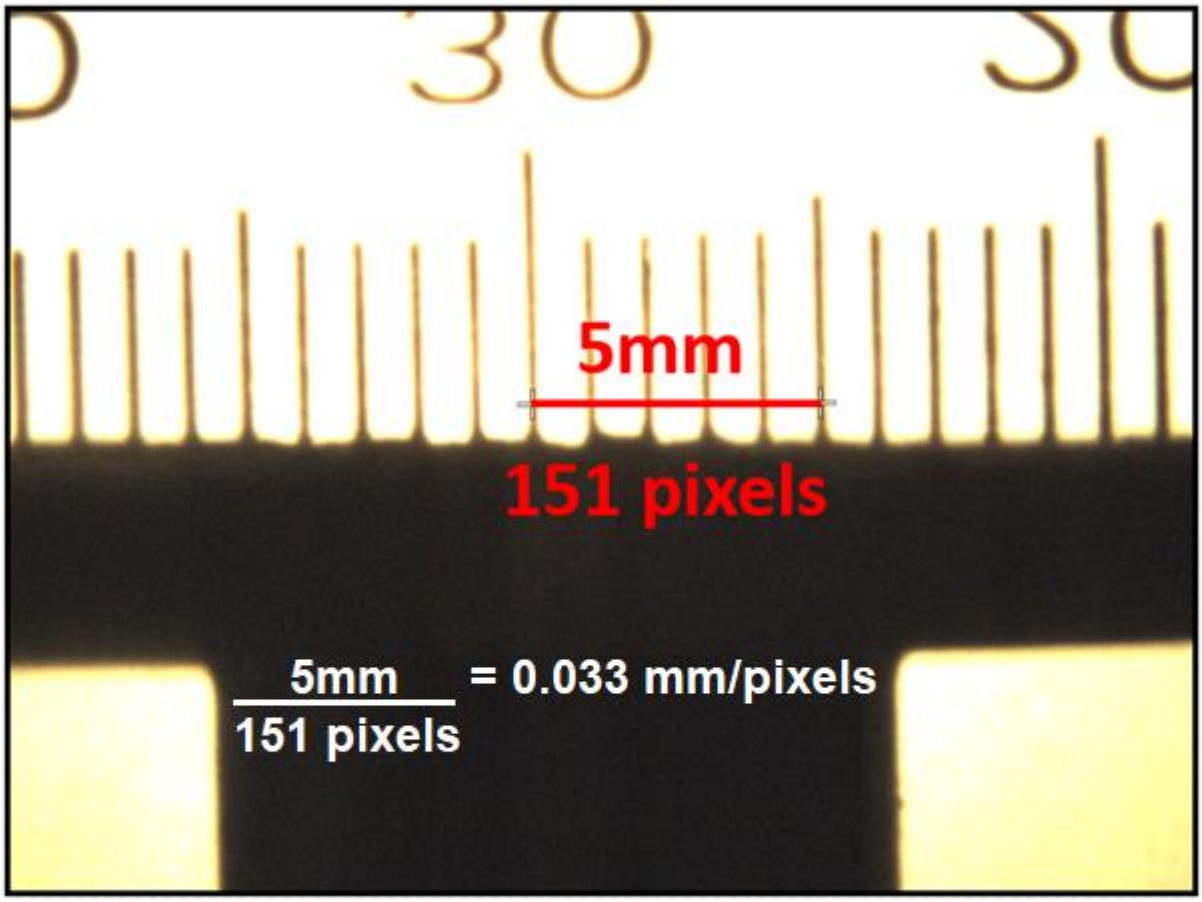


Figure 5.3: A diagram showing how the calibration constant is obtained from measurements taken from a still image of a measuring ruler secured in line with the laser (as shown in figure 5.4).

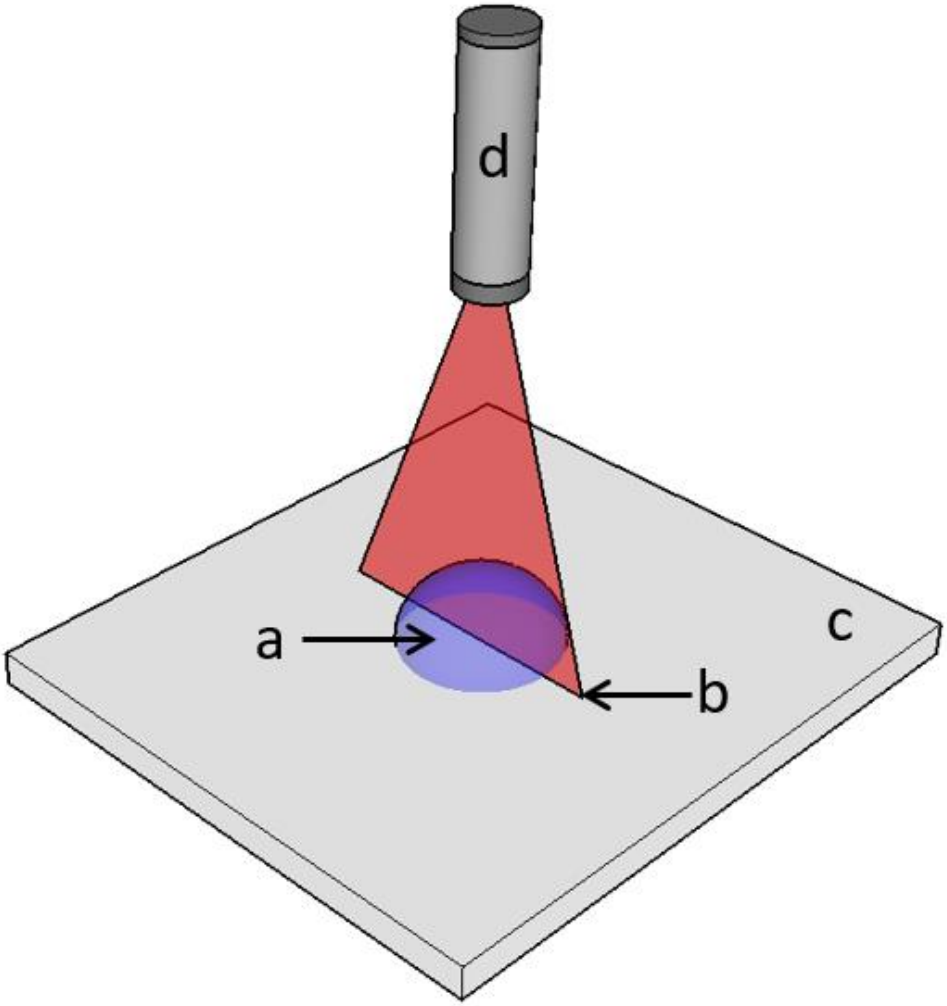


Figure 5.4: An illustration showing how the laser beam from the modified board pointer(d) was used to provide a point of reference (b) when aligning the sessile droplet (a) to the correct position relative to the camera. This was done via the translational stages (figure 5.2d) which could move the wave-driver that the substrate (c) was attached to.

The desired substrate was secured onto the wave-driver platform with double sided adhesive tape. A small sessile drop was placed onto the substrate using a hypodermic needle (with a diameter of 0.455mm). This needle had its tapered end removed in order to decrease the surface area of the tip and allow for ease of transfer between the needle and the substrate. A hypodermic needle was chosen over a pipette tip simply because it allowed for a smaller amount of liquid to be deposited more easily. Once the sessile droplet was placed on the substrate, the position of the wave-driver was adjusted to ensure that the droplet was aligned with the laser line (as shown in figure 5.4). Once the sessile droplet was in the correct position, the laser light was switched off.

As mentioned previously, LabView was used to control the experiment via the use of a DAQ card. The high-speed camera was set to begin recording 0.3 seconds before the impulse was applied to the sessile droplet via the wave driver.

The impulse from the wave driver was controlled via a digital signal that was sent from the DAQ card. This signal has an amplitude of 1.0 volts and had a duration of 5ms. A digital signal was used in order to produce a sharp impulse that would allow the wave-driver to stimulate the sessile droplet and then rapidly return to a resting positing, allowing for the surface of the sessile droplet to oscillating without further external influence.

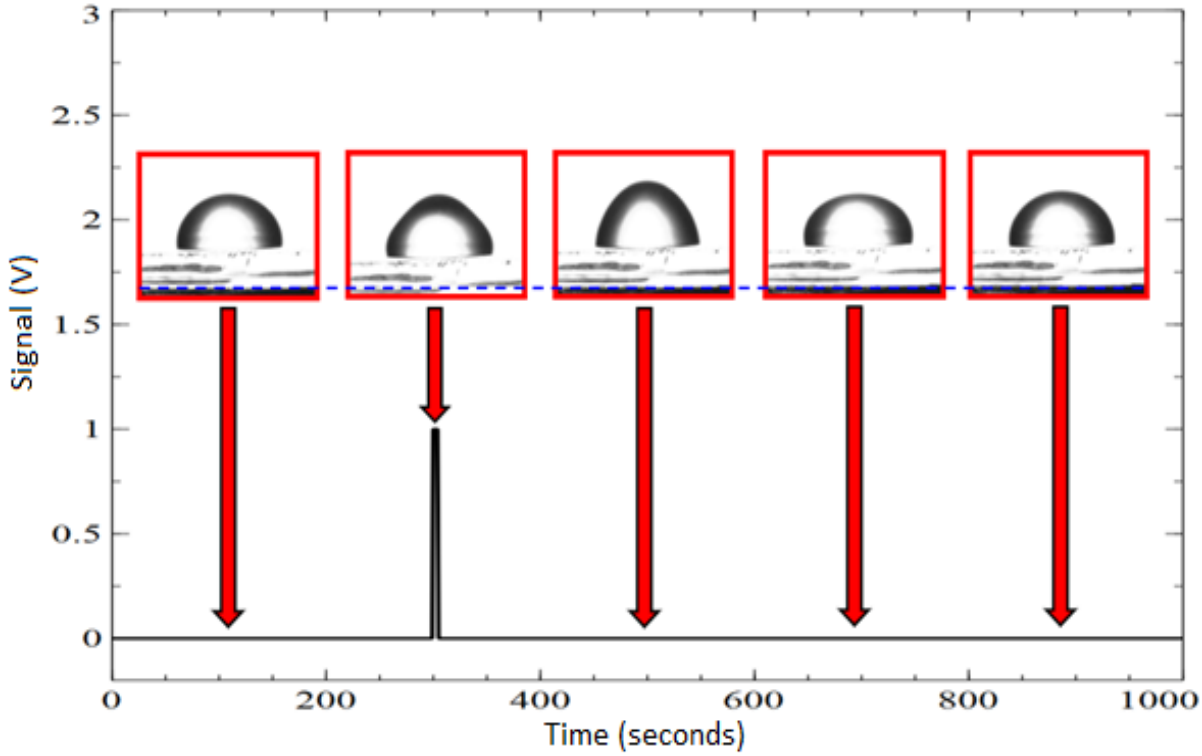


Figure 5.5: A graph to show the digital signal which was sent to the wave driver, with corresponding images of the sessile droplet which was placed upon the substrate which was attached to the wave driver. Note: the wave driver platform actually moved downwards when the pulse was applied (as can be seen by studying the blue dotted line).

The camera would record the entire oscillation of the droplet (recording for one second, which was more than enough time to capture the entire oscillation). The oscillation of the sessile droplet over time, and the timing of the impulse being applied to the droplet can be seen in figure 5.5.

Once the oscillation of the droplet had been successfully filmed, the size of the droplet was increased slightly, and the measurement procedure was repeated. This process was repeated until the sessile droplet showed signs of exceeding its capillary length.

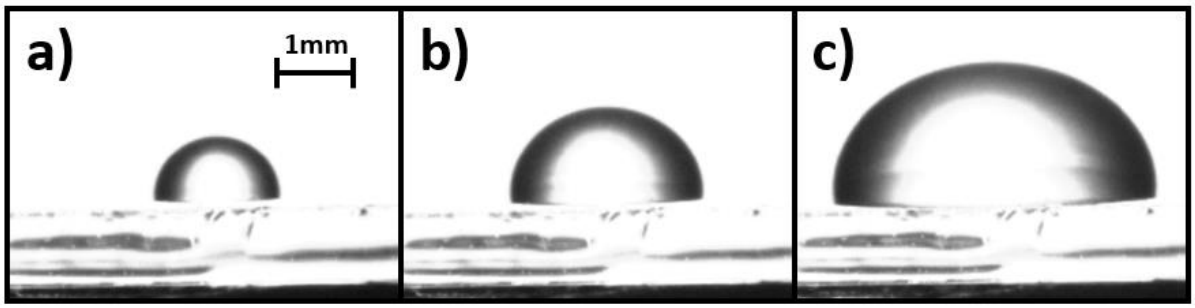


Figure 5.6: A set of images to show how the sessile droplet increase in size. Image a shows the initial size of the droplet, image b shows the same droplet with its volume increased slightly, and image c shows the upper most limit of the droplet size, as the surface of the droplet is behind to deviate from a smooth spherical curve.

If the sessile droplet had not exceeded its capillary length, its profile would follow a smooth spherical curve. Deviation from a smooth spherical curve indicates that the capillary length had been exceeded (as shown in figure 5.6c). For low contact angle substrates such as silicon this would result in effectively a 'puddle' of liquid forming on the surface. For high contact angle substrates, such as candle soot, exceeding the capillary length would result in the droplet becoming laterally elongated, forming an oblate spheroid.

This measurement sequence was repeated three times for every concentration across all substrates to prove that the results were consistent. The time taken to take the measurements for each individual droplet was kept to a minimum in order to reduce the extent of evaporation. All solutions were kept in sealed vials when not in use.

5.3 Pre-vibration

Initial experimentation showed that there was an issue with getting the sessile droplets to properly reach a state of equilibrium when placed on the substrates. The sessile droplets would often have a contact angle which was higher than that of their equilibrium state (as discussed in chapter 2). After the sessile droplet had been vibrated, it would settle into its equilibrium state. This presented the issue that simply growing the sessile droplet and then immediately taking measurements from droplets oscillation results in inaccurate data being acquired. This data would not be accurate because the sessile droplet would experience additional damping effects as it moves across the surface of the substrate, as the surface of the droplet is not properly pinned to the substrate.

Initially a pre-vibration technique was used that involved vibration the sessile droplet at high frequency (50Hz) for three seconds with an amplitude of 0.5V. This technique however resulted in the contact angle of the sessile droplet dropping significantly. The sessile droplet would eventually reach the point of equilibrium, but it was decided that it would be far more expedient to simply use three 5ms 1.0V impulses, with a two second interval.

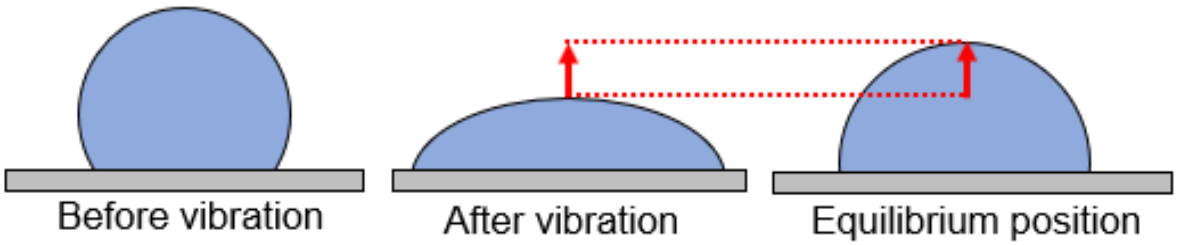


Figure 5.7: A diagram to show how rapidly vibrating the sessile droplet reduced the contact angle significantly. The sessile droplet would then move to a point of equilibrium over time.

Once the equilibrium contact angle had been reached (as shown in figure 5.7), further small impulses would not cause the contact line to change. This technique resulted in the contact angle of the sessile droplet being consistence before and after the oscillation measurements were taken.

5.4 Impulse amplitude

Initially in this experiment a 5V/5ms pulse was used to stimulate the sessile droplets, however this pulse proved to be too large, and would result in the contact line of the sessile droplet moving as the droplet oscillated. This movement would not only cause additional damping effects to occur through the surface area of the droplet being increase and decreased repeatedly (resulting in energy being lost as heat), but also damping effects from the sessile droplet increasing and decreasing its interfacial area with the substrate, as the contact line moved back and forth.

The trade off with decreasing the initial impulse is that by doing so the amplitude of the surface waves are decreased. This decrease in amplitude can result in difficulties when it comes to measuring the oscillation of the droplets. It was found that an initial impulse of 1V/5ms (as shown in figure 5.5) produced wave amplitudes which were large enough to be easily measured, but did not result in the contact line of the sessile droplet moving.

5.5 Sessile droplet growth

As the size of the sessile droplet is increased (through additional solution being added to the droplet), its contact line will expand across the substrate. If the substrate was perfectly uniform then the sessile droplet should grow evenly in all directions, however slight imperfections and contaminations on the surface can prompt the sessile droplet to grow in an asymmetric fashion. Temperton et al [10] demonstrated that sessile droplets which are not symmetrical can have standing waves along their minor and major axis. Such a phenomenon would significantly complicate the experiment and invalidate the results in multiple ways. If the droplet is not spherical then the measurement of the profile length could be incorrect, and the frequency measured could potentially be measured from multiple standing waves at the same time. Fourier analysis would reveal this, but it's an added complication which is not necessary. To prevent this from occurring, additional solution is always added at the apex of the droplet, and measuring sequences were aborted and discarded if the sessile droplet appeared to be growing in a non-symmetric fashion.

5.6 High contact angle substrates

For superamphiphobic substrates such as candle soot the experimental procedure is complicated by the fact that the sessile droplets do not become effectively pinned to the substrate very strongly. This makes taking measurements for such sessile droplets difficult as the droplets tend to move across the surface (figure 5.8a) once excited. To compensate for this, a small amount of the substrate was removed in order to expose the glass slide (figure 5.8b). This small exposed area allowed for the droplet (figure 5.8c) to remain pinned in place, yet did not notably affect the contact angle of the sessile droplet. The area of substrate removed was significantly smaller than the area confined within the contact line (figure 5.8d).

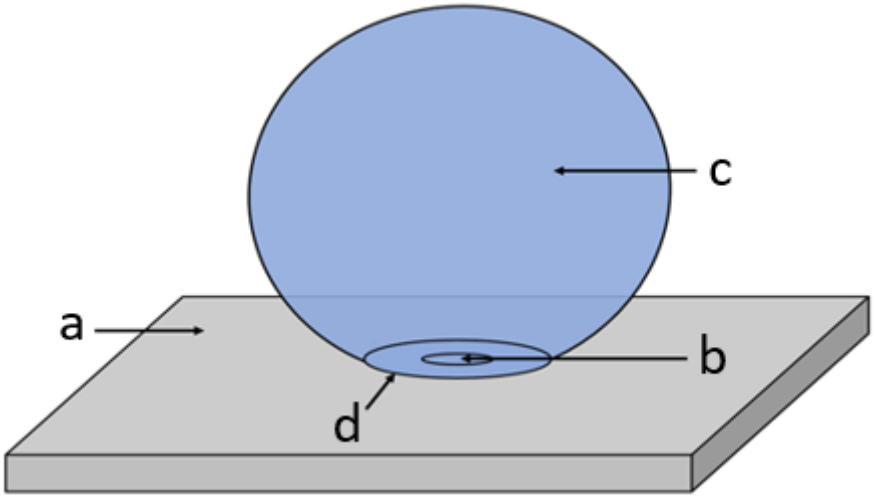


Figure 5.8: An illustration of how the candle soot substrate (a) was modified by removing a small area of the substrate's surface(b) revealing the glass slide below. This allows the sessile droplet (c) to remain stationary and prevents the contact line (d) from moving.

5.7 Experimental procedure

This section will be dedicated to explaining the steps that were taken in examining the sessile droplets, along with an explanation on how the power spectra that were obtained from the measurement of the surface waves on these sessile droplets was used to calculate the frequency dependent storage (G') and loss (G'') moduli for each individual polymer solution. To begin with, the surface wave oscillation of each individual sessile droplet was measured from video footage (as explained in section 3.4). The variation in height of the sessile droplet over time was then Fourier transformed to obtain the power spectrum for the surface waves on the sessile droplet.

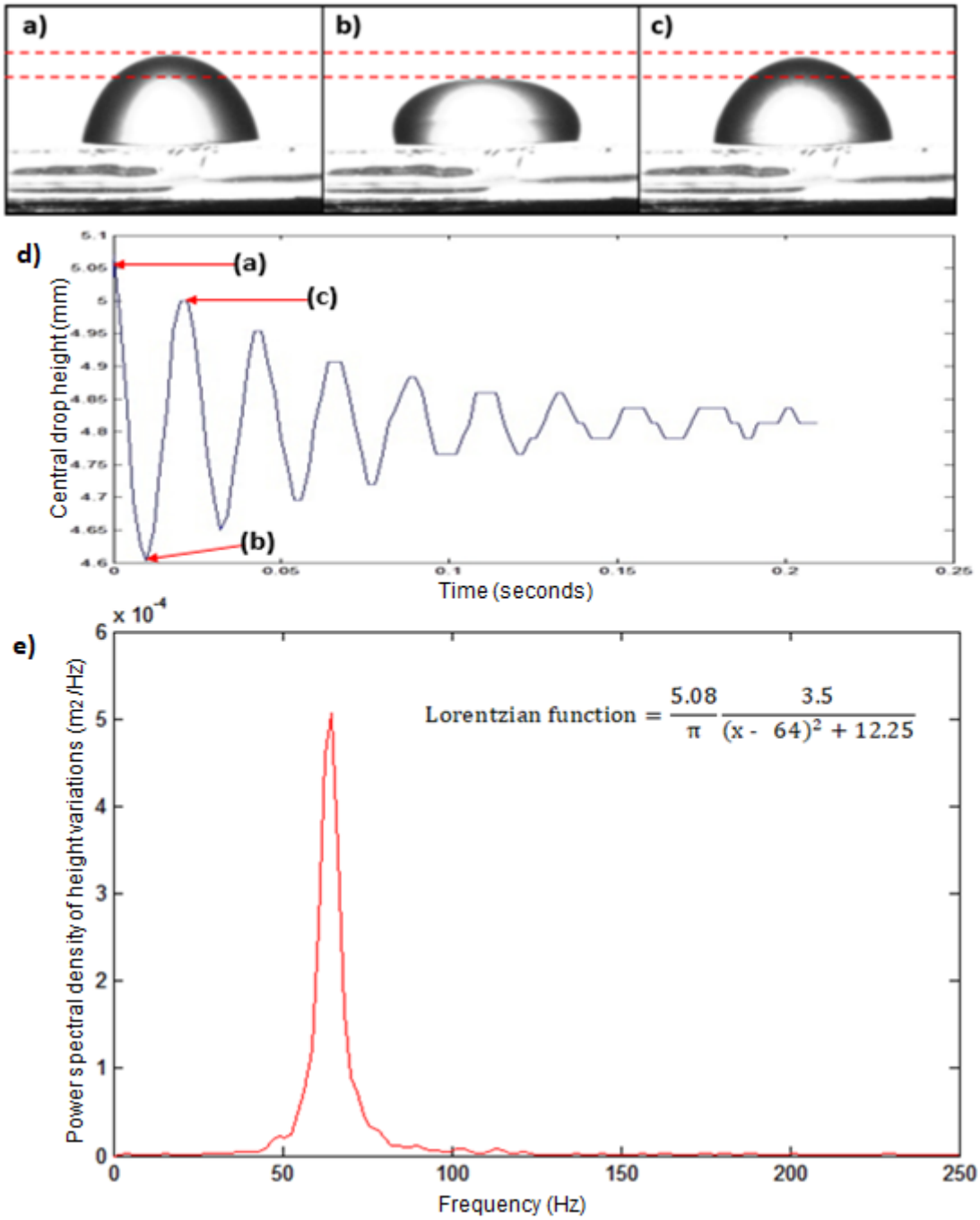


Figure 5.9: A brief overview of how the oscillation of a sessile droplet (a-b) is used to acquire the waveform of the surface waves (d), which is then Fourier transformed to acquire the power spectrum of the surface waves (e), with the corresponding Lorentzian function.

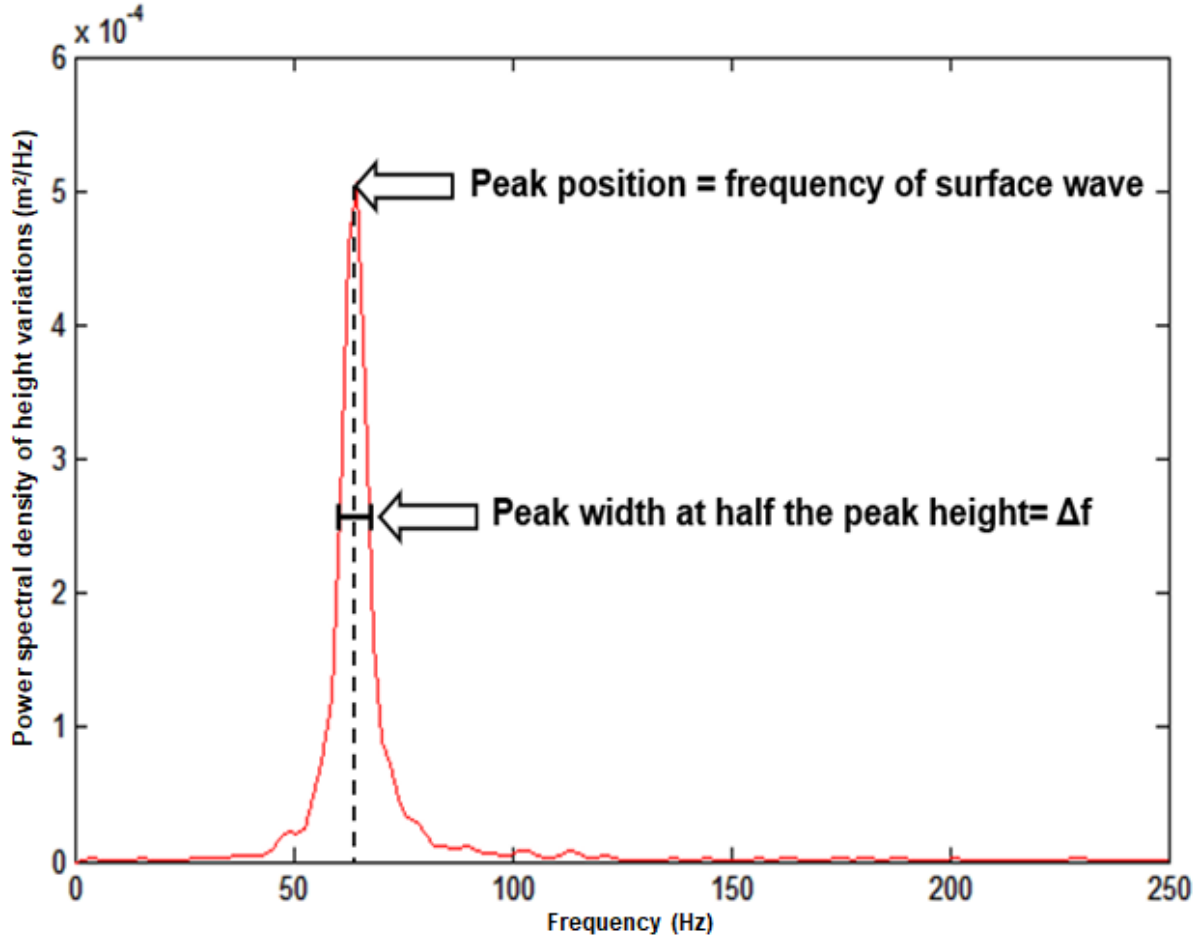


Figure 5.10: A diagram to show how the frequency and spectral width of a sessile droplet surface wave is acquired via examination of the wave's power spectrum.

Once the power spectrum of the surface wave had been acquired (as shown in figure 5.9), the frequency of the surface wave and the peak width (related to the damping of the surface wave) could be measured directly from the power spectrum (as shown in figure 5.10).

5.8 Initial results

The first step in this experiment was to examine how the frequency and damping of the surface waves on sessile droplets was dependent upon the size, polymer concentration, and contact angle of the sessile droplets. First, the profile length dependence of the surface wave frequency will be analysed.

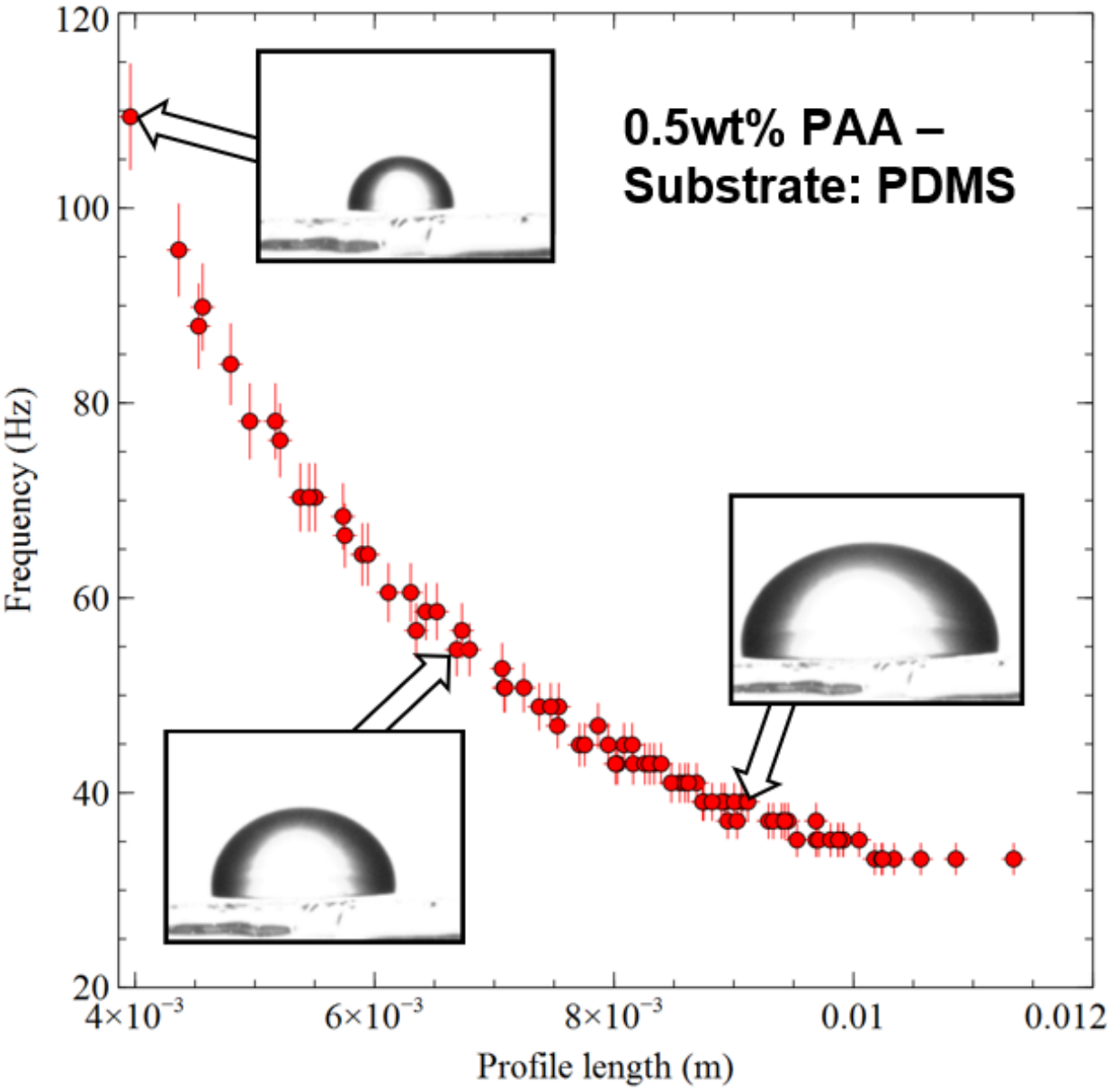


Figure 5.11: A graph to show the frequency of surface waves on 0.5wt% PAA solution sessile droplets supported on a PDMS substrate.

As shown in figure 5.11, the frequency of surface waves is inversely proportional to the profile length of the sessile droplet. The first comparison to the data to be made is to compare how the frequency of sessile droplet surface waves are related to the polymer concentration of the solution which make up the sessile droplets.

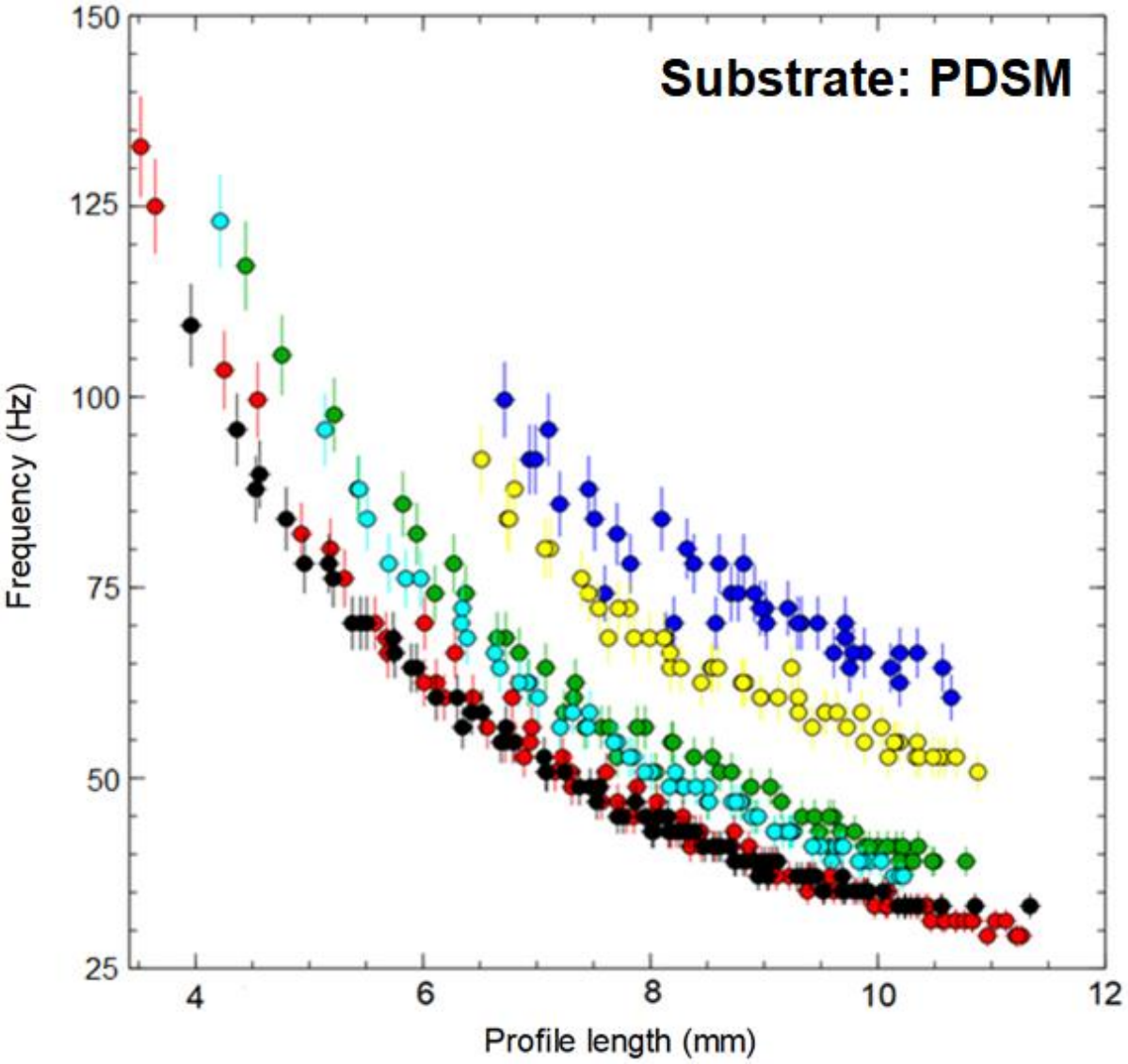


Figure 5.12: A graph to show the PAA polymer concentration dependence of the frequency of surface waves on sessile droplets. These particular sessile droplets were supported on a PDMS substrate. Concentration: 0.5wt% (red), 1.0wt% (black), 1.5wt% (cyan), 2.0wt% (green), 2.5wt% (yellow), and 3.0wt% (blue).

As can be seen in figure 5.12, the frequency of sessile droplet surface waves is dependent upon the polymer concentration of the solution which comprises the sessile droplet. It is interesting to note a concentration dependence only seems to occur once the polymer concentration rises above 1.0wt%. The contact angle on PDMS for these polymer solution sessile droplets remains fairly constant as polymer concentration increases, with only a 7 degree increase from 0.5wt% to 3.0wt% (as shown in table 3.2). Next, the contact angle dependence of the surface wave frequency was investigated.

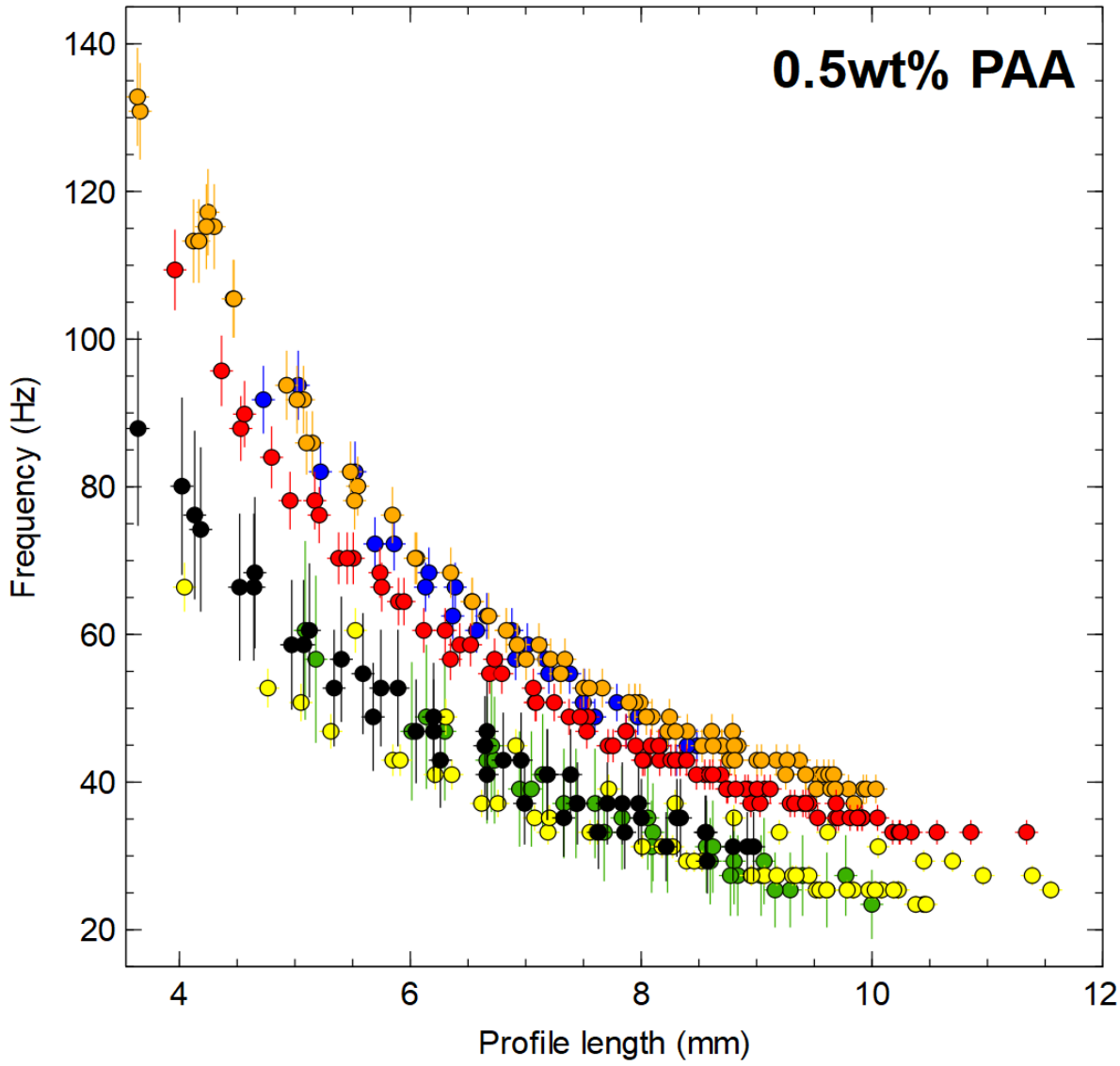


Figure 5.13: A graph to show the contact angle dependence of the frequency of surface waves on sessile droplets (0.5wt% PAA). Contact angles: 30˚ (silicon) – green, 55˚(aluminium) – black, 60˚(polystyrene) – blue, 90˚(wax) - orange, 90˚(PDMS) – red, 145˚(Candle-soot) – yellow.

As shown in figure 5.13, the frequency of sessile droplet surface waves is highly dependent on the contact angle of the sessile droplet. After investigating the frequency dependency for all of the polymer solutions being investigated, it was found that the frequency of surface wave is highest when the contact angle of the sessile droplet is around 75°. This finding is similar to that found by Sharp [41], who determined that for pure water the frequency of sessile droplet oscillation peaks at a contact angle of 70°. Another interesting aside is that PDMS and wax both produce a 90˚ contact angle, yet seem to induce a slightly different surface wave frequency in the sessile droplets. This difference could indicate that the polymer solution may interact slightly different with different substrates. This might mean that just because two different substrates producing the same sessile droplet contact angle does not necessarily mean that the way in which the polymer solution interacts with these substrates is completely identical.

Contact angles						
PAA concentration	0.5wt%	1.0wt%	1.5wt%	2.0wt%	2.5wt%	3.0wt%
Silicon	30±1	30±1	33±1	35±1	37±1	38±1
Aluminium	55±1	60±1	70±1	75±1	80±1	82±1
Polystyrene	60±1	70±1	75±1	75±1	85±1	92±1
Wax	90±1	90±1	91±1	93±1	93±1	95±1
PDMS	90±1	93±1	95±1	96±1	97±1	97±1
Candle soot	145±1	145±1	145±1	145±1	145±1	145±1

Table 5.1: A colour codes version of table 3.2. For the sake of convenience, the substrate names have been colour coded to correspond with the graphs displaying the results of the experiment.

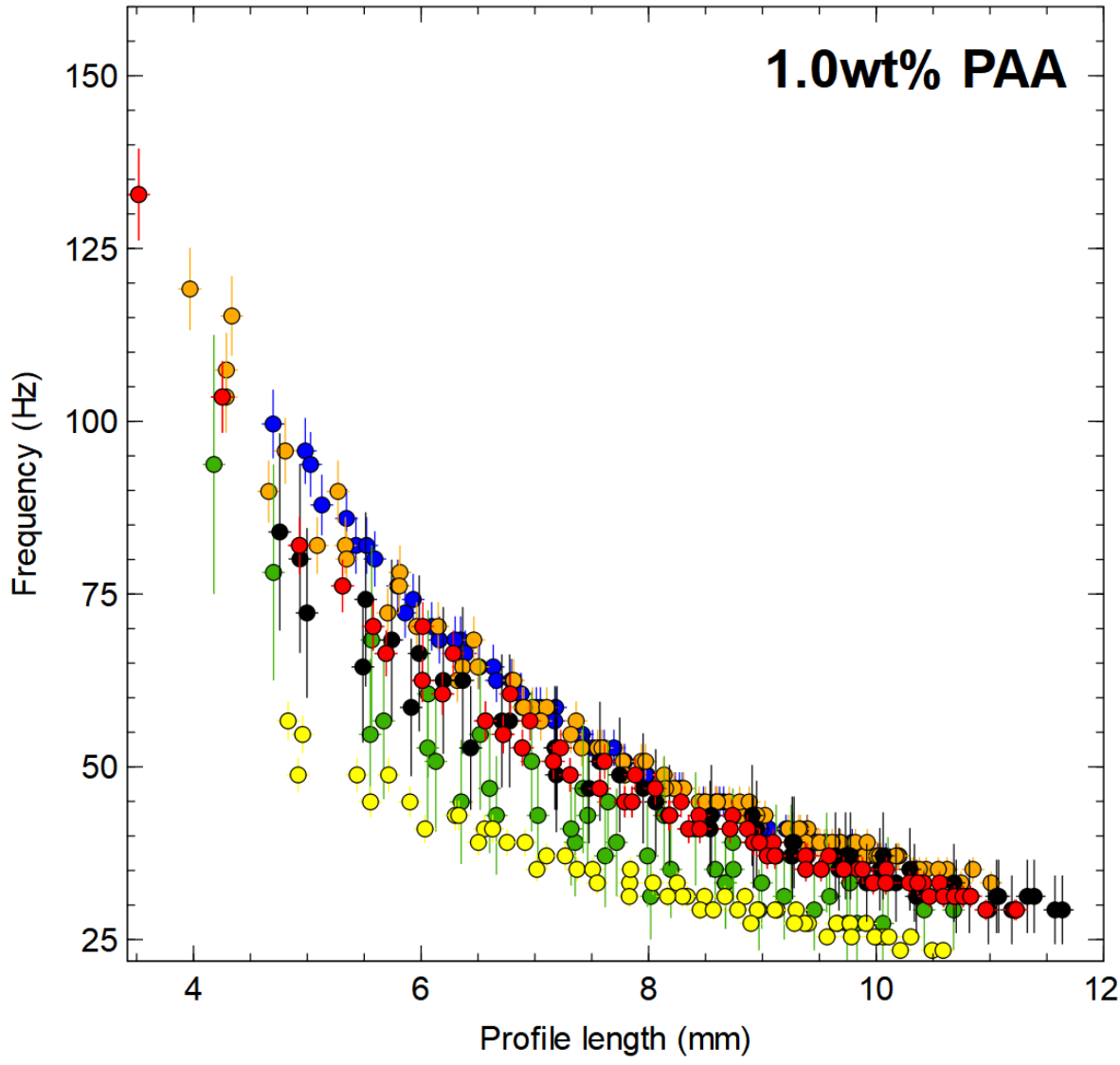


Figure 5.14: A graph to show the contact angle dependence of the frequency of surface waves on sessile droplets (1.0wt% PAA). Contact angles: 30° (silicon) – green, 60°(aluminium) – black, 70°(polystyrene) – blue, 90°(wax) - orange, 93°(PDMS) – red, 145°(Candle-soot) – yellow.

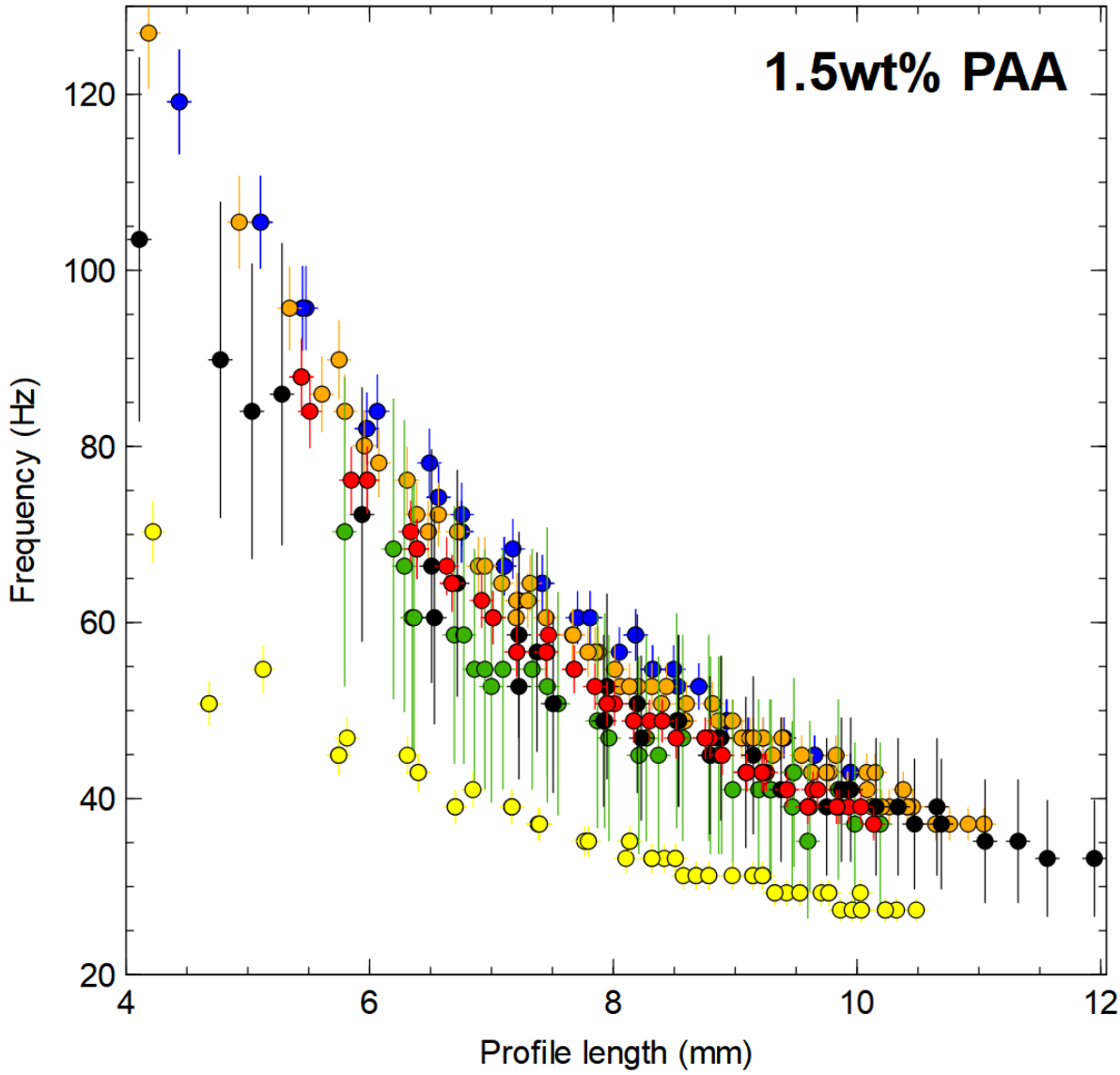


Figure 5.15: A graph to show the contact angle dependence of the frequency of surface waves on sessile droplets (1.5wt% PAA). Contact angles: 33˚ (silicon) – green, 70˚(aluminium) – black, 75˚(polystyrene) – blue, 91˚(wax) - orange, 95˚(PDMS) – red, 145˚(Candle-soot) – yellow.

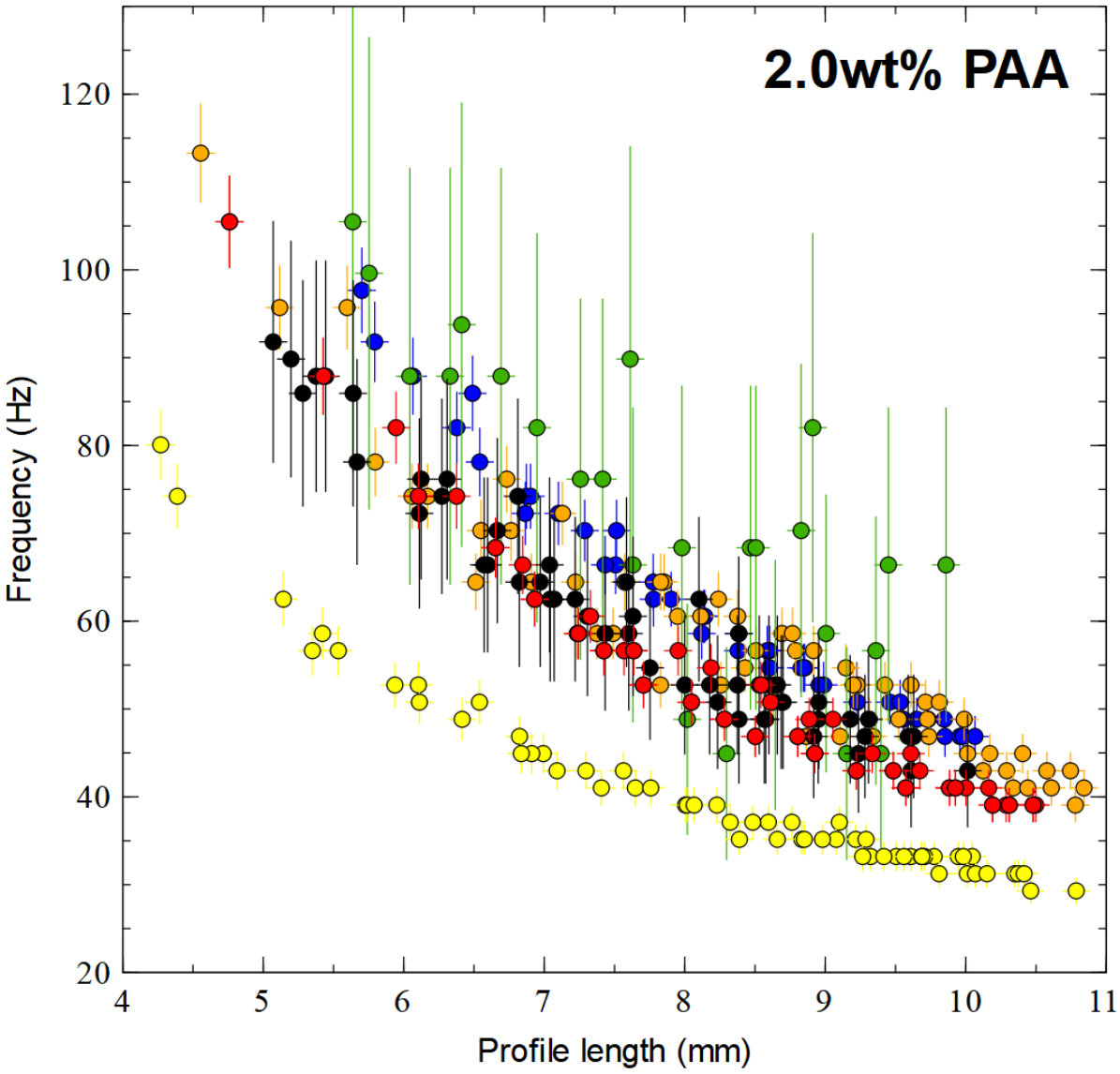


Figure 5.16: A graph to show the contact angle dependence of the frequency of surface waves on sessile droplets (2.0wt% PAA). Contact angles: 35˚ (silicon) – green, 75˚(aluminium) – black, 75˚(polystyrene) – blue, 93˚(wax) - orange, 96˚(PDMS) – red, 145˚(Candle-soot) – yellow.

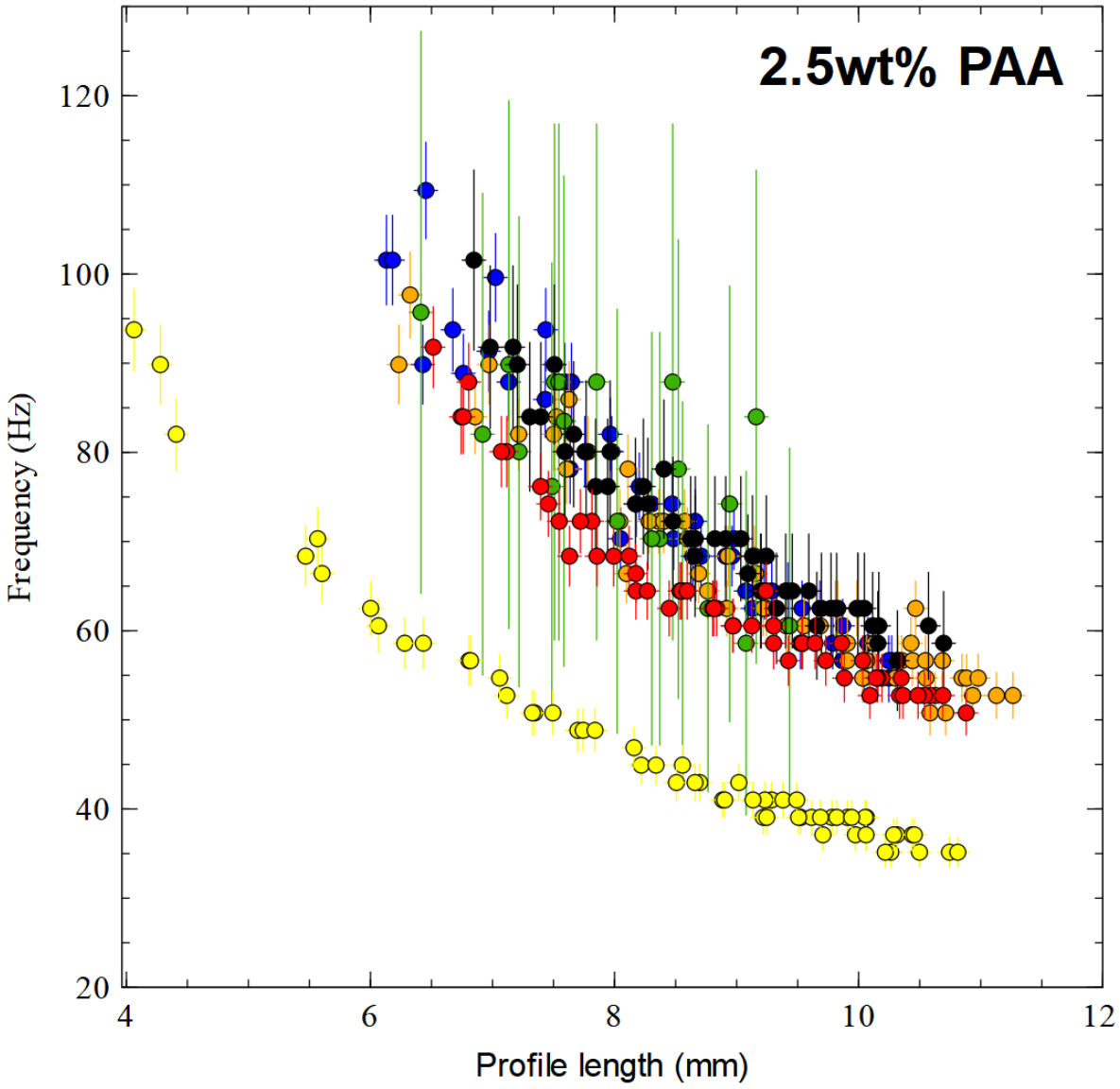


Figure 5.17: A graph to show the contact angle dependence of the frequency of surface waves on sessile droplets (2.5wt% PAA). Contact angles: 37° (silicon) – green, 80°(aluminium) – black, 85°(polystyrene) – blue, 93°(wax) - orange, 97°(PDMS) – red, 145°(Candle-soot) – yellow.

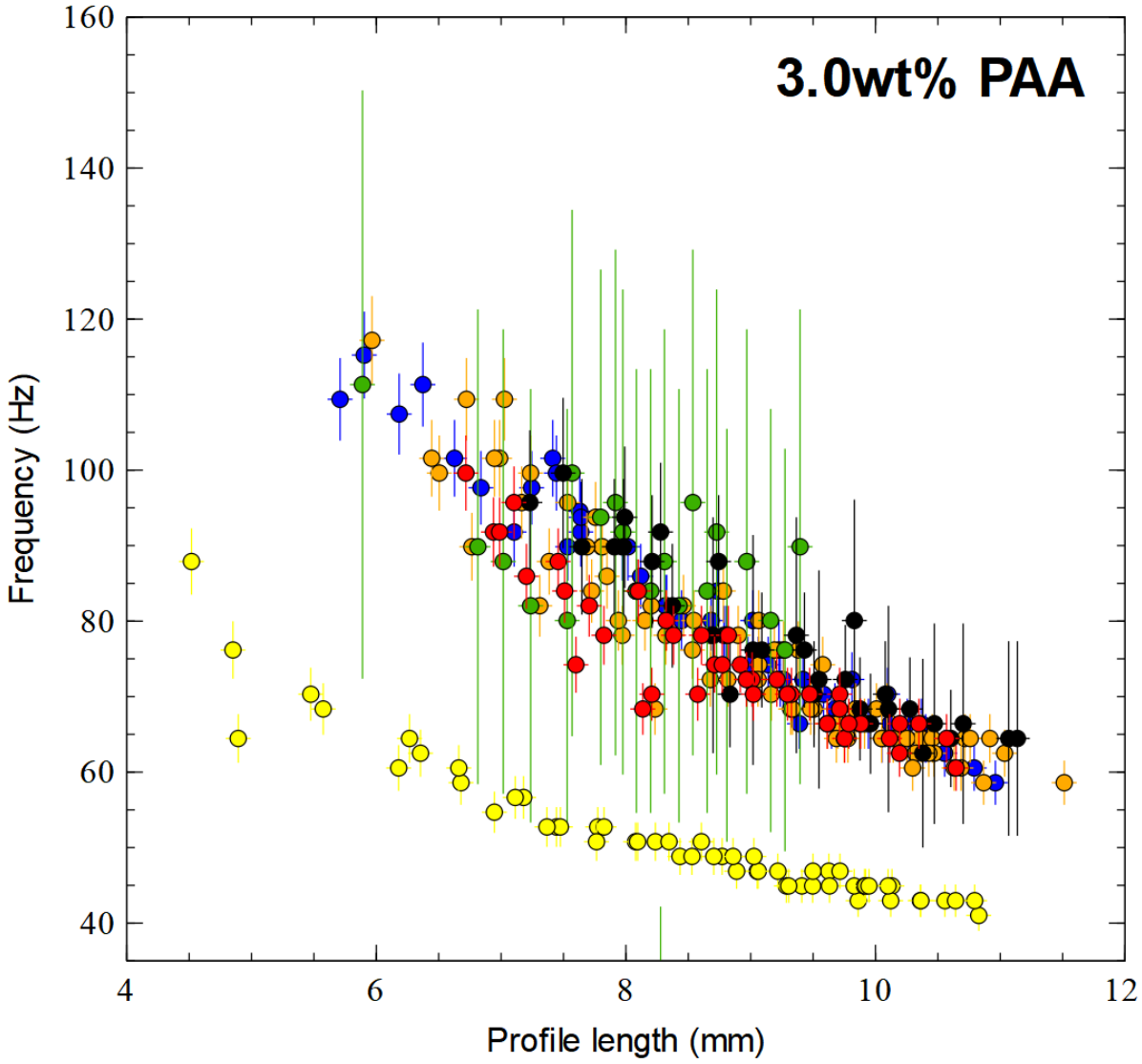


Figure 5.18: A graph to show the contact angle dependence of the frequency of surface waves on sessile droplets (3.0wt% PAA). Contact angles: 38˚ (silicon) – green, 82˚(aluminium) – black, 92˚(polystyrene) – blue, 95˚(wax) - orange, 97˚(PDMS) – red, 145˚(Candle-soot) – yellow.

As can be seen in figures 5.13-518, the frequency of oscillation is highly dependent on the contact angle of the sessile droplet. The frequency of oscillation appears to be greatest for sessile droplets which have a contact angle close to 90˚. Sessile droplets above or below 90˚ appear to have a lower frequency of oscillation. An exception to this seems to be sessile droplets with a concentration of 2.0wt% PAA or higher which are supported on a silicon substrate. These sessile droplets have a notably higher frequency of oscillation than what would be expected given the results for concentrations 0.5-1.5wt%. There is also notably higher level of scatter within the results for silicon at 2.0-30wt% when compared to the results for lower polymer concentrations. The phenomenon might be as a result of boundary layer interactions taking place between the polymer chains within the solution and the surface of the substrate, which would form a layer of polymer which is effectively snagged on the surface of the substrate. This would in turn make the sessile droplet more rigid and therefore increase the frequency of oscillation.

The results for the higher concentrations for the silicon substrate contain a much higher level of scatter than the other sets of data, so it is not clear if these results are legitimate, or simply a result of the difficulties associated with acquiring data from sessile droplets which have both a low contact angle and a high polymer concentrate. Sessile droplets with low contact angles typically do not have high amplitudes of oscillation without stimulating them beyond the point at which the contact line becomes unpinned. Combine this fact with a high polymer concentration and the sessile droplet oscillations become very small, making it difficult to take accurate measurements.

Once the surface wave frequencies had been investigated, the next step was to examine how the spectral width of these surface waves were dependent upon profile length, polymer concentration, and contact angle. First, the profile length dependence of the spectral width was investigated.

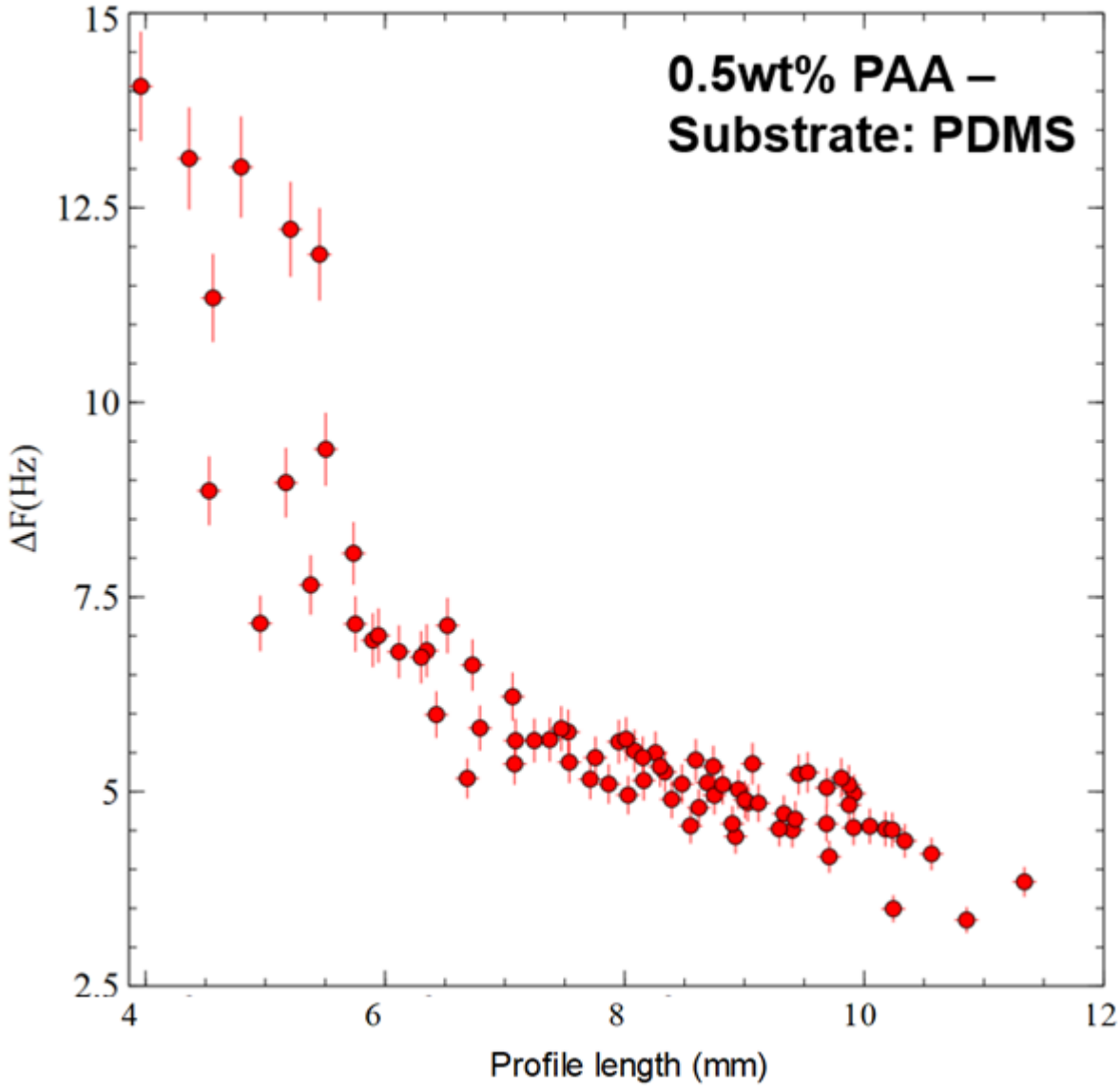


Figure 5.19: A graph to show the spectral width of surface waves on 0.5wt% PAA solution sessile droplets supported on a PDMS substrate.

As seen when examining the frequency of the surface waves (figure 5.19), the spectral width of the surface waves decreased as the profile length of the sessile droplet was increased, meaning that the damping of the surface waves decreased as the size of the droplet increased. Next, the concentration dependence of the surface wave spectral width was investigated.

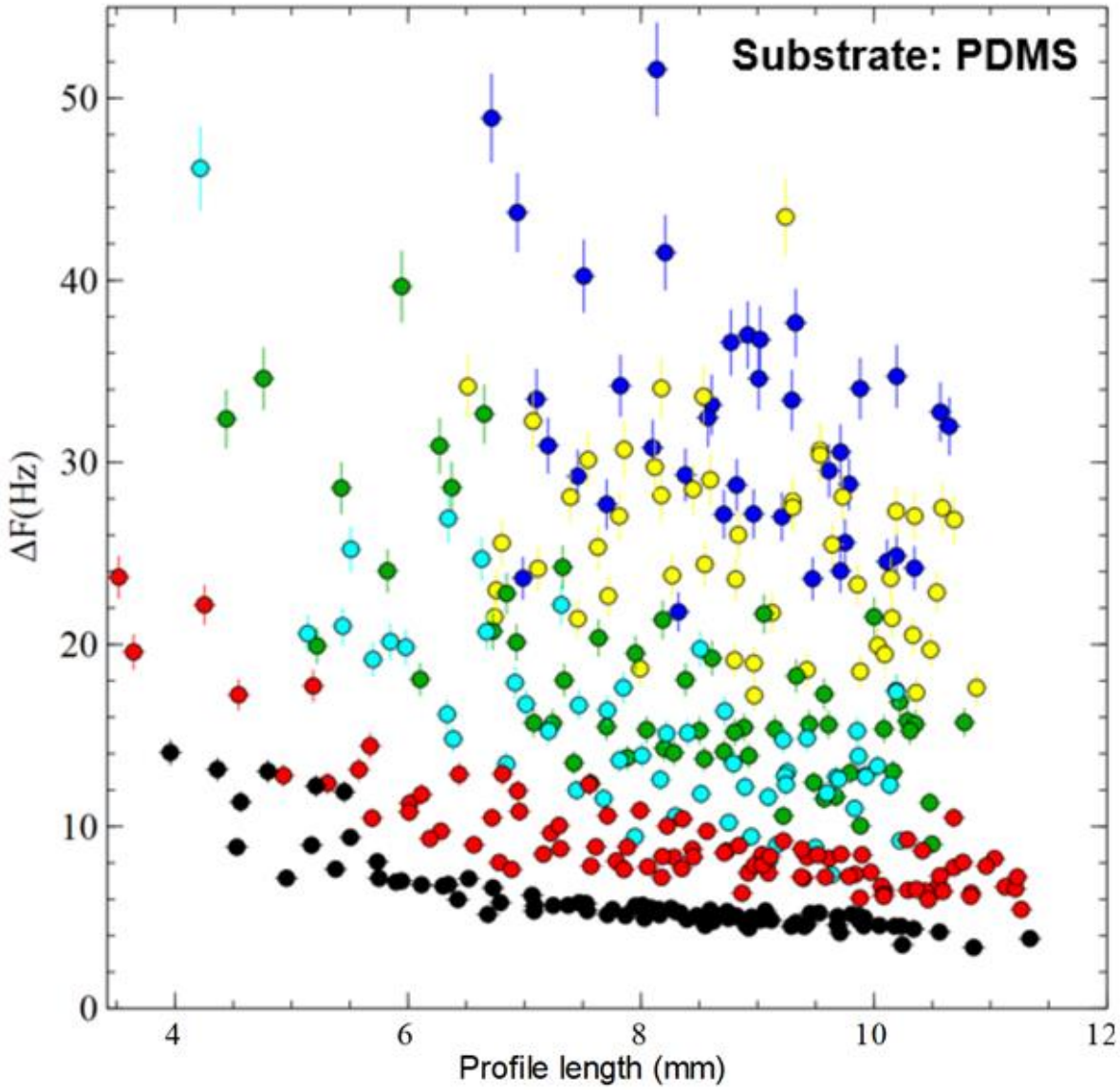


Figure 5.20: A graph to show the PAA polymer concentration dependence of the spectral width of surface waves on sessile droplets. These particular sessile droplets were supported on a PDMS substrate. Concentration: 0.5wt% (black), 1.0wt% (red), 1.5wt% (cyan), 2.0wt% (green), 2.5wt% (yellow), and 3.0wt% (blue).

As can been seen in figure 5.20, the polymer concentration dependence of the surface wave spectral width follows much the same pattern as the frequency. The size of the spectral width is shown to increase with concentration. Note that the variation in the data also increases with concentration, which is most likely due to that fact that the amplitude of the surface waves becomes smaller as the concentration increases. This makes acquiring accurate measurements of the surface waves harder to achieve. Finally, the contact angle dependence of the spectral width was investigated.

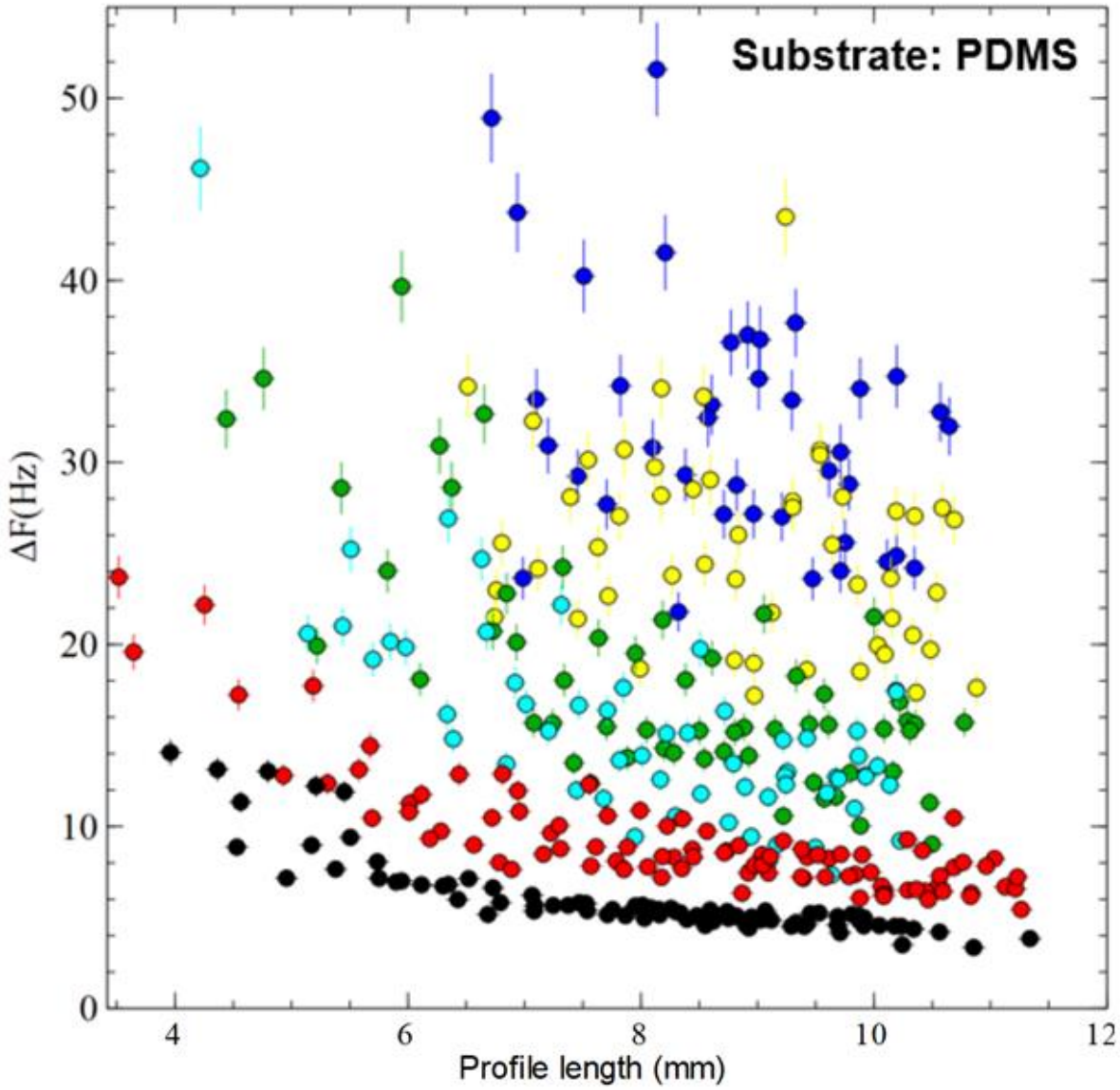


Figure 5.21: A graph to show the PAA polymer concentration dependence of the spectral width of surface waves on sessile droplets. These particular sessile droplets were supported on a PDMS substrate. Concentration: 0.5wt% (black), 1.0wt% (red), 1.5wt% (cyan), 2.0wt% (green), 2.5wt% (yellow), and 3.0wt% (blue).

As can been seen in figure 5.21, the polymer concentration dependence of the surface wave spectral width follows much the same pattern as the frequency. The size of the spectral width is shown to increase with concentration. Note that the variation in the data also increases with concentration, which is most likely due to that fact that the amplitude of the surface waves becomes smaller as the concentration increases. This makes acquiring accurate measurements of the surface waves harder to achieve. Finally, the contact angle dependence of the spectral width was investigated.

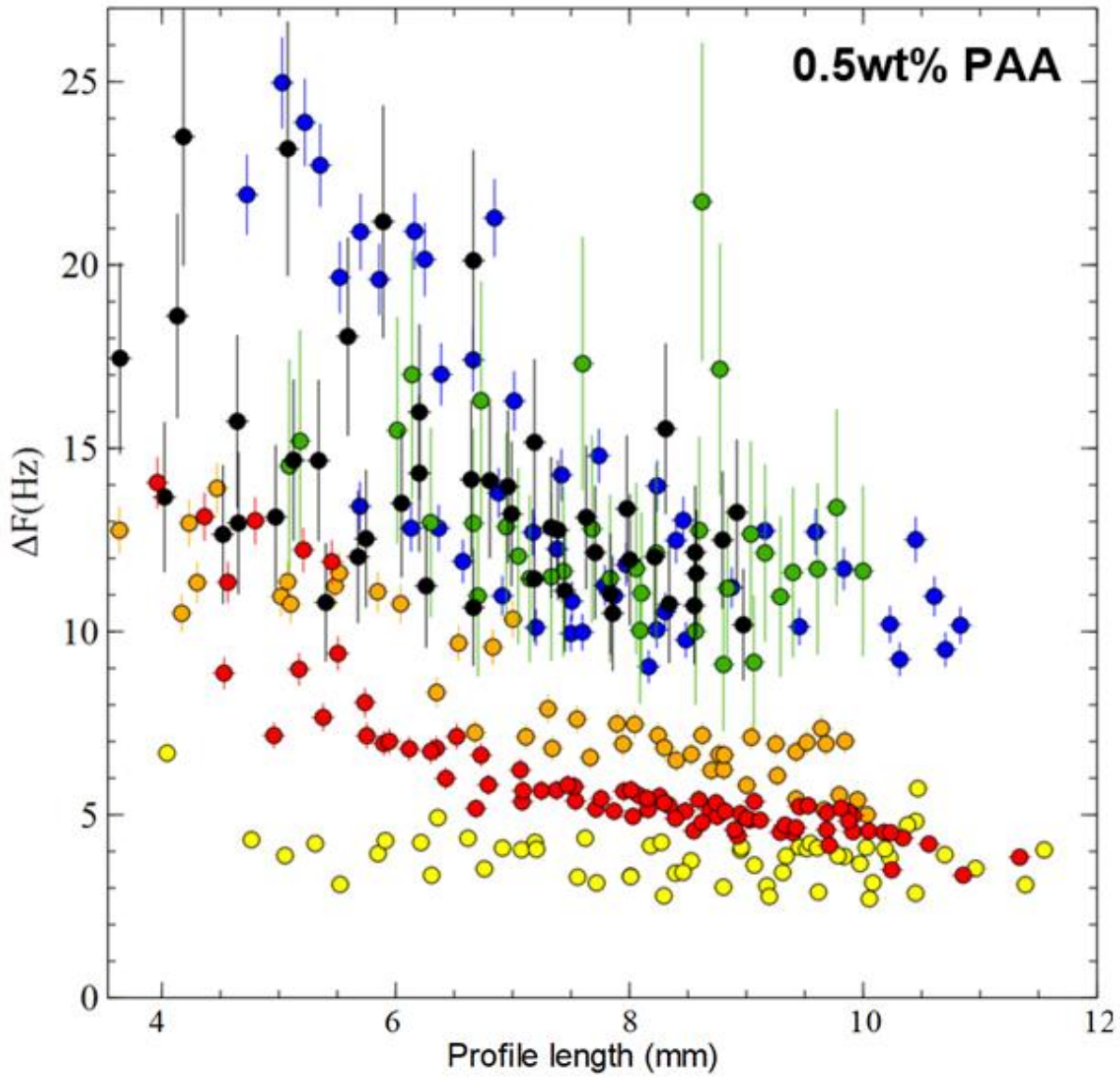


Figure 5.22: A graph to show the contact angle dependence of the spectral width of surface waves on sessile droplets (0.5wt% PAA). Contact angles: 30˚ (silicon) – green, 55˚(aluminium) – black, 60˚(polystyrene) – blue, 90˚(orange), 90˚(PDMS) – red, 145˚(Candle-soot) – yellow.

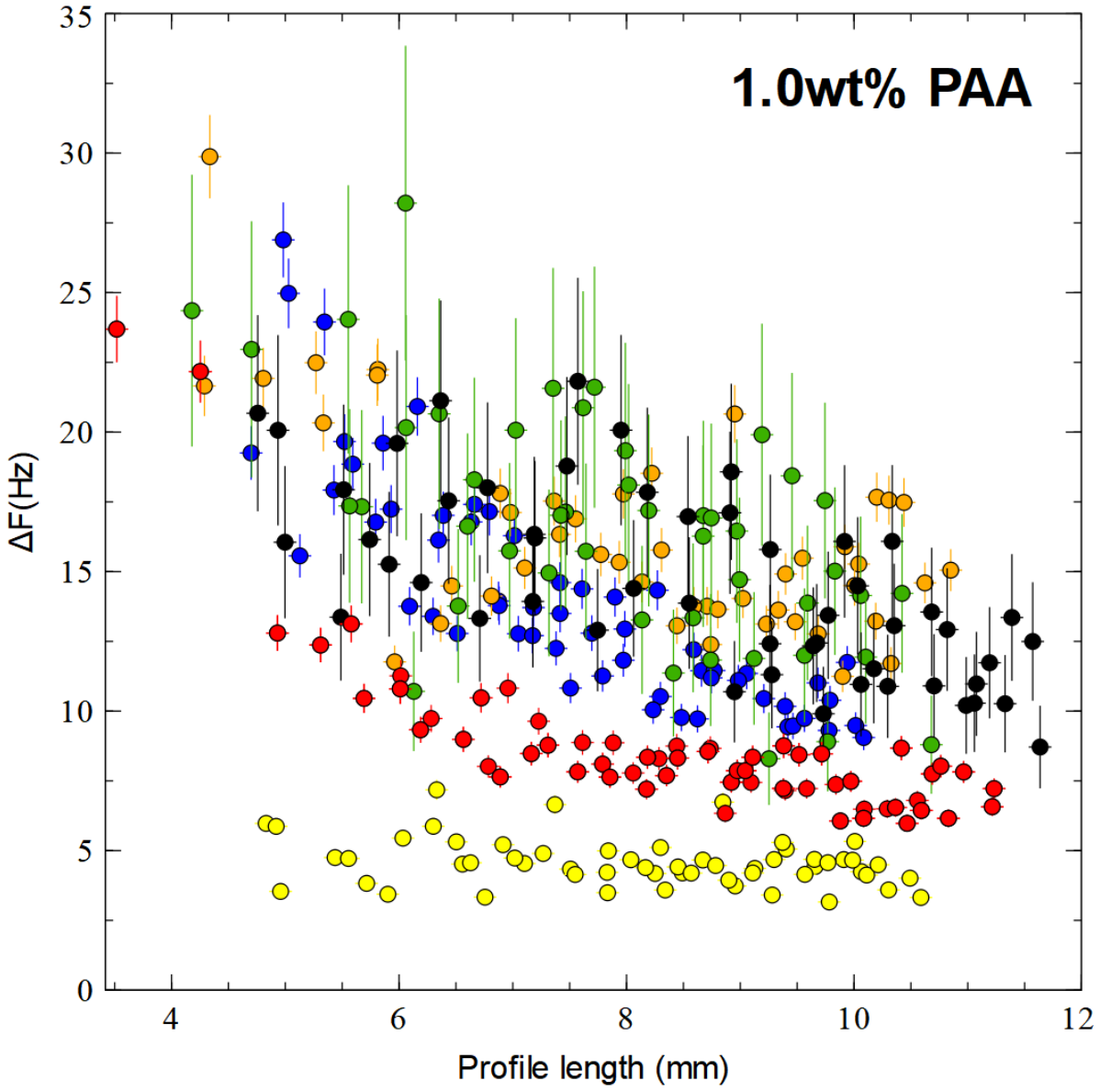


Figure 5.23: A graph to show the contact angle dependence of the spectral width of surface waves on sessile droplets (1.0wt% PAA). Contact angles: 30˚ (silicon) – green, 60˚(aluminium) – black, 70˚(polystyrene) – blue, 90˚(orange), 93˚(PDMS) – red, 145˚(Candle-soot) – yellow.

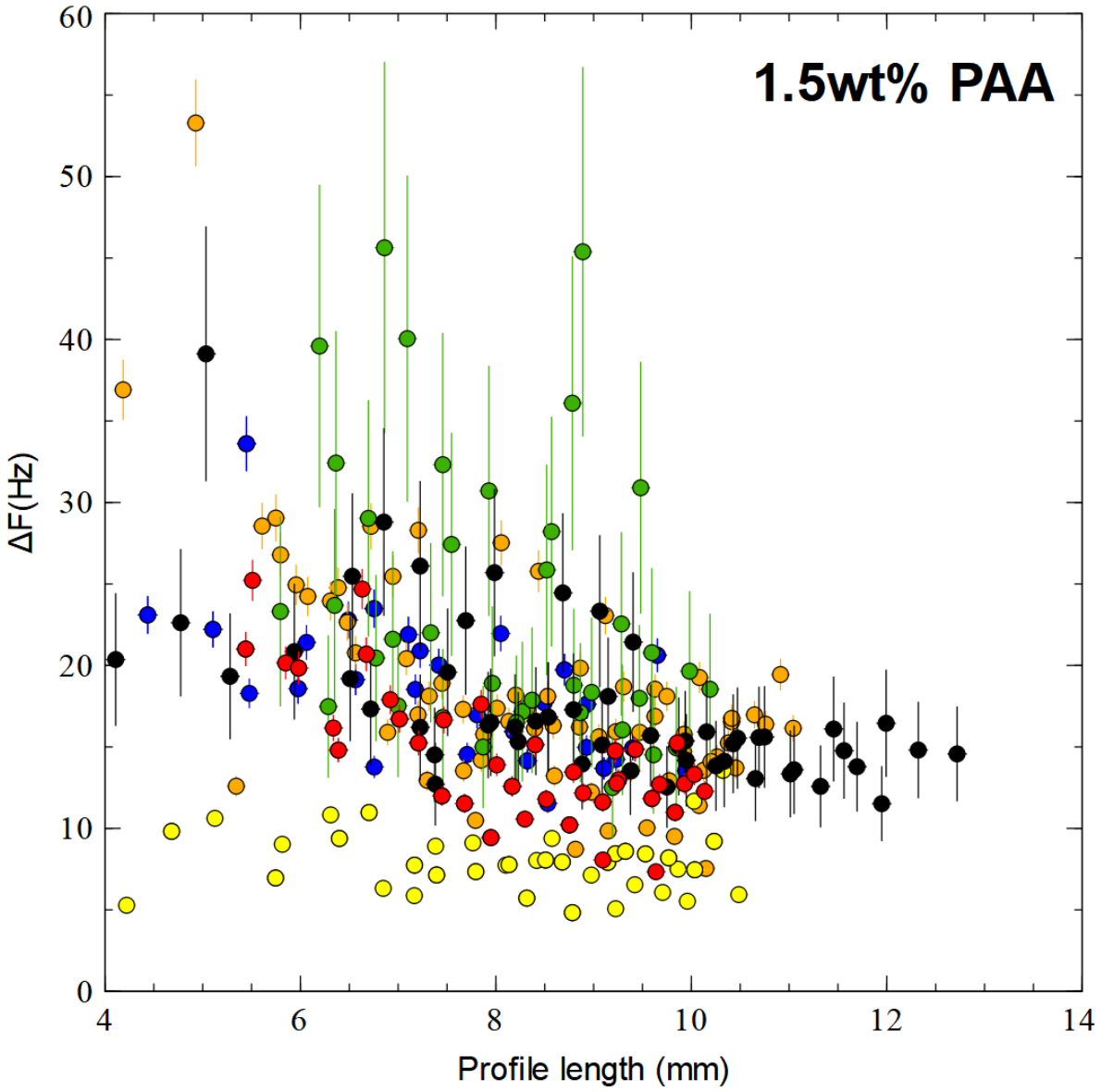


Figure 5.24: A graph to show the contact angle dependence of the spectral width of surface waves on sessile droplets (1.5wt% PAA). Contact angles: 33˚ (silicon) – green, 70˚(aluminium) – black, 75˚(polystyrene) – blue, 91˚(orange), 95˚(PDMS) – red, 145˚(Candle-soot) – yellow.

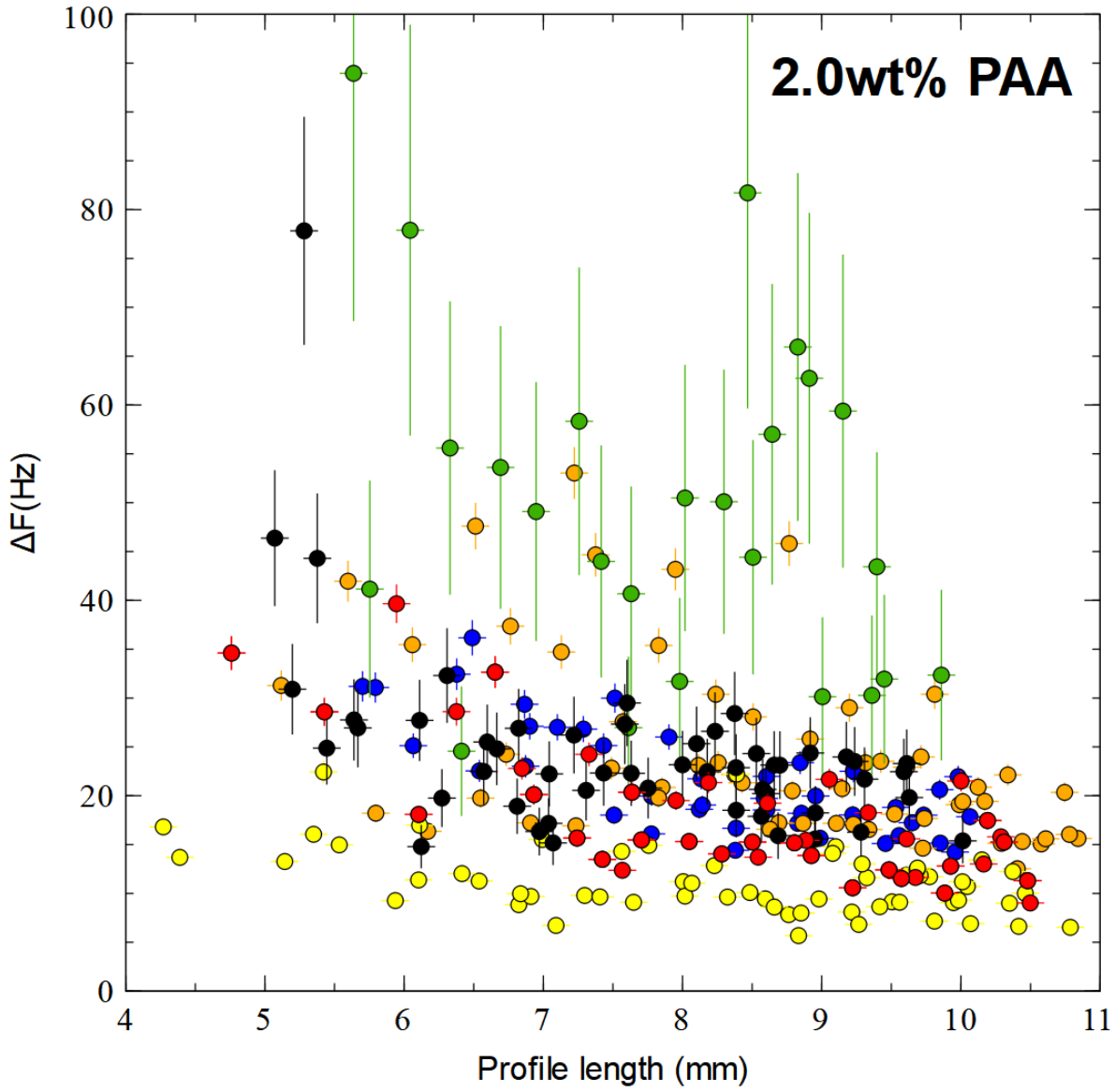


Figure 5.25: A graph to show the contact angle dependence of the spectral width of surface waves on sessile droplets (2.0wt% PAA). Contact angles: 35˚ (silicon) – green, 75˚(aluminium) – black, 75˚(polystyrene) – blue, 93˚(orange), 96˚(PDMS) – red, 145˚(Candle-soot) – yellow.

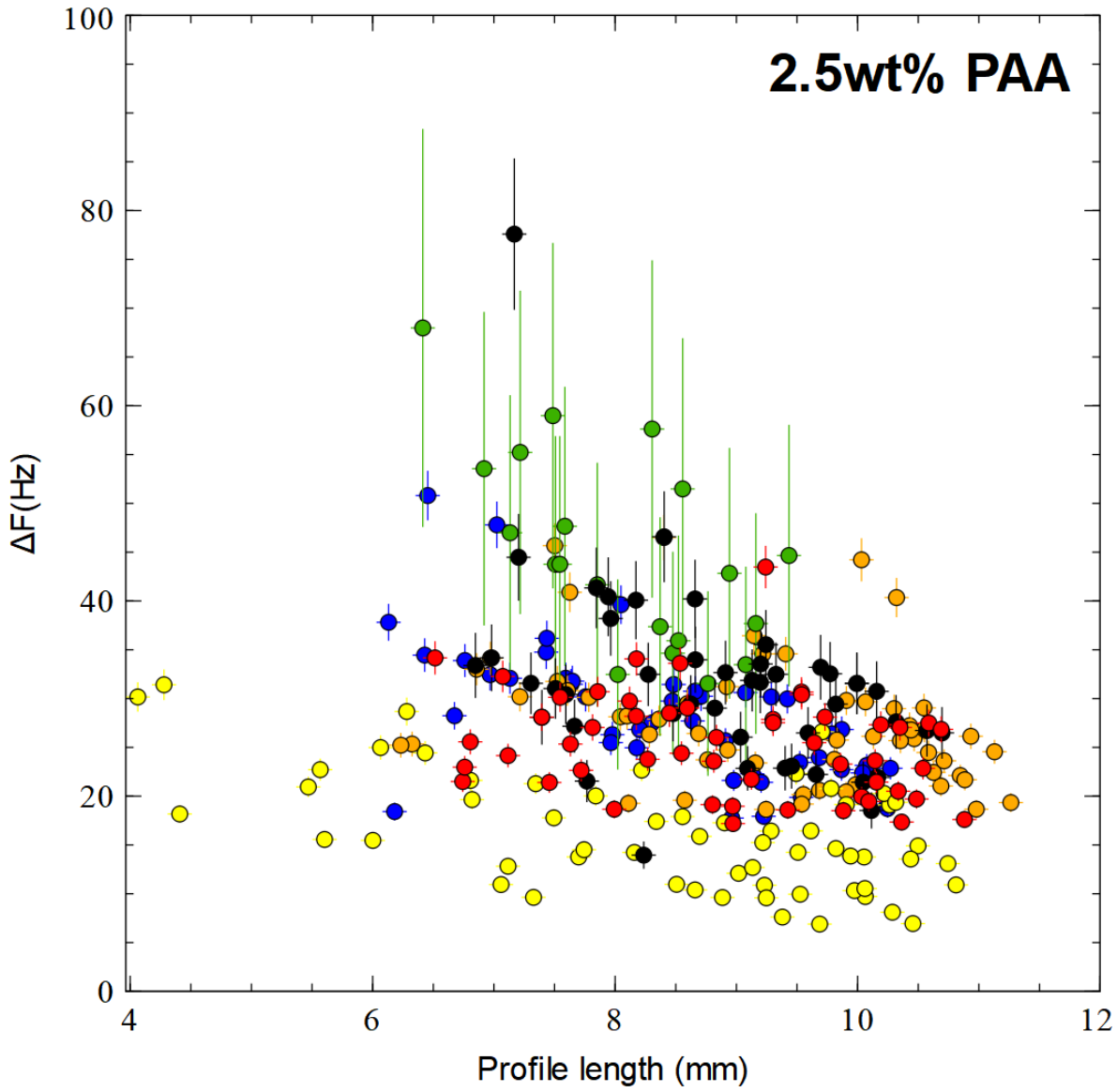


Figure 5.26: A graph to show the contact angle dependence of the spectral width of surface waves on sessile droplets (2.5wt% PAA). Contact angles: 37˚ (silicon) – green, 80˚(aluminium) – black, 85˚(polystyrene) – blue, 93˚(orange), 97˚(PDMS) – red, 145˚(Candle-soot) – yellow.

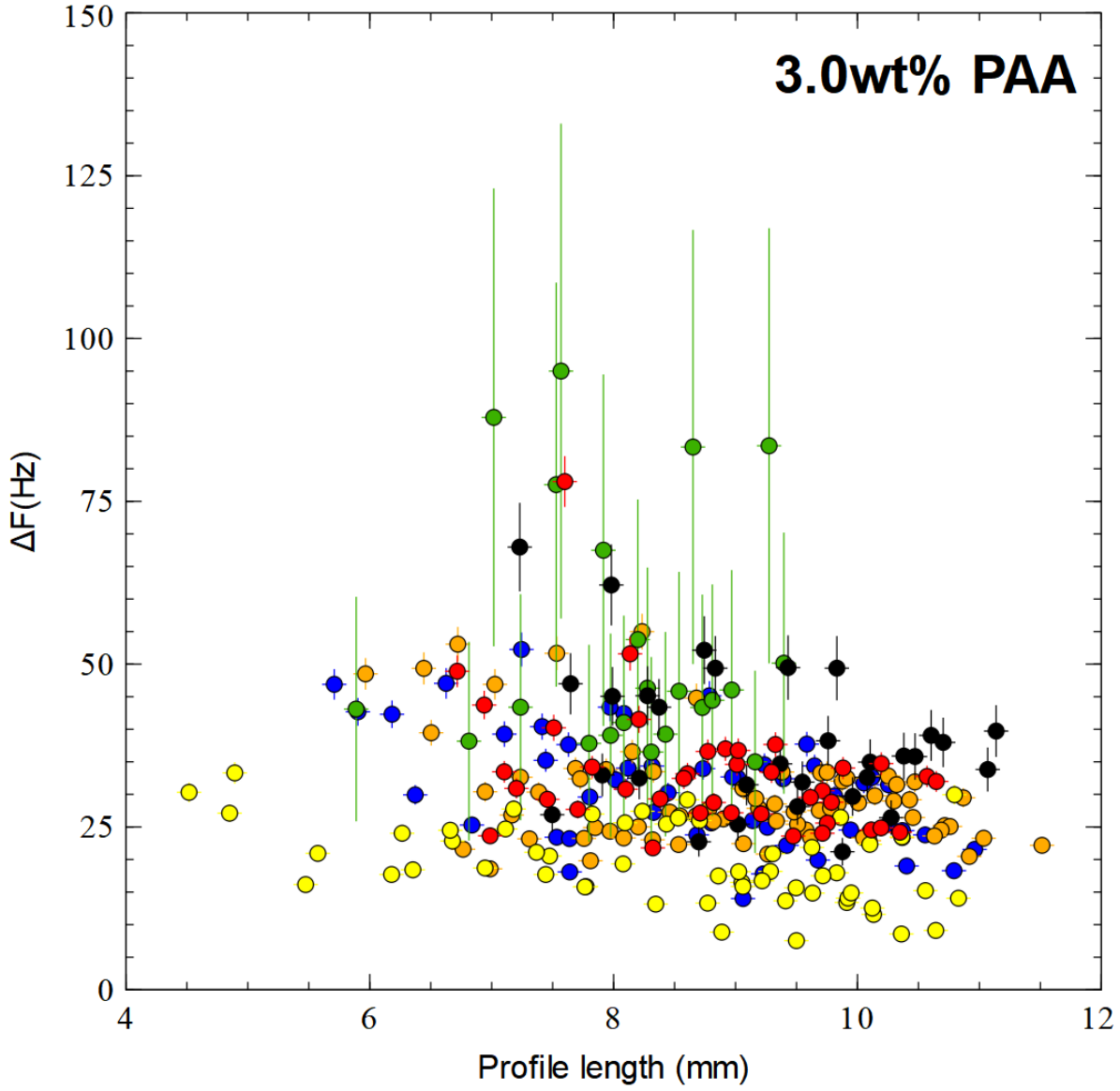


Figure 5.27: A graph to show the contact angle dependence of the spectral width of surface waves on sessile droplets (3.0wt% PAA). Contact angles: 38˚ (silicon) – green, 82˚(aluminium) – black, 92˚(polystyrene) – blue, 95˚(orange), 97˚(PDMS) – red, 145˚(Candle-soot) – yellow.

Just as with the surface wave frequency, the spectral width is heavily dependent upon contact angle, however it does not appear to peak in the same manner as the frequency does. After examining the contact angle dependence for all of the polymer solutions, it would appear that the spectral width increases as the contact angle of the sessile droplets decreases. As previously stated, the lower the contact angle and the higher the polymer concentration, the smaller the amplitude of oscillation will be, which in turn will reduce the accuracy of the measurement.

Once the spectral widths had been analysed, the mathematical relationships that were introduced in chapter 2 were used in an attempt to discern the source of the change in frequency of oscillation with a change in polymer concentration.

The two most obvious sources of this change were the change in surface tension (which will have a direct effect on the capillary waves which travel across the surface of the sessile droplet), and a change in the elasticity of the medium itself. The mathematical relationship for capillary waves on the surface of a theoretical liquid bath (as described by the Noblin model [35]) were utilised to determine to what extent the surface tension of the droplets was influencing the frequency of oscillation of the sessile droplets. Specifically, equation 2.14 was used in order to find a relationship between the frequency of oscillation and surface tension.

$$f^2 = \frac{\Omega \pi n^3}{4\rho L^3} \tanh(q\bar{h}) \qquad \text{(2.24 - page 16)}$$

As disgusted previously, Sharp [36] determined that $\tanh(q\bar{h}) \approx 0.6561$. This means that the relationship between f^2 and $1/L^3$ is dependent on the variable $\Omega/4\rho$.

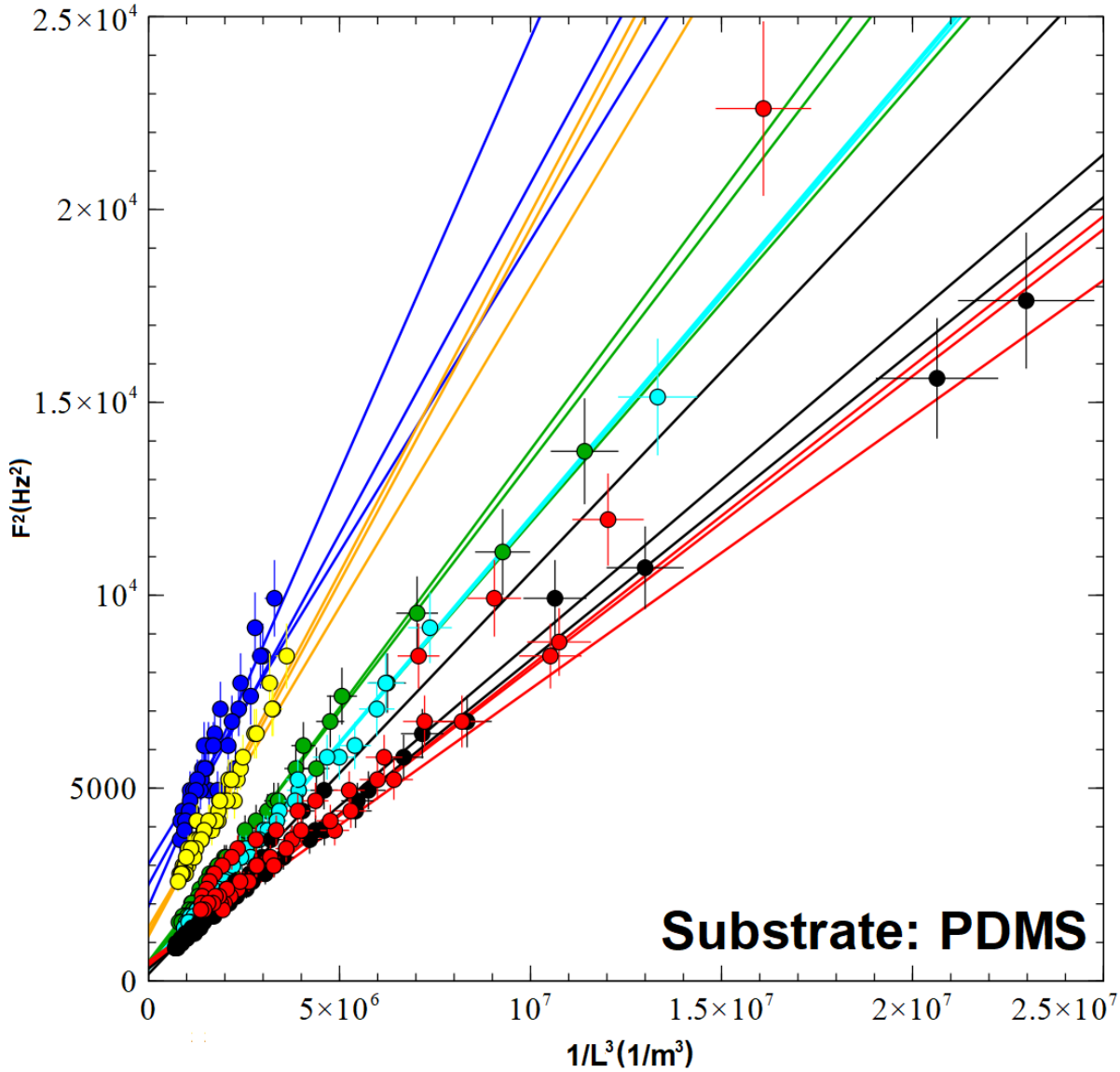


Figure 5.28: A graph to show the frequency of oscillate of sessile droplets (supported on a PDMS substrate) squared against the inverse of the cube of the profile length, with lines of best fit added to the data. Polymer concentration: 0.5wt% (red), 1.0wt% (black), 1.5wt% (cyan), 2.0wt% (green), 2.5wt% (yellow), and 3.0wt% (blue).

The gradients of the lines of best fit for the results displayed in figure 5.28 are show in table 5.2.

PAA concentration	Gradient of line of best fit (average)	$\Omega/4\rho$ ($Jmkg^{-1}$)
0.5wt%	0.002242827	17711.71
1.0wt%	0.002684993	17686.24
1.5wt%	0.003494579	17262.19
2.0wt%	0.003772981	17187.3
2.5wt%	0.005361405	16313.675
3.0wt%	0.005685492	16143.75

Table 5.2: The average gradient of the lines of best fit for the frequency of oscillate of sessile droplets (supported on a PDMS substrate) squared against the inverse of the cube of the profile length (as displayed in figure 5.28). The variable $\Omega/4\rho$ is also displayed in this table.

As can be seen in table 5.2, the gradient of the lines of best fit decreases as $\Omega/4\rho$ (and the polymer concentration) increases. If the relationship described in equation 2.24 was to hold, the exact opposite should occur. The gradient of the lines of best fit should decrease as $\Omega/4\rho$ decreases. This indicates that the surface tension of the sessile droplet is not responsible for the change in oscillation frequency, which in turn indicates that the change in oscillation frequency is due to a 'stiffening' of the polymer solution itself. This would indicate that the bulk elasticity of the sessile droplets is increased with polymer concentration, as well as indicating that the physical properties of the bulk of sessile droplets has a much greater effect on sessile droplet oscillation than surface tension.

In summary, the analysis of the oscillation frequencies and spectral widths of these sessile droplets revealed that the frequency of oscillation is primarily determined by the contact angle of the sessile droplets and the elastic properties of polymer solution, as opposed to the surface tension of the liquid-gas interface. The frequency of oscillation of the sessile droplets also appears to peak when the contact angle of the droplet approaches 90˚. The spectra widths increase with polymer concentration, which is not overly surprising, as the viscosity of the solution would be increasing, resulting in increased damping. The spectral widths appear to also peak around 80/90˚ for polymer concentration of 1.0wt% and over, however once again the results from silicon possess a large amount of scatter which makes drawing a clear conclusion difficult.

The 0.5wt% concentration produces some interesting results, as the spectral widths seem to peak around 60˚, as opposed to 90˚. The results for 0.5wt% (as shown in figure 5.22) also shows a distinct difference between the spectral widths produced from sessile droplets supported on polystyrene and those supported on PDSM, despite both sets of sessile droplets having the same contact angle. This suggests that the interaction between the sessile droplets and the substrates is more complicated than assumed. It would appear that just because two substrates produce the same contact angle for a polymer solution, does not necessarily mean that the sessile droplet will interest with the two substrates in exactly the same way. A basic hypothesis is that polymer chains within the solution might physically interact with the surface of the substrate, potentially getting snagged on imperfections and subsequently entangled with other polymer chains. This might have the effect of increasing the damping of sessile droplet oscillations, as the droplets would effectively become more viscous (as the anchored polymer chains would oppose movement).

After investigating the contact angle dependence of the frequency and spectral width of sessile droplet surface waves, an attempt can be made to create a model which can compensate for this contact angle dependence and allow for the viscoelastic properties of the polymer solutions to be ascertained.

5.9 Power spectrum analysis

As mentioned previously, the approach that was taken to deriving the mechanical properties of viscoelastic sessile droplets was to treat the sessile droplet as a liquid bath, the dimensions of which are defined by the geometry of the sessile droplet. Because of this, the first step in constructing this model is to define the dimensions of this theoretical liquid bath. The width of the liquid bath is simply defined as the profile length of the sessile droplet, and the depth is defined as the average height of the droplet. There are many different ways of defining the average height of a spherical cap. The technique that was used in this experiment was to divide the spherical cap into thin cylindrical sections, which were then used to find the volume of the spherical cap and by extension the average height of the spherical cap (a full explanation can be found in the appendix, section A.1). This is the technique which will be initially used to define the height of the sessile droplet. The height of the sessile droplet is given by the equation:

$$\bar{h} = \frac{R}{4}\frac{\left(3-8\cos(\theta)+6\cos(\theta)^2-\cos(\theta)^4\right)}{\left(2-3\cos(\theta)+\cos(\theta)^3\right)} \tag{5.1}$$

where θ is the contact angle of sessile droplet, and R is the radius of sessile droplet (which is defined by the contact angle and profile length of the droplet, as shown in figure 5.29). The full derivation of equation 5.1 can be found in the appendix (section A.1).

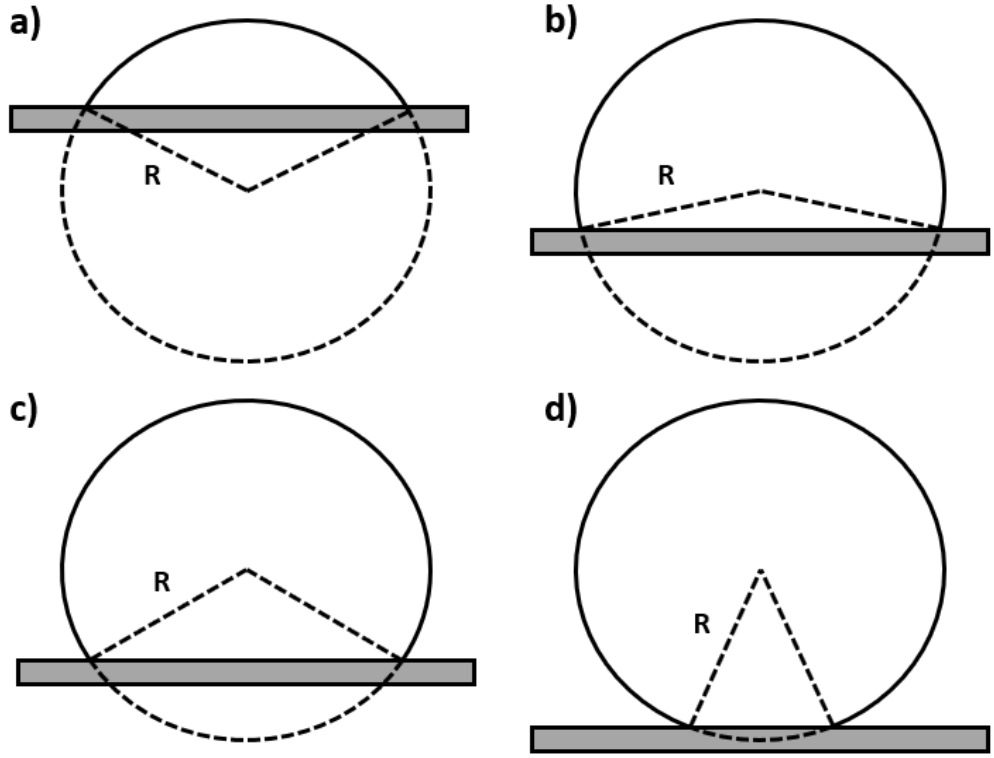


Figure 5.29: A figure to show how the radius of a sessile droplet is defined, with a low (a), intermediate (b-c) and high (d) contact angle.

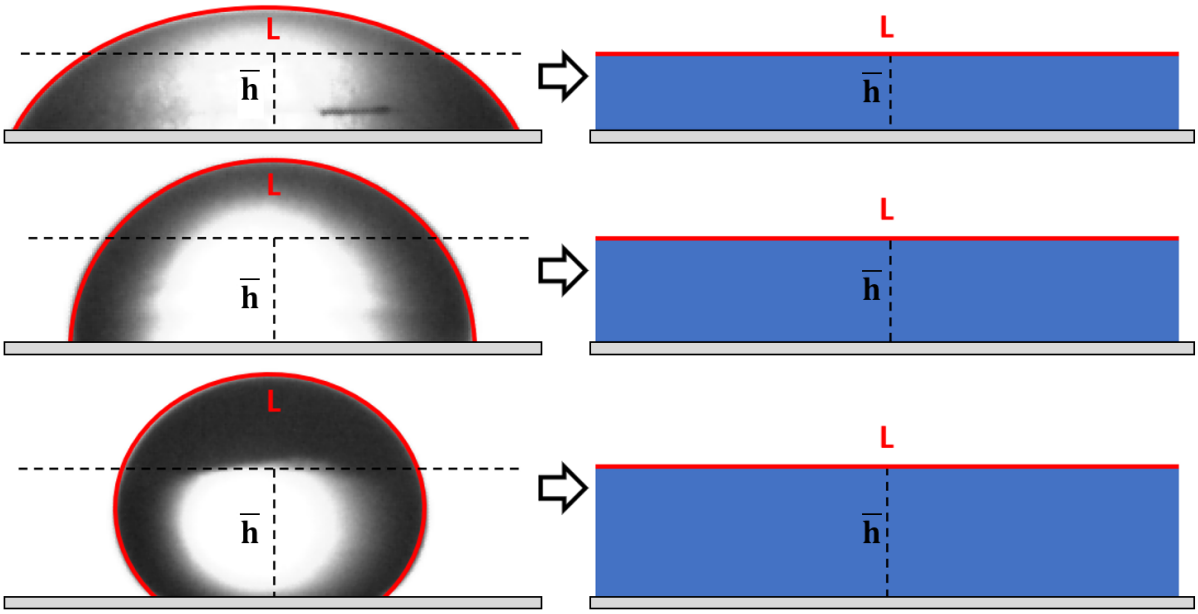


Figure 5.30: A diagram to show how sessile droplets (as shown on the left) and models as liquid baths (as shown on the right). The width of the liquid bath is dictated by the profile length of the sessile droplet, while the depth of the bath is dictated by the sessile droplet's average height.

Since the wave number was determined to be n=3, the surface wave was considered to have cylindrical symmetry, therefore justifying the application of a two-dimensional model onto a three-dimensional sessile droplet. Once the dimensions of the theoretical liquid bath have been established, the Jäckle equation can be applied in order to compute the viscoelastic properties of the polymer solution. The Jäckle equation (equation 2.24) for the dynamic susceptibility is given by:

$$\chi_{zz}(q,\omega) = \frac{1}{\rho\omega}\frac{A\left(K\sinh(q\bar{h}) - q\sinh(K\bar{h})\right) - Bq\left(\cosh(q\bar{h}) - \cosh(K\bar{h})\right)}{AD - BC} \qquad (2.37 - \text{page } 22)$$

Where the variables A, B, C, D, K, and ω are defined in equations 2.38 to 2.43 on page 22.

The variables in the Jäckle equation are density (ρ), the wavenumber (q, defined in equation 2.11 on page 21), surface tension (Ω), average height ($\bar{h}$), frequency (f), the acceleration due to gravity (g), and kinematic viscosity (ν). The density of the solutions was determined by weighing known volumes of polymer solution (as discussed in section 3.1). The surface tension of each polymer solution was determined via pendant drop analysis (as discussed in chapter 4).

Since the radius of these sessile droplets was below the capillary length the gravitational term can be omitted. Finally, the wavenumber is calculated using the mode number of the surface wave (which from observation was found to match the n=3 wave mode) and the profile length. The wave-vector is calculated using the equation:

$$k = \frac{n\pi}{L} \qquad (5.2)$$

where n is the mode number and L is the profile length of the sessile droplet.

This equation is a result of the fact that only half integer wave modes can exist along the surface (as discussed in chapter 2 and demonstrated in figures 2.10 and 2.11). The only variable which is not known is the kinematic viscosity, which is what needs to be determined. Kinematic viscosity can be broken down into the storage and loss moduli using the equation:

$$\nu = \frac{\left(\frac{G_{ii}}{\omega}\right) - i\left(\frac{G_i}{\omega}\right)}{\rho} \tag{5.3}$$

Since both the storage (G′) and loss (G″) moduli are unknown variables, this equation cannot be solved analytically and therefore must be solved numerically.

To analyse the power spectra acquired from this experiment a specific Matlab program was created. This program would take the acquired power spectra and correlate a theoretical power spectrum using the Jäckle along will all of the variables that it requires. First, the acquired power spectrum was loaded into the Matlab program, and the height and position of the largest peak was calculated. The power spectrum was then cropped for a range of twice the FWHH value, below and above the peak position (as show in figure 5.31). For example, if the peak position was at 20 Hz and the FWHH of the peak was 5 HZ, then the power spectrum would be cropped at 10Hz and 30Hz. The power spectrum was cropped because the Jäckle equation (2.37) is only valid at values close to the peak position, and attempting to fit the curve to irrelevant positions along the power spectrum would result in a less accurate fit.

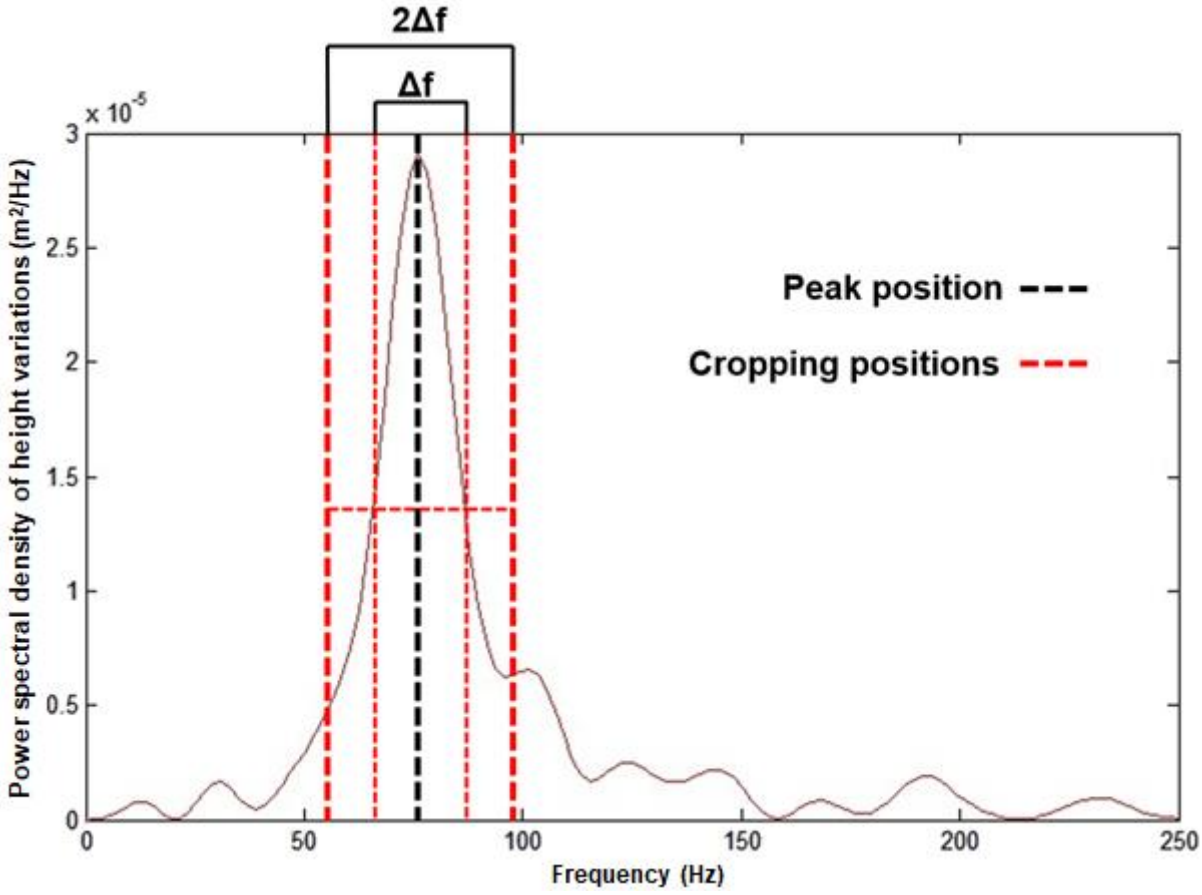


Figure 5.31: A diagram to show how a power spectrum is cropped. The width of the cropped power spectrum is defined as being twice that of the peak width.

Once the power spectrum had been cropped, the process of fitting a theoretical curve to the data could begin. A general scaling factor S was required to make the graph of $\chi''\omega^{-1}$and the acquired power spectrum line up with one another. Since this scaling factor does not change the width or the position of the peaks within the power spectrum (as demonstrated in figure 2.17), this factor has no effect on the result. A shown in section 2.5, the scaling factor for thermally driven waves is $2k_BT$. Since only the common factor of $\chi''\omega^{-1}$ is relevant, the scaling factor is simply used as a means of fitting the theoretical curve generated from the Jäckle equation) to the experimental data (as shown in figure 5.32).

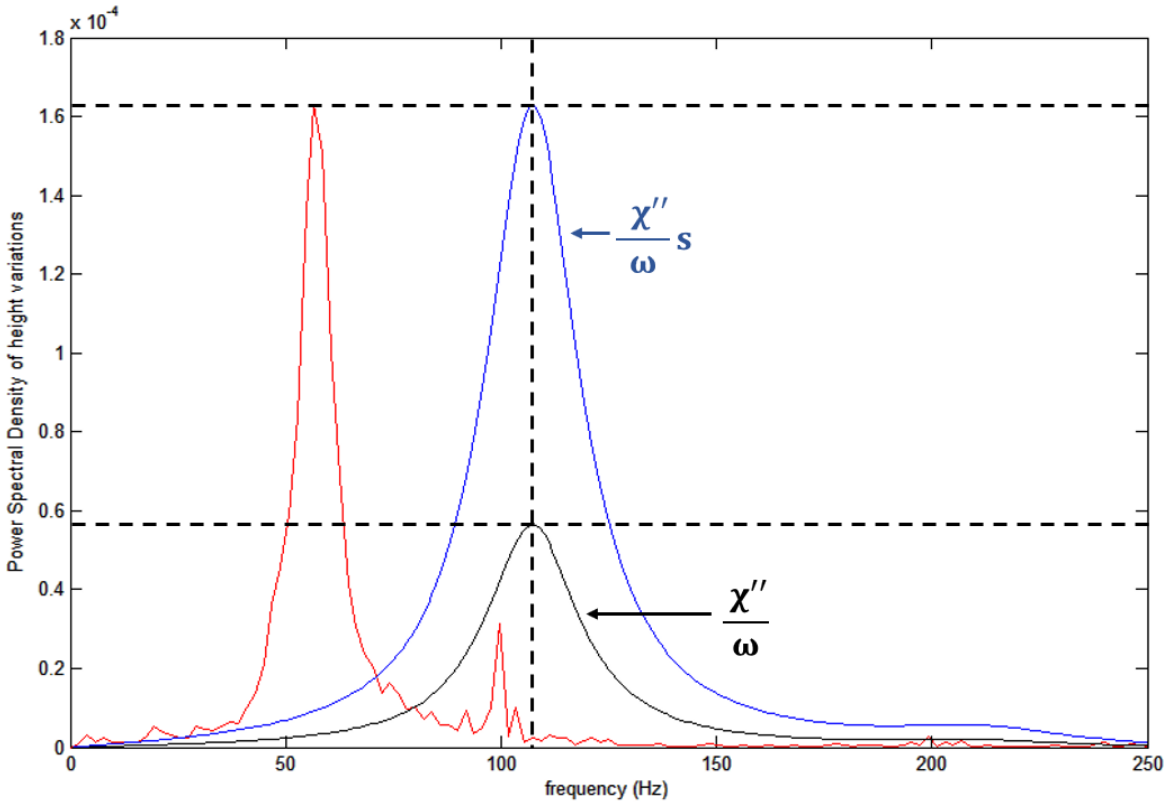


Figure 5.32: A diagram to show how the raw output from the Jäckle equation (shown in black) can be scaled up to be the same height was the experimental power spectrum (shown in red) by multiply by a scaling factor S (shown in blue). This scaled blue curve will then compared with the red data curve to see if the two curves correlate (which in this example they do not).

By starting with a general guess for the value of G′, G″, and the general scaling factor S, the Matlab program (written by the author) cycled through possible combinations for the storage and loss moduli. For each guess, the sum of the difference squared between the theoretical values for the power spectrum and the experimental data was calculated (as shown in figure 5.33). The fact that the experimental power spectrum had been interpolated significantly increased the accuracy of the calculated difference between the two spectra. The Matlab program then found the combination of G′, G″, and scaling factor which minimised the sum of the difference squared between the generated curve and experimental power spectrum. Figure 5.34a shows how the program starts with an initial guess for G′ and G″, then gradually converges towards the correct fit (figures 5.34b and 5.34c), until eventually determining the optimal combination of variables required to make the two curves match (figure 5.34d).

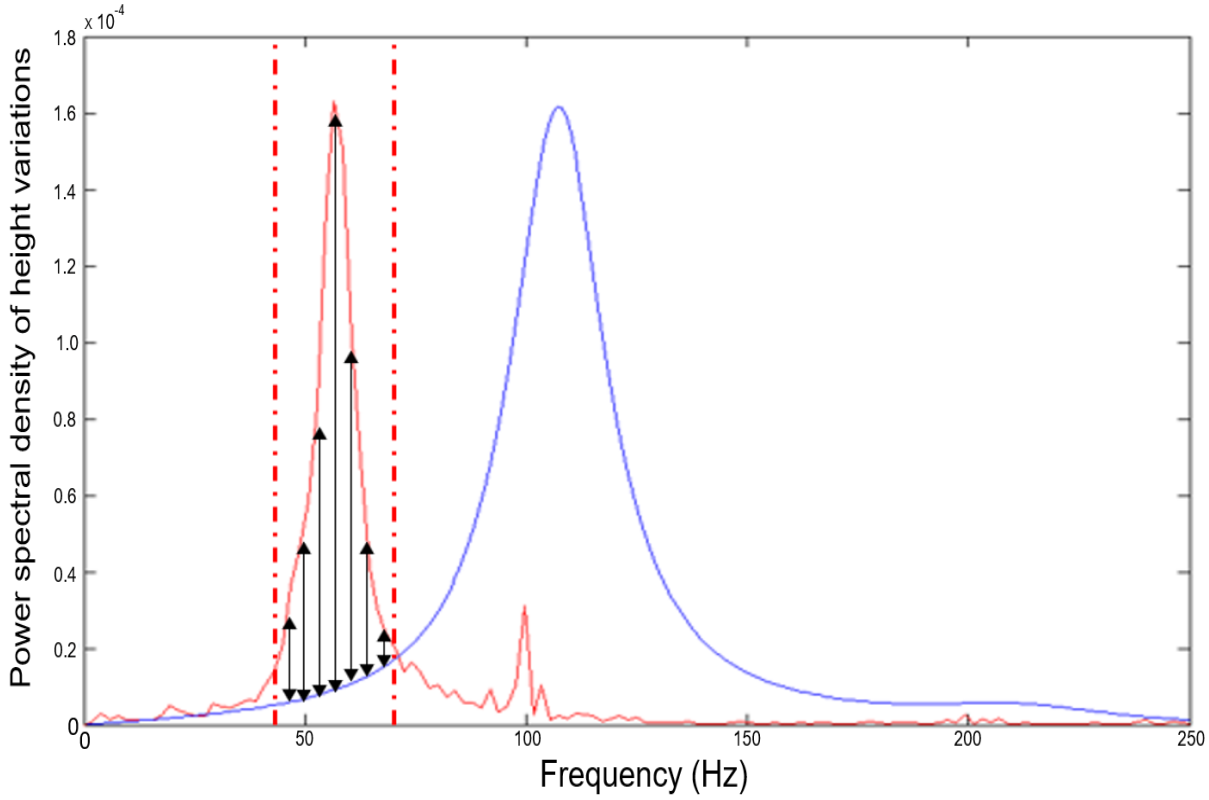


Figure 5.33: A diagram to show how the difference between the theoretical power spectrum (blue and he experimental power spectrum (red) are calculated. The red dashed lined indicate the region of the power spectrum which is being analysed. The black arrows show the difference between the two power spectra. factor S (shown in blue).

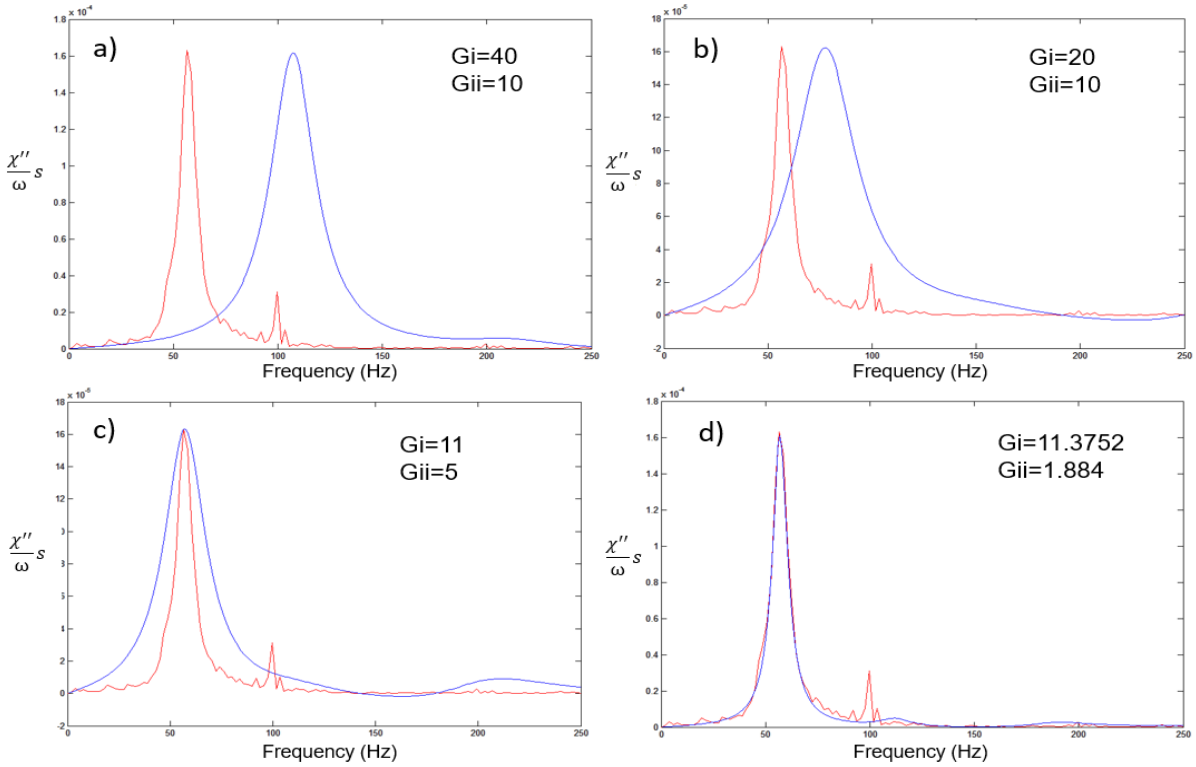


Figure 5.34: The acquired power spectrum (red) plotted alongside the theoretical curve generated from the Jäckle equation (blue). The first initial guess for the values of G′ and G″ is shown in figure (a), with subsequent modifications to these values converging towards the optimum values for the variables G′, G″, and S (figures b and c). Finally, the optimum values are determined, producing a curve which matches the experiment curve (figure d).

As can been seen in figure 5.34 the position of the peak is primarily dictated by the value of the elastic modulus (G′), whereas the width of the peak is primarily dictated by the viscous modulus (G″). This is to be expected, as the elastic component of a viscoelastic material will control the rate at which it oscillates, were as the viscous component will dictate how quickly oscillations are damped. Every individual power spectrum was analyses using this technique, resulting in the acquisition of values for the Storage and loss moduli for all concentrations of polymer solution across a range of frequencies and contact angles.

5.10 Results

This section contains the results obtains for the storage and loss moduli for the PAA polymer solutions that were described in section 3.1. for ease of reference, the concentration dependent contact angles for the substrates being investigated (as shown in table 3.2) are shown again:

PAA concentration	0.5wt%	1.0wt%	1.5wt%	2.0wt%	2.5wt%	3.0wt%
Silicon	30±1	30±1	33±1	35±1	37±1	38±1
Aluminium	55±1	60±1	70±1	75±1	80±1	82±1
Polystyrene	60±1	70±1	75±1	75±1	85±1	92±1
Wax	90±1	90±1	91±1	93±1	93±1	95±1
PDMS	90±1	93±1	95±1	96±1	97±1	97±1
Candle soot	145±1	145±1	145±1	145±1	145±1	145±1

Table 5.3: A replica of table 3.2, replicated for ease of reference.

First, the polymer concentration dependence for the values of G' and G'' will be investigated. This was carried out using the wax substrate, as it was shown to produce the least variation in contact angle across the range of polymer solutions being investigated (with the exception of candle soot, which wasn't used due to the difficulties that were described in section 5.6). The values for concentration dependent storage and loss modulus are shown in figures 5.35 and 5.36 respectively. The errors in these measurements were given by the upper and lower values for the errors in the frequency and spectral width, and fitting the Jäckle model to these modified power spectra.

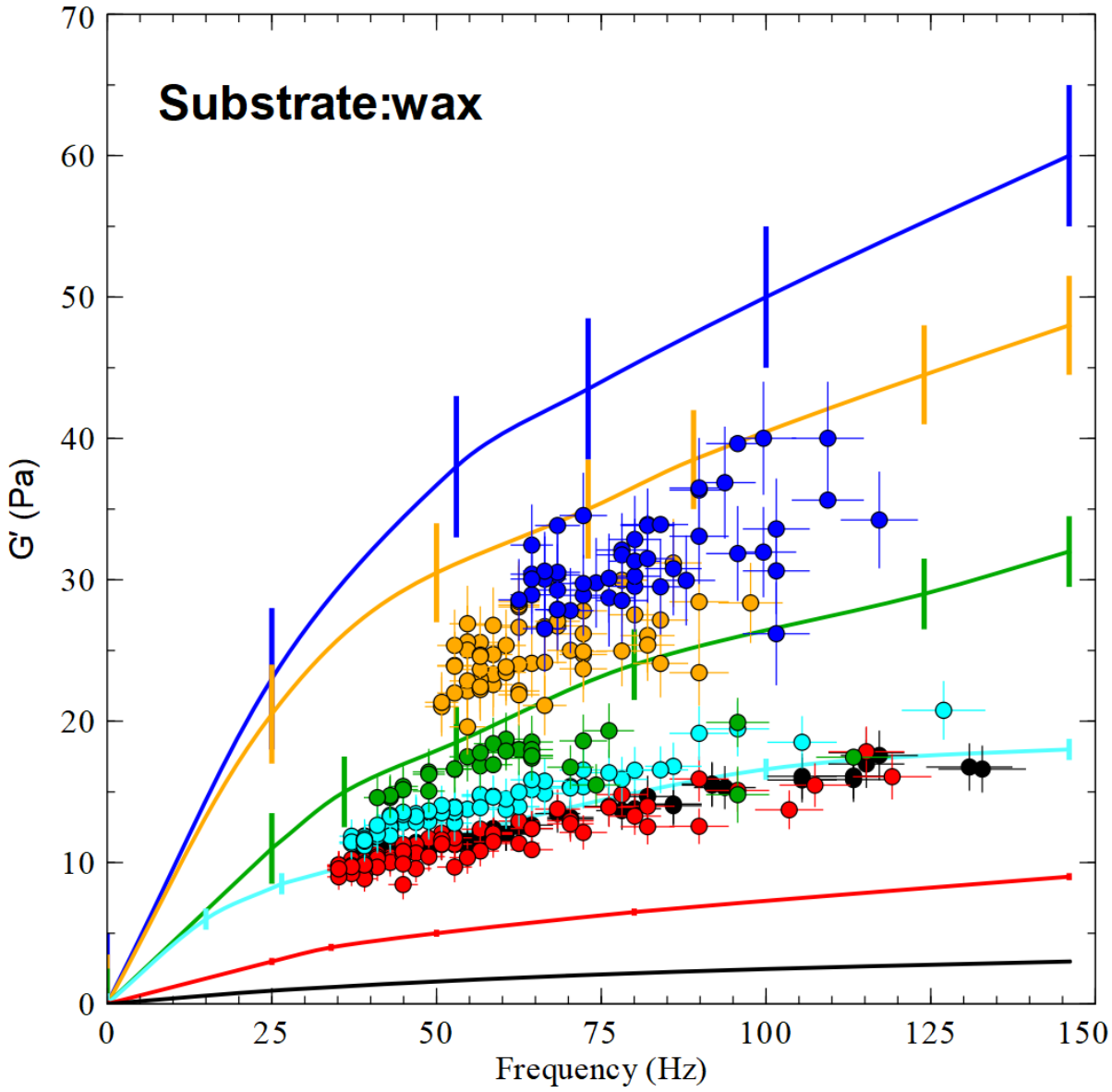


Figure 5.35: The values for the frequency dependent storage modulus (G′) acquired from the Jäckle model evaluation of sessile droplets supported on a wax substrate. The solid lines represent the data for the frequency dependent storage moduli acquired through dynamic light scattering analysis. Polymer concentration: 0.5wt% - black, 1.0wt% - red, 1.5wt% - cyan, 2.0wt% - green, 2.5wt% - yellow, 3.0wt% - blue.

As can be seen through this data, the results obtained from the Jäckle model are somewhat similar to those obtained through dynamic light scattering analysis, with deviations being noticeable when examining very low polymer concentrations such as 0.5wt% and 1.0wt%.

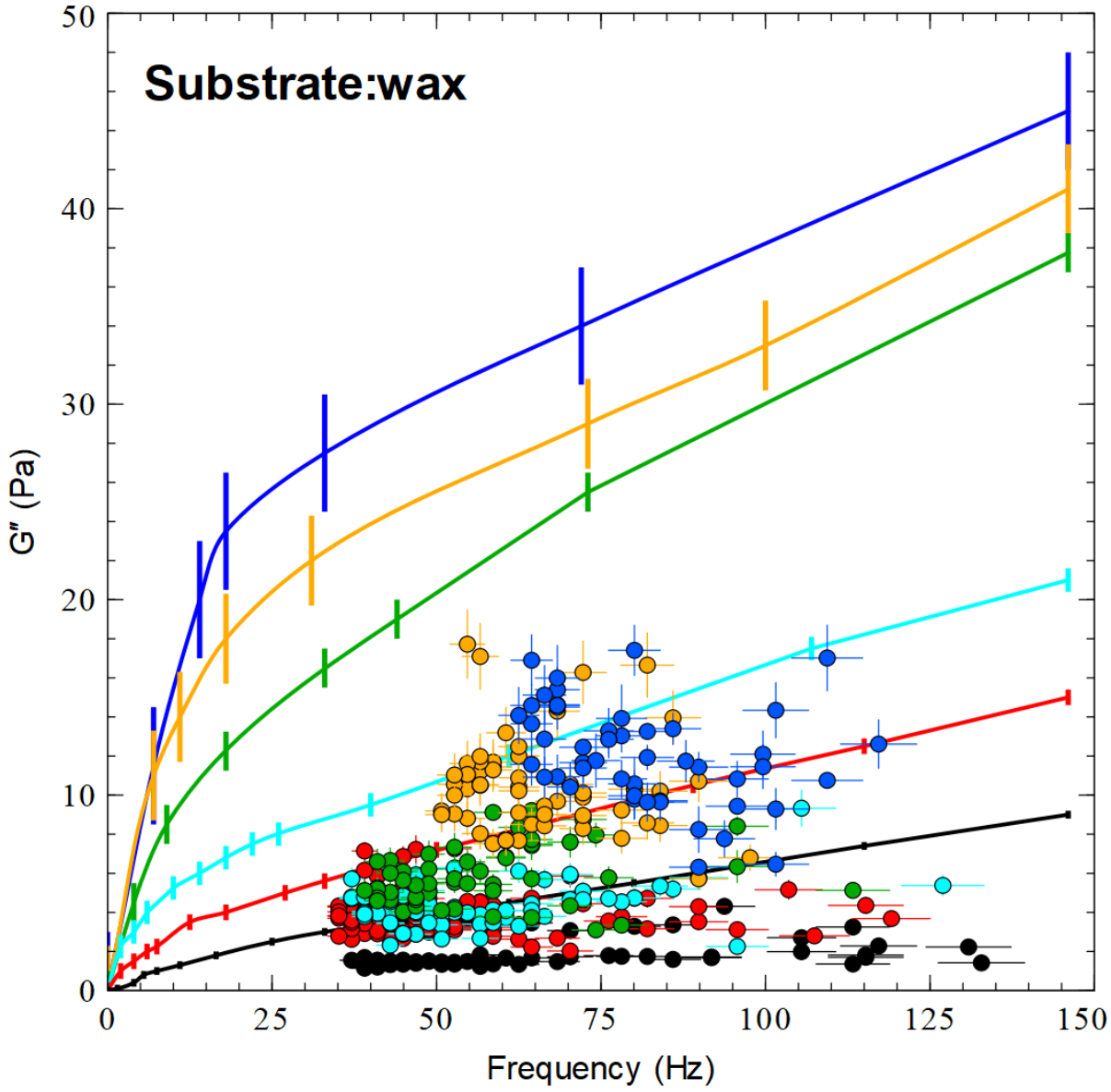


Figure 5.36: The values for the frequency dependent loss modulus (G″) acquired from the Jäckle model evaluation of sessile droplets supported on a wax substrate. The solid lines represent the data for the frequency dependent loss modulus acquired through dynamic light scattering analysis. Polymer concentration: 0.5wt% - black, 1.0wt% - red, 1.5wt% - cyan, 2.0wt% - green, 2.5wt% - yellow, 3.0wt% - blue.

Once again, the data obtained from the Jäckle model does appear to follow a similar pattern to that obtained from the dynamic light scattering analysis, although there does appear to be a larger amount of scatter in the data compared to the data obtained for the storage modulus. Once the concentration dependence had been investigated, the contact angle dependence was analysed.

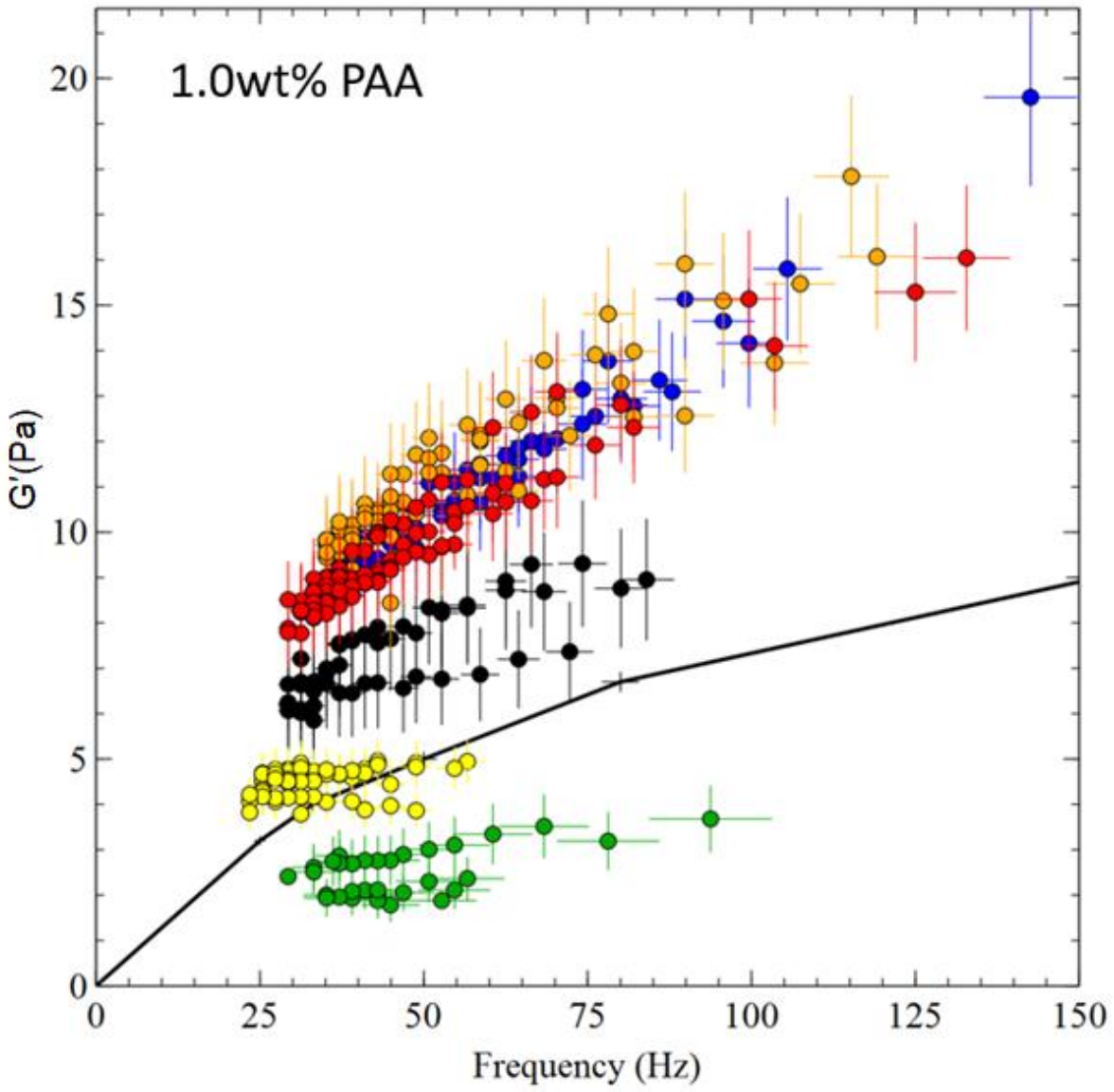


Figure 5.37: The contact angle dependent values for the frequency dependent storage modulus obtained from the Jäckle model evaluation of 1.0wt% PAA solution sessile droplets. The solid black line indicates the data for the storage modulus obtained through dynamic light scattering analysis. Contact angles: Silicon (30˚) – green, Aluminium (60˚) – black, polystyrene (70˚) – blue, wax (90˚) - orange, PDMS (93˚) – red, Candle soot (145˚) – yellow.

The values for the storage modulus show clear variation with sessile droplet contact angle. In order to bring the experimental data in like with the data acquired through the dynamic light scattering analysis, each individual data set was multiplied by a scaling. The results of this are shown in figure 5.38.

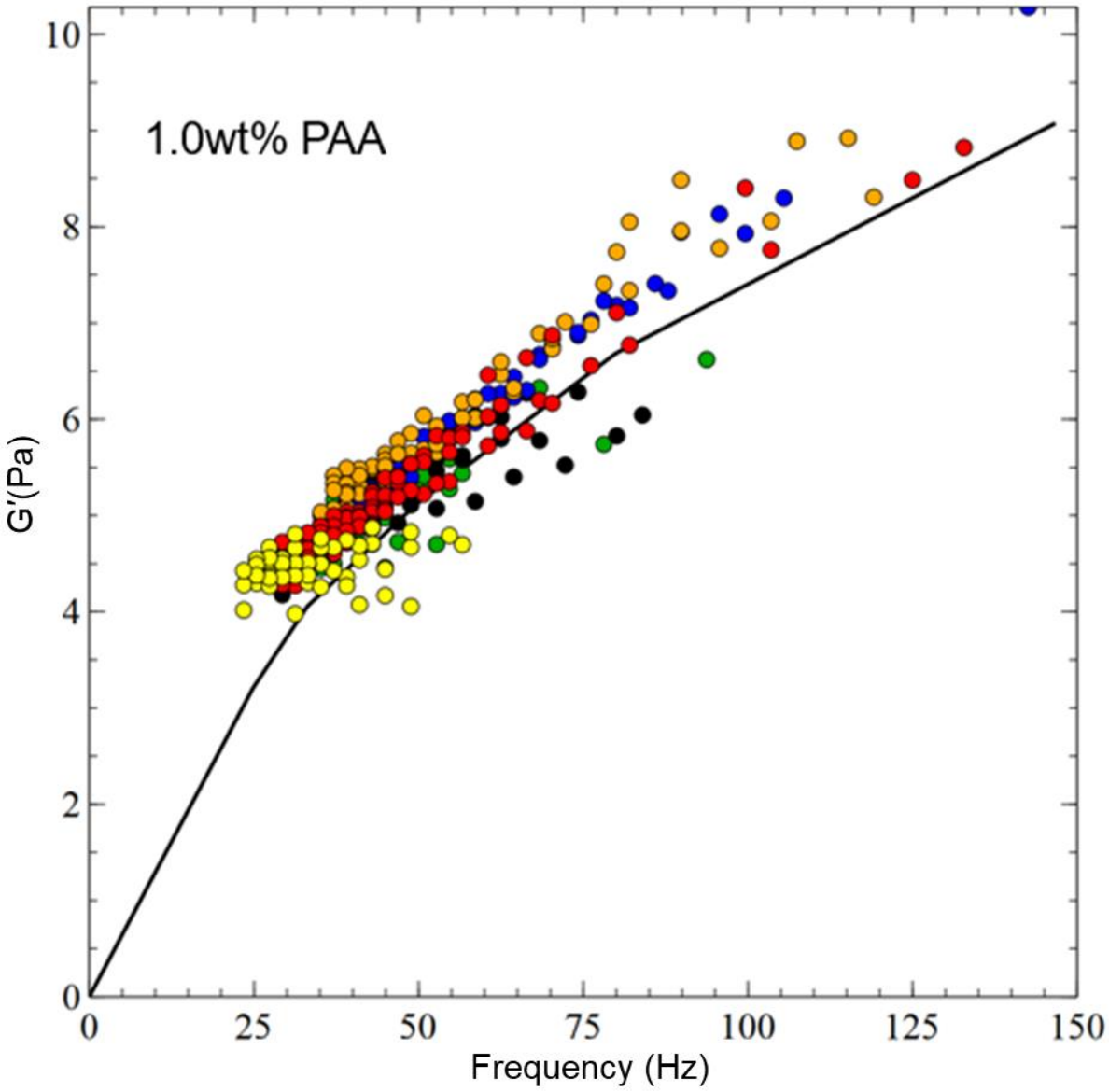


Figure 5.38: The results of scaling the values shown in figure 5.24 in order to bring the results in line with the data acquired from dynamic light scattering analysis.

As can be seen in figure 5.38, the data collapses onto the DLS data via the application of a single scaling factor. This procedure was carried out for all polymer concentrations, the results of which are shown in figure 5.39. The contact angles for each individual substrate at a particular polymer concentration can be found in the table shown on page 102.

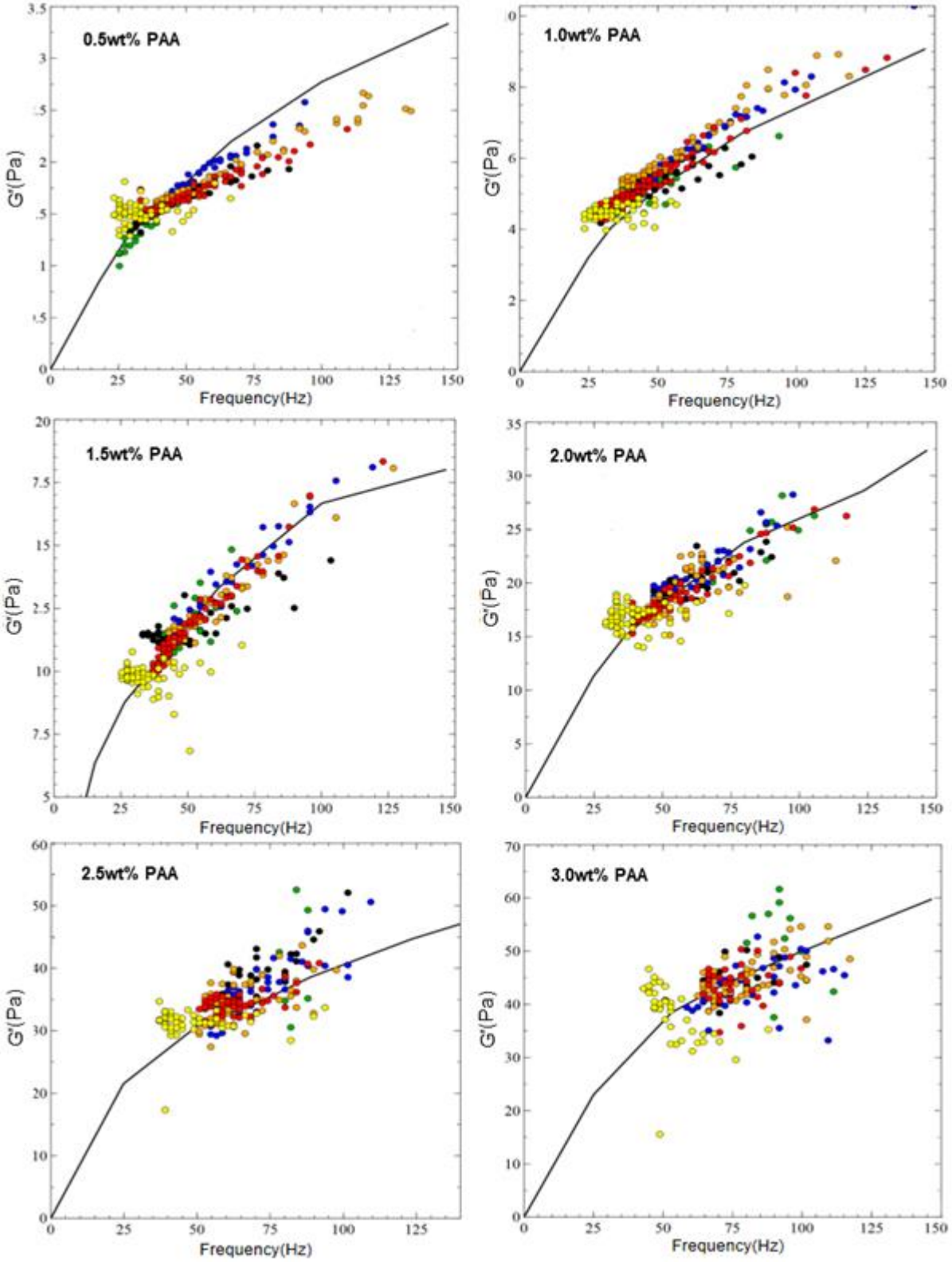


Figure 5.39: The contact angle dependent values for the frequency dependent storage modulus for all six polymer solutions, scaled so that the results correlate with the data obtained from DLS analysis. Substrate: Silicon-green, Aluminium – black, polystyrene – blue, wax – orange, PDMS – red, Candle soot – yellow.

The scaling factor that was used to bring the acquired values for the frequency dependent storage modulus in line with the data acquired through dynamic light scattering analysis was then plotted against contact angle for each individual polymer concentration. The results of which are shown below.

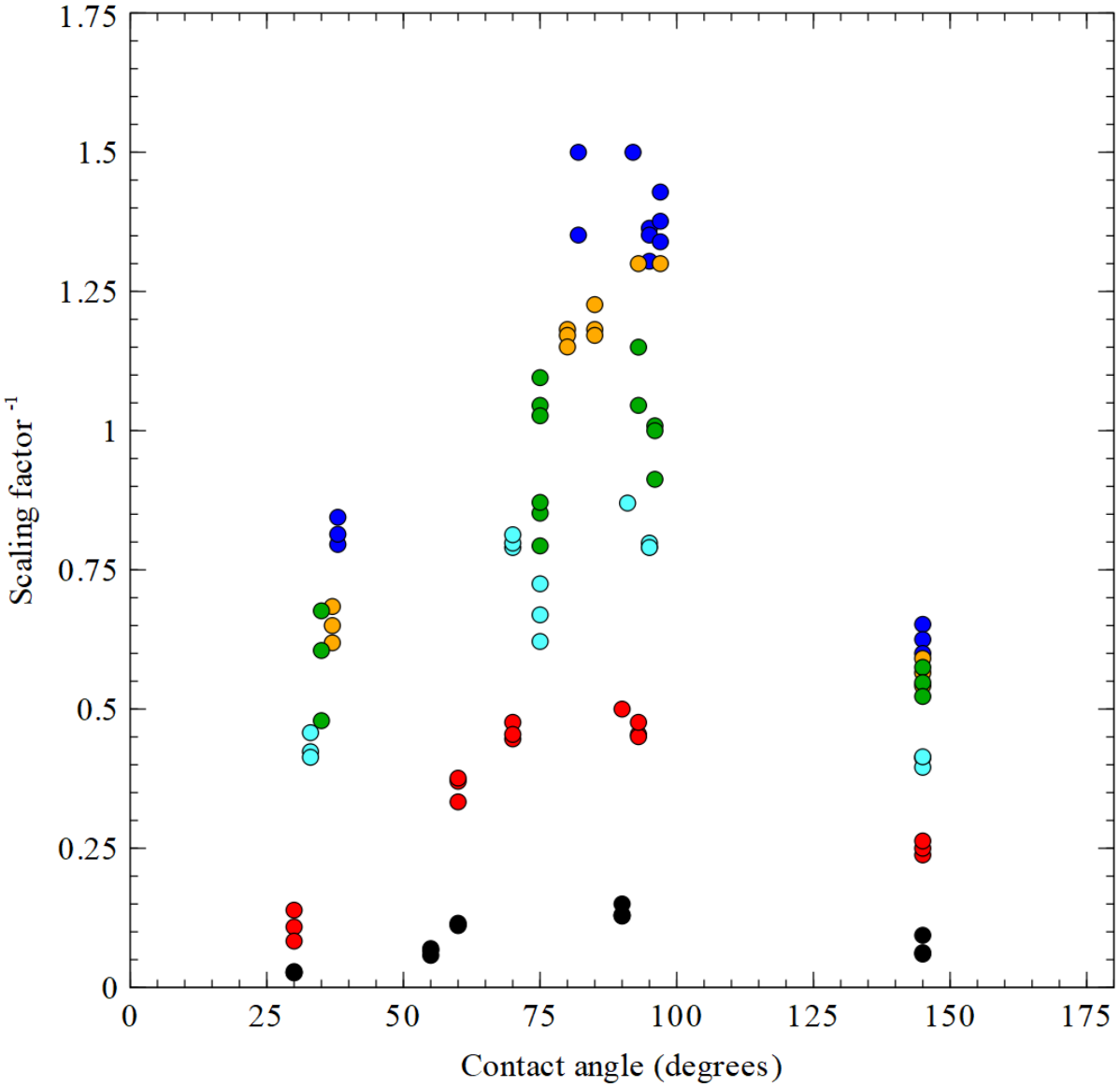


Figure 5.40: The inverse of the scaling factor used to bring the measured values for the storage modulus in line with the DLS data. Polymer concentration: 0.5wt% - black, 1.0wt% - red, 1.5wt% - cyan, 2.0wt% - green, 2.5wt% - yellow, 3.0wt% - blue.

Upon first inspection, the inverse scaling factor appears to follow a contact angle dependence, peaking at a contact angle of 90°. In order prove that this is the case a linear equation was fitted to the data (following the equation $y=mx+c$). Once this linear line of best fit was found, the data was then fitted with a curved line of best fit (following the equation $y=a\cdot\sin(x)$). the deviation between these lines of best fit and the data points was analysed using several statistical analytical techniques.

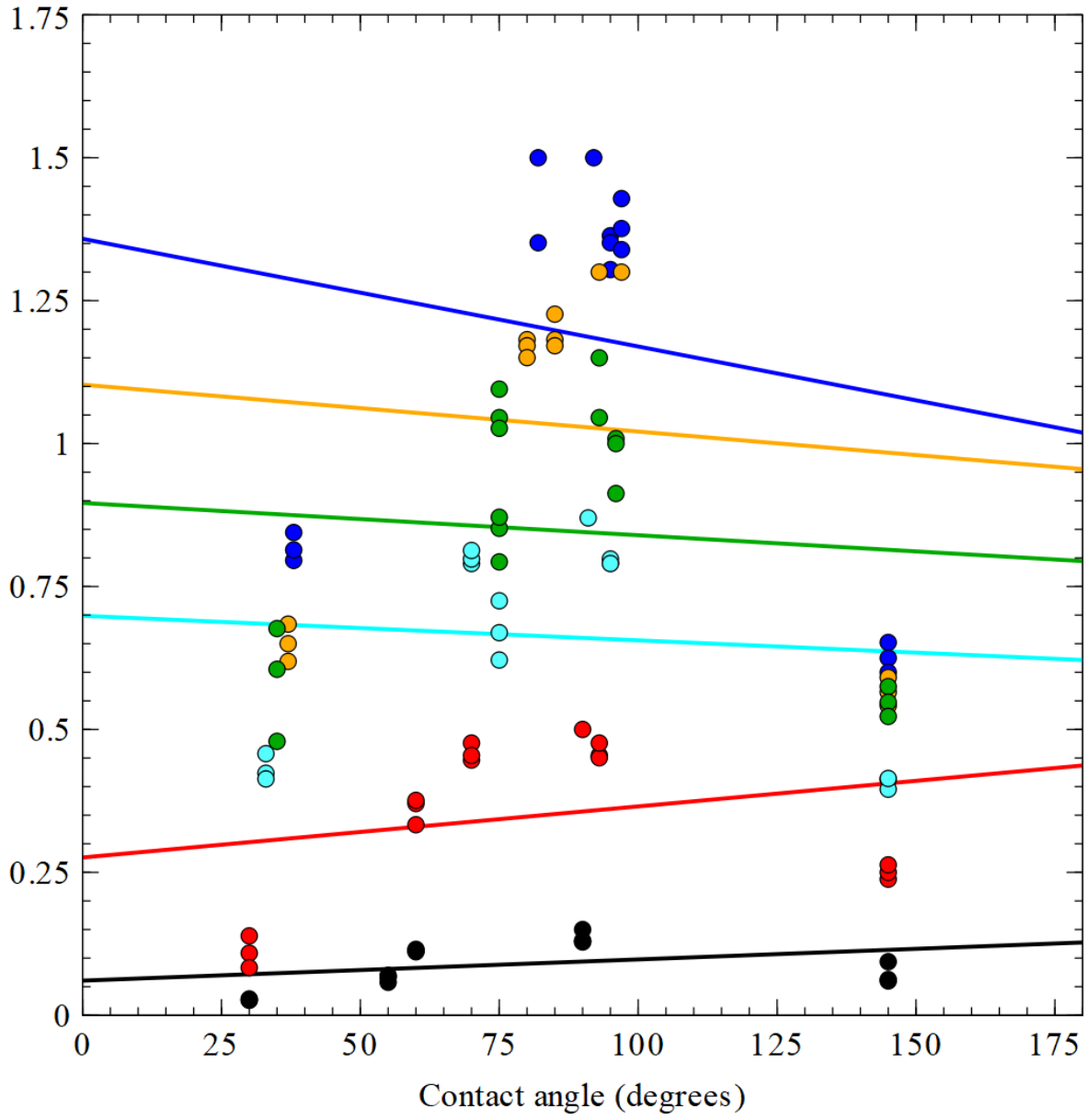


Figure 5.41: The inverse of the scaling factor used to bring the measured values for the storage modulus in line with the DLS data, fitted with lines of best fit (following the equation y=mx+c). Polymer concentration: 0.5wt% - black, 1.0wt% - red, 1.5wt% - cyan, 2.0wt% - green, 2.5wt% - yellow, 3.0wt% - blue.

Polymer concentration (wt%)	Line of best fit equation (y=mx+c)
0.5	y=0.0003711826·x+0.06057305
1.0	y=0.0008940821·x+0.2759822
1.5	y=-0.0004300497·x+0.6988662
2.0	y=-0.0005653332·x+0.8962498
2.5	y=-0.0008205721·x+1.103102
3.0	y=-0.00188357·x+1.358239

Table 5.4: A table to show the mathematical equations for the lines of best fit depicted in figure 5.41.

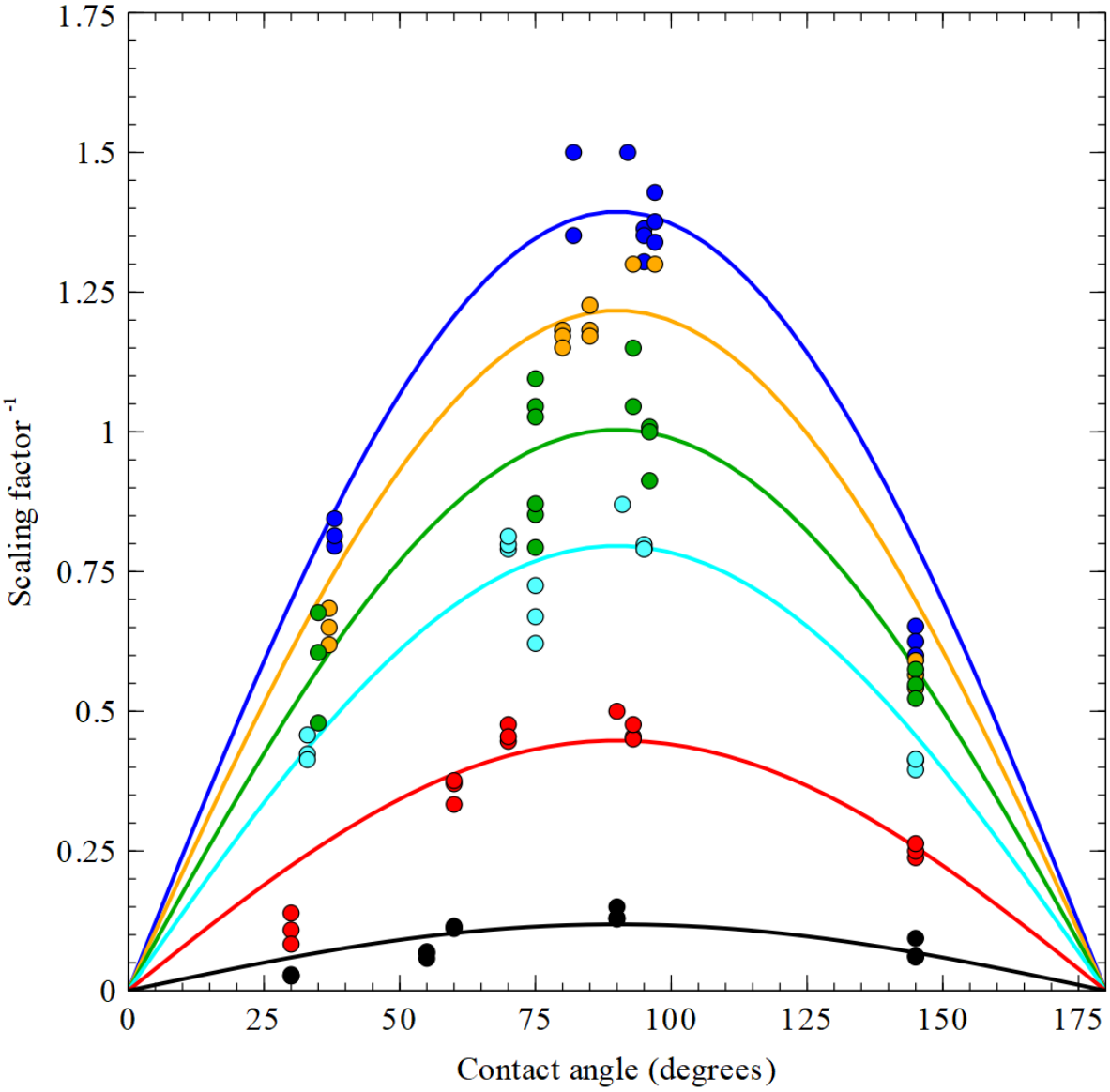


Figure 5.42: The inverse of the scaling factor used to bring the measured values for the storage modulus in line with the DLS data, fitted with lines of best fit (following the equation y=a·sin(x)). Polymer concentration: 0.5wt% - black, 1.0wt% - red, 1.5wt% - cyan, 2.0wt% - green, 2.5wt% - yellow, 3.0wt% - blue.

Polymer concentration (wt%)	Line of best fit equation (y=a·sin(x))
0.5	y=0.1187303·sin(x)
1.0	y=0.447613·sin(x)
1.5	y=0.7961178·sin(x)
2.0	y=1.004038·sin(x)
2.5	y=1.217393·sin(x)
3.0	y=1.394148·sin(x)

Table 5.5: A table to show the mathematical equations for the lines of best fit depicted in figure 5.42.

Once these lines of best fit have been computed, the variation between the acquired data and these lines of best fit can be calculated. The data was analysed using three different analytical techniques. These analytical techniques were regression analysis (the outcome of which is known as the coefficient of determination, denoted by R^2), multiple regression analysis (known as adjusted regression analysis, aR^2), and standard error analysis (SE). For the regression analysis and the adjusted regression analysis, the closer the result is to one, the more accurate the fit is to the data. For Standard error analysis, the smaller the standard error, the closer the fitted line is to the data set.

Polymer concentration (wt%)	R^2 (straight line fit)	R^2 (curved line fit)
0.5	0.1126	0.6635
1.0	0.0553	0.8289
1.5	0.0063	0.8880
2.0	0.0073	0.8401
2.5	0.0073	0.9223
3.0	0.9152	0.9152

Table 5.6: A table to show the result of the regression analysis preformed on the straight-line fits shown in figure 5.41, and the curved line fits shown in figure 5.42.

Polymer concentration (wt%)	aR^2 (straight line fit)	aR^2 (curved line fit)
0.5	0.0534	0.6425
1.0	-0.0077	0.8182
1.5	-0.0559	0.8814
2.0	-0.0058	0.8307
2.5	-0.0547	0.9178
3.0	-0.0304	0.9102

Table 5.7: A table to show the result of the adjusted regression analysis preformed on the straight-line fits shown in figure 5.41, and the curved line fits shown in figure 5.42.

Polymer concentration (wt%)	SE (straight line fit)	SE (curved line fit)
0.5	0.0414	0.02468
1.0	0.1427	0.05881
1.5	0.1931	0.06288
2.0	0.2300	0.08957
2.5	0.3206	0.08699
3.0	0.3535	0.10140

Table 5.8: A table to show the result of the standard error analysis preformed on the straight-line fits shown in figure 5.41, and the curved line fits shown in figure 5.42.

As can be seen in figures 5.41 and 5.42, the curved lined of best fit is a much better fit for the scaling data compared to the basic straight line fit. This is proven mathematically in tables 5.6-5.8. All analytical methods used indicate that the curved fit most accurately represents the scaling data. This would suggest that scaling factor for the storage modulus is indeed dependent upon contact angle, with an apparent minimum at 90°.

Once the analysis of the storage modulus was complete, the same analytical process was applied to the results for the frequency dependent loss modulus (G″) acquired via the Jäckle model. The example being used below are the G″ measurements which were taken from the same data set as the G' measurements shown in figures 5.37 and 5.38.

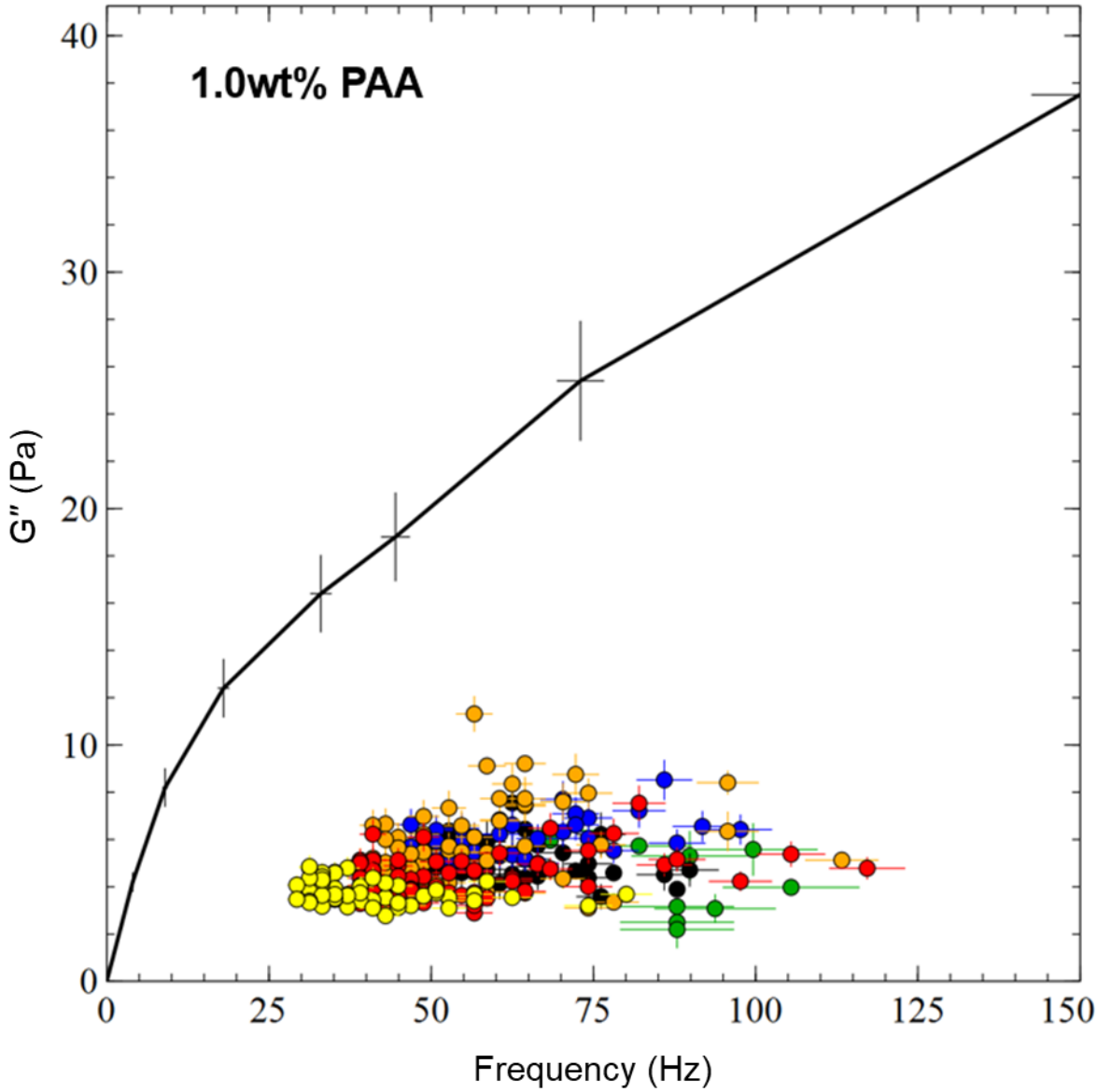


Figure 5.43: The contact angle dependent values for the frequency dependent loss modulus obtained from the Jäckle model evaluation of 1.0wt% PAA solution sessile droplets. The solid black line indicates the data for the storage modulus obtained through dynamic light scattering analysis. Contact angles: Silicon (30°) – green, Aluminium (60°) – black, polystyrene (70°) – blue, wax (90°) - orange, PDMS (93°) – red, Candle soot (145°) – yellow.

The values for the loss modulus appear to have a much greater degree of scatter then the results for the storage modulus, as well as showing a larger degree of deviation from the DLS results.

These results were then scaling in the same manner as the results for the storage modulus in order to bring them in line with the DLS data, the results of which are shown in figure 5.43.

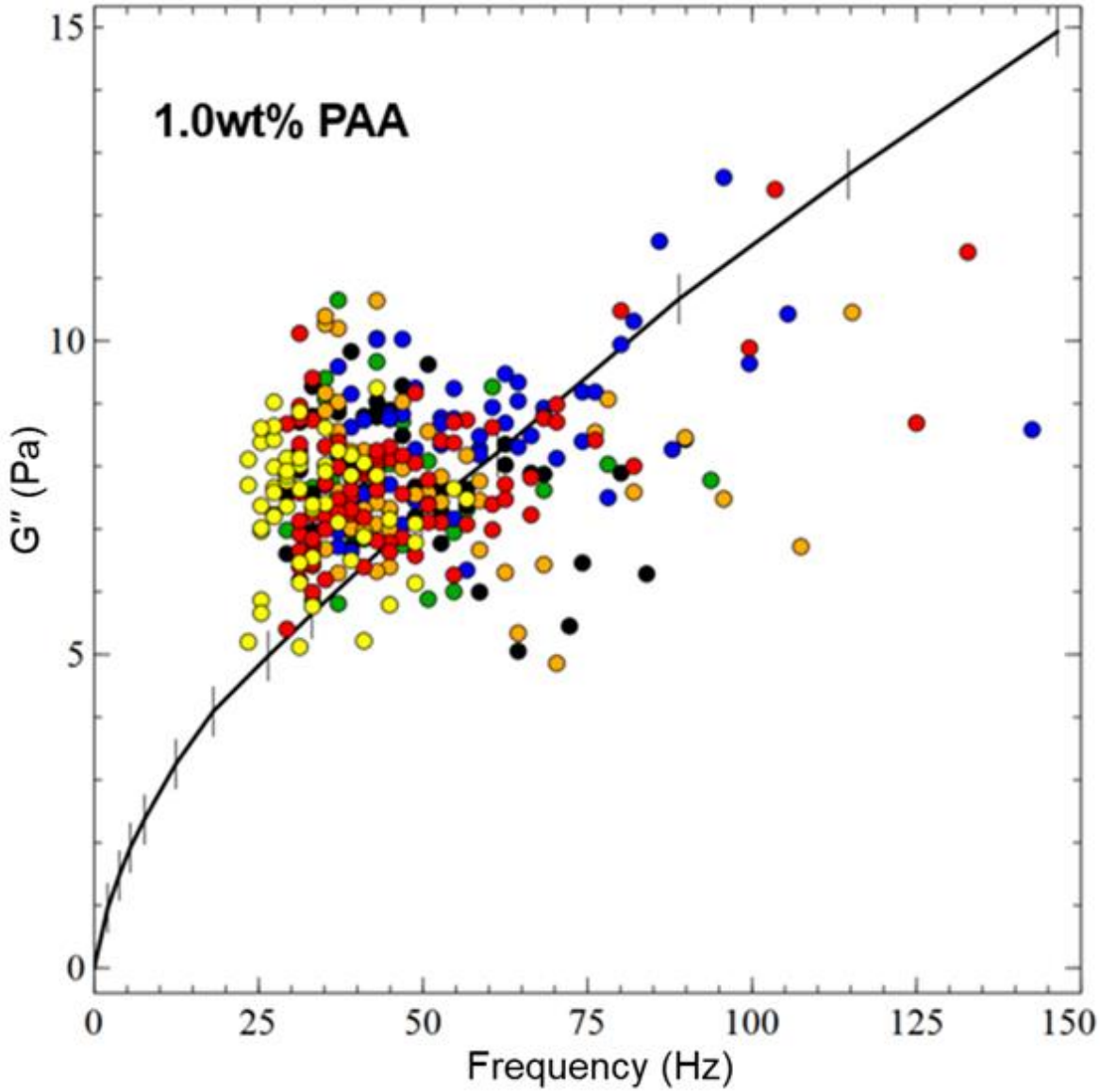


Figure 5.44: The results of scaling the values shown in figure 5.28 in order to bring the results in line with the data acquired from dynamic light scattering analysis.

As can be seen in figure 5.44, the data for the loss modulus is considerably more scattered than that obtained for the storage modulus, making accurate scaling to the DLS data much more difficult. Just as with the storage modulus, this scaling procedure was carried out for each polymer concentration being investigated. As stated previously, the contact angles for each individual substrate at a particular polymer concentration can be found in the table shown on page 102.

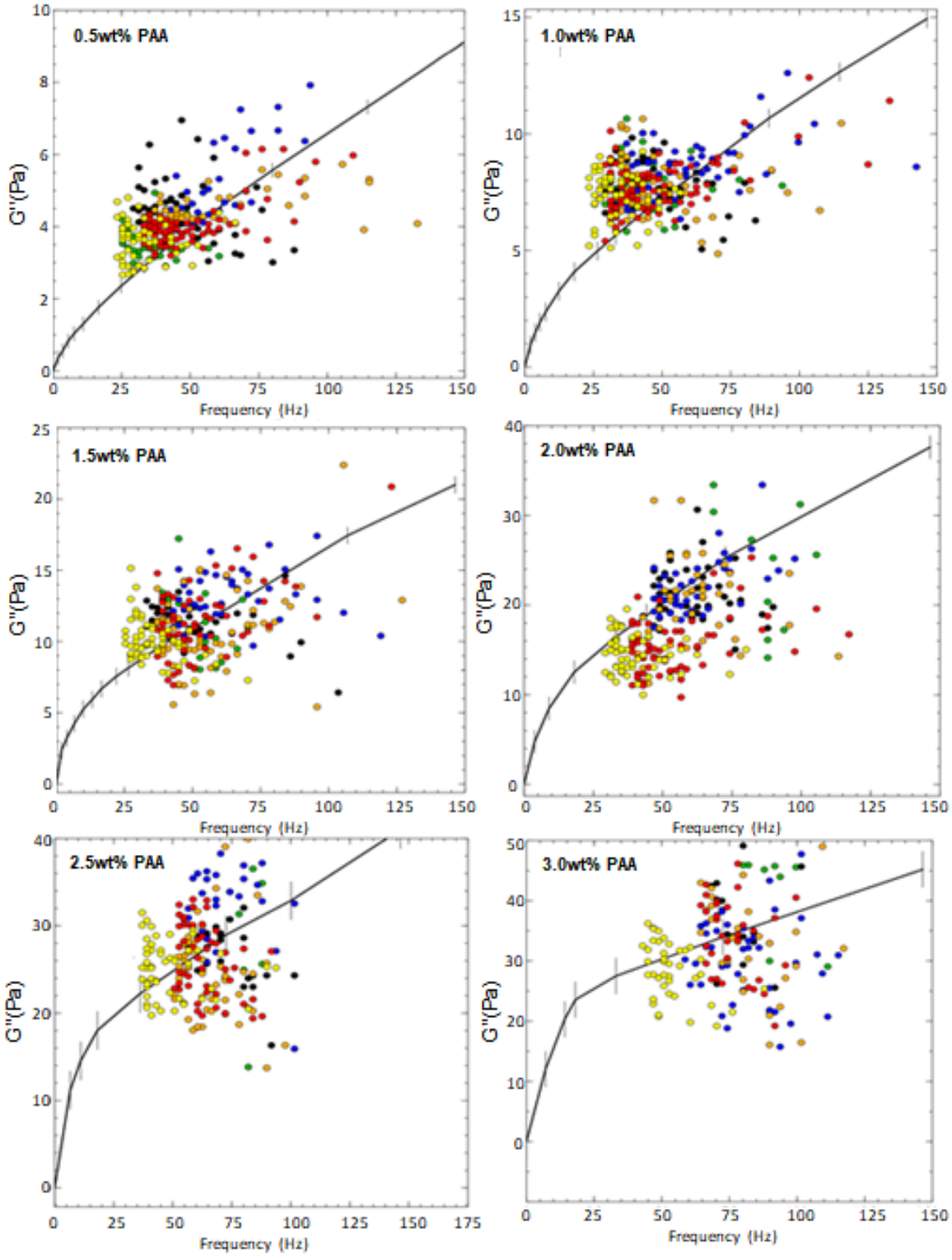


Figure 5.45: The contact angle dependent values for the frequency dependent loss modulus for all six polymer solutions, scaled so that the results correlate with the data obtained from DLS analysis. Substrate: Silicon-green, Aluminium – black, polystyrene – blue, wax – orange, PDMS – red, Candle soot – yellow.

Finally, the inverse of this scaling factor used to bring the data for the loss modulus in line with the DLS data was plotted against contact angle for each individual polymer solution.

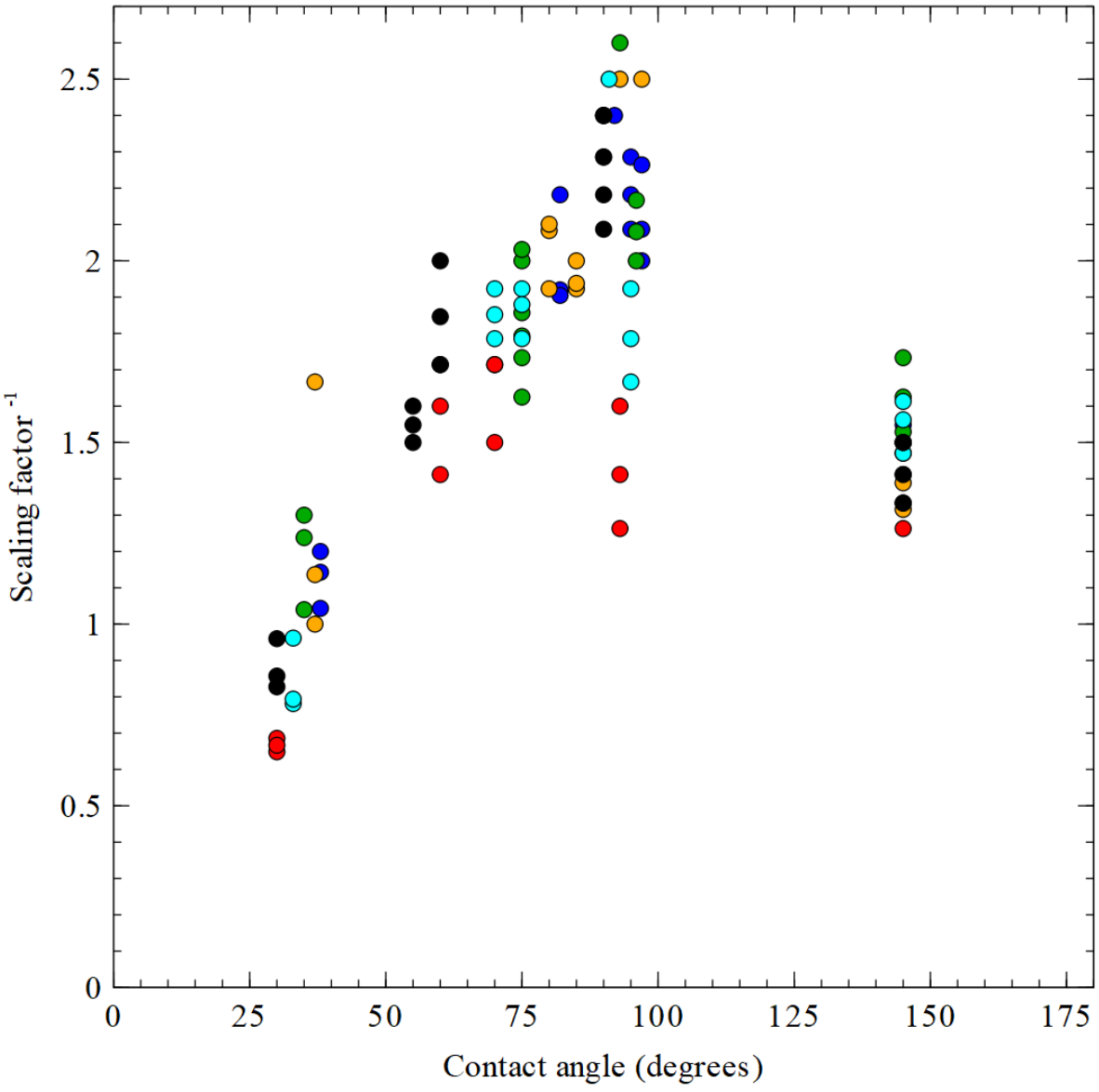


Figure 5.46: The inverse of the scaling factor used to bring the measured values for the loss modulus in line with the DLS data. Polymer concentration: 0.5wt% - black, 1.0wt% - red, 1.5wt% - cyan, 2.0wt% - green, 2.5wt% - yellow, 3.0wt% - blue.

Just as with the storage modulus (G'), straight and curved lines of best fit were applied to the data set for the inverse scaling factor used to bring the results for the loss modulus (G″) in line with the values of the storage modulus that were obtained through dynamic light scattering measurements.

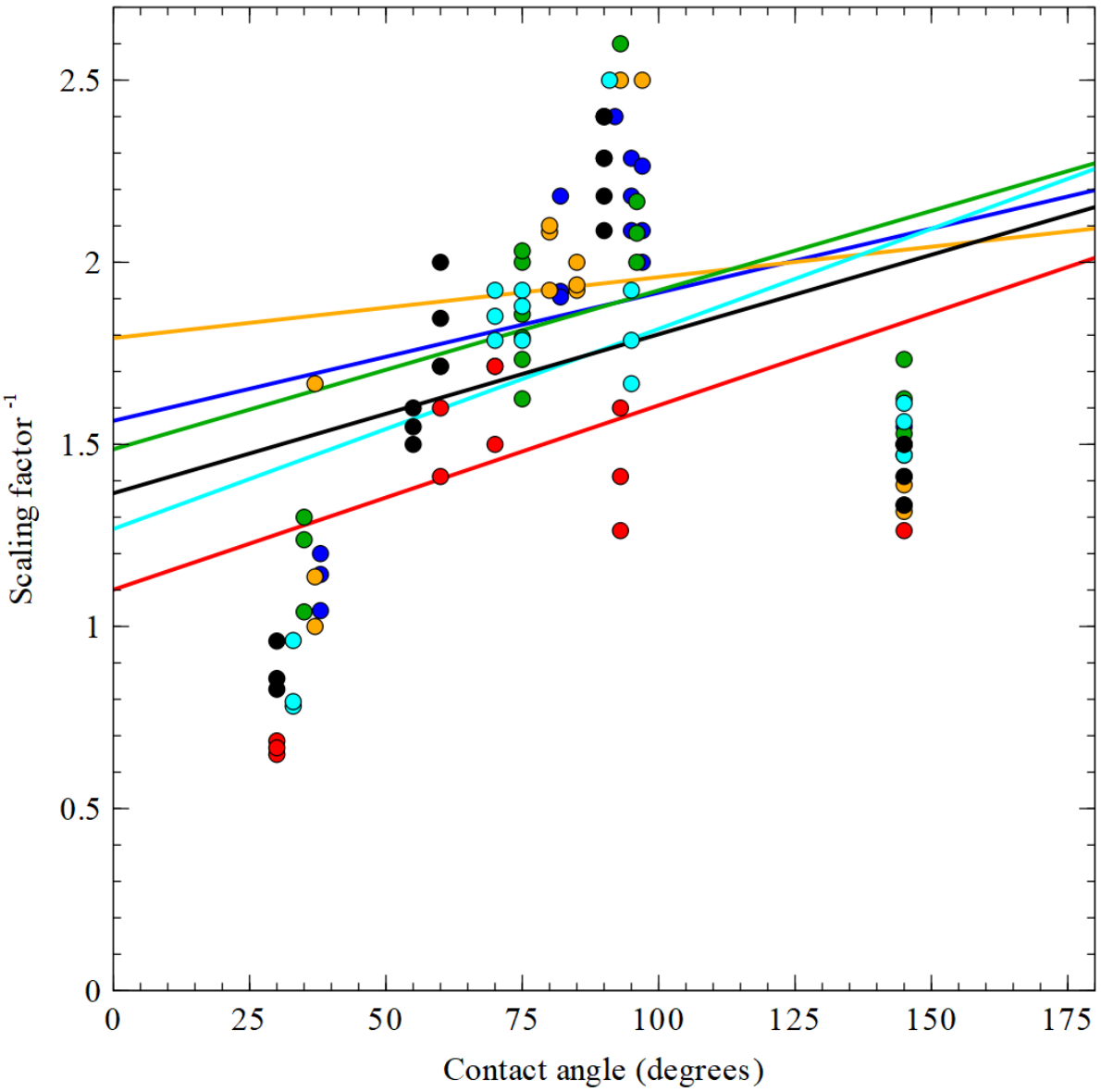


Figure 5.47: The inverse of the scaling factor used to bring the measured values for the loss modulus in line with the DLS data, fitted with lines of best fit (following the equation y=mx+c). Polymer concentration: 0.5wt% - black, 1.0wt% - red, 1.5wt% - cyan, 2.0wt% - green, 2.5wt% - yellow, 3.0wt% - blue.

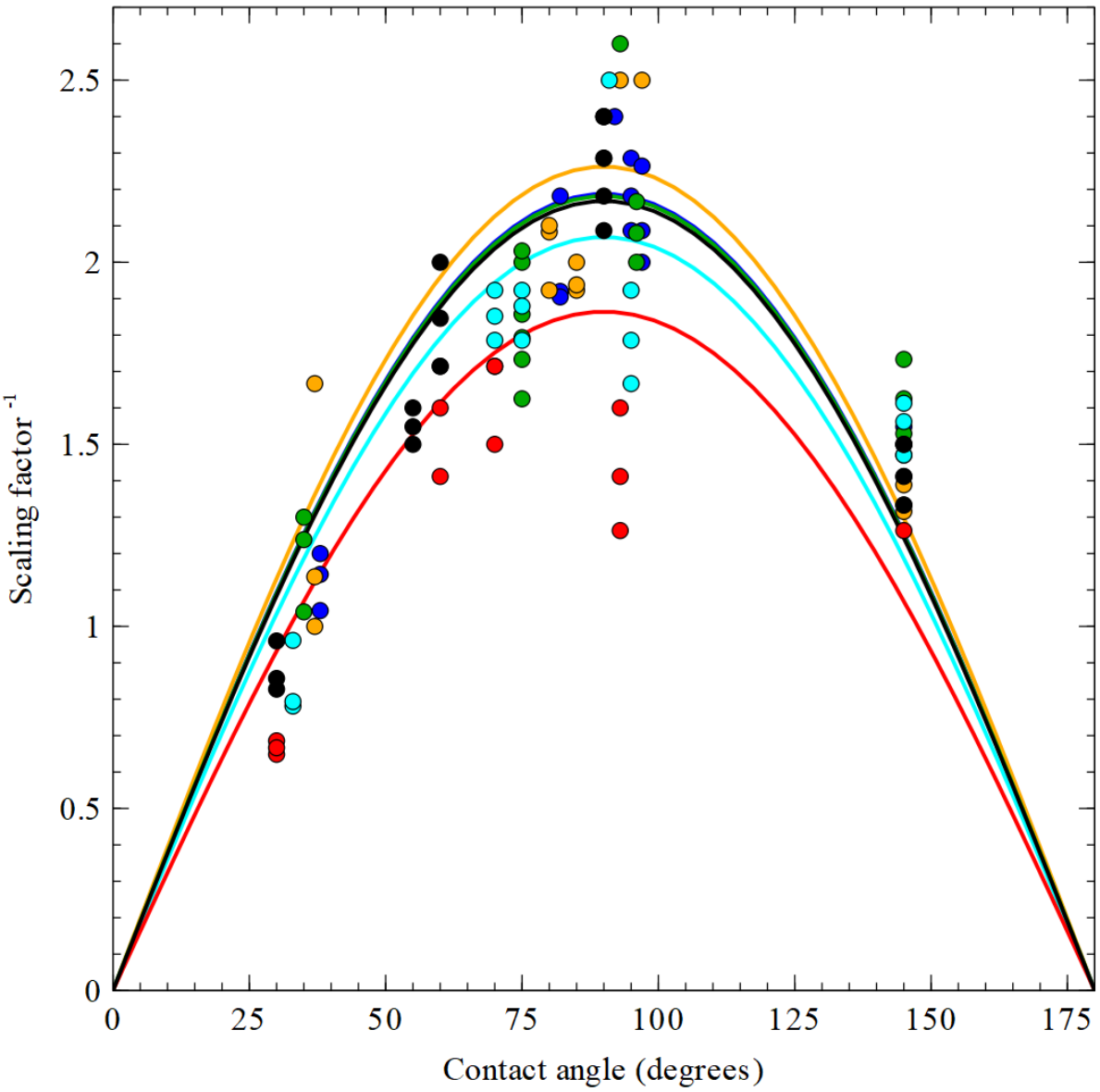


Figure 5.48: The inverse of the scaling factor used to bring the measured values for the loss modulus in line with the DLS data, fitted with lines of best fit (following the equation y=a·sin(x)). Polymer concentration: 0.5wt% - black, 1.0wt% - red, 1.5wt% - cyan, 2.0wt% - green, 2.5wt% - yellow, 3.0wt% - blue.

Polymer concentration (wt%)	R^2 (straight line fit)	R^2 (curved line fit)
0.5	0.1006	0.8717
1.0	0.1194	0.5621
1.5	0.1387	0.6448
2.0	0.1062	0.5357
2.5	0.0113	0.7562
3.0	0.0607	0.8167

Table 5.9: A table to show the result of the regression analysis preformed on the straight-line fits shown in figure 5.47, and the curved line fits shown in figure 5.48.

Polymer concentration (wt%)	aR^2 (straight line fit)	aR^2 (curved line fit)
0.5	0.0442	0.8642
1.0	0.0643	0.5363
1.5	0.0849	0.6239
2.0	0.0500	0.5084
2.5	-0.0051	0.7419
3.0	0.0020	0.8059

Table 5.10: A table to show the result of the adjusted regression analysis preformed on the straight-line fits shown in figure 5.47, and the curved line fits shown in figure 5.48.

Polymer concentration (wt%)	SE (straight line fit)	SE (curved line fit)
0.5	0.5034	0.1844
1.0	0.5152	0.3525
1.5	0.4876	0.3038
2.0	0.4411	0.3084
2.5	0.5244	0.2526
3.0	0.4588	0.1967

Table 5.11: A table to show the result of the standard error analysis preformed on the straight-line fits shown in figure 5.47, and the curved line fits shown in figure 5.48.

As can be seen in tables 5.9-5.11, the curve fit once again proves to fit the scaling factor data far more effectively than the straight line fit. This once again indicates that the scaling factor is indeed dependent upon the contact angle of the sessile droplet, and just like the storage modulus, the reciprocal of the scaling factor appears to peak at a contact angle of 90°. Unlike the results seen for the storage modulus (shown in figure 5.42), it would appear that the scaling factor for the loss modulus does not have the same polymer concentration dependence. With the possible exception of the 1.0wt% concentration (as shown in red in figure 5.48), all of the other concentrations that were tested appear to require roughly the same scaling factor to be brought in line with the DLS data. However, it must be reiterated that the amount of scatter in the data for the loss modulus is notably higher than that of the data for the storage modulus, and the scaling factor is simply the best fit to the DLS data.

It would appear from these results that the damping of the sessile droplets is dominated by the physical geometry of the droplet, whereas the elasticity of the droplet is dependent upon both the physic geometry of the sessile droplet and the physical properties of droplet. This is an unfortunate finding, as it would appear knowledge of the liquid's elasticity is required in order to find the correct scaling factor, which is obviously not very helpful considering the point of the exercise is to discern this information from the measurement of the sessile droplet alone.

Chapter 6

Conclusion and future work

6.1 Conclusion

The attempt at deducing the viscoelastic properties of polymer solutions from sessile droplet vibration produced a number of interesting results. The model appears to show significant promise at being able to determine the viscoelastic properties of sessile droplets which have a contact angle approaching 90°. The results shown in figures 5.35 and 5.36 are very encouraging, despite slight discrepancies when it comes to examining weakly viscoelastic fluids. These results are encouraging and may suggestion that development of this model is worth further investigation.

However, the model has been shown to possess a number of shortcomings, chief among which appears to be an inability to negate the effects of contact angle upon the measured properties of sessile droplets. The scaling factor which is applied to the acquired data sets in order to bring them in line with the data acquired from dynamical light scattering analysis does appear to show a distinct contact angle dependence which appears to be independent of the physical properties of the sessile droplet in regard to the loss modulus. However, data acquired for the loss modulus has such a high degree of scatter that such a conclusion cannot be made with certainty.

Another shortcoming is that the scaling factor for the storage modulus appears to show a distinct dependence on the viscoelastic properties of the sessile droplet (as shown in figure 5.42). This is a serious issue for the model, since the properties of solution must already be known in order acquire the correct information from the model, which makes the entire exercise pointless.

Since this scaling factor (for the storage modulus) does not depend exclusively upon the geometry of the sessile droplet, it must depend upon the physical properties of the solution. A significant flaw in the Jäckle model is that it treats the liquid as a uniform body and does not take into account the possibility of phenomenon such as boundary layers, the depth of which depends upon the viscoelastic properties of the liquid in question (as explained in chapter 2). The Jäckle equation itself has been used previously when describing viscoelastic systems which are typically much thinner than the theoretical models being used in this thesis [61-62], often in the nanometre or micrometre range.

It might well be the case that the Jäckle model is an oversimplification for macroscopic environments, in which the presents of phenomena such as boundary layers can significantly complicate the physical behaviour of viscoelastic media.

The frequency and spectral width of sessile droplet surface waves were shown to have a distinct dependence upon the viscoelastic properties of the sessile droplet being studied, as were shown in figures 5.12 and 5.20. Both the frequency and spectral width increase with polymer concentration, just as the storage and loss moduli also increase with polymer concentration. Since the storage modulus dictates the frequency of the surface wave, and the loss modulus dictates the damping of these surface waves, it may well be possible to directly correlate the frequency and spectra width with the storage and loss moduli. This could potentially provide an effective tool for determining the viscoelastic properties of a sessile droplet, bypassing the need to model the sessile droplet as a liquid bath, or use other complicated analytical techniques.

To summarise, the Jäckle model experiment met with partial success. The model produced encouraging results, which may well indicate that with further development the technique could provide a means through which the viscoelastic properties of sessile droplet may be determined. Despite a number of encouraging results, the model has shown to have a number of fundamental flaws, which must be addressed if the technique is to prove a viable means of analysing viscoelastic liquids.

6.2 Future work

6.2.1 Modification to the Jäckle equation

As explained in chapter 2, the Jäckle model is a model of a liquid bath, not a sessile droplet. The approximation used in this thesis only treat a sessile droplet as a liquid bath, but does not compensate for the droplets geometry, which has been shown to have a significant effect on not only how a sessile droplet oscillates, but also on the results of the Jäckle model. A potential modification that could be made to the Jäckle model would be to have the wavevector k modified with film height, allowing for the "film" to be in effect curved to fit the physical model of the droplet. This could be done by modelling the liquid bath so that its width decreases with depth, as shown in figure 6.1.

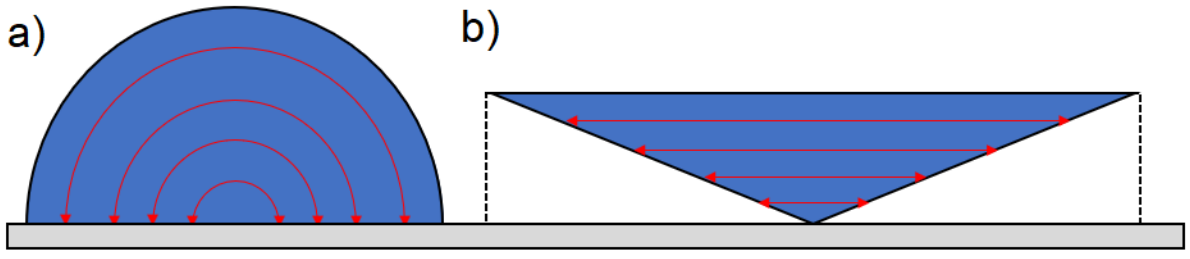


Figure 6.1: A sessile droplet (a) modelled as a liquid bath (b), the width of which decreases with depth, until eventually its width reaches zero when contact is made with the bottom of the liquid bath. The width of this bath is analogous to the circumference of the sessile droplet.

This modification would probably only work with sessile droplets that had a contact angle of 90° or above, but it could potentially allow for the geometry of the system to be compensated for. However, this would not compensate for factors such as the boundary layer, and could simply compensate for the scaling factor, and not address issues such as why the values of G′ vary with polymer concentration. Such a modification would also be extremely complicated.

6.2.2 Further investigation of the Jäckle model

Since the Jäckle model has been proven to work with extremely thin films, it could potentially prove fruitful to use the model described in chapter 5 to investigate sessile droplets which are notably smaller than those investigated in this experiment. If it does prove to be the variation in the boundary layer which causes the concentration dependence on the values of G′, then decreasing the size of the sessile droplets so that their height is below the boundary layer should result in a more uniform set of results.

6.2.3 Direct comparison between surface wave characteristics and viscoelastic properties

In the course of this thesis, it has been demonstrated that both the frequency and spectral widths of sessile droplet surface waves are dictated by the viscoelastic properties of the sessile droplets themselves. A direct comparison between, for example, the frequency of sessile droplet surface waves and the storage modulus (G′) may reveal that these properties can simply be deduced by comparing observations with known values for G′ which correlate with a certain frequency for a sessile droplet of a given size and contact angle. A similar method could potentially be used for determining the lose modulus (G″), comparing the values of spectral width, as opposed to surface wave frequency. Such a tool could prove to be highly valuable as it would facilitate the analysis of viscoelastic droplets with relative ease, and would avoid the complications of attempting to model the droplets, which is proving to be quite a challenge.

6.2.4 Electrostatic levitation

Electrostatic levitation as a technique for analysing surface wave on viscoelastic droplets has been overlooked due to potential complication that might arise due to introducing a charge to the levitated droplet. One major concern is that the surface tension would be modified by this surface charge, which would make calculation (equation 2.19 and 2.20) invalid. However, Millot et al [24] demonstrated a technique which allows for the surface tension of a levitated droplet to be derived. This was demonstrated with aerodynamic levitation, however there is no reason for why the same technique could not be used with electrostatic levitation. If such a technique was proven to be viable, it could prove a very powerful tool for viscoelastic analysis, as electrostatic levitation is notably easier to perform when compared to other forms of levitation, such as magnetic levitation.

6.2.5 Complex biological fluid analysis

As mentioned in the introduction of this thesis, one of the potential application of sessile droplet analysis is to provide a low-cost method for analysing the clotting of blood for the potential diagnosis of conditions such as thrombophilia (a condition which results in blood clotting too readily). The finding in this thesis show a change in viscoelastic properties directly effects the surface waves of sessile droplets, and therefore could potentially be used to track the rate of change in the physical properties of a liquid, for example, the clotting of blood. This particular avenue of research was beginning to be investigated during the course of this research project, with a collaboration forming between Doctor Sharp (of Nottingham University) and Doctor Nash (of Birmingham University). A specialised vibrational stage (a diagram of which is shown in figure 6.2 and a photograph in figure 6.3) was constructed which would allow for sessile droplets of blood to be kept at body temperature (37˚C) within a closed environment (in order to reduce evaporation). The temperature of the stage was maintained via regulating the supply of current to a Peltier device that was imbedded with stage. The temperature of the state was monitored via a thermocouple, which was also imbedded into the stage. The Peltier device itself was controlled via a transistor, which in turn was connected to a DAQ card (along with the thermocouple). This DAQ card would then be used to interface with a labview program, which would monitor the temperature of the stage via the thermocouple and supply current to the Peltier device accordingly. This control over the temperature of the sessile droplets would allow for the rate of coagulation to be investigate in such a way as to allow for the enzymes within the blood to function as they would inside the body.

Unfortunately, time constraints prevented this particular project from being concluded. It is the author's hope that this project in particular be pursued, as its application in the field of medicine has the potential of being able to provide a very simple and cost-effective method for diagnosing potentially fatal illnesses, which might otherwise go unnoticed.

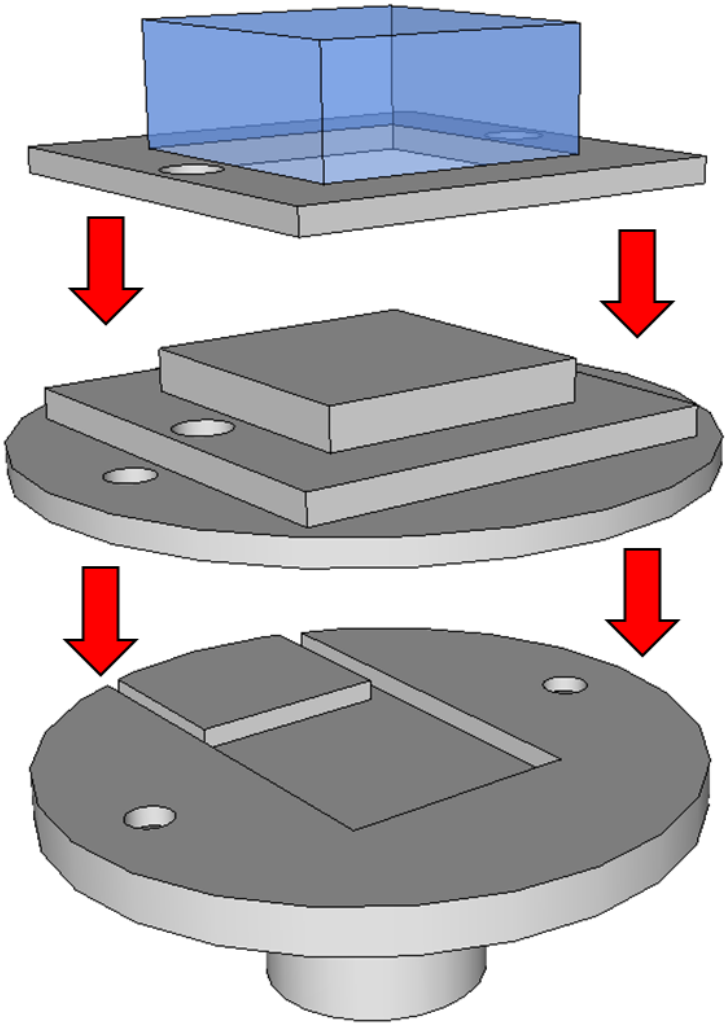


Figure 6.2: A diagram to show the three components (the hood, the stage, and the Peltier device housing) which make up the vibrational stage which is designed to allow the temperature of sessile droplets to be regulated.

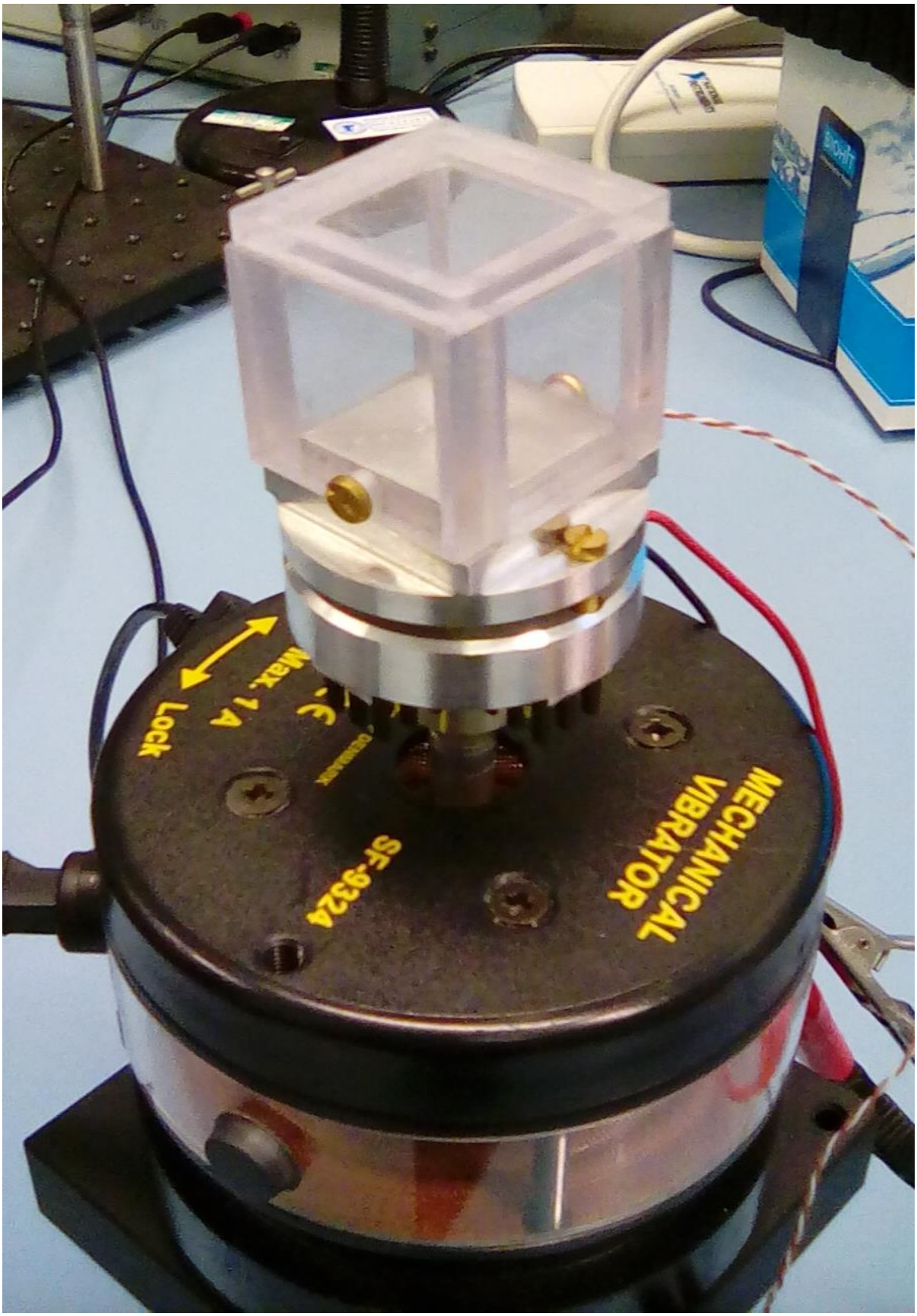


Figure 6.3: A photograph of the fully assembled thermally regulated vibrational stage, connect to a Pasco scientific SF-9324 wave-driver.

Appendix

A.1 Average height of spherical cap weighted by volume

The volume of a spherical cap can be defined as the sum of tube like volume elements, of volume dV, defined by contours of constant height around the surface of the spherical cap.

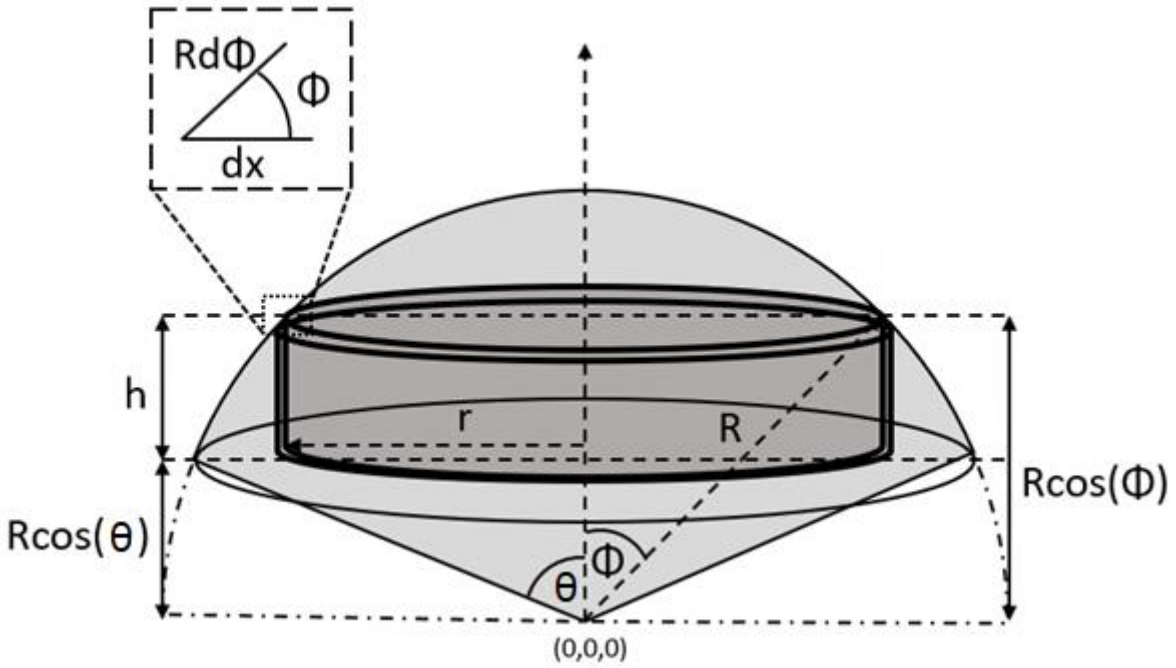


Figure A.1: The geometry of a spherical cap

From the diagram above, it can be seen that:

$$dV = h(2\pi r)(R\cos(\Phi)d\Phi) \quad \text{A.1}$$

Substituting in expressions for the radius and height of the tube:

$$r = R\sin(\Phi) \quad \text{A.2}$$

$$h = R\cos(\Phi) - R\cos(\theta) \quad \text{A.3}$$

yields the equation:

$$dV = 2\pi R^3\left(\sin(\Phi)\cos^2(\Phi) - \sin(\Phi)\cos(\Phi)\cos(\theta)\right)d\Phi \quad \text{A.4}$$

This can be solved for V by integration between $\Phi=0$ and $\Phi=\theta$

$$V = \int_{\Phi=0}^{\Phi=\theta} dV \quad \text{A.5}$$

$$V = 2\pi R^3 \int_0^{\Theta} \left(\sin(\Phi)\cos^2(\Phi) - \sin(\Phi)\cos(\Phi)\cos(\theta)\right) \quad \text{A.6}$$

$$V = \frac{\pi R^3}{3}\left(\cos^3(\Theta\theta) - 3\cos(\theta) + 2\right) \quad \text{A.7}$$

The mean height of the cap can be evaluated by defining dV/V as the probability distribution that describes the volume under the surface of the spherical cap at points of height h. The mean height is therefore defined as:

$$\bar{h} = \sum_i \frac{dV_i}{V} h_i \quad \text{A.8}$$

For continuous distribution this becomes:

$$\bar{h} = \frac{1}{V}\int_a^b h dV \quad \text{A.9}$$

Which can be solved by substitution in the expression for dV (equation A.1),

$$\bar{h} = \frac{1}{V}\int_{\Phi=0}^{\Phi} h\left(2\pi R^2 h\sin(\Phi)\cos(\Phi)\right)d\Phi \quad \text{A.10}$$

$$\bar{h} = \frac{2\pi R^4}{V}\int_{\Phi=0}^{\Phi}\left(\cos(\Phi) - \cos(\theta)\right)^2 \sin(\Phi)\cos(\Phi)d\Phi \quad \text{A.11}$$

$$\bar{h} = \frac{R}{4}\frac{\left(3 - 8\cos(\theta) + 6\cos(\theta)^2 - \cos(\theta)^4\right)}{\left(2 - 3\cos(\theta) + \cos(\theta)^3\right)} \quad \text{A.12}$$

Where R can be defined as:

$$R = \frac{L}{2\theta} \quad \text{A.13}$$

References

[1] B. Vukasinovic, M. K. Smith, A. Glezer (2007) 'Dynamics of a sessile drop in forced vibration', *Journal of Fluid Mechanics,* **587**, pp. 395.

[2] P Gravesen, J Branebjerg, O S Jensen (1993) 'Microfluidics-a review', *Journal of Micromechanics and Microengineering,* **3**(4), pp. 168.

[3] Yager P1, Edwards T, Fu E, Helton K, Nelson K, Tam MR, Weigl BH (2006) 'Microfluidic diagnostic technologies for global public health.', *Nature,* **442**, pp. 412.

[4] Gopalakrishnan N, Hannam R, Casoni GP, Barriet D, Ribe JM, Haug M, and Halaas Ø. (2015) 'Infection and immunity on a chip: a compartmentalised microfluidic platform to monitor immune cell behaviour in real time.', *Lab on a chip,* **15**, pp. 1481.

[5] H. Eltoukhy, K. Salama, A.E. Gamal (2006) 'A 0.18-µm CMOS Bioluminescence Detection Lab-on-Chip', *IEEE Journal of solid-state circuits,* **41**(3).

[6] Thanh-Vinh Nguyen, Minh-Dung Nguyen, Hidetoshi Takahashi, Kiyoshi Matsumoto, Isao Shimoyama (2015) 'Viscosity measurement based on the tapping-induced free vibration of sessile droplets using MEMS-based piezoresistive cantilevers', *Lab on a Chip,* **15**, pp. 3670.

[7] Chien-Han Lin, Chien-Kai Wang, Yu-An Chen, Chien-Chung Peng, Wei-Hao Liao and Yi-Chung Tung (2016) 'Measurement of in-plane elasticity of live cell layers using a pressure sensor embedded microfluidic device', *Scientific Reports,* **6**(36425).

[8] Y. Bayazitoglu, U. B. R. Sathuvalli, P. V. R. Suryanarayana, G. F. Mitchell (1998) 'Determination of surface tension from the shape oscillations of an electromagnetically levitated droplet', *Physics of Fluids,* **8**, pp. 370.

[9] J Brillo (2006) 'Density and Surface Tension of Liquid Ternary Ni–Cu–Fe Alloys',*International Journal of Thermophysics,* **27**(6), pp. 1778.

[10] Robert H. Temperton, Richard J. A. Hilla, James S. Sharp (2014) 'Mechanical vibrations of magnetically levitated viscoelastic droplets', *Soft Matter,* **10**(29), pp. 5375.

[11] Victoria C. Harrold, Maxime Paven, Doris Vollmer, James S. Sharp (2016) 'Rheological Properties of Viscoelastic Drops on Superamphiphobic Substrates', *Langmuir,* **32**(16), pp. 4071.

[12] Victoria C. Harroldam and James S. Sharp (2016) 'Optovibrometry: tracking changes in the surface tension and viscosity of multicomponent droplets in real-time', *Soft Matter;***42**(12), pp. 8790.

[13] Volpatti LR, Yetisen AK (2014) 'Commercialization of microfluidic devices', *Trends Biotechnology,* **32**(7), pp. 347.

[14] Lord Rayleigh (1879) 'On the capillary phenomena of jets', *Proceedings of the Royal Society of London,* **29**, pp. 196.

[15] Lord Kelvin (1890) 'Oscillations of a liquid sphere', *Mathematical and Physical Papers,* **3**, pp. 384.

[16] S. Chandrasekhar (1959) 'The Oscillations of a Viscous Liquid Globe', *London Mathematical Society,* **3**(1), pp. 141.

[17] C. L. Shen, W. J. Xie, and B. Wei (2010) 'Parametrically excited sectorial oscillation of liquid drops floating in ultrasound', *Physics review,* **81**(4).

[18] Jork Leiterer, Markus Grabolle, Knut Rurack, Ute Resch-Genger, Jan Ziegler, Thomas Nann, and Ulrich Panne (2008) 'Acoustically Levitated Droplets: A Contactless Sampling Method for Fluorescence Studies', *The New York Academy of Sciences,***1130**(1), pp. 78.

[19] A. L. Yarin , M. Pfaffenlehner, and C. Tropea (1998) 'On the acoustic levitation of droplets', *Journal of Fluid Mechanics,* **356**, pp. 65.

[20] E. H. Trinh, J. Robey, A. Arce, and M. Gaspar. (1986) 'Experimental Studies in Fluid Mechanics and Materials Science Using Acoustic Levitation', *Materials Research Society ,* **87**, pp. 57.

[21] Zang D, Yu Y, Chen Z, Li X, Wu H, Geng X. (2017) 'Acoustic levitation of liquid drops: Dynamics, manipulation and phase transitions.', *Advances in Colloid and Interface Science,* **243**, pp. 77.

[22] E. Trinh, and T. G. Wang (1982) 'Large-amplitude free and driven drop-shape oscillations: experimental observations', *Journal of Fluid Mechanics,* **122**, pp. 315.

[23] W. Tao Shi and Robert E. Apfel (1995) 'Instability of a deformed liquid drop in an acoustic field', *Physics of Fluids ,* **7**(11).

[24] Francis Millot, Jean Claude Rifflet, Guillaume Wille, Vincent Sarou-Kanian, and Benoit Glorieux (2004) 'Analysis of Surface Tension from Aerodynamic Levitation of Liquids',*American Ceramic Society,* **85**(1).

[25] P. Piluso, J. Monerris, C. Journeau, and G. Cognet (2002) 'Viscosity Measurements of Ceramic Oxides by Aerodynamic Levitation', *International Journal of Thermophysics,***23**(5), pp. 1229.

[26] Sang K. Chung and Eugene H. Trinh (2000) 'Internal flow of an electrostatically levitated droplet undergoing resonant shape oscillation', *Physics of Fluids,* **12**(249).

[27] H. Chetouani, C. Jeandey, V. Haguet, H. Rostaing, C. Dieppedale ; G. Reyne (2006) 'Diamagnetic Levitation With Permanent Magnets for Contactless Guiding and Trapping of Microdroplets and Particles in Air and Liquids', *IEEE Transactions on Magnetics,* **42**(10), pp. 3557.

[28] R. J. A. Hill, and L. Eaves (2012) 'Shape oscillations of an electrically charged diamagnetically levitated droplet', *Applied Physics Letters,* **100**(11).

[29] Robert H. Temperton, Richard J. A. Hilla, James S. Sharp (2014) 'Mechanical vibrations of magnetically levitated viscoelastic droplets', *Soft Matter,* **10**(29), pp. 5375.

[30] Zonglin Chu, Stefan Seeger (2014) 'Superamphiphobic surfaces', *Chemical Society Reviews ,* **43**(8), pp. 2784.

[31] M. Strani and F. Sabetta (1984) 'Free vibrations of a drop in partial contact with a solid support', *Journal of Fluid Mechanics,* **141**, pp. 233.

[32] M. Strani and F. Sabetta (1988) 'Viscous oscillations of a supported drop in an immiscible fluid', *Journal of Fluid Mechanics,* **189**, pp. 397.

[33] Franck Celestini and Richard Kofman (2006) 'Vibration of submillimeter-size supported droplets', *Physical Review,* **73**(4).

[34] Dmitry V. Lyubimov, Tatyana P. Lyubimova, Sergey V. Shklyaev (2006) 'Behavior of a drop on an oscillating solid plate', *Physics of Fluids,* **18**(1).

[35] Noblin X, Buguin A, Brochard-Wyart F. (2004) 'Vibrated sessile drops: transition between pinned and mobile contact line oscillations.', *The European Physical Journal. E, Soft Matter,* **14**(4), pp. 395.

[36] James S. Sharp, David J. Farmer, and James Kelly (2011) 'Contact Angle Dependence of the Resonant Frequency of Sessile Water Droplets', *Langmuir,* **27**(15).

[37] Josef Jäckle (1998) 'The spectrum of surface waves on viscoelastic liquids of arbitrary depth', *Journal of Physics: Condensed Matter,* **10**(32), pp. 7121.

[38] R. Bowers, K. Mendelssohn (1950) 'The viscosity of liquid helium between 2 and 5° K', *Proceedings of the Royal Society,* **204**(1078).

[39] Shucai Li, Pentti K. Järvelä, and Pirkko A. Järvelä (1997) 'A comparison between apparent viscosity and dynamic complex viscosity for polypropylene/maleated polypropylene blends', *Polymer engineering and science,* **37**(1).

[40] Husnu Yildirim Erbil (2009) *Contact Angle Dependence of the Resonant Frequency of Sessile Water Droplets*, : Wiley-Blackwell. pp. 86.

[41] James S. Sharp (2012) 'Resonant properties of sessile droplets; contact angle dependence of the resonant frequency and width in glycerol/water mixtures', *Soft matter,* **8**(2), pp. 399.

[42] L D Landau, E. M. Lifshitz (1987) *Fluid Mechanics* 2nd edn, Pergamon Press. pp. 92.

[43] S. T. Milner (2006) 'Square patterns and secondary instabilities in driven capillary waves', *Journal of Fluid Mechanics,* **225**, pp. 81.

[44] H. Pleiner, J. L. Harden, and P. Pincus (1988) 'Surface Modes on a Viscoelastic Medium', *Europhysics letters,* **7**(5).

[45] Vernon F. Cormier (1989) 'Seismic, Viscoelastic Attenuation', *Encyclopedia of Earth Sciences,* **1**, pp. 1279.

[46] Kadanoff, Leo P.; Martin, Paul C. (1963) 'Hydrodynamic equations and correlation functions', *Annals of Physic,* **24**, pp. 419.

[47] Sigma Aldrich. Poly(acrylamide-co-acrylic acid) 434957, 2017.

[48] (1978) *Linear Polydimethylsiloxanes CAS No. 63148-62-9*, 2nd edn., 4 Avenue E. Van Nieuwenhuyse (Bte 6), B-1160 Brussels, Belgium.: European centre for ecotoxicology and toxicology of chemicals.

[49] A.F. Stalder, G. Kulik, D. Sage, L. Barbieri, P. Hoffmann (2006) 'A Snake-Based Approach to Accurate Determination of Both Contact Points and Contact Angles', *Colloids And Surfaces A: Physicochemical And Engineering Aspects,* **286**(1-3), pp. 92.

[50] Bruce J. Berne and Robert Pecora (2013) *Dynamic Light Scattering: With Applications to Chemistry, Biology, and Physics*, Courier.

[51] Shaoxin Li, Da Xing, Junfeng Li (2004) 'Dynamic Light Scattering Application to Study Protein Interactions in Electrolyte Solutions', *Journal of Biological Physics,* **30**(4), pp. 313.

[52] Bernard Lorber (2006) 'Dynamic Light Scattering For the Noninvasive Detection of Protein Aggregation', *American laboratory ,* **38**(3), pp. 58.

[53] Laurence G. Wilsona and Wilson C. K. Poona (2011) 'Small-world rheology: an introduction to probe-based active microrheology', *Physical Chemistry Chemical Physics,* **13**, pp. 10617.

[54] Albert Einstein and R Fürth (1926) *Investigations on the theory of Brownian movement*, New York, N.Y. Dover Publications.

[55] Pietro Cicuta and Athene M. Donald (2007) 'Microrheology: a review of the method and applications', *Soft Matter,* **3**(12), pp. 1449.

[56] Alastair G Mailer, Paul S Clegg, and Peter N Pusey (2015) 'Particle sizing by dynamic light scattering: non-linear cumulant analysis', *Journal of Physics: Condensed Matter,* **27**(14).

[57] William W. Graessley (1974) *The Entanglement Concept in Polymer Rheology*, Springer Berlin Heidelberg.

[58] Y. Leong Yeow, Christopher J. Pepperell, Firdaus M. Sabturani, Yee-Kwong Leong (2008) 'Obtaining surface tension from pendant drop volume and radius of curvature at the apex', *Colloids and Surfaces A: Physicochemical and Engineering Aspects,* **315**(1-3), pp. 136.

[59] Clyde E. Stauffer (1965) 'The Measurement of Surface Tension by the Pendant Drop Technique', *The Journal of Physical Chemistry,* **69**(6), pp. 1933.

[60] Joseph D.Berry, Michael J.Neeson, Raymond R.Dagastine, Derek Y.C.Chan, Rico F.Taborf (2015) 'Measurement of surface and interfacial tension using pendant drop tensiometry', *Journal of Colloid and Interface Science,* **454**(15), pp. 226.

[61] A. K. Doerr, M. Tolan, W. Prange, J.P. Schlomka, T. Seydel, W. Press, D. Smilgies, and B. Struth (1999) 'Observation of Capillary Waves on Liquid Thin Films from Mesoscopic to Atomic Length Scales', *Physical review letters,* **83**(17), pp. 3470.

[62] Xuesong Hu, Zhang Jiang, Suresh Narayanan, Xuesong Jiao, Alec R. Sandy, Sunil K. Sinha, Laurence B. Lurio, and Jyotsana Lal (2006) 'Observation of a low-viscosity interface between immiscible polymer layers', *Physical review,* **74**(1)

[63] Hyunjung Kim, A. Rühm, L. B. Lurio, J. K. Basu, J. Lal, D. Lumma, S. G. J. Mochrie, and S. K. Sinha (2003) 'Surface Dynamics of Polymer Films', *Physics review letters,* **90**(6)